Kimika Fisikoko Saila
Departamento de Química Física

Synergism between organic and inorganic moieties: In the search of new hybrid materials for optics and biomedicine

DOCTORAL THESIS

Thesis report submitted by

Rebeca Sola Llano

Under supervision of

Dr. Virginia Martínez-Martínez and Prof. Iñigo López Arbeloa

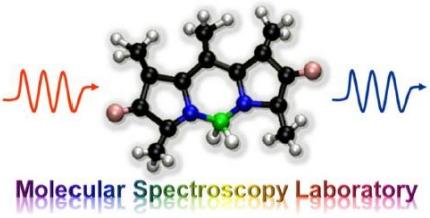

Leioa, January 2017

AGRADECIMIENTOS

Mis agradecimientos van en primer lugar dirigidos a l@s que han hecho posible la realización de esta tesis doctoral, desde la Prof. Teresa Arbeloa, quién tuvo en cuenta mi interés en trabajar en el grupo de Espectroscopía Molecular gracias a una beca de colaboración del Gobierno Vasco, hasta mis directores, la Dra. Virginia Martínez Martínez y el Prof. Iñigo López Arbeloa, que me han enseñado, aconsejado y guiado hasta conseguir lo que hoy tengo en mis manos.

Desde luego, quiero dar las gracias a la Universidad del País Vasco por la concesión de una beca predoctoral, y a todos los grupos de investigación con los que hemos colaborado y que han hecho posible que lleve a cabo esta tesis. En concreto a los compañeros del Instituto de Catálisis y Petroleoquímica (CSIC), especialmente a Almudena Alfayate, Luis Gómez-Hortigüela y Joaquín Pérez Pariente; al equipo de la Katholieke Universiteit de Leuven, Yasuhiko Fujita, Eduard Fron e Hiroshi Uji-i; a Shuhei Furukawa y Susumu Kitagawa de la Universidad de Kioto; a Mª José Ortiz y su grupo de Química Orgánica de la Universidad Complutense, y a Ángeles Villanueva y su equipo de la Universidad Autónoma de Madrid.

Imprescindible dar las gracias a todos y cada uno de los miembros del laboratorio por estar siempre dispuestos a echar una mano. Fue un lujo encontrar el buen ambiente que se respiraba cuando llegué. Leire, Nerea, Ixone y Edu, ¡hacíamos un gran equipo! A todo el resto de compañeros, Jorge, Ruth, Edurne, Hegoi, Virginia, Teresa e Iñigo, gracias por los buenos ratos que hemos pasado. De aquí me llevo grandes amigos. ¡Y los que ya traía de la carrera! Maider, Aimar e Iratxe, porque estos años han dado para mucho.

Por último, pero ni de lejos menos importante, quiero agradecer todo, absolutamente todo, a las personas que hacen que me olvide de todo lo demás. Por estar ahí siempre, por hacerme desconectar cuando más me hacía falta, por un abrazo en el momento preciso y por las sonrisas que alegran el día, por las palabras que no hace falta decir, por el apoyo incondicional, por los ronroneos de mi gordita, los tupper de mi comida favorita, el zumo a primera hora, los viernes de pizza, y los domingos de “manta y peli”. Aita, Ama, Abuelo, Abuela y Aingeru, mil gracias por todas esas pequeñas cosas tan sumamente grandes. Asko maite zaituztet.

SUMMARY

In this work different versatile photoactive hybrid materials with interesting features for diverse applications in the fields of optics and biomedicine are achieved and exhaustively characterized.

Firstly, by means of the occlusion of different fluorescent dyes, by the crystallization inclusion method, into several 1D-channeled magnesium aluminophosphate (MgAPO) hosts (with different sized and shaped pores), optically dense fluorescent hybrid materials which show highly anisotropic response to linearly polarized light are obtained. Depending on the dye embedded within the selected MgAPO framework, interesting applications have been attained, such as one-directional artificial photonic antenna systems covering the whole UV-Visible spectral range, Second Harmonic Generators under NIR radiation, optically switchable hybrid systems and white light emitters.

White light emission is also obtained from the luminescence that arises from embedding simultaneously different small aromatic molecules into a Metal Organic Framework (MOF), so-called $[Zn_2(bdc)_2(dpNDI)]_n$, which contains a photoactive naphtalenediimide as organic pillar. The incorporation of halide-substituted aromatic molecules into this MOF also promotes phosphorescence at room temperature.

Finally, the attachment of a BODIPY chromophore to a cyclometalated Ir(III) metallic centre results in the achievement of efficient photosensitizers for singlet oxygen generation upon visible excitation light. Moreover, these hybrid compounds also show fluorescence emission, thus, they are interesting for bioimaging as well, and as a consequence, extensible to their use in theragnosis.

The photophysical properties of the hybrid materials are deeply analyzed by means of steady-state and time correlated techniques (absorption and emission spectroscopies) and different microscopies (optical and confocal). Furthermore, the final applicability of the materials is proven by sophisticated techniques such as remote excitation measurements, detection of Second Harmonic Generation signal and phototoxicity experiments *in vitro*.

RESUMEN

A lo largo de este trabajo se obtienen y caracterizan exhaustivamente diferentes materiales híbridos fotoactivos muy versátiles que presentan propiedades interesantes para su aplicación en áreas como la óptica y la biomedicina.

En primer lugar, mediante la encapsulación de distintos colorantes fluorescentes por el método de oclusión durante la cristalización en aluminofosfatos dopados con magnesio (MgAPO), todos ellos con estructuras acanaladas unidimensionales (con poros de diferentes tamaños y formas), se han logrado materiales ópticamente densos y con buenas propiedades fluorescentes, que además ofrecen una respuesta altamente anisótropa a la luz linealmente polarizada. Dependiendo del colorante ocluido en una matriz anfitriona de MgAPO concreta, se han alcanzado interesantes aplicaciones, como antenas artificiales unidireccionales que cubren todo el rango espectral del ultravioleta-visible, generadores del segundo armónico bajo radiación infrarroja cercana, sistemas híbridos ópticamente conmutables y emisores de luz blanca.

La emisión de luz blanca se obtiene a su vez a partir de la luminiscencia procedente de la oclusión simultánea de pequeñas moléculas aromáticas en un determinado MOF (Metal Organic Framework), denominado $[Zn_2(bdc)_2(dpNDI)]_n$, en cuya estructura presenta una naftaleno diimida fotoactiva como pilar orgánico. La incorporación de moléculas aromáticas sustituidas con átomos halogenados en dicho MOF promueve además la fosforescencia a temperatura ambiente.

Finalmente, la unión de cromóforos tipo BODIPY a un centro metálico de Ir(III) ciclometalado da como resultado la obtención de fotosensibilizadores que generan oxígeno singlete eficientemente bajo luz de excitación visible. Además, estos compuestos híbridos también muestran emisión fluorescente, por lo que son asimismo interesantes para bioimagen y, como consecuencia, extensibles a su uso en teragnosis.

Las propiedades fotofísicas de los materiales híbridos se analizan en profundidad mediante técnicas estacionarias y resueltas en el tiempo (espectroscópicas de absorción y emisión) y diferentes microscopías (óptica y confocal). Asimismo, la aplicabilidad final de los materiales se comprueba mediante técnicas sofisticadas como son las medidas por excitación remota, detección del segundo armónico y experimentos *in vitro* para el estudio de la fototoxicidad.

LABURPENA

Lan honetan zehar optikan eta biomedikuntzan aplikatuak izateko material hibrido ezberdinak lortu eta sakonki karakterizatu dira.

Lehenik eta behin, dimentsio bakarreko kanalak dituzten magnesioz dopaturiko alumiofosfatoetan (MgAPO, tamaina eta forma desberdinetako poroekin) koloratzaile fluoreszente desberdinak kapsulatu dira materialaren kristalizazioa gertatzen den bitartean, eta horrela, optikoki dentsoak diren eta argi linealki polarizatuarekiko erantzun anisotropoa aurkezten duten material hibridoak lortu dira. MgAPO egituretan txertatzen den koloratzailearen arabera, aplikazio interesgarriak lortu dira, hala nola, ultramore-ikuskor eremu espektral guztia betetzen duten norabide bakarreko antena artifizialak, bigarren harmonikoaren sorgailuak infragorri hurbileko erradiaziopean, sistema hibrido optikoki aldakorrak eta argi zuriko igorleak.

Halaber, naftaleno diimida molekula fotoaktiboa euskarri gisa duen $[Zn_2(bdc)_2(dpNDI)]_n$ egitura metal-organikoan (Metal Organic Framework, MOF) molekula aromatiko txikiak aldi berean kapsulatzean agertzen den luminiszentziaren ondorioz, igorpen zuria lortu da. Gainera, haluroak ordezkatzaile gisa dituzten molekula aromatikoak MOF egitura berdinean sartuz gero, fosforeszentzia giro tenperaturan ere sustatu egiten da.

Amaitzeko, BODIPY kromoforoak Ir(III)-dun ziklo batera lotuz gero, fotosensibilizatzaile eraginkorrak lortu dira, oxigeno singletea sor dezaketenak argi ikuskorrarekin kitzikatuz. Bestalde, material hibrido hauek fluoreszenteak ere badirenez, bioimaginerako eta ondorioz, teragnosirako ere interesgarriak dira.

Material hibridoen ezaugarri fotofisikoak egoera geldikorreko eta denboran ebatzitako teknikak (absortzio- eta emisio-espektroskopiak) eta mikroskopia desberdinak (optikoa eta konfokala) erabiliz aztertu dira. Horretaz gain, material hibridoen aplikagarritasuna teknika sofistikatuak erabiliz frogatu da, hain zuzen ere, urrutiko kitzikapen bidezko neurketen bidez, bigarren harmonikoaren detekzioaz eta *in vitro* fototoxikotasun esperimentuak eginez.

INDEX

Chapter 1: Introduction……...…1

References…….…..7

Chapter 2: Theoretical bases: photophysical processes and systems description……..9

2.1.- Photophisical processes……....11

2.1.1.- Unimolecular processes……11

2.1.1.1.- Fluorescence…….15

2.1.1.2.- Phosphorescence……...20

2.1.1.3.- Delayed fluorescence……21

2.1.2.- Bimolecular processes……..23

2.1.2.1.- Molecular aggregation……..23

2.1.2.2.- Excitation energy transfer processes: FRET…….27

2.1.2.3.- Singlet oxygen generation…….29

2.1.3.- Other optical phenomena interesting for anisotropic systems……..33

2.1.3.1.- Linearly polarized light - matter interaction…….33

2.1.3.2.- Non-Linear Optical Interaction……..…37

2.2.- Host systems……..…40

2.2.1.- Magnesium Aluminophosphates (MgAPOs).……...40

2.2.1.1.- Types of MgAPOs used……43

2.2.1.2.- Fluorescent dye incorporation method……..45

2.2.2.- Metal Organic Frameworks (MOFs)……...……47

References……..…50

Chapter 3: Experimental section……...59

3.1.- Preparation and structural characterization of dye-loaded MgAPOs…….…..61

3.1.1.- Synthesis of dye/MgAPO-5 materials……...…63

3.1.2.- Synthesis of dye/MgAPO-36 materials……64

3.1.3.- Synthesis of dye/MgAPO-11 materials……64

3.1.4.- Dye content determination……....64

3.1.5.- Structural characterization……...….65

3.2.- Preparation of MOF-guest systems……..……66

3.2.1.- Determination of guest content per unit cell……66

3.3.- Photophysical characterization of the hybrid materials……....66

3.3.1.- UV-Vis spectroscopy……....67

3.3.2.- Singlet oxygen emission detection by direct measurements……...70
3.3.3.- Laser flash-photolysis……...71
3.3.4.- Fluorescence microscopy……..72
3.4.- Remote excitation experiments: antenna effect……75
3.5.- NLO measurements……..76
3.6.- Computational details……...78
References……..……...79

Chapter 4: Dye-doped MgAPOs for multiple optical applications……..……..83
4.1.- Dye encapsulation into MgAPO-5 and MgAPO-36: Antenna systems……..…..85
4.1.1.- MgAPO-5/PY hybrid system……....87
4.1.2.- MgAPO-36/PY hybrid system……..91
4.1.3.- MgAPO-36/AC hybrid system……....96
4.1.4.- MgAPO-36/AC-PY hybrid systems……...103
4.1.5.- MgAPO-5/cyanine and MgAPO-36/cyanine hybrid systems…….112
4.2.- Dye encapsulation into MgAPO-11: Hybrid materials for diverse optical applications…….121
4.2.1.- Blue emitting dyes into MgAPO-11……...…122
4.2.2.- Green emitting dyes into MgAPO-11……127
4.2.3.- Red emitting dyes into MgAPO-11……....142
4.2.4.- New optical properties by combination of dyes into MgAPO-11…..158
References……..……..……...168

Chapter 5: Luminescent MOF by host-guest interactions……..……..175
5.1.- Overview of preceding works with $[Zn_2(bdc)_2(dpNDI)]_n$….……...177
5.2.- White Light emission in $[Zn_2(bdc)_2(dpNDI)]_n$ MOF…….180
5.3.- Phosphorescence at room temperature in $[Zn_2(bdc)_2(dpNDI)]_n$ MOF ……....185
References……..……..……...193

Chapter 6: Organometallic complexes as singlet oxygen photosensitizers……..195
6.1.- BODIPY-Biscyclometalated Iridium (III) complexes……....197
References……..……..……...213

Conclusions……....217

Future Outlook……..……....221
References……..……..……...229

List of Publications……....231

1

INTRODUCTION

1

INTRODUCTION

Hybrid organic-inorganic materials are those which combine inorganic and organic components at the nanoscale; thereby, they can be also categorized as nanocomposites.[1] The term "hybrid material" is certainly very wide, and it includes many different systems, such as crystalline highly ordered coordination polymers, amorphous sol-gel compounds, or any molecular system with organic and inorganic moieties of a few Å.[2] Indeed, hybrid compounds can be differently classified. The widespread classification is focused on the nature of the interactions between the organic and inorganic fragments composing the structure.[2,3] In this context, Class I hybrid materials are systems where the different moieties are connected through weak interactions such as van der Waals, hydrogen or ionic bonds.[2,3] On the other hand, Class II hybrids are formed by strong connection between the compounds, such as covalent bonding or coordination bonds.[2,3] Some examples of the different types of hybrid materials are shown in Figure 1.1.

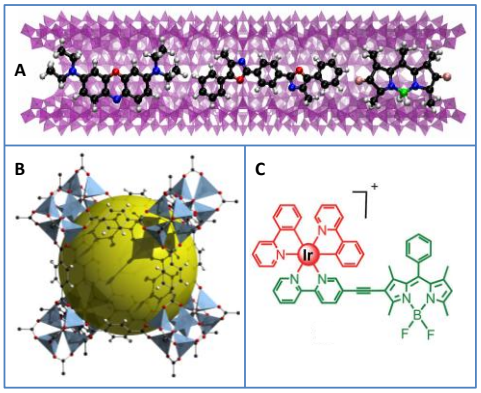

Figure 1.1. Examples of different hybrid materials: A) organic dyes occluded within a zeolite solid (Class I), B) a Metal Organic Framework (MOF), a 3D-crystalline structure composed of inorganic clusters linked by organic ligands (Class II), and C) an organometallic compound (Class II).[4]

Nowadays, research and development of novel hybrid materials has become one of the most expanding fields in materials chemistry. The interest in this type of systems comes because recent advances in many technological applications require specific features of the materials, and frequently the widely known and well established materials such as metals, ceramics of plastics do not meet them.[2,5] In this context, hybrid materials give the opportunity of favorably combining the different properties of organic and inorganic components in a unique system, where the final properties are not mere sum of the individual contributions of both moieties; new or enhanced characteristics can appear by synergistic effects.[1,2]

Although the development of hybrid materials can seem far sophisticated, such intimate blending has been successfully accomplished by nature leading to multifunctional and hierarchical multiscale systems for energy production, sensing, self-healing, surfaces with different properties (insulator, antireflective, superhydropobic, adhesive) and so on.[1,6] It was later when mankind started mixing available sources to improve the utility of the resultant materials for diverse applications; for example, clay-based hybrid composites have been historically employed for different requests such as in laundry processes (mixed with urine) or in paintings (mixed with organic dyes).[1,3,7] A widely known example of the later is the ancient Maya Blue pigment. Maya Blue is a typical Class I hybrid system where the organic indigo dye, derived from the leaves of the *Indigofera suffruticosa*,[8] is intercalated into the nanochannels of palygorskite, a natural clay (Figure 1.2.). Due to the protection provided by the inorganic matrix, Maya Blue is an extremely resistant pigment, and the paintings have not faded over time in spite of the harsh weathering conditions or chemical aggression.

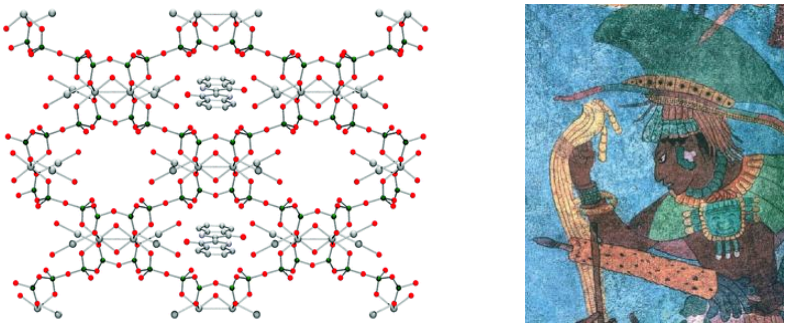

Figure 1.2. Left: Schematic depiction of the structure of Maya Blue pigment, representing the organic indigo molecules into the open sites of the palygorskite framework.[9] Right) Painting in Bonampak Maya city, Mexico, in which Maya Blue was employed.

The interest in hybrid materials continues increasing due to the versatility in their composition and therefore in their properties.[1,2,10] One of the key factors to develop hybrid materials involves the understanding of the structures and principles of the systems found in nature, together with the design and fabrication of commercially appealing devices. At present, the large variety of existing hybrid materials has offered numerous possibilities for a wide range of applications in areas such as optics, electronics, mechanics, energy, environment, medicine and so on.[1,2,5,11–13] Consequently, this research field is of great interest, and future development will bring more complex hybrid materials.

Particularly in this work, very different organic-inorganic hybrid systems will be studied, finding new materials with interesting properties for diverse fields such as optics and biomedicine.

The first type of hybrid materials, described in chapter 4, is based on dye doped zeotypes. Particularly, these materials have been achieved embedding photoactive organic molecules into rigid 1D-magnesium aluminophosphate inorganic hosts. Through this approach diverse interesting systems for numerous optical applications have been developed.[14,15] In this sense, an improvement of the photophysical characteristics and of the photo-, thermal- and chemical-stabilities of the organic dyes have been achieved due to the rigidity and the protection imposed by the host matrix. Furthermore, owing to the occlusion into the one-dimensional channeled zeotypes, a preferential organization of the confined molecules is attained, and as a result, these materials have demonstrated interesting optical properties for potential applications, such as artificial antenna systems, color switching devices or second harmonic generators.[16–18]

On the other hand, studies carried out in a Metal Organic Framework will be detailed in chapter 5. The particular $[Zn_2(bdc)_2(dpNDI)]_n$ MOF used has a photoactive naphtalenediimide organic molecule (N,N'-dipyrid-4-yl-1,4,5,8-naphtalenediimide) as ligand, and as a result of its strong interaction with diverse aromatic guest molecules, the MOF shows different emission colors in the whole visible spectral range under UV excitation light.[19,20] Taking advantage of this molecular sensor feature, white light emission has been achieved by the rational mixing of some of those aromatic guests. It is worth noting that white light emitters are of great interest in the development of new lighting devices. Moreover, also by means of the enhanced interaction between the

organic linker of the MOF and small aromatic guests containing heavy atoms in their structure, phosphorescence at room temperature has been attained.[21]

Finally, based on iridium organometallic complexes, with anticancer action by means of reactive oxygen species, new singlet oxygen photosensitizers have been developed by incorporating BODIPY chromophores to the metallic centre through an appropriate bonding (chapter 6). The significance of these compounds resides in the broadening of the absorption range of the typical iridium complexes from the UV to the visible region, bringing it closer to the biological window, especially necessary for biomedical applications. Their photodynamic therapy (PDT) activity is demonstrated through *in vitro* experiments, showing high phototoxicity even at low concentration-rates, and minimal dark toxicity, minimizing side effects of killing not-irradiated healthy cells. Moreover, a multifunctional hybrid system has been obtained, with a suitable balance between singlet oxygen generation and fluorescence emission that can be very attractive for theragnosis due to the convergence of therapeutic and diagnostic action.

Thus, by the synergistic effect consequence of combining organic and inorganic units, several photoactive hybrid materials exhibiting extremely interesting features have been developed. In this particular case, organic moieties are dye-guest molecules or ligands, and zeotypes and metallic coordination centers are used as inorganic moieties. As a result of these combinations, very versatile materials with potential applications in areas as different as optics and biomedicine are developed.

References

(1) Nicole, L.; Laberty-Robert, C.; Rozes, L.; Sanchez, C. Hybrid Materials Science: A Promised Land for the Integrative Design of Multifunctional Materials. *Nanoscale* **2014**, *6*, 6267–6292.

(2) Kickelbick, G. Introduction to Hybrid Materials. In *Hybrid Materials. Sinthesis, Characterization and Applications*; Kickelbick, G., Ed.; Wiley-VCH Verlag GmbH & Co.: Weinheim, **2007**; pp 1–48.

(3) Sanchez, C.; Julián, B.; Belleville, P.; Popall, M. Applications of Hybrid Organic–inorganic Nanocomposites. *J. Mater. Chem.* **2005**, *15*, 3559–3592.

(4) Zhao, J.; Xu, K.; Yang, W.; Wang, Z.; Zhong, F. The Triplet Excited State of Bodipy: Formation, Modulation and Application. *Chem Soc Rev* **2015**, *44*, 8904–8939.

(5) Parola, S.; Julián-López, B.; Carlos, L. D.; Sanchez, C. Optical Properties of Hybrid Organic-Inorganic Materials and Their Applications. *Adv. Funct. Mater.* **2016**, *26*, 6506–6544.

(6) Bhushan, B. Biomimetics: Lessons from Nature - an Overview. *Philos. Trans. R. Soc. A Math. Phys. Eng. Sci.* **2009**, *367*, 1445–1486.

(7) Ouellet-Plamondon, C.; Aranda, P.; Favier, A.; Habert, G.; van Damme, H.; Ruiz-Hitzky, E. The Maya Blue Nanostructured Material Concept Applied to Colouring Geopolymers. *RSC Adv.* **2015**, *5*, 98834–98841.

(8) Sánchez del Río, M.; Martinetto, P.; Reyes-Valerio, C.; Dooryhée, E.; Suárez, M. Synthesis and Acid Resistance of Maya Blue Pigment. *Archaeometry* **2006**, *48*, 115–130.

(9) Berke, H. Chemistry in Ancient Times: The Development of Blue and Purple Pigments. *Angew. Chemie - Int. Ed.* **2002**, *41*, 2483–2487.

(10) Sanchez, C.; Ribot, F.; Lebeau, B. Molecular Design of Hybrid Organic-Inorganic Nanocomposites Synthesized via Sol-Gel Chemistry. *J. Mater. Chem.* **1999**, *9*, 35–44.

(11) Rottman, C.; Ottolenghi, M.; Zusman, R.; Lev, O.; Smith, M.; Gong, G.; Kagan, M. L.; Avnir, D. Doped Sol-Gel Glasses as pH Sensors. *Mater. Lett.* **1992**, *13*, 293–298.

(12) Shapiro, L.; Avnir, D. Multiple One-Pot Reaction Steps Using Organically Doped Metallic Hybrid Catalyst. *ChemCatChem* **2013**, *5*, 2195–2198.

(13) Sanchez, C.; Lebeau, B.; Chaput, F.; Boilot, J.-P. Optical Properties of Functional Hybrid Organic-Inorganic Nanocomposites. *Adv. Mater.* **2003**, *15*, 1969-1994.

(14) Martínez-Martínez, V.; García, R.; Gómez-Hortigüela, L.; Pérez-Pariente, J.; López-Arbeloa, I. Modulating Dye Aggregation by Incorporation into 1D-MgAPO Nanochannels. *Chem. - A Eur. J.* **2013**, *19*, 9859–9865.

(15) García, R.; Martínez-Martínez, V.; Gómez-Hortigüela, L.; López Arbeloa, I.; Pérez-Pariente, J. Anisotropic Fluorescence Materials: Effect of the Synthesis Conditions over the Incorporation, Alignment and Aggregation of Pyronine Y within MgAPO-5. *Microporous Mesoporous Mater.* **2013**, *172*, 190–199.

(16) García, R.; Martínez-Martínez, V.; Sola Llano, R.; López-Arbeloa, I.; Pérez-Pariente, J. One-Dimensional Antenna Systems by Crystallization Inclusion of Dyes (One-Pot Synthesis) within Zeolitic MgAPO-36 Nanochannels. *J. Phys. Chem. C* **2013**, *117*, 24063–24070.

(17) Martínez-Martínez, V.; García, R.; Gómez-Hortigüela, L.; Sola Llano, R.; Pérez-Pariente, J.; López-Arbeloa, I. Highly Luminescent and Optically Switchable Hybrid Material by One-Pot Encapsulation of Dyes into MgAPO-11 Unidirectional Nanopores. *ACS Photonics* **2014**, *1*, 205–211.

(18) Sola-Llano, R.; Martínez-Martínez, V.; Fujita, Y.; Gómez-Hortigüela, L.; Alfayate, A.; Uji-i, H.; Fron, E.; Pérez-Pariente, J.; López-Arbeloa, I. Formation of a Nonlinear Optical Host-Guest Hybrid Material by Tight Confinement of LDS 722 into Aluminophosphate 1D Nanochannels. *Chem. - A Eur. J.* **2016**, *22*, 15700–15711.

(19) Takashima, Y.; Martínez-Martínez, V.; Furukawa, S.; Kondo, M.; Shimomura, S.; Uehara, H.; Nakahama, M.; Sugimoto, K.; Kitagawa, S. Molecular Decoding Using Luminescence from an Entangled Porous Framework. *Nat. Commun.* **2011**, *2*, 1–8.

(20) Martínez-Martínez, V.; Furukawa, S.; Takashima, Y.; López Arbeloa, I.; Kitagawa, S. Charge Transfer and Exciplex Emissions from a Naphthalenediimide-Entangled Coordination Framework Accommodating Various Aromatic Guests. *J. Phys. Chem. C* **2012**, *116*, 26084–26090.

(21) Martínez-Martínez, V.; Sola Llano, R.; Furukawa, S.; Takashima, Y.; López Arbeloa, I.; Kitagawa, S. Enhanced Phosphorescence Emission by Incorporating Aromatic Halides into an Entangled Coordination Framework Based on Naphthalenediimide. *ChemPhysChem* **2014**, *15*, 2517–2521.

2

THEORETICAL BASES: PHOTOPHYSICAL PROCESSES AND SYSTEMS DESCRIPTION

2

THEORETICAL BASES: PHOTOPHYSICAL PROCESSES AND SYSTEMS DESCRIPTION

In this chapter the theoretical background of the main aspects of this thesis is detailed. In the first part, the most important photophysical processes that will take place in the different systems under study are explained, such as different luminescence types (fluorescence, phosphorescence and delayed fluorescence) followed by relevant bimolecular processes (molecular aggregation including the Exciton Theory, FRET energy transfer and singlet oxygen generation). Next, a brief description of Non-Linear Optics (NLO) and spectroscopy with polarized light are introduced as they are important aspects for the 1D-ordered materials presented in this work. In the second part of this chapter the nanostructured materials used as hosts systems for different organic guests are presented. In particular, the main features of some one-dimensional aluminophosphates with different pore size (MgAPO-5, MgAPO-36 and MgAPO-11) used as hosts for fluorophores are detailed, along with the dye inclusion method; and also the hybrid systems known as Metal Organic Frameworks (MOFs) are briefly described.

2.1. Photophysical Processes

2.1.1. Unimolecular processes

The photophysical processes are those involving transitions among excited electronic states and the ground state after the excitation of the sample through non-ionizing electromagnetic radiation. Photophysical transitions do not cause changes in the chemical composition of the system, which differentiates them from the photochemical phenomena;[1] and they include excitation processes by light absorption from the ground state to excited electronic states and the deactivation processes, as it is shown in the Jablonski diagram in Figure 2.1,[2] useful for unimolecular systems, *i.e.* in gas phase or in diluted solution.

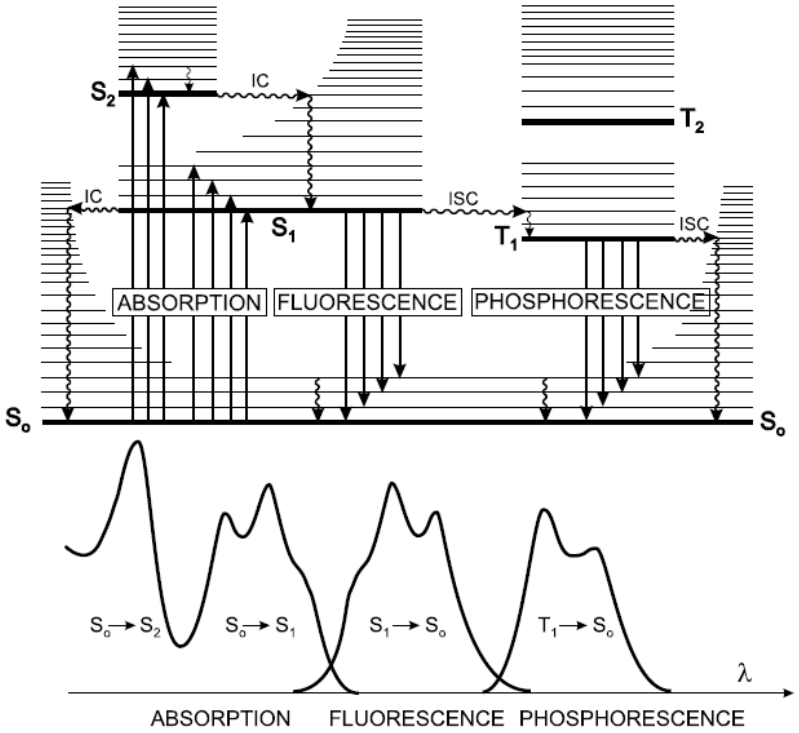

Figure 2.1. Jablonski diagram. Here, the radiant transitions are represented as solid arrows and non-radiant transitions as zigzagging arrows. Every transition that can take place between the ground state (S_0) and singlet (S_1, S_2,…) and triplet (T_1, T_2,…) excited states are shown.[2] IC denotes internal conversion; and ISC, intersystem crossing.

In this diagram (Figure 2.1.), it is considered that the ground state corresponds to a S_0 singlet state because most organic molecular systems are at this level at room temperature. The electronic excitation involves the transition of an electron of the S_0 state to an excited state that can be singlet or triplet state depending on whether the electron keeps or reverses its spin.

Excitation processes consist on the absorption of a photon, by means of which, and depending on its energy, an electron passes from the ground electronic state to one of its excited states. The absorption process is very fast (~10^{-15} s), and in this time range the electron has no time to reverse its spin, so that the excitation usually involves estates of the same multiplicity, *i.e.* from S_0 to S_1 or from S_0 to S_2. This leads to the appearance of electronic absorption bands with a more or less resolved vibrational structure. The absorption band located at lower energies, or at longer wavelengths (λ_{abs}), would correspond to the S_0-S_1 transition, assuming as allowed.

After excitation at a certain wavelength, the intensity of the incident light (I_0) is reduced due to the absorption (I_a) of the sample when light passes through it:

$$I_a = I_0 - I_T \quad \text{(eq. 2.1.)}$$

where I_T is the transmitted intensity.

The absorption intensity is at the same time related to the absorbance (A) of the sample, proportional to the concentration in M (c) and to the optical path of the sample in cm (l), by means of Beer's law:[2]

$$A = lg(I_0/I_T) = \varepsilon cl \quad \text{(eq. 2.2.)}$$

being ε the molar absorption coefficient in $M^{-1}cm^{-1}$, which denotes the capability of a chromophore to absorb light at a given wavelength. This parameter is characteristic of each molecular system. Another way to evaluate the absorption probability is through the oscillator strength (f), determined via the integration of the area under the curve of the absorption band:[3]

$$f = \frac{4.39x10^{-9}}{n} \int \varepsilon(\bar{\nu}) d\bar{\nu} \quad \text{(eq. 2.3.)}$$

where *n* is the diffraction index and $\bar{\nu}$ the wavenumber in cm^{-1}. The oscillator strength is a dimensionless parameter that takes values ranging between 0 and 1. When this value is 0, it means that the transition is forbidden, while if it is near 1, the transition is allowed.

Under a quantum-mechanical point of view, the absorption of the electromagnetic radiation produces a perturbation in the electronic distribution of the molecular system due to the interaction between the electric vector of the radiation ($\vec{E}$) and the electric dipolar moment of the molecule ($\vec{D}$). The absorption probability is given by the square of the modulus of the transition dipolar moment vector ($\vec{M}$), defined as the change in the dipole moment induced by the displacement of charges during the spectroscopic transition. This module can be determined by the following expression:

$$\left|\vec{M}\right| = \int \psi_0^* \hat{\mu} \psi_1 d_T \quad \text{(eq. 2.4.)}$$

where ψ_0^* and $\psi_1$are the wave functions of the initial and final levels respectively, and $\hat{\mu}$ is the dipole moment operator, whose magnitude is equal to the charge multiplied by the distance between the charges of every charge center ($\hat{\mu} = \sum_i q_i r_i$). $\left|\vec{M}\right|^2$is related

to the experimental parameter of oscillator strength, and consequently to the molar absorption (eq. 2.3.), and to the Einstein's coefficient of stimulated absorption (B):

$$B = \frac{8\pi^3}{3h^2c}\left|\vec{M}\right|^2 \qquad \text{(eq. 2.5.)}$$

$$f = \frac{m_e h\nu}{\pi e^2} B \qquad \text{(eq. 2.6.)}$$

being $\left|\vec{M}\right|^2$ and B the sum (integral over $\bar{\nu}$) of the transition moment and Einstein's coefficients respectively for transitions between S_1 (v = 0) and all the vibrational levels of S_0, for example $B = \sum_m B_{0m-10}$. h and c are Planck's constant and light-speed in vacuum, respectively, and e and m_e are the charge and the mass of the electron, respectively.

The concept of the transition moment vector is extremely important in the experiments with polarized radiation since the absorption probability will depend on the relative orientation between this vector and the direction of the electric field of the linearly polarized light, which will allow the elucidation of the orientation of the molecules in macroscopically ordered systems.[2] The basis of the spectroscopy with linearly polarized light will be described later in detail (section 2.1.3.1.).

Regardless of which state is populated after excitation, usually the deactivation to the ground state occurs from the lowest vibrational state (v = 0) of the first electronic excited state (S_1). This is a typical fact since molecular systems promptly lose the excess of excitation energy of high vibrational levels of S_1 or higher electronic states (S_2, etc) through vibrational relaxations together with non-radiative processes of internal conversion. These processes use to occur in hundreds of femptoseconds, particularly the vibrational relaxation in the 10^{-14}-10^{-11} s range and the internal conversion in around 10^{-11}-10^{-8} s. Indeed, they are much faster than the lifetime of the first excited state, which is usually of several nanoseconds.

Following this line, several unimolecular deactivation processes, which are competitive to each other, can occur during the lifetime of the S_1 (v = 0). These processes are depicted in Figure 2.1., and are described now more in detail:

- Firstly, the deactivation to the S_0 ground state can occur directly through radiative deactivation emitting a photon, process denoted as fluorescence. It corresponds to a spectroscopic transition between electronic states with the same multiplicity and it is characterized by a k_{fl} rate constant in the range of

10^7-10^9 s^{-1}. Both absorption and emission are very fast processes and there is no time enough for the nuclei to change their excited state configuration. As a matter of fact, according to the Born-Oppenheimer approximation, the electronic motions are much faster than those of the nuclei, and therefore no changes in the configuration of the nuclei are considered during the electronic transitions (Franck-Condon principle).[2] For this reason, electronic transitions are represented by vertical lines in the Jablonski diagram (Figure 2.1.).

- Another possibility is the deactivation from the first excited state S_1 (v = 0) to a high vibrational level of the ground state S_0 (v) followed by an extremely fast vibrational relaxation (10^{-14}-10^{-11}s). The isoenergetic non-radiative process of conversion from S_1 to S_0 is called internal conversion (IC) and it is defined by the constant rate k_{ic} (10^8-10^{11} s^{-1}). This process is represented as a horizontal arrow in the Jablonski diagram (Figure 2.1.).
- Finally, there might also appear a non-radiative deactivation process from S_1 to T_1 or other triplet state (10^{-9}-10^{-7} s), involving a change in the multiplicity. This process is called intersystem crossing (ISC) and its constant rate is denoted as k_{isc} (10^9-10^7 s^{-1}). Here, T_1 (v = 0) is populated and it can deactivate to the ground state through a radiative deactivation, named phosphorescence, or through a non-radiative process also called intersystem crossing (Figure 2.1.). As special case, sometimes it can occur a reverse intersystem crossing (RISC) from T_1 to S_1, giving rise to the so-called delayed fluorescence, which will be further discussed in detail (section 2.1.1.3.).

2.1.1.1. Fluorescence

As mentioned before, fluorescence is a radiative deactivation process from S_1 (v = 0) to S_0 (v). The fluorescence band will have in this case the vibrational structure corresponding to the ground state. The shape of this band will be the mirror image of the first absorption band provided that there are no important changes in the molecular geometry after excitation (Figure 2.2.), *i.e.* both states have the same vibrational levels distribution.

It must be noted that the 0-0 transition should be the same for both absorption and emission but, as shown in Figure 2.2., the fluorescence band appears at higher wavelengths (lower energies) than the absorption band. This is due to solvent relaxation, which is usually larger in S_1 owing to the typical increase of the dipolar

moment upon excitation. The energy gap between the maximum of the bands of absorption and fluorescence is called the Stokes shift ($\Delta\upsilon_{St}$).

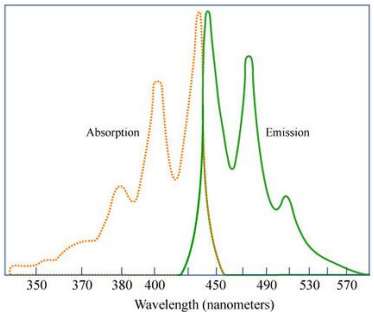

Figure 2.2. Absorption and emission spectra of perylene as illustrative example of the "mirror image" rule.

Regarding the fluorescence intensity (I_{fl}), this will depend on the corresponding deactivation constant (k_{fl}) and on the molecule population in the emissive state ($[S_1]$):

$$I_{fl} = k_{fl}[S_1] \qquad \text{(eq. 2.7.)}$$

$[S_1]$ concentration will be ruled by the number of photons absorbed in the excitation process, and consequently it is proportional to the absorption intensity of the sample at the excitation wavelength (two photon absorption is rejected for conventional excitation lamps or non-powerful lasers). On the other hand, k_{fl} is directly given by the sum (integral over $\bar{\nu}$) of the Einstein's spontaneous emission coefficient of the transitions to all the vibrational levels of S_0; $k_{fl} = A = \sum_m A_{0m-10}$. From a quantum mechanical point of view, the radiation-matter interaction that defines absorption and emission phenomena is of the same type. Then, the probability of transition between two states agrees for both absorption and emission. In fact, Einstein's coefficients of stimulated absorption (B) and spontaneous emission (A) are related to each other:

$$A = \frac{8\pi h\nu^3}{c^3} B \qquad \text{(eq. 2.8.)}$$

Therefore, the experimental parameters that control these probabilities, *i.e.* k_{fl} in fluorescence and the oscillator strength, *f*, in absorption, are related to each other through an equation that states that the more probable is an absorption transition, the more probable will be also the corresponding fluorescence emission:

$$k_{fl} = \frac{8\pi^2 e^2 \nu^2}{m_e c^3} f \qquad \text{(eq. 2.9.)}$$

However, the fluorescence intensity will not only depend on the emission probability; all the non-radiative deactivation processes from the first excited state compete with the fluorescent emission, *i.e.* the unimolecular non-radiative processes of internal conversion and intersystem crossing.[3] The fluorescence efficiency is quantified by the fluorescence quantum yield (ϕ_{fl}) that is the relation between the intensity of emitted radiation and the total radiation absorbed in the excitation process, or the number of emitted photons relative to the number of absorbed photons[2,4]:

$$\phi_{fl} = \frac{I_{fl}}{I_a} \qquad \text{(eq. 2.10.)}$$

It is worth remembering that the typical spectroscopic processes involve a single photon, and generally after excitation all the excited states reach the fluorescent state S_1 (v = 0) before the deactivation to S_0. This means that in stationary excitation conditions, and for unimolecular systems (in gas phase or diluted solution), every absorbed photon is released by one of the deactivation processes from S_1, *i.e.* the number of absorbed photons equals the number of deactivation processes from S_1:

$$I_a = k_{fl}[S_1] + k_{ic}[S_1] + k_{isc}[S_1] \qquad \text{(eq. 2.11.)}$$

and considering also eq. 2.7., equation 2.10 results in:

$$\phi_{fl}^{o} = \frac{k_{fl}}{k_{fl}+k_{ic}+k_{isc}} \qquad \text{(eq. 2.12.)}$$

i.e., the fluorescence quantum yield is given by the ratio between fluorescence rate over the rate of all possible deactivation processes of the S_1 state.

Normally, the fluorescence quantum yield is experimentally determined in solution comparing the fluorescent emission of the sample with a reference whose emission efficiency is known. Those reference compounds have an established fluorescence quantum yield value that is independent of the excitation wavelength; therefore, they can be used as reference as long as they display suitable absorption in the same excitation range of the unknown sample, among other requirements. Usually the absorbance of the sample and the reference are nearly matched at the excitation wavelength and, after recording the emission spectra of both solutions in the same conditions, the areas behind each fluorescence band curve are compared[4]:

$$\phi_{fl} = \phi_{fl,R}\frac{F}{F_R}\frac{A_R}{A}\frac{n^2}{n_R^2} \qquad \text{(eq. 2.13.)}$$

where *F* is the area behind the curve of the emission band, *A* is the absorbance at the excitation wavelength and *n* is the refractive index of the medium where each compound is dissolved. Note that the subscript *R* refers to the values for the reference fluorophore.

However, this procedure cannot be followed to determine the absolute fluorescent quantum yield of solid systems, for example powder samples, as most of the samples that will be studied later. For an accurate measurement of powders an integrating sphere is required. In this case, the quantum yield is measured using a white scatterer, non-fluorescent, which must have diffuse reflectance of 100%. The reference scatterer and the sample are measured in the same conditions in the integrating sphere, recording also the emission region of the lamp scatter, and both spectra are compared.

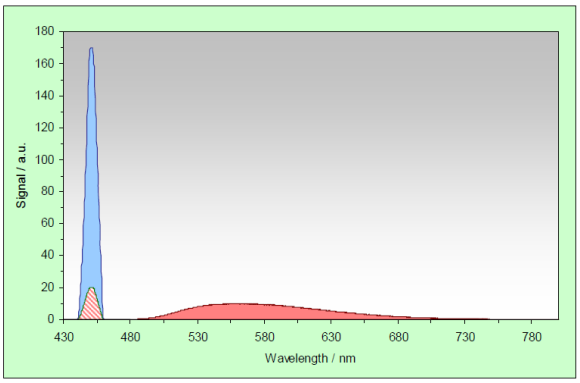

Figure 2.3. Example of the spectra recorded for determining the absolute fluorescence quantum yield of a powder sample. Photo taken from Edinburgh Instruments technical data.

The parameters to consider in order to determine the quantum yield of solid samples are the following: i) the area of the spectrum of the reference, which is only the scatter of the lamp (S_R), blue area in Figure 2.3.; ii) the area under the curve of the reflection of the sample powder (S_S) which is the red hatched area in Figure 2.3.; and iii) the area under the curve of the emission band of the sample powder (F_S), solid red in Figure 2.3. Then, the absolute quantum yield is calculated as follows:

$$\phi_{fl} = \frac{F_S}{S_R - S_S} \qquad \text{(eq. 2.14.)}$$

As a rule, the fluorescence quantum yield is also related to the lifetime of the first singlet excited state. The lifetime of an excited state (τ) is defined as the average time the molecule is in the excited state prior to return to the ground state.[4] Given that the deactivation of this S_1 state can involve different paths (fluorescence emission,

internal conversion or intersystem crossing), the lifetime is related to the constant rates of those processes involving a single molecule that participate in the deactivation, by the following equation:

$$\tau_{fl}^{o} = \frac{1}{k_{fl}+k_{ic}+k_{isc}} \qquad \text{(eq. 2.15.)}$$

Therefore, combining the equations 2.12 and 2.15, it is demonstrated that fluorescence lifetime and fluorescence quantum yield are closely related to each other:

$$\phi_{fl}^{o} = k_{fl}\tau_{fl}^{o} \qquad \text{(eq. 2.16.)}$$

The fluorescence lifetime can be experimentally determined by following the evolution of the fluorescent emission intensity over time after excitation. The fluorescence intensity for a fluorescent molecule that shows a decay with monoexponential kinetics can be described like this[4]:

$$I_{fl}(t) = I_{fl,0}e^{-t/\tau_{fl}} \qquad \text{(eq. 2.17.)}$$

where $I_{fl,0}$ is the intensity immediately after the excitation pulse. The logarithmic representation of equation 2.17. will give a straight line from whose slope the lifetime is obtained:

$$ln\left(I_{fl}(t)\right) = \ln\left(I_{fl,0}\right) - {}^{t}/_{\tau_{fl}} \qquad \text{(eq. 2.18.)}$$

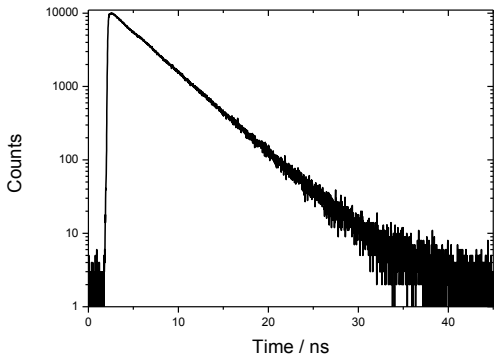

Figure 2.4. Example of a fluorescence decay curve.

Thus, lifetime (τ_{fl}) can be obtained from the fluorescence decay curve (Figure 2.4.) performed by a time resolved fluorescence measurement (more details of the set up in the experimental section, section 3.3.1. in chapter 3).

2.1.1.2 Phosphorescence

Phosphorescence is other radiative deactivation process. While fluorescence occurs by the emissive relaxation from S_1 to S_0 ground state, phosphorescence emission occurs from the first triplet excited state T_1 to the ground state S_0, and it appears at higher wavelengths than fluorescent emission given that the energy of the lowest vibrational level of the first triplet state (v = 0) is lower than that of the S_1 (Figure 2.1.). As previously cited, singlet-triplet processes are forbidden (they involve two states of different multiplicity), therefore they are in general less probable than singlet-singlet processes, and their radiative rate constant (k_{ph}) is low.[2,5] Generally the triplet state (T_1) is populated by intersystem crossing (ISC) from the singlet excited state within its lifetime (10^{-9}-10^{-7} s). This ISC process is fairly inefficient in most organic dyes, but there are some strategies to substantially increase the intersystem crossing probability via spin-orbit coupling mechanism, such as π-system loops, carbonyl substituent groups or the presence of heavy atoms. Indeed, focusing on the presence of heavy atoms, it is known that it increases the interaction between the spin of an electron and its movement around the nucleus; in fact, the extent of the spin-orbit coupling increases with the atomic number Z.[2,3] As a consequence of this coupling both singlet and triplet energy levels acquire a mixed character, assisting the spin-forbidden transitions.[5] This approach to enlarge the spin-orbit coupling is of great interest in applications such as in singlet oxygen generation (described later in detail, see section 2.1.2.3.).

However, owing to the long lifetime of the triplet state (10^{-6}-10 s) in comparison with the average lifetime of an excited singlet state (10^{-7}-10^{-9} s) it is difficult to see the phosphorescent emission in solution at room temperature, because it is more common that the systems relax by non-radiative deactivation, losing excitation energy for example by collisions with dissolved oxygen molecules. In this sense, phosphorescence emission can be activated at low temperatures or in rigid systems where collisional processes are minimized. Note here that phosphorescence will have a decay time approximately equal to the lifetime of the triplet state (ca. 10^{-6} to 10 sec), which can be visible even after switching off the excitation radiation.

2.1.1.3. Delayed fluorescence

Another luminescence phenomenon involving intersystem crossing from singlet to triplet excited state is the so-called delayed fluorescence. What makes this case special is the subsequent reverse intersystem crossing (RISC) from triplet to singlet that follows the first ISC, resulting in fluorescent emission from the S_1 but with a much longer lifetime than the commonly observed prompt fluorescence (lasting several nanoseconds). In contrast, delayed fluorescence can show lifetimes of several milliseconds or even seconds, making the fluorescent emission visible to the naked eye after removing the excitation source. Despite this difference, the band corresponding to the delayed fluorescence is identical to that for the prompt fluorescence, since the transition responsible for the emission is the same in both processes ($S_1 \rightarrow S_0$).

Delayed fluorescence can arise by two different mechanisms, and therefore it is sub-classified into "E-type" delayed fluorescence or thermally activated delayed fluorescence (TADF); or "P-type" delayed fluorescence or triplet-triplet annihilation (TTA).[5] In this work we have specifically dealt with TADF, so this type will be further explained.

In the E-type delayed fluorescence the triplet excited state is thermally activated after the intersystem crossing, *i.e.* the energy needed to jump back to the singlet excited state through the reverse intersystem crossing is achieved because of the effect of temperature (Figure 2.5.).[5] Other conditions that must be met to produce thermally activated delayed fluorescence are a small energy difference between the triplet and the singlet excited states involved in the RISC, and a long enough lifetime of the triplet excited state.[2] This phenomenon was first clearly demonstrated with eosin in glycerol, so sometimes it is referred to as *eosin-type* (*E-type*) delayed fluorescence.[5–7]

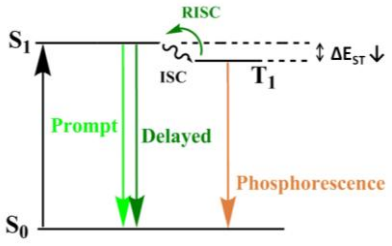

Figure 2.5. Schematic representation of the possible radiative relaxations subsequent to intersystem crossing (delayed fluorescence and phosphorescence) and prompt fluorescence. Green arrows correspond to fluorescent paths.

In case of TADF, it is evident that the constant rate of thermal activation of the step back from the triplet to the excited singlet level (k_e) depends on both the energy gap between S and T, and temperature, through the Arrhenius equation:

$$k_e = Ae^{-\frac{\Delta E_{ST}}{RT}} \qquad \text{(eq. 2.19.)}$$

were A is a frequency factor.

Even if in some cases room temperature is energetic enough to drive a reverse intersystem crossing towards delayed fluorescence, it is not usual to find this phenomenon. Indeed, RISC has to compete with triplet state deactivation processes, *i.e.* with non-radiative decay processes and phosphorescence.

2.1.2. Bimolecular processes

Up to this point, only unimolecular photophysical processes have been considered, in which a single molecule is involved. However, there are important bimolecular processes that can have a significant impact in the photophysical features of the chromophores. In this section only bimolecular processes that are related to the systems under study during this work will be described, *i.e.*, molecular aggregation, Fösters Resonance Energy Transfer, and singlet oxygen generation.

2.1.2.1. Molecular aggregation

One of the main objectives in this work is the preparation of organic-inorganic hybrid systems containing photoactive molecules with the intention of obtaining highly fluorescent materials suitable for different optical applications (Chapter 4). However, optically very dense materials are needed for this purpose, and in these conditions typical fluorescent dyes tend to aggregate, which affects significantly to the photophysical behavior of the monomers due to the coherent coupling of molecular excitons, or Davydov coupling.

In this sense, molecular aggregation in ground state can drastically modify the absorption characteristic of the dyes inducing spectral shifts and band splitting.[8] Moreover, the fluorescence quantum yield and decay times could also be significantly decreased by this associative process.[9,10]

In general, the increase of dye concentration above a certain value characteristic of each system, causes deviations from Beer's law (eq. 2.2.) in the absorption spectra.[11] Under these conditions, the main absorption band of the chromophore decreases and new absorption bands at higher or lower energies appear depending on the geometry of the aggregates, phenomenon denoted as metachromatic effect. In the first stage of dye aggregation (at moderate dye concentrations) dimers are usually formed, but further increase of dye concentration will lead to the formation of high-order aggregates. The proportion in which each molecular species is found will depend not only on the concentration of the dye but also on the aggregation constants. These constants are at the same time dependent on other factors such as the molecular structure of the dye the medium and temperature.[11]

Based on the absorption spectrum of the dimers, the ***Exciton Theory*** can predict some geometrical parameters of those aggregates. The Exciton Theory,[12,13] is a

quantum mechanics method that take into account the electrostatic interactions between the dipole moments of the monomeric units, and can predict different electronic energy diagrams, and consequently, spectroscopic properties, depending on the geometric distribution of the monomer units forming the dimer.

This theory predicts a splitting of the excited state of the monomer into two excited states for the dimer formed when two monomeric species are in a close distance to each other (2-10 Å). The energy gaps between these split excited states and the transition probabilities from the ground state to those excited states depend on the relative orientation of the transition dipole vectors of the monomeric units in the aggregate. Diverse specific cases must be considered taking into account two angles of each dimer's geometry: θ and α. The first one, θ, is the angle between the direction of the dipolar moments of the monomeric units and the line which links the two molecular centers. On the other hand, α is the angle between the orientations of the transition dipole moments of the monomers in the dimer. The different geometries of the dimers and their characteristic spectroscopic properties according to the angles and positions between monomes are schematically depicted in Figure 2.6.

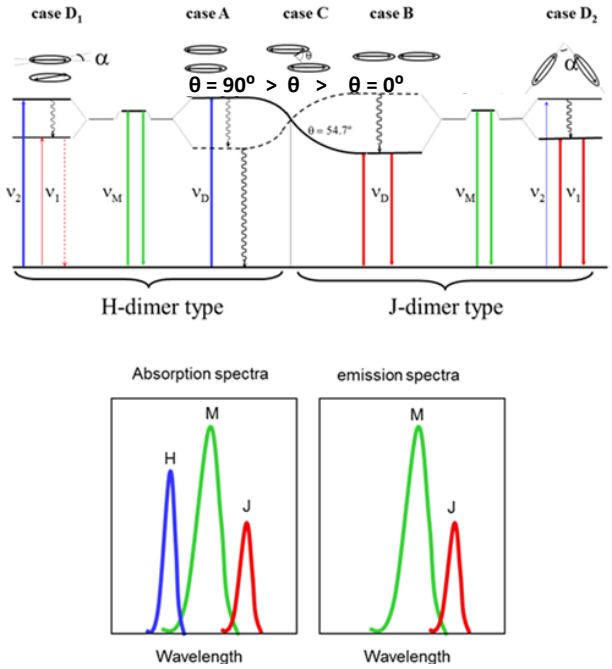

Figure 2.6. Up: Exciton splitting of the electronic states for different geometric dispositions of the monomer units in a dimer. Down: schematic representation of the shifting on the absorption and emission bands of H and J aggregates respect to the monomer.

Dimers are classified in two main types, H- and J-type dimers, and their characteristics are further described below:

- Case A: perfect sandwich dimer (H-dimer). The dipole moment of the monomeric units are perfectly aligned and disposed in parallel planes, therefore, the angles defining the arrangement of the dimer are $\theta = 90º$ and $\alpha = 0º$. After the splitting of the excited state of the monomeric species, the spectroscopic transition from the ground state to the most energetic excited state is the allowed transition (equal to 2f, *i.e.* twice the oscillator strength of the monomer transition, f), while the transition to the lowest energetic excited state is forbidden (the subtraction vector becomes zero). As a result, the absorption spectrum of the dimer would consist on an absorption band placed at higher energies with respect to the typical absorption band of the monomer. This blue-shifted band is so-called H-band. These H-aggregates turn out to be non-fluorescent because of a fast non-radiative deactivation to the lowest excited state which is not fluorescent, and they are also potential quenchers of the fluorescence of the monomeric units.[12]

- Case B: in-line head-to-tail dimer (J-dimer). The dipole moments are coplanar to each other and the molecules are arranged in-line ($\theta = 0º$ and $\alpha = 0º$). This is the opposite case to the H-dimer; the spectroscopically allowed transition (with an oscillator strength of 2f) is now between the ground and the lowest excited state, and the dimer can be potentially fluorescent.[12] In this case, a bathochromically shifted band (J-band) with respect to the monomer band would be observed in both the absorption and fluorescence spectra.

However, these two cases represent extreme and idealistic geometries, but generally aggregates adopt structures with intermediate θ and α angles. Indeed, the geometry of the dimers should be that in which monomers are oriented so that attractive permanent/induced/instantaneous dipole interactions are optimized and repulsive interactions and steric hindrances between monomeric units in the aggregate are minimized.[14] Intermediate cases between A and B are explained below:

- Case C: displaced co-planar dimer, where angles are $\alpha = 0º$ and $0º < \theta < 90º$. In this case, the location of the absorption band of the dimer depends on the θ angle. If it is higher than 54.7º ($\theta > 54.7º$) an absorption band would appear at higher energies comparing with the absorption band of the monomer, *i.e.*

hypsochromically shifted (H-type band). Note that if the θ angle reaches 90º it would be the same as case A. On the other hand, if θ is lower than 54.7º (θ < 54.7º) the absorption band of the aggregate would be placed at lower energies, bathochromically shifted (J-type band), in comparison with the monomer band. Again, if θ angle becomes as small as 0º, it would be the same as case B. For θ < 54.7º the dimers, also called J-type dimers but in a displaced sandwich-like disposition, could be fluorescent, once again with red-shifted emission bands respect to the fluorescent band of the monomers. It is worth noting here that for an angle θ = 54.7º, there will be no splitting effect.

- Case D: there are two cases here, D_1 and D_2, but in both cases H and J absorption bands will be observed in the absorption spectrum if these dimers appear. For D_1 case, the dimer is called twisted sandwich dimer, with θ = 90º and a α angle that can show any value. On the other hand, for the dimer in case D_2, named oblique head-to-tail dimer, the angles are θ = 0º and α again showing any value. As can be expected, the H type blue-shifted absorption band will be more intense for the sandwich dimer (D_1), whereas for head-to-tail dimer (D_2) the J red-shifted absorption band will be more intense. Fujii *et al*.[15] proposed that the ratio between the absorption intensities of those H and J bands, obtained from the area under the curve, is an indicative parameter for the type of dimer. Thus, if this ratio is $A_H/A_J \geq 1.3$, it would be indicative of the presence of the twisted sandwich dimer; while if the value is $A_H/A_J \leq 0.7$ it would be indicative of a head-to-tail geometry.

It is noteworthy here that although it has been mentioned that in some geometries the aggregates can theoretically be fluorescent, their relative quantum yield is generally much smaller than that of the monomer[16]. However, based in this theory it could not be ensured if the fluorescence quantum yield of the dimers would be high or low because it does not detail the non-radiative deactivation processes. On the other hand, some of those aggregates could be non-fluorescent but they could become phosphorescent,[12] since non-radiative deactivations like intersystem crossing can be significant.

2.1.2.2. Excitation energy transfer processes: FRET

Amongst the excitation energy transfer processes, Resonance Energy Transfer (RET) is an extensively studied energy transfer mechanism that can be described as the result of long-range dipole-dipole interactions (Coulombic interaction) between chromophores.[2,4] The term FRET refers to Föster Resonance Energy Transfer, and consists on an energy transfer process between a donor molecule (D) in the excited state and an acceptor molecule (A) in the ground state (Figure 2.7.). It is a nonradiative energy transfer that can take place over relatively long distances (10-100 Å).

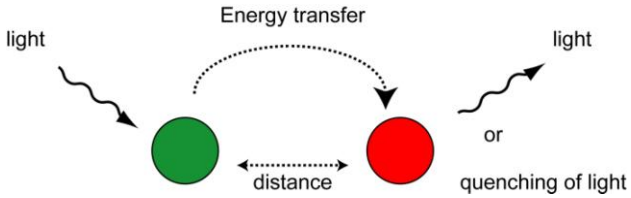

Figure 2.7. Schematic illustration of FRET process between D and A molecules.

The rate of the energy transfer depends on several factors: i) the extent of the overlap between the emission band of D and the absorption spectrum of A; ii) the quantum yield and lifetime of D, iii) the relative orientation between the transition dipole moments of D and A, and iv) the distance between them.[4] Indeed, the distance between D and A at which the efficiency of the energy transfer reaches 50% is called the Förster distance (R_0), and it is typically between 20 and 60 Å (Figure 2.8). Knowing this distance, one can calculate the energy transfer rate in a certain donor-acceptor pair (equation depicted in Figure 2.8.).

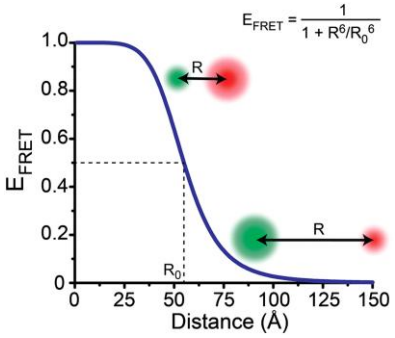

Figure 2.8. FRET efficiency (E_{FRET}) as a function of the distance (R) between a donor fluorophore (green sphere) and an acceptor fluorophore (red sphere) with a R_0 of 55 Å. When $R < R_0$, $E_{FRET} > 0.50$; when $R = R_0$, $E_{FRET} = 0.50$; and when $R > R_0$, $E_{FRET} < 0.50$.

As cited above, Förster's theory is based on long-rate dipole-dipole transfers, characterized by a very weak coupling.[2] Note here the huge influence of the distance between D and A in the efficiency of the FRET (R^6 dependent, Figure 2.8.), and as a result, FRET is often considered a "spectroscopic ruler",[4] for example in measurements of distances between two active sites on proteins that have been labeled with a suitable donor-acceptor chromophore pair, and therefore, the conformational changes can be monitored through the extent of FRET.

It is worth noting that the theory for resonance energy transfer is moderately complex, and only a derived final equation by Föster has been considered here.[4,17]

$$k_T(r) = \frac{\phi_D \kappa^2}{\tau_D r^6}\left(\frac{9000(ln10)}{128\pi^5 N n^4}\right)\int_0^\infty F_D(\lambda)\varepsilon_A(\lambda)\lambda^4 d\lambda \qquad \text{(eq. 2.20.)}$$

where ϕ_D is the quantum yield of the donor in absence of an acceptor, n is the refractive index of the medium and N is Avogadro's number. $F_D\ (\lambda)$ is the corrected fluorescence intensity of the donor in the wavelength range λ to $\lambda + \Delta\lambda$ respect to the total intensity (area under the curve) normalized to unity. ε_A (λ) is the absorption coefficient of the acceptor at λ (typically in units of $M^{-1}cm^{-1}$). The term κ^2 is a factor describing the relative orientation of the transition dipoles of the donor and acceptor species. This orientation factor will play a key role in some of the systems that are going to be part of this work, so it will be described in detail.

The orientation factor κ^2 is given by the following equation:

$$\kappa^2 = (cos\theta_T - 3cos\theta_D cos\theta_A)^2 = (sin\theta_D sin\theta_A cos\phi - 2cos\theta_D cos\theta_A)^2 \text{ (eq. 2.21.)}$$

were θ_T would be the angle between the transition dipoles of the donor and acceptor moieties; and θ_D and θ_A would be the angles between the dipoles of donor and acceptor, correspondingly, respect to the vector that joins the two species. On the other hand, ϕ is the angle between the planes in which the dipole moments of donor and acceptor fall. A schematic representation is added for a better understanding (Figure 2.9.):[4]

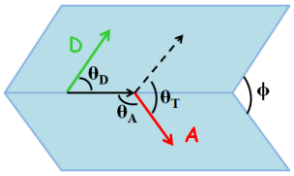

Figure 2.9. Schematic depiction of the angles that contribute in the orientation factor for FRET.

Thus, it can be easy now to predict if an energy transfer is feasible by looking at the relative orientations of the dipoles of the donor and acceptor molecules. For example, if the transition dipole moments of those species are distributed in a head-to-tail arrangement, the orientation factor would have the maximum value possible, 4. Nevertheless, if the dipoles are located perpendicular to each other the value would be the minimum, *i.e.* 0, and this would mean that the FRET is forbidden.

2.1.2.3. Singlet oxygen generation

Singlet oxygen generation is intrinsically related to some of the above mentioned photophysical processes, in particular to the intersystem crossing and FRET processes. Here a molecule called photosensitizer (PS) goes through intersystem crossing to a triplet excited state after excitation with appropriate wavelength, and before the deactivation to the ground state it collides with an oxygen molecule from the surroundings producing the singlet oxygen species $^1O_2$ ($^1\Delta_g$) through an energy transfer process from the photosensitizer to the molecular oxygen.[18]

Schematically, the conversion of the ground oxygen to singlet oxygen can be depicted as in Figure 2.10. The produced singlet oxygen species can be directly detected by its characteristic phosphorescence band centered at around 1270 nm.

$$PS\ (S_0) \xrightarrow{hv} PS\ (S_1) \xrightarrow{ISC} PS\ (T_1)$$

$$PS\ (T_1) + {}^3O_2 \rightarrow PS\ (S_0) + {}^1O_2$$

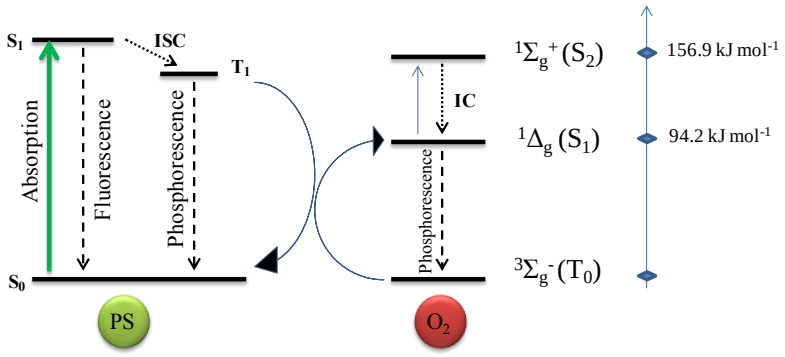

Figure 2.10. Schematic depiction of the photosensitized singlet oxygen generation process.

It is worth noting here that singlet oxygen generation is the basis of photodynamic therapy (PDT),[19–21] since it is a cytotoxic species. Photodynamic therapy (PDT) is a

minimally invasive procedure that offers many advantages over traditional cancer treatments, such as the possibility of PS confinement in the tumor region and the selective light irradiation over the tumor cell. Therefore, the tumor cell can be destroyed while the effects on healthy tissues are limited (Figure 2.11). Moreover, PDT has been proven to be able to kill microbial cells, including bacteria, fungi and viruses, besides being used in clinical treating of a wide range of medical conditions such as acne and malignant cells.[22]

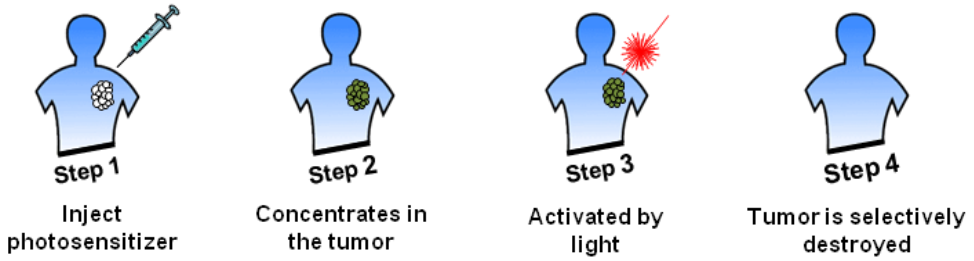

Figure 2.11. Illustration of the different steps in photodynamic therapy.

The conditions that a photosensitizer must fulfill to efficiently generate singlet oxygen are the following: it should show high absorption coefficient in the excitation region; it must show high intersystem crossing performance; and the triplet excited state should be long-lived and with a higher energy than the energy gap between ground and $^1\Delta_g$ states of O_2 (ΔE = 94.2 kJ·mol^{-1}, Figure 2.10.). Furthermore, for application in PDT, a photosensitizer must meet this requirements: i) its toxicity in the absence of light should be low or even null, ii) it should accumulate selectively in cancer tissues, iii) its stability *in-vivo* should be limited in order to favor its removal from the tissues, iv) it should show high molar absorption coefficient in the red region of the electromagnetic spectrum ($\lambda_{abs} > 620$ nm, $\varepsilon \geq 5 \cdot 10^4$ M^{-1}cm^{-1}) to maximize light penetration depth in skin, and v) it should exhibit high quantum efficiency of singlet oxygen generation.[19] Besides, it can be also significant the solubility of the PSs into the aqueous media, since water presence is always important in biological systems, but they should also posses at the same time a hydrophobic moiety to help their diffusion through membranes.[23]

Regarding the different photosensitizers usually employed for the production of singlet oxygen and other reactive oxygen species (ROS), there are a wide variety of chromophore families, such as xanthenes-type dyes, anthracenes, porphyrins, antraquinone derivatives, benzophenone derivatives, metal-based complexes and

fullerenes (Figure 2.12.).[19] The most widespread strategy to promote intersystem crossing (ISC) in order to enhance singlet oxygen generation is the use of the heavy atom effect (spin-orbit coupling). This is based on the enhancement of the rate of a spin-forbidden process by the presence of an atom of high atomic number that can be part of the excited molecular entity (internal heavy-atom effect) or even external to it, *i.e.* in the solvent environment (external heavy-atom effect).[3,24]

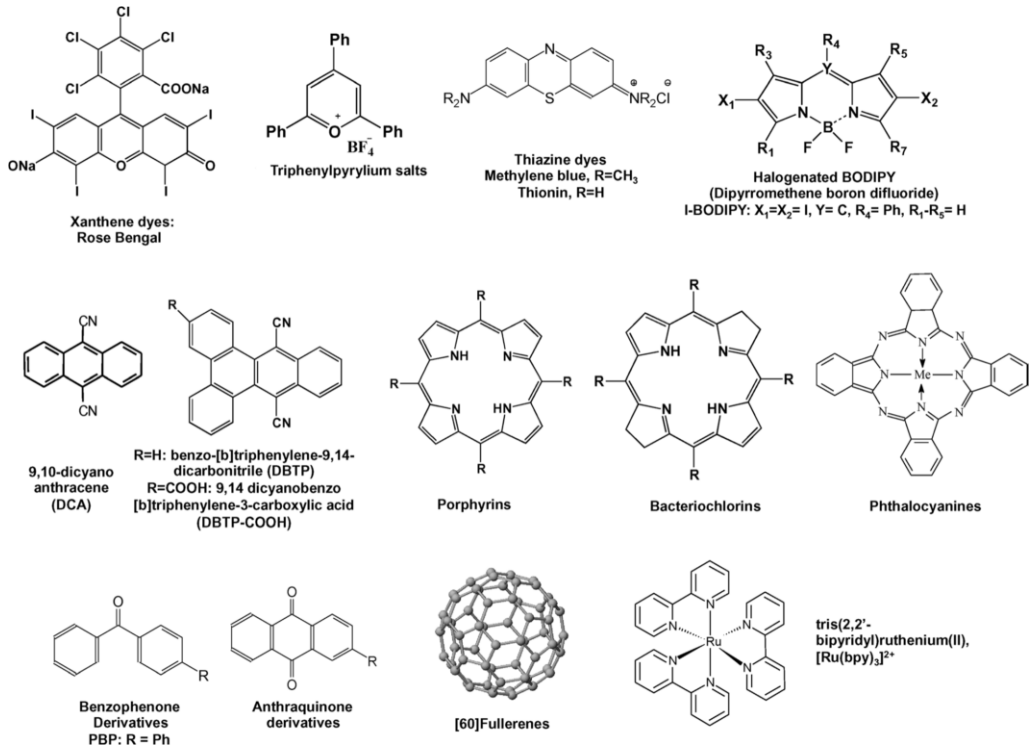

Figure 2.12. Molecular structure of different photosensitizers (PSs).[25]

The capability of singlet oxygen generation of a photosensitizer is quantified by its quantum yield Φ_Δ:

$$\Phi_\Delta = \frac{number\ of\ produced\ \ ^1O_2 molecules}{number\ of\ absorbed\ photons} \qquad \text{(eq. 2.22.)}$$

As happens in the case of fluorescence, one method to measure the singlet oxygen efficiency of a photosensitizer in solution involves the use of a reference compound with a known singlet oxygen production quantum yield. When the singlet oxygen generation efficiency of a PS is close to unity, it means that the intersystem crossing to its triplet state is highly favored and the spin-allowed energy transfer from ^{3}PS* to

ground state molecular oxygen is very efficient. Indeed, the maximum Φ_Δ value is 1, as it happens in the case of fluorescence. An example of a very efficient singlet oxygen photosensitizer usually used as a reference compound is the 1H-phenalen-1-one, or phenalenone, which shows a singlet oxygen generation quantum yield of around 1 in a wide variety of solvents.[18,26,27]

It has been mentioned above that the $^1O_2$ species can relax again to the ground state by phosphorescent emission, but once it is formed, it can be deactivated via several paths. The other routes of deactivation can be i) chemical reaction with a substrate, or ii) physical quenching by collisions with the solvent or other quencher molecules.

Regarding singlet oxygen lifetime (τ_Δ), it should be mentioned that it is proportional to the inverse of k_d, being k_d the constant rate of $^1O_2$ quenching by the solvent $\left(\tau_\Delta \propto \frac{1}{k_d}\right)$. Thus, the lifetime of this reactive oxygen species (ROS) is strongly dependent on the solvent, and it can be as different as 81 μs in acetonitrile or 201 μs in chloroform, experimentally determined in our set up (see chapter 3, section 3.3.1.).

In this work we are going to focus particularly on the singlet oxygen generation of PSs based on iridium containing organometalic complexes with attached BODIPY chromophores (chapter 6).

2.1.3. Other optical phenomena interesting for anisotropic systems

All the photophysical processes described so far are typical for isotropic systems, *i.e.* chromophores in solution. However, since one of the main aims in this work is to achieve hybrid systems with an extraordinarily-preferential alignment of the occluded chromophores, other aspects are here considered. In this sense, the basis of the spectroscopy with polarized light, a powerful tool to determine the degree of alignment, and the second harmonic generation, a nonlinear property consequence of the anistropic distribution of the chromophores within an inorganic matrix are now described.

2.1.3.1. Linearly polarized light - matter interaction

To set the basis of spectroscopy with linearly polarized light, it is first necessary to establish the electromagnetic wave properties of light. Light is electromagnetic radiation that consists on an oscillating electric field ($\vec{E}$) and a magnetic field ($\vec{B}$), which are both perpendicular to each other and perpendicular to light propagation direction.

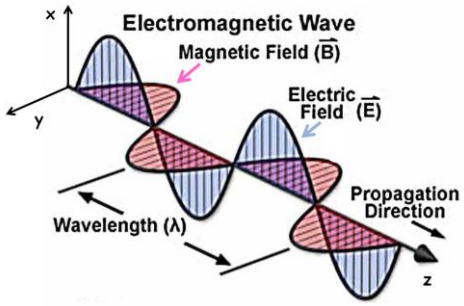

Figure 2.13. Spatial representation of the electromagnetic radiation.

These fields can be described as follows considering z the direction of wave propagation:

$$E\,(z,t) = E^o \sin\,(\omega t - kz + \phi_0) \qquad \text{(eq. 2.23.)}$$

$$B\,(z,t) = B^o \sin\,(\omega t - kz + \phi_0) \qquad \text{(eq. 2.24.)}$$

were E^o and B^o are the amplitudes of each field, ω the angular frequency, k the circular wave number and ϕ_0 a constant that specifies the absolute phase. At the same time, ω and k can be defined as follows:

$$\omega = 2\pi\upsilon \quad \text{(eq. 2.25.)}$$

$$k = \frac{2\pi}{\lambda} \quad \text{(eq. 2.26.)}$$

were υ is the wavenumber and λ the wavelength.

In most cases, electromagnetic radiation is depolarized or, in other words, electric and magnetic fields can take any orientation in the xy plane, being all planes of propagation equally probable. However, when the probabilities in the xy plane are different, it is said that the light is polarized. There are different types of light polarizations, which are applied in different espectroscopies.[28]

- Linearly polarized light. A unique plane of oscillation exist for the electric field, and hence for the magnetic field, in one direction of the xy plane. Thus, if light is linearly polarized in the x direction, the y component of the electric field is zero ($E_y^o = 0$); and y polarized light appears when $E_x^o = 0$. In order to obtain polarized light in any other direction, two radiations in phase have to be combined, and their amplitude ratio has to match with the tangent of the inclination angle:

  $$\frac{E_x^o}{E_y^o} = tg\sigma \quad \text{(eq. 2.27.)}$$

  For example, for a 45º polarized light respect to the x plane, the ratio would have a value of 1. The spectroscopy with linearly polarized light is extensively applied in a wide variety of systems due to its versatility, and it can be useful to obtain information about:
  - Optical properties and molecular structures.[29–31] Lineal dichroism (absorption) and anisotropy (emission) can be applied to determine the directions of the moments of the electronic transitions (UV-Vis) or vibrations (IR) of molecules with low symmetry or new dyes when the prediction of those directions is complicated through theoretical calculations.
  - Orientation of molecules into ordered or partially ordered structures,[32–34] which represents one of the goals of the present work and will be further discussed later in chapter 4. Note here that other phenomena such as Second Harmonic Generation (SHG) and birefringence have been applied for this aim,[35–37] but the application of linearly polarized light is a more versatile procedures.

- Circularly polarized light. In this case the x and y components of the electric field show the same amplitudes ($E_x^o = E_y^o$) but they are 90º out of phase. This way the electric field does not change strength, but it only changes direction in a rotary manner.

  $\phi_0(x) = \phi_0(y) \pm \pi/2$ (eq. 2.28.)

  Circular polarization may be referred to as right-handed or left-handed, clockwise or anti-clockwise, depending on the direction in which the electric field vector rotates. As an example of application, the spectroscopy of circular dichroism is based on the absorption of circularly polarized light of chiral molecular systems, which allows the determination of the absolute configuration of molecules that have asymmetric centers, or are optically active.[38]

- Elliptically polarized light. This case includes the two previous cases since it is obtained with waves of different amplitudes in E_x and E_y and 90º out of phase to each other. If $E_y^o < E_x^o$, the elliptically polarized light has the major axis in the x direction, and vice versa.

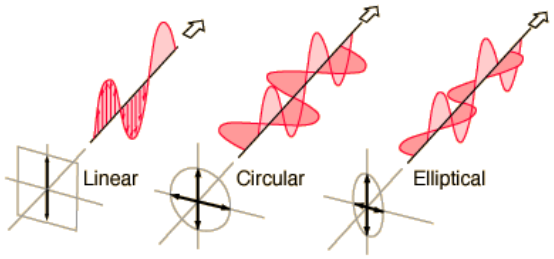

Figure 2.14. Schematic representation of the different polarizations of light.

Now, focusing on the spectroscopy with linearly polarized light, it is worth mentioning that it is based on the probability of absorption/emission of the molecule along a direction, which is proportional to the square of the cosine of the angle between the vectors $\vec{M}$ (transition dipolar moment) and $\vec{E}$ (electric vector oscillating in a given incident polarized light plane), Figure 2.15.

$$A \propto (\vec{E}.\ \vec{M}) = \left|\vec{E}\right|^2 \left|\vec{M}\right|^2 \cdot cos^2\phi \quad \text{(eq. 2.29.)}$$

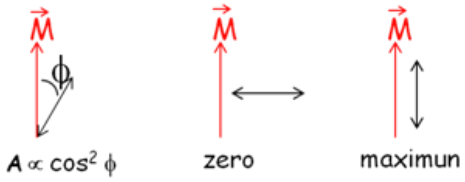

Figure 2.15. Absorption probability of M for different orientations of the linearly polarized light.

Therefore, in isotropic systems, where every molecule orientation is equally probable, the absorption and emission do not depend on the polarized light plane. On contrast, in ordered systems (anisotropic media), the response to the polarized light plane direction will give information about the preferential orientation of the molecular units.

In absorption, different transitions from the S_0 ground state to S_i (S_1, S_2,…) singlet excited states exist, and each transition can have a distinct polarization. Thus, each absorption band will respond in a different way to the plane of polarized incident light.

For emission, since the transition generally occurs from the lowest excited singlet state S_1 to the S_0 ground state, and if S_1 is a Franck-Condon state obtained through absorption, both bands (absorption and emission) will respond in the same manner to the plane of polarized light.

The final probability of emission involves both processes, absorption followed by emission, and experimentally it will link to two different polarizations: the one of the incident light, and which corresponds to the emission towards the detector. Therefore, the fluorescence intensity will be proportional to the individual product of the probabilities of both processes (absorption and emission):

$$I_{u,w} \propto \left|\vec{M}\right|^4 \cdot cos^2\phi_u \cdot cos^2\phi_w \qquad \text{(eq. 2.30.)}$$

were ϕ_u and ϕ_w are the angles between the transition moment and the polarization axis of the excitation light; and between the transition moment and the axis of the emission direction, respectively. $\vec{M}$ is the transition dipolar moment.

One of the bests ways to determine the preferential orientation of a molecular system is through the ***dichroic ratio***, ***D***. In fluorescence measurements, the dichroic ratio is defined as the ratio between intensities registered for orthogonal emission polarizations, keeping constant the excitation polarization. For example, if the

excitation is polarized in X, and the emission in X' and Y', the emission intensity will be proportional to the following:

$$I_{XX'} \propto \left|\vec{M}\right|^4 \cdot cos^2\phi_X \cdot cos^2\phi_{X'} \quad \text{(eq. 2.31.)}$$

$$I_{XY'} \propto \left|\vec{M}\right|^4 \cdot cos^2\phi_X \cdot sin^2\phi_{X'} \quad \text{(eq. 2.32.)}$$

And the consequent dichroic ratio will be given by:

$$D_{X',Y'} \equiv \frac{I_{XX'}}{I_{XY'}} = \frac{cos^2\phi_{X'}}{sin^2\phi_{X'}} = cotg^2\phi_{X'} \quad \text{(eq. 2.33.)}$$

In the present work, polarization experiments will be focused on the fluorescent emission of ordered systems. In this sense, fluorescence emission will be maximum if the polarizer before detection is placed collinear to the transition dipole moment of the molecules, and minimum signal will be collected if the polarizer is set perpendicularly. Indeed throughout this work both linearly polarized light and SHG techniques have been employed to estimate the molecular ordering in different rigid systems, which is one of the main objectives, although the first method has been the more widely used.

2.1.3.2. Non-Linear Optical interaction

The field of nonlinear optics (NLO) covers a wide variety of interesting effects and applications, and it can be quite complex. Although it is not one of the foundations of this thesis, some of the materials here have been prepared so that they show promising properties in this field. Therefore, certain phenomena of NLO are going to be explained for a better understanding in the following chapters.

Generally, nonlinear optics is of high interest in numerous fields, such as in communication technologies, computing, laser technology and so on.[39,40] Moreover, materials which show NLO properties are even being applied in biomedicine research, particularly in bioimaging and photodynamic therapy.[41,42]

Nonlinear optics refers to a particular interaction of electromagnetic fields in diverse media, and as a consequence new electromagnetic fields are produced which are altered in phase, frequency, amplitude or other propagation characteristics, comparing with the incident field.[43] These phenomena are considered nonlinear as the response of the material depends on a nonlinear way on the strength of the incident

field.[44] For the purpose of describing that nonlinearity, it is considered that the polarization of the material, or the dipole moment per unit volume ($\widetilde{P}(t)$), depends on the strength of the applied field ($\widetilde{E}(t)$). Note that the tilde (~) is used to express a magnitude that varies quickly in time. In the case of linear optics there is a linear dependence that can be expressed as follows:

$$\widetilde{P}(t) = \epsilon_0 \chi^{(1)} \widetilde{E}(t) \qquad \text{(eq. 2.34.)}$$

where $\chi^{(1)}$ and ϵ_0 are the linear susceptibility and the permittivity of free space, respectively. On the other hand, in nonlinear optics the polarization response of the medium changes with the strength of the applied field, and it can be described as a sum of the linear term and nonlinear terms:

$$\widetilde{P}(t) = \epsilon_0 [\chi^{(1)} \widetilde{E}(t) + \chi^{(2)} \widetilde{E}^{\,2}(t) + \chi^{(3)} \widetilde{E}^{\,3}(t) + \cdots] \qquad \text{(eq. 2.35.)}$$

Here, $\chi^{(2)}$ and $\chi^{(3)}$ coefficients are second- and third-order nonlinear optical susceptibilities of the medium, respectively.[44] For instance, a second-order nonlinear process will be characterized by $\chi^{(2)}$.[45] It should be noted here that second-order nonlinear interactions with the incident field can only appear in noncentrosymmetric crystals, *i.e.* in crystals where inversion symmetry does not exist. Otherwise $\chi^{(2)}$ vanishes. However, for third-order nonlinear optical interactions, described by a $\chi^{(3)}$ susceptibility, both centrosymmetric and noncentrosymmetric media are suitable.[44]

NLO materials can be classified by their chemical nature, *i.e.* depending on if they are inorganic or organic materials, both of which show several advantages and disadvantages. Historically, the most widely used materials were inorganic crystals such as quartz, potassium dihydrogen phosphate (KDP), β-barium borate (BBO) or semiconductors such as cadmium sulfide (CdS). Despite showing good physical properties and bulk susceptibility, the choice of these inorganic materials is limited besides other disadvantages such as low NLO response (semiconductors), the need of a sophisticated synthesis process, poor response time and so on.[46–48] Organic compounds emerge as an alternative to the above materials, with a long list of advantages, for instance strong NLO properties, low cost and ease of fabrication, and short response time to excitation, to name a few. Their NLO signal can be also tuned by straightforward variations into their structure, so they can be very versatile.[46,49] Specifically, the second order response of an organic molecule can be predicted by the magnitude of its first hyberpolarizability value (β), or molecular second-order response coefficient. In this sense, the second order response of a molecule can be

enhanced by either increasing the electronic asymmetry (with stronger donating or accepting substituent groups) and increasing the conjugation length between substituents.[50] Conversely, organic compounds are more susceptible to degradation than inorganic ones, and also the packing of the molecules plays a crucial role in the final properties of the material. As an example for this type of materials, urea is one of the most widely known organic compounds for NLO applications.[51]

Among others, ***Second Harmonic Generation (SHG)*** is one of the most common NLO properties. It is a second-order nonlinear effect that consists on the conversion of the incident laser beam into a beam with twice the frequency.[44] It was first seen by Franken *et al*. in a quartz crystal, obtaining UV output radiation from a laser beam with a wavelength of 694.2 nm.[52] Since it is a second-order nonlinear effect, the material capable to generate the second harmonic must be noncentrosymmetric.

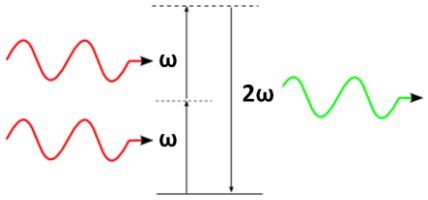

Figure 2.16. Schematic energy-level diagram describing SHG. Dashed lines correspond to virtual levels.

Thus, throughout this process light with half the wavelength tan the precursor light is obtained (from $\lambda \rightarrow {}^{\lambda}/_{2}$), *i.e.* with twice the energy (from $h\upsilon \rightarrow 2h\upsilon$), by the combination of two equal photons.

In this work, a hybrid organic-inorganic material suitable for SHG was obtained by means of a preferentially aligned chromophore guest into an inorganic host. The SHG response is thoroughly studied in chapter 4.

2.2. Host systems

In this work, different host-guests systems have been used. On the one hand, in chapter 4, different organic fluorophores have been encapsulated into inorganic zeolitic hosts, particularly into one-dimensional magnesium aluminophosphates of different pore size, in order to get an improvement of the photophysical properties of the chromophores and to obtain new features such as the antenna effect or SHG, among others. On the other hand, in chapter 5, an entangled porous coordination polymer (PCP) or Metal-Organic Framework (MOF) based on naphthaleediimide (NDI) is used as host for small aromatic guests to develop interesting photophysical properties such as phosphorescence at room temperature or white light emission. In this section, the two different host systems are briefly described.

2.2.1. Magnesium Aluminophosphates (MgAPO)

Crystalline materials with an open structure have attracted great scientific interest since before the middle of the last century. Specifically, in the 30s it was discovered that natural zeolites behave as molecular sieves, and since then their study increased exponentially, finding them useful as catalysts and in molecular sieving processes and selective ion exchange.[53,54] Due to the interest they aroused, synthetic zeolites have been also developed, with Barrer, Milton, Breck and co-workers as pioneers, who synthesized an aluminosilicate zeolite mimicking the geothermal formation of natural zeolites.[55,56]

Zeolites are crystalline aluminosilicates composed by elements of IA and IIA groups, with this general chemical depiction: $M_{2/n} : Al_2O_3 : y\ SiO_2 : w\ H_2O$, where y goes from 2 to infinite, n is the valence of the cation and w represents the water contained in the zeolite cavities. Its structure consists on a three-dimensional network built of AlO_4 and SiO_4 tetrahedra interconnected forming a porous system which is usually filled with cations and water molecules. The need to contain cations is given by the negative charge of the framework, which comes from the charge deficiency of Al(III) in contrast to Si(IV). Thus, cations are required to compensate the net negative charge, and their presence into the structure gives rise to the formation of Brønsted acid sites. Water molecules and cations can be removed from inside the zeolite without losing the structure of the host material, and therefore a large empty space that can accommodate many types of compounds is available. This property makes the

zeolites very attractive materials from the point of view of applications, along with other features as their environmentally friendly nature and their stability under vacuum up to high temperatures, interesting for industrial usage.

By 2007 (in the last edition, 6th, of *Atlas of Zeolite Framework Types*),[57] 176 unique zeolite framework types were approved by the Structure Commission of the IZA (International Zeolite Association), but this number seems to grow exponentially.[57] Indeed, the number of zeolite framework structures described in 2001 was 133, and in 1970 only 27 were known.[58] These structures are described depending on their assembly of Primary Building Units (PBUs), *i.e.* depending on how SiO_4 or AlO_4 tetrahedra are disposed. The tetrahedra are generally described as TO_4, where T a Si or Al atom. The PBUs connect to each other sharing a corner, and forming a system of secondary building units (SBUs) that can be simple polyhedral like cubes or hexagonal prisms, or more complex (see Figure 2.17.).

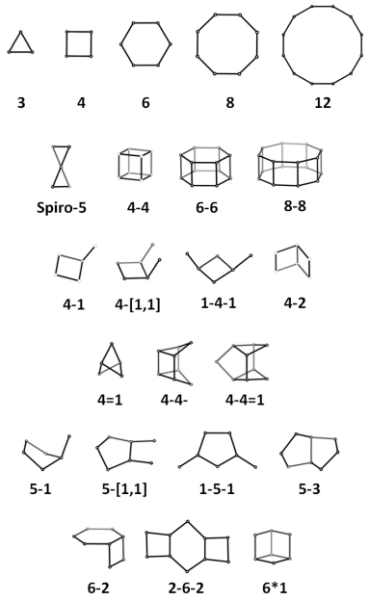

Figure 2.17. Structures of the Secondary Building Units (SBUs) found until 2007. Every T atom is represented with a little sphere, and the oxygen atoms have been omitted for a more clear view, but the T-O-T bridges are represented as straight lines between the small spheres.[57]

The final structure of the inorganic material will consist on the assembly of those SBUs.[57] However, the process that leads to the building of the final microporous structure is complicated. The different ways of assembly will result in the diverse zeolitic microsporous structures.

In this work in particular, the zeolitic inorganic structures used are the so-called alumiophosphates. It has been over 30 years since Wilson *et al*. released the groundbreaking report about the synthesis of new microporous aluminophophates,[59] leading to a myriad of new and varied three-dimensional framework structures. Each framework in this family of aluminophosphates was named as $AlPO_4$-*n*, where the *n* denotes a particular structure type.[59]

The aluminophosphates, generally referred to as AlPOs, are built corner-sharing TO_4 tetrahedra of AlO_4 and PO_4 strictly alternated, shaping a neutral and open framework. This means that there is no need for extra-cations to counterbalance the net charge into the structure, as in the case of typical zeolites.[60] Only water or organic molecules are then occupying the pore space. Indeed, the precursor gel for the synthesis of this kind of molecular sieves is aqueous, and an organic additive is needed to act as the structure directing agent (SDA) towards the crystallization of a stable microporous material of this type. Note that SDAs used for particular aluminophosphate frameworks, usually amines, are less specific than in the case of aluminosilicate zeolites.[60]

However, sometimes it is required a net charge into the aluminophosphate structure, for instance to help the incorporation of some kind of guest molecules. Thereby different heteroatoms can be incorporated into the framework by diverse methods such as incipient wetness impregnation, ion exchange or isomorphous substitution.[61–64] The isomorphous substitution strategy is quite straightforward, just adding the new metal source to the synthesis mixture. Particularly, in this work the divalent Mg (II) cation was used as dopant to promote a negative charge into the aluminophosphate. This Mg^{2+} cation is able to adopt tetrahedral coordination, and therefore Al^{3+} atoms are substituted in some sites of the framework without causing any perturbation in the structure, but generating Brønsted acid sites (Figure 2.18.). As a consequence, the resulting material is called magnesium aluminophosphate, or MgAPO in acronyms.

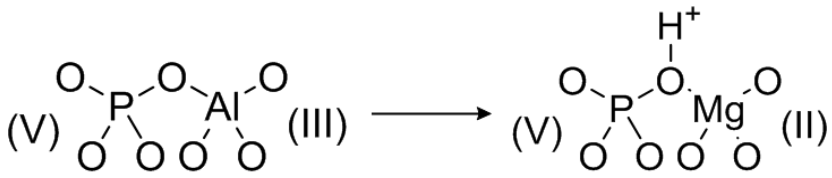

Figure 2.18. Schematic representation of the tetrahedra forming AlPO (left, neutral) and MgAPO (right) frameworks. In the second case a Brønsted acid site due to charge compensation has been represented.

2.2.1.1. Types of MgAPOs used

As it is cited above in the introduction of this section, crystalline systems with one-dimensional channels afford a supramolecular organization for embedded guest molecules and enhance their properties (better photo- and thermal-stabilities and higher luminescent efficiencies) provided by the protection and rigidity imposed by the host matrix. Among zeolitic materials, 1D-aluminophosphates show interesting features such as i) the variability of their pore size, making it relatively easy to find an appropriate aluminophosphate host for a particular guest molecule; and ii) the easiness of the preparation, for further implementation in devices or other industrial applications. Furthermore, the possibility of generating a net negative charge inside the structure would help the incorporation of cationic guests by crystallization inclusion method (see section 2.2.1.2), that otherwise would barely enter the structure. Due to all the above mentioned, several MgAPO structures with non-interconnected channels, with different size and shape, running along one direction (along the c-axis of the structure) are used for the encapsulation of various cationic fluorescent dyes. These 1D-aluminophosphates are MgAPO-5, MgAPO-36 and MgAPO-11, further described below.

- **MgAPO-5**

The MgAPO-5 framework has an AFI structure type, which contains straight and cylindrical one-directional channel system. These channels have a diameter of 7.3 Å, and are formed by rings of 12 tetrahedra (denoted as 12-member ring or 12 MR). Channels are joined together by smaller channels of 6 and 4 tetrahedra. The walls of the larger channels are formed by rings of 6 fused tetrahedra. This framework is considered a large pore molecular sieve.[64,65]

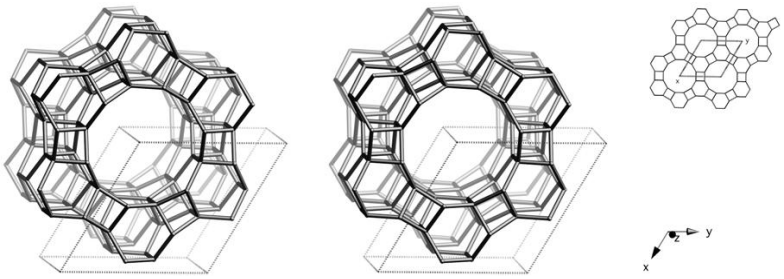

Figure 2.19. Structure of AFI framework, viewed with the c-axis perpendicular to the plane of the paper.[57]

AFI structure can be obtained with different SDAs; the choice of this additive is not decisive in the final result of the synthesis in this case. The wide range of possible SDAs demonstrates the stability of this microporous structure.

In our case, the aluminophosphate has been doped with magnesium, but this structure has been obtained by other authors with many different compositions, for example with heteroatoms such as Zn, Co, Cr or Fe.[66–69] Nevertheless, this structure has been also extensively studied without extra heteroatoms in it, *i.e.* $AlPO_4$-5, as it attracted considerable attention due to the simplicity in its synthesis procedure.[68] This material has demonstrated interesting features for its use as absorbent or catalyst support, and is also considered a novel material for diverse optical applications.[65,70–72]

- **MgAPO-36**

The MgAPO-36 framework has an ATS structure type. This structure is also formed by one-directional channels of 12 tetrahedra (12 MR) parallel to the c-axis, but in this case they are elliptical instead of cylindrical as in the case of the AFI structure-type. The pore-entry dimensions are here slightly smaller, specifically of 6.7 x 7.5 Å.[34]

Once again, this framework typically appears as an aluminophosphate ($AlPO_4$-36), but it has been also prepared incorporating different metal heteroatoms into the structure, for example Zn and Fe.[69,73] Generally, this framework is obtained using tripropilamine as organic template, or SDA, but this amine can also lead to the formation of $AlPO_4$-5, with AFI phase, so it is not as easy as in the previous case to get a pure ATS phase.[74]

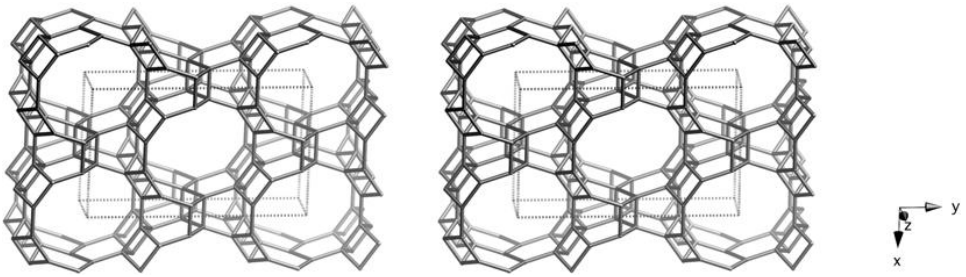

Figure 2.20. Structure of ATS framework, viewed with the c-axis perpendicular to the plane of the paper.[57]

- **MgAPO-11**

The MgAPO-11 framework has an AEL structure type. This crystalline microporous aluminophosphate shows a one-directional elliptical channel system of smaller

dimensions comparing with the two frameworks mentioned above. The channels are composed of rings of 10 tetrahedra (10 MR), and they have a dimension of 4 x 6.5 Å.[57] It is noteworthy in this structure that it possesses a special channel-topology, containing pockets along the channel direction.[34]

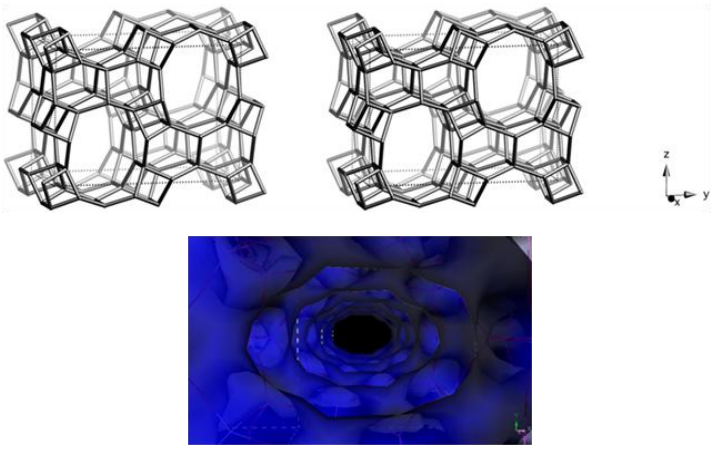

Figure 2.21. Up: Structure of AEL framework, viewed with the c-axis perpendicular to the plane of the paper.[57] Down: detail of the topology of AEL channels.

The synthesis of this type of framework has been also performed adding other heteroatoms to replace Al or P atoms.[75] It has shown important application as catalyst, for example in the particular case of the material known as SAPO-11, *i.e.* an aluminophosphate with AEL structure-type doped with silicon.[76]

The synthesis procedure of the three MgAPOs used in this work (in this particular case with encapsulated dyes) is thoroughly described in the experimental section (section 3.1. in chapter 3). However, a special mention about the method of inclusion of the different fluorescent dyes is now detailed.

2.2.1.2. Fluorescent dye incorporation method

Owing to the large number of existing fluorophores, a wide range of possibilities is offered depending on the needs in each case. However, both the elected dyes and host frameworks must meet certain requirements. For example, in order to reach a very tight confinement of the dye molecules into the nanochannels of the MgAPO, a host framework with a pore size close to the molecular structure dimensions must be

chosen. However, the widely known post-synthetic methods based on diffusional processes, such as molecular absorption from solution by cationic exchange or from a gas phase after sublimation of the dyes,[77–79] do not allow such a tight confinement. Thus, in this work dye incorporation is accomplished by *crystallization inclusion method*,[80] in which dyes are directly added to the synthesis gel and they are occluded "in situ" inside the pores of the inorganic framework whilst it crystallizes. This method is also known as *bottle-around-the-ship approach*.[81] Thus, dyes are added to the synthesis gel together with the structure directing agent (SDA), which remains also occluded into the material. This incorporation method requires guest molecules soluble in the synthesis gel, mainly aqueous, and they should have molecular structures not very different from those of the SDAs commonly used in the synthesis of aluminophosphates and other zeotypes and zeolites, in order not to disrupt the final phase of the system.[82] Therefore, all the fluorescent dyes incorporated here are cationic with amine or ammonium groups in their structure (see the general structure of most of the dyes used in Figure 2.22.). A further description of the dyes used (molecular structure and photophysical properties) will be made along the chapter 4.

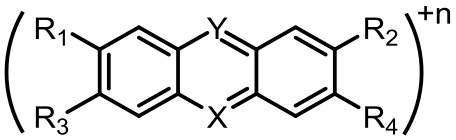

Figure 2.22. General molecular structure of many of the encapsulated fluorescent dyes, being X or Y a nitrogen or a oxygen atom and at least one R = NR_3 or NR_3^+ group.

Importantly, this approach has some advantages over the post-synthetic diffusion processes; for example, i) the traffic jam at the entrances of the pores is completely avoided, attaining a more homogeneous filling of particles that can reach dimensions of even hundreds of micrometers; ii) dye molecules with a molecular size exceeding the entrance pore openings can also be encapsulated, impossible via the other mentioned methods; iii) the leakage of the encapsulated molecules is prevented due to the tight fit between channels and molecular dimensions; and iv) the sample preparation time is considerably reduced since the synthesis is carried out in one unique step, reason for what this synthesis procedure is also called *one-pot synthesis*.[64]

2.2.2. Metal Organic Frameworks (MOFs)

There is a relatively new class of advanced hybrid materials called PCPs (Porous Coordination Polymers) or MOFs (Metal-Organic Frameworks). Here, we are going to refer to them as MOFs since it is a more general term. They are built up by strong coordination bonds between transition-metal cations and multidentate organic linkers. Therefore, a wide variety of structures are accessible, depending on the linker and the coordination geometry adopted by the metal ion. In the same way as mentioned above for purely inorganic zeolitic frameworks, their structure can be described by the association of secondary building units (SBUs).[57,83]

Moreover, not only can be MOF materials formed by a single 3D-hybrid net, but there can also exist interpenetration between MOF nets. Although it may seem that these entangled structures play against the porosity of the system, the interpenetration can help adjusting the pore architecture of MOFs, and it is interesting to obtain more stable structures, or to get stimuli responsive behaviors.[84,85]

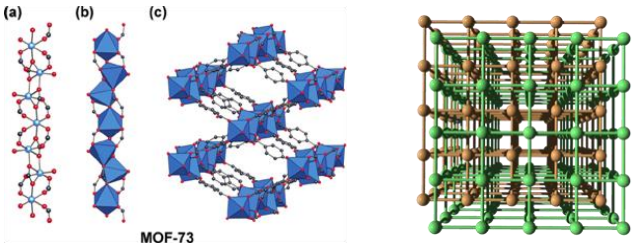

Figure 2.23. Left: Example of MOF-73: a) ball-and-stick representation of SBU; b) SBU with metal (Mn) shown as polyhedra; and c) view of the crystalline framework with inorganic SBUs linked together via an organic linker (1,4-benzenedicarboxylate). Right: schematic illustration of an interpenetrated MOF structure.

As inherent properties of hybrid materials, MOFs exhibit advantages of both organic and inorganic materials, and here some of those numerous advantages are summed up. The possible combinations between inorganic metal ions and organic ligands are unlimited, so the possibilities are endless. They have highly periodical structures and changeable porosity, pore surface and flexibility throughout the rational choice of the organic ligands.[83,84] Owing to this versatility, MOFs have found usefulness in numerous applications, such as gas separation, storage and purification, catalysis, molecular sensing as well as in biomedicine and photonic technology.[86–89]

The research on MOFs is currently expanding towards new applications wherein their porous nature and physical properties are synergistically linked. In particular,

MOFs appear as fascinating platforms for the development of solid-state luminescent materials, due to their potential collaborative multifunctionalities. This can be achieved rationally incorporating emissive building blocks into the framework scaffolds, such as π-conjugated ligands or luminescent metal ions; or by Ligand-to-Metal Charge Transfer (LMCT) and Metal-to-Ligand Charge Transfer (MLCT) processes. Besides the inherent luminescent properties of some MOFs, the capability to accommodate guest species in their well-defined porous structure leads also to very attractive luminescent features, denoted as *Guest-Induced Luminescence*. In this sense, guests are confined in the nanospace and do not interact with each other, creating unique properties via nanoconfinement. Therefore, MOFs can serve as rigid/flexible hosts for the encapsulation of luminescent guest species such as lanthanide ions and fluorescent dyes. Moreover, specific host-guest interactions can also trigger luminescent properties not observed in other hybrid systems. Generally, three main guest-MOF interactions are considered to generate luminescence properties:

1. Formation of charge transfer complexes or exciplexes (in the excited state) between the organic linkers and guest species leading to new species or new states with characteristic fluorescent bands different from the isolated host and guest species.
2. Energy transfer processes between host frameworks and guest species that can result in the shift of emission wavelength, luminescence quenching or antenna effect.
3. Guest accommodation that can cause a structural transformation of the MOF (Figure 2.24.), inducing differences in the luminescent intensity. For instance, guest species incorporated into the pores often restrict the structural vibrations of the host framework and reduce the quenching effect on the luminescence.

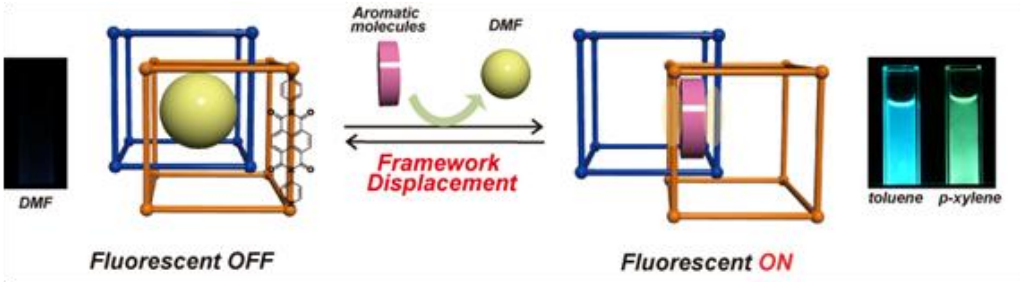

Figure 2.24. Scheme of how the fluorescence is triggered by the encapsulation of aromatic molecules into $[Zn_2(bdc)_2(dpNDI)]_n$.

In this work, the entangled MOF formulated as $[Zn_2(bdc)_2(dpNDI)]_n$ is used towards the achievement of room temperature phosphorescence and white light emission, as will be detailed in chapter 5. This special MOF incorporates N,N'-dipyrid-4-yl-1,4,5,8-naphthalenediimide (dpNDI) as photoactive pillar, and has already demonstrated a dynamic confinement to trap volatile organic compounds (VOCs) such as benzene, toluene, xylene or anisole, forming CT complexes and generating a wide range of emission colors (Figure 2.24).[90,91]

References

(1) Perkampus, H.-H. *UV-Vis Spectroscopy and Its Applications*; Springer-Verlag: Berlin, **1992**.

(2) Valeur, B. *Molecular Fluorescence: Principles and Applications*; Wiley-VCH Verlag GmbH: Weinheim, **2001**.

(3) Birks, J. B. *Photophysics of Aromatic Molecules*; Wiley-Interscience: London, **1970**.

(4) Lakowicz, J. R. *Principles of Fluorescence Spectroscopy*, 3rd ed.; Springer: Singapore, **2006**.

(5) Parker, C. A. *Photoluminescence of Solutions*; Elsevier Publishing Company: Amsterdam, **1968**.

(6) Boudin, S. Phosphorescence of Glycerol Solutions of Eosin, Influence of Iodides. *J. Chim. Phys.* **1930**, *27*, 285-290.

(7) Parker, C. A.; Hatchard, C. G. Triplet-Singlet Emission in Fluid Solutions. Phosphorescence of Eosin. *Trans. Faraday. Soc.* **1961**, *51*, 1894–1904.

(8) López Arbeloa, F.; Llona González, I.; Ruiz Ojeda, P.; López-Arbeloa, I. Aggregate Formation of Rhodamine 6G in Aqueous Solution. *J. Chem. Soc., Faraday Trans. 2* **1982**, *78*, 989–994.

(9) Scheblykin, I. G.; Varnavsky, O. P.; Verbouwe, W.; De Backer, S.; Van der Auweraer, M.; Vitukhnovsky, A. G. Relaxation Dynamics of Excitons in J-Aggregates Revealing a Two-Component Davydov Splitting. *Chem. Phys. Lett.* **1998**, *282*, 250–256.

(10) Tsukanova, V.; Lavoie, H.; Harata, A.; Ogawa, T.; Salesse, C. Microscopic Organization of Long-Chain Rhodamine Molecules in Monolayers at the Air/Water Interface. *J. Phys. Chem. B* **2002**, *106*, 4203–4213.

(11) Michaelis, L.; Granick, S. Metachromasy of Basic Dyestuffs. *J. Am. Chem. Soc.* **1945**, *67*, 1212–1219.

(12) Kasha, M.; Rawls, H. R.; El-Bayoumi, M. A. The Exciton Model in Molecular Spectroscopy. *Pure Appl. Chem.* **1965**, *11*, 371–392.

(13) McRae, E. G.; Kasha, M. The Molecular Exciton Model. In *Physical Process in Radiation Biology*; Augenstein, L., Mason, R., Rosenberg, B., Eds.; Academy Press: New York, **1964**; pp 23–42.

(14) Antonov, L.; Gergov, G.; Petrov, V.; Kubista, M.; Nygren, J. UV – Vis Spectroscopic and Chemometric Study on the Aggregation of Ionic Dyes in Water. *Talanta* **1999**, *49*, 99–106.

(15) Fujii, T.; Nishikori, H.; Tamura, T. Absorption Spectra of Rhodamine B

Dimers in Dip-Coated Thin Films Prepared by the Sol-Gel Method. *Chem. Phys. Lett.* **1995**, *233*, 424–429.

(16) Ballet, P.; Van der Auweraer, M.; De Schryver, F. C.; Lemmetyinen, H.; Vuorimaa, E. Global Analysis of the Fluorescence Decays of N,N′-Dioctadecyl Rhodamine B in Langmuir-Blodgett Films of Diacylphosphatidic Acids. *J. Phys. Chem.* **1996**, *100*, 13701–13715.

(17) Medintz, I.; Hildebrandt, N. *FRET-Föster Resonance Energy Transfer*; Wiley-VCH: Singapore, **2014**.

(18) Oliveros, E.; Suardi-Murasecco, P.; Aminian-Saghafi, T.; Braun, A. M.; Hansen, H.-J. 1H-Phenalen-1-One: Photophysical Properties and Singlet-Oxygen Production. *Helv. Chicica Acta* **1991**, *74*, 79–90.

(19) DeRosa, M. C.; Crutchley, R. J. Photosensitized Singlet Oxygen and Its Applications. *Coord. Chem. Rev.* **2002**, *233–234*, 351–371.

(20) Ogilby, P. R. Singlet Oxygen: There Is Indeed Something New under the Sun. *Chem. Soc. Rev.* **2010**, *39*, 3181–3209.

(21) Wilkinson, F.; Helman, W. P.; Ross, A. B. Quantum Yields for the Photosensitized Formation of the Lowest Electronically Excited Singlet State of Molecular Oxygen in Solution. *J. Phys. Chem. Ref. Data* **1993**, *22*, 113–262.

(22) Chen, J.; Keltner, L.; Christophersen, J.; Zheng, F.; Krouse, M.; Singhal, A.; Wang, S.-S. New Technology for Deep Light Distribution in Tissue for Phototherapy. *Cancer J.* **2002**, *8*, 154–163.

(23) Sobolev, A. S.; Jans, D. A.; Rosenkranz, A. A. Targeted Intracellular Delivery of Photosensitizers. *Prog. Biophys. Mol. Biol.* **2000**, *73*, 51–90.

(24) Zhao, J.; Wu, W.; Sun, J.; Guo, S. Triplet Photosensitizers : From Molecular Design to Applications. *Chem. Soc. Rev.* **2013**, *42*, 5323–5351.

(25) Lacombe, S.; Pigot, T. Materials for Selective Photo-Oxygenation vs. Photocatalysis: Preparation, Properties and Applications in Environmental and Health Fields. *Catal. Sci. Technol.* **2016**, *6*, 1571–1592.

(26) Schmidt, R.; Tanielian, C.; Dunsbach, R.; Wolff, C. Phenalenone, a Universal Reference Compound for the Determination of Quantum Yields of Singlet Oxygen $O_2(^1\Delta_g)$ Sensitization. *J. Photochem. Photobiol. A Chem.* **1994**, *79*, 11–17.

(27) Martí, C.; Jürgens, O.; Cuenca, O.; Casals, M.; Nonell, S. Aromatic Ketones as Standards for Singlet Molecular Oxygen Photosensitization. Time-Resolved Photoacoustic and near-IR Emission Studies. *J. Photochem. Photobiol. A Chem.* **1996**, *97*, 11–18.

(28) Kliger, D. S.; Lewis, J. W.; Randall, C. E. *Polarized Light in Optics and*

Spectroscopy; Academic Press, Inc.: London, **1990**.

(29) Gorski, A.; Lament, B.; Davis, J. M.; Sessler, J.; Waluk, J. Electronic States of a Novel Smaragdyrin Isomer: Polarized Spectroscopy and Theoretical Studies. *J. Phys. Chem. A* **2001**, *105*, 4992–4999.

(30) Nielsen, Jakob Toudahl Kulminskaya, Natalia V. Bjerring, M.; Linnanto, J. M.; Rätsep, M.; Pedersen, M. O.; Lambrev, P. H.; Dorogi, M.; Garab, G.; Thomsen, K.; Jegerschöld, C.; Frigaard, N.-U.; Lindahl, M.; Nielsen, N. C. In Situ High-Resolution Structure of the Baseplate Antenna Complex in Chlorobaculum Tepidum. *Nat. Commun.* **2016**, *7*, 12454.

(31) Levitus, M.; Garcia-Garibay, M. A. Polarized Electronic Spectroscopy and Photophysical Properties of 9,10-Bis(phenylethynyl)anthracene. *J. Phys. Chem. A* **2000**, *104*, 8632–8637.

(32) Rosell, F. I.; Boxer, S. G. Polarized Absorption Spectra of Green Fluorescent Protein Single Crystals: Transition Dipole Moment Directions. *Biochemistry* **2003**, *42*, 177–183.

(33) Inoué, S.; Shimomura, O.; Goda, M.; Shribak, M.; Tran, P. T. Fluorescence Polarization of Green Fluorescence Protein. *Proc. Natl. Acad. Sci. U. S. A.* **2002**, *99*, 4272–4277.

(34) Martínez-Martínez, V.; García, R.; Gómez-Hortigüela, L.; Pérez-Pariente, J.; López-Arbeloa, I. Modulating Dye Aggregation by Incorporation into 1D-MgAPO Nanochannels. *Chem. - A Eur. J.* **2013**, *19*, 9859–9865.

(35) Turcotte, R.; Mattson, J. M.; Wu, J. W.; Zhang, Y.; Lin, C. P. Molecular Order of Arterial Collagen Using Circular Polarization Second-Harmonic Generation Imaging. *Biophys. J.* **2016**, *110*, 530–533.

(36) Dadap, J. I.; Eisenthal, K. B. Probing the Relative Orientation of Molecules Bound to DNA by Second-Harmonic Generation. *J. Phys. Chem. B* **2014**, *118*, 14366–14372.

(37) Gómez, J.; Jiang, J.; Gujral, A.; Huang, C.; Yu, L.; Ediger, M. D. Vapor Deposition of a Smectic Liquid Crystal: Highly Anisotropic, Homogeneous Glasses with Tunable Molecular Orientation. *Soft Matter* **2016**, *12*, 2942–2947.

(38) Riehl, J. P.; Richardson, F. S. Circularly Polarized Luminiscence Spectroscopy. *Chem. Rev.* **1986**, *86*, 1–16.

(39) Suresh, S.; Arivuoli, D. Nanomaterials for Nonlinear Optical (NLO) Applications: A Review. *Rev. Adv. Mater. Sci.* **2012**, *30*, 243–253.

(40) Cambré, S.; Campo, J.; Beirnaert, C.; Verlackt, C.; Cool, P.; Wenseleers, W. Asymmetric Dyes Align inside Carbon Nanotubes to Yield a Large Nonlinear Optical Response. *Nat. Nanotechnol.* **2015**, *10*, 248–252.

(41) Li, L.; Ge, J.; Wu, H.; Xu, Q. H.; Yao, S. Q. Organelle-Specific Detection of Phosphatase Activities with Two-Photon Fluorogenic Probes in Cells and Tissues. *J. Am. Chem. Soc.* **2012**, *134*, 12157–12167.

(42) Boreham, E. M.; Jones, L.; Swinburne, A. N.; Blanchard-Desce, M.; Hugues, V.; Terryn, C.; Miomandre, F.; Lemercier, G.; Natrajan, L. S. A Cyclometallated Fluorenyl Ir(III) Complex as a Potential Sensitiser for Two-Photon Excited Photodynamic Therapy (2PE-PDT). *Dalt. Trans.* **2015**, *44*, 16127–16135.

(43) Williams, D. J. Organic Polymeric and Non-Polymeric Materials with Large Optical Nonlinearities. *Angew. Chemie Int. Ed. English* **1984**, *23*, 690–703.

(44) Boyd, R. W. *Nonlinear Optics*, Third Edit.; Academic Press: New York, **2008**.

(45) Liu, J.-M. *Photonic Devices*; Cambridge University Press: Cambridge, **2005**.

(46) Du, S.; Zhang, H. Metal-Organic Frameworks for Second-Order Nonlinear Optics. In *Metal-Organic Frameworks for Photonic Applications*; Chen, B., Qian, G., Eds.; Springer-Verlag: Berlin, **2014**; pp 145–165.

(47) Prasad, P. N.; Williams, D. J. *Introduction to Nonlinear Optical Effects in Molecules and Polymers*; John Wiley & Sons, Inc.: New York, **1991**.

(48) Wan, S. The Growth of Borate Nonlinear Optical Crystals. In *New Developments in Crystal Growth Research*; Karas, G. V., Ed.; Nova Science Publishers, Inc.: New York, **2005**.

(49) Bharathi, M. D.; Ahila, G.; Mohana, J.; Chakkaravarthi, G.; Anbalagan, G. Structural, Optical, Thermal and Mechanical Characterization of an Organic Nonlinear Optical Material: 4-Methyl-3-Nitrobenzoic Acid Single Crystal. *J. Phys. Chem. Solids* **2016**, *98*, 290–297.

(50) Kanis, D. R.; Ratner, M. A.; Marks, T. J. Design and Construction of Molecular Assemblies with Large Second-Order Optical Nonlinearities. Quantum Chemical Aspects. *Chem. Rev.* **1994**, *94*, 195–242.

(51) Donaldson, W. R.; Tang, C. L. Urea Optical Parametric Oscillator. *Appl. Phys. Lett.* **1984**, *44*, 25-27.

(52) Franken, P. A.; Hill, A. E.; Peters, C. W.; Weinreich, G. Generation of Optical Harmonics. *Phys. Rev. Lett.* **1961**, *7*, 118–119.

(53) Davis, M. E. New Vistas in Zeolite and Molecular Sieve Catalysis. *Acc. Chem. Res.* **1993**, *26*, 111–115.

(54) Naber, J. E.; de Jong, K. P.; Stork, W. H. J.; Kuipers, H. P. C. E.; Post, M. F. M. Industrial Applications of Zeolite Catalysis. *Stud. Surf. Sci. Catal.* **1994**, *84*, 2197–2219.

(55) Barrer, R. M. Syntheses and Reactions of Mordenite. *J. Chem. Soc.* **1948**, 2158–2163.

(56) Breck, D. W.; Eversole, W. G.; Milton, R. M. New Synthetic Crystalline Zeolites. *J. Am. Chem. Soc.* **1956**, *78*, 2338–2339.

(57) Baerlocher, C.; McCusker, L. B.; Olson, D. H. *Atlas of Zeolite Framework Types*; Elsevier, **2007**.

(58) Meier, W. M.; Olson, D. H. Zeolite Frameworks. *Adv. Chem. Ser.* **1970**, *101*, 155–170.

(59) Wilson, S. T.; Lok, B. M.; Messina, C. A.; Cannan, T. R.; Flanigen, E. M. Aluminophosphate Molecular Sieves: A New Class of Microporous Crystalline Inorganic Solids. *J. Am. Chem. Soc.* **1982**, *104*, 1146–1147.

(60) Szostak, R. *Molecular Sieves: Principles of Synthesis and Identification*, 2nd ed.; Blackie academic & Professional: London, **1998**.

(61) Chen, C. M.; Jehng, J. M. Structure Control of Metal Aluminum Phosphate (MeAlPO-5) Molecular Sieves and Applications in Polyethylene Glycol Amination. *Catal. Letters* **2004**, *93*, 213–223.

(62) Hernandez-Maldonado, A. J.; Cabanzo-Olarte, A. C.; Maldonado-Aviles, S. M. Modification of a Cobalt-Aluminophosphate (Co/Al ~ 1) with a Multidimensional Pore System via Coupled Partial Detemplation and Solid State Ion Exchange with Alkali Metals for the Adsorption of Light Gases. *Microporous Mesoporous Mater.* **2012**, *161*, 148–153.

(63) Wei, Y.; Zhang, L.; Tian, Z. Isomorphous Substitution Induced Ionothermal Synthesis of Magnesium Aluminophosphate Zeolites in Fluoride-Free Media. *RSC Adv.* **2016**, *6*, 61915–61919.

(64) García, R.; Martínez-Martínez, V.; Gómez-Hortigüela, L.; López Arbeloa, I.; Pérez-Pariente, J. Anisotropic Fluorescence Materials: Effect of the Synthesis Conditions over the Incorporation, Alignment and Aggregation of Pyronine Y within MgAPO-5. *Microporous Mesoporous Mater.* **2013**, *172*, 190–199.

(65) Choi, S.-E.; Kim, H.; Park, Y.-S.; Lee, J. S. In-Situ Thickness Controlled Growth of AlPO4-5 Films. *Microporous Mesoporous Mater.* **2016**, *219*, 155–160.

(66) Christensen, A. N.; Hazell, R. G. Use of Hydrofluoric Acid as Mineralizer in Hydrothermal and Organothermal Synthesis of Me^{2+}-Substituted Aluminophosphates. I. *Acta Chem. Scand.* **1999**, *53*, 403–409.

(67) Radaev, S. F.; Joswig, W.; Baur, W. H. Synthesis and Precise Characterization of Large Single Crystals of as-Synthesized CrAPO-5, $H_{2.1}[Cr_{0.08}Al_{11.62}P_{12}O_{48}]F_{1.2}\cdot 1.6TEA$. *J. Mater. Chem.* **1996**, *6*, 1413–1418.

(68) Zenonos, C.; Sankar, G.; Corà, F.; Lewis, D. W.; Pankhurst, Q. A.; Catlow, C. R. A.; Thomas, J. M. On the Nature of Iron Species in Iron Substituted Aluminophosphates. *Phys. Chem. Chem. Phys.* **2002**, *4*, 5421–5429.

(69) Saha, S. K.; Maekawa, H.; Waghmode, S. B.; Mulla, S. A. R.; Komura, K.; Kubota, Y.; Sugi, Y.; Cho, S. J. Zincoaluminophosphate Molecular Sieves with AFI and ATS Topologies : Synthesis by Dry-Gel Conversion Methods and Their Catalytic Properties in the Isopropylation of Biphenyl. *Mater. Trans.* **2005**, *46*, 2659–2667.

(70) Sheng, N.; Chu, Y.; Xin, S.; Wang, Q.; Yi, X.; Feng, Z.; Meng, X.; Liu, X.; Deng, F.; Xiao, F. Insights of the Crystallization Process of Molecular Sieve $AlPO_4$-5 Prepared by Solvent-Free Synthesis. *J. Am. Chem. Soc.* **2016**, *138*, 6171–6176.

(71) Vietze, U.; Krauß, O.; Laeri, F.; Ihlein, G.; Schüth, F.; Limburg, B.; Abraham, M. Zeolite-Dye Microlasers. *Phys. Rev. Lett.* **1998**, *81*, 4628–4631.

(72) Ganschow, M.; Schulz-Ekloff, G.; Wark, M.; Wendschuh-Josties, M.; Wöhrle, D. Microwave-Assisted Preparation of Uniform Pure and Dye-Loaded AlPO4-5 Crystals with Different Morphologies for Use as Microlaser Systems. *J. Mater. Chem.* **2001**, *11*, 1823–1827.

(73) Ristic, A.; Thibault-starzyk, F.; Czyzniewska, J. Large-Pore FAPO-36 : Synthesis and Characterization. *Chem. Mater.* **2003**, *15*, 3643–3649.

(74) Machado, M. da S.; Cardoso, D.; Sastre, E.; Pérez-Pariente, J. Synthesis and Characterization of $AlPO_4$-36 and MAPO-36 with Different Magnesium Content. *Chem. Mater.* **1999**, *11*, 3238–3244.

(75) Yang, X.; Ma, H.; Xu, Z.; Xu, Y.; Tian, Z.; Lin, L. Hydroisomerization of N - Dodecane over Pt / MeAPO-11 (Me = Mg , Mn , Co or Zn) Catalysts. *Catal. Commun.* **2007**, *8*, 1232–1238.

(76) Geng, C.; Zhang, F.; Gao, Z.; Zhao, L.; Zhou, J. Hydroisomerization of N - Tetradecane over Pt / SAPO-11 Catalyst. *Catal. Today* **2004**, *93–95*, 485–491.

(77) Hoppe, R.; Schulz-Ekloff, G.; Wöhrle, D.; Shpiro, E. S.; Tkachenko, O. P. X.P.S. Investigation of Methylene Blue Incorporated into Faujasites and AlPO Family Molecular Sieves. *Zeolites* **1993**, *13*, 222–228.

(78) Macchi, G.; Botta, C.; Calzaferri, G.; Catti, M.; Cornil, J.; Gierschner, J.; Meinardi, F.; Tubino, R. Weak Forces at Work in Dye-Loaded Zeolite Materials: Spectroscopic Investigation on Cation-Sulfur Interactions. *Phys. Chem. Chem. Phys.* **2010**, *12*, 2599–2605.

(79) Gomes, R.; Albuquerque, R. Q.; Pina, F.; Parola, A. J.; De Cola, L. Supramolecular Host-Guest Flavylium-Loaded Zeolite L Hybrid Materials: Network of Reactions of Encapsulated 7,4'-dihydroxyflavylium. *Photochem.*

Photobiol. Sci. **2010**, *9*, 991–995.

(80) García Salas, R.; Pérez-Pariente, J.; Gómez-Hortigüela, L.; Martínez-Martínez, V.; López-Arbeloa, I. Photoactive Hybrid Material, Method for Obtaining Same and Use of the Material. WO 2014020225, **2014**.

(81) Gándara, F.; López-Arbeloa, F.; Ruiz-Hitzky, E.; Camblor, M. A. "Bottle-around-a-Ship'' Confinement of High Loadings of Acridine Orange in New Aluminophosphate Crystalline Materials. *J. Mater. Chem.* **2006**, *16*, 1765–1771.

(82) Wöhrle, D.; Schulz-Ekloff, G.; Bräuchle, C.; Laeri, F. Nanoporous Networks of Si- , Al- , P-Oxygen Tetrahedra with Encapsulated Dyes as New Composite Materials. *Macromol. Symp.* **2008**, *270*, 123–134.

(83) Férey, G. Hybrid Porous Solids: Past, Present, Future. *Chem. Soc. Rev.* **2008**, *37*, 191–214.

(84) Zhang, J.-P.; Chen, X.-M. Metal-Organic Frameworks: From Design to Materials. In *Metal-Organic Frameworks for Photonic Applications*; Chen, B., Qian, G., Eds.; Springer-Verlag: Berlin, **2014**; pp 1–26.

(85) Wang, X. X.; Zhai, Q. G.; Li, S. N.; Jiang, Y. C.; Hu, M. C. Porous Cd-Carboxylate Frameworks Tuned by the Bulk of Linker: Interpenetrated Nets, Selective CO2 Uptakes and High Water Vapor Adsorption. *Inorg. Chem. Commun.* **2015**, *61*, 200–203.

(86) Czaja, A. U.; Trukhan, N.; Müller, U. Industrial Applications of Metal–organic Frameworks. *Chem. Soc. Rev.* **2009**, *38*, 1284–1293.

(87) Cheng, X. N.; Zhang, W. X.; Lin, Y. Y.; Zheng, Y. Z.; Chen, X. M. A Dynamic Porous Magnet Exhibiting Reversible Guest-Induced Magnetic Behavior Modulation. *Adv. Mater.* **2007**, *19*, 1494–1498.

(88) Horcajada, P.; Gref, R.; Baati, T.; Allan, P. K.; Maurin, G.; Couvreur, P. Metal-Organic Frameworks in Biomedicine. *Chem. Rev.* **2012**, *112*, 1232–1268.

(89) Cui, Y.; Li, B.; He, H.; Zhou, W.; Chen, B.; Qian, G. Metal-Organic Frameworks as Platforms for Functional Materials. *Acc. Chem. Res.* **2016**, *49*, 483–493.

(90) Martínez-Martínez, V.; Furukawa, S.; Takashima, Y.; López Arbeloa, I.; Kitagawa, S. Charge Transfer and Exciplex Emissions from a Naphthalenediimide-Entangled Coordination Framework Accommodating Various Aromatic Guests. *J. Phys. Chem. C* **2012**, *116*, 26084–26090.

(91) Takashima, Y.; Martínez-Martínez, V.; Furukawa, S.; Kondo, M.; Shimomura, S.; Uehara, H.; Nakahama, M.; Sugimoto, K.; Kitagawa, S. Molecular

Decoding Using Luminescence from an Entangled Porous Framework. *Nat. Commun.* **2011**, *2*, 168.

3

EXPERIMENTAL SECTION

3

EXPERIMENTAL SECTION

Along this chapter it is described in the first place the synthesis procedure of the different dye-loaded magnesium aluminophosphates (section 3.1.) studied in chapter 4, followed by the instrumental techniques employed for their structural characterization. Besides, a short section is dedicated to the preparation of MOF-guest systems (section 3.2.). Then, all the set-ups and the methods related to the photophysical characterization of all the hybrid materials studied along this work (dye/MgAPO, MOF and organometallic complexes) are presented (section 3.3.).

This thesis is the result of a coordinated work with groups specialized not only in organic and inorganic synthesis, but also in sophisticated optical techniques for materials characterization. In this sense, details regarding the measurements of the antenna effect (section 3.4.) and nonlinear optical properties (section 3.5.) are given, together with a brief description of the theoretical calculations used to support the experimental evidences (section 3.6.).

3.1. Preparation and structural characterization of dye-loaded MgAPOs

The zeolitic materials are typically obtained by hydrothermal synthesis, mimicking the conditions in which natural zeolites are formed, *i.e.* under high temperature and pressure conditions.[1,2] However, there are some differences between the synthesis of zeolites and aluminophosphates, for example, the AlPOs can be synthesized in acidic or neutral medium, while zeolites are typically formed under strong basic conditions.

Although the synthesis of the AlPO materials can be carried out via different synthetic approaches (for example solvothermal synthesis, dry gel conversion and ionothermal synthesis, among others),[3–5] the most common method is the hydrothermal synthetic approach, based on sol-gel chemistry. Here, aluminum and phosphorous sources are mixed in water together with the structure directing agent,

which is generally an amine or an ammonium salt. In the case of AlPO materials that contain another metallic atom as dopant, it is also added to the synthesis gel in usually its salt form.

The synthesis of the MgAPOs used along this work are carried out at the Catalysis and Petrochemistry Institute of CSIC (Madrid) according to the following steps: orthophosphoric acid is mixed with water in a Teflon vessel and it is kept under vigorous stirring for 2 minutes. In order to obtain magnesium doped aluminophosphates, the magnesium source, magnesium acetate tetrahydrate in our case, is added to the reactive mixture. Then, aluminum hydroxide, as the aluminum source, is gently added. The resultant mixture is left under stirring for another 5-10 minutes. The structure directing agent (SDA) is added then. In this work we have used three different amines as SDAs, one for each MgAPO structure: triethylamine (TEA) for MgAPO-5, tripropylamine (TPA) for MgAPO-36 and ethylbutylamine (EBA) for MgAPO-11.

Since the aim of this work is to obtain dye-doped magnesium aluminophosphates, the organic dye is added to the synthesis gel at this point. Thus, the dye is incorporated by the so-called *crystallization inclusion method*, detailed in chapter 2 (section 2.2.1.2.).

Figure 3.1. Teflon liner and stainless steel autoclave used for the synthesis of aluminophosphate materials.

Then, the mixture in the vessel is covered with film and it is kept under stirring for one hour before measuring the pH of the gel. The pH values of the different gels are between 3 and 5. Then the mixture is transferred to a Teflon liner, leaving an empty space of about one third of the total volume of the container to ensure an optimal pressure, and it is closed up into a stainless steel autoclave (Figure 3.1.). The aqueous

mixture is then heated into the sealed autoclave in a conventional oven at temperatures between 180 and 195ºC, depending on the case, under autogenous pressure, and for reaction times no longer than 24h. To ensure that there has not been any loss, the autoclave is weighted before and after the reaction process in the oven. When the reaction is finished, the autoclave is cooled abruptly in water to stop crystal growth.

In this work, most of the syntheses have been carried out statically, but in some cases dynamic regime was used by keeping the autoclave continuously rotating.

The resulting material is recovered by filtration, exhaustively washed with distilled water and ethanol, and dried overnight.

Up to now only the general synthesis procedure has been described. However, depending on the case, synthesis conditions or reactant proportions slightly change in order to obtain certain phases. These particular syntheses are described below for each framework.

3.1.1. Synthesis of dye/MgAPO-5 materials

This dye-loaded microporous magnesium aluminophosphate was prepared by hydrothermal synthesis, using phosphoric acid (Aldrich, 85 wt%), magnesium acetate tetrahydrate (Aldrich, 99 wt%), aluminium hydroxide (Aldrich) and triethylamine (TEA) as structure directing agent together with the dye of interest (pyronin Y, PY, or 1,1'-diethyl-2,2'-cyanine, PIC). With these reagents gels with the following general molar composition are prepared: 0.2 MgO: 1 P_2O_5: 0.9 Al_2O_3: 0.75 TEA: *x* dye: 300 H_2O. The molar proportion of the dye was varied from 0.008 to 0.024. Note that highly diluted gels are prepared, promoting on the one hand the synthesis of large and single crystals, and on the other hand to facilitate the solution of the dyes, since the solubility in water of most of the dyes used for encapsulation in this type of material is relatively low. In a typical preparation, 1.61 g phosphoric acid are mixed with 37.99 g water and 0.30 g magnesium acetate tetrahydrate. Then 0.98 g aluminum hydroxide and 0.54 g TEA are added over this mixture, together with the required amount of dye in each case, to yield the previously described gel composition. After stirring for 1 h, the resulting gel (pH ~ 3-4) is introduced into 10 mL Teflon lined stainless steel autoclaves, which are heated statically at 180 °C under autogenous pressure for 24 h. The solid products are recovered by filtration, exhaustively washed with water and ethanol, and dried at room temperature overnight.

3.1.2. Synthesis of dye/MgAPO-36 materials

The reagents for the hydrothermal synthesis of this dye-loaded microporous magnesium aluminophosphate are the same as in the previous section 3.1.1., except for the SDA, which is in this case tripropylamine (TPA). With these reagents gels with the following general molar composition are prepared: 0.2 MgO: 1 P_2O5: 0.9 Al_2O_3: 0.75 TPA: *x* dye: 300 H_2O. The molar proportion of the total dye amount (*x*) was 0.024, and the dyes used in the synthesis of MgAPO-36 were pyronin Y (PY), acridine (AC) and 1,1'-diethyl-2,2'-cyanine (PIC). In these syntheses, gels are heated statically at 180ºC under autogenous pressure for 12 hours.

3.1.3. Synthesis of dye/MgAPO-11 materials

The hybrid materials consisting of MgAPO-11 framework are once again hydrothermically prepared with the same reagents and synthesis procedure as in the previous cases. The SDA is in this case N-ethylbutylamine (EBA), and gels with the following molar composition are prepared: 0.2 MgO: 1 P_2O_5: 0.9 Al_2O_3: 1 EBA: *x* Dye: 300 H_2O. The molar proportion of the total dye amount (*x*) varies between 0.008 and 0.024 in this case. The dyes occluded in this structure were acridine (AC), methyl acridine (MeAC), pyronin Y (PY), acridine yellow (AY), acridine orange (AO), methylene blue (MB), oxacine 1 (Ox1), oxacine 4 (Ox4) and LDS 722. Except for the LDS 722 dye, the gels are heated statically at 180 ºC under autogenous pressure for 18 hours. However, the synthesis of LDS772/AEL materials required a specific optimization of all the synthesis parameters to achieve pure MgAPO-11, as detailed in chapter 4, section 4.2.3. Those syntheses were done during my stay at the Catalysis and Petrochemistry Institute of CSIC (Madrid) in 2014.

3.1.4. Dye content determination

The real dye uptake of each sample was quantified spectrometrically, after dissolving certain amount of the sample powder in hydrochloridric acid (5 M). The absorption spectra of the samples are compared with the spectra of standard solutions prepared from known concentrations of the dyes in analogous conditions. The absorption spectra were recorded with a UV-Vis spectrophotometer (Varian, model Cary 4E), described later in detail.

However, the dye-quantification of the AEL systems with three dyes simultaneously encapsulated (section 4.2.4. in chapter 4) is not a trivial task. In this case, the quantification of PY has been carried out as described above, but the determination of the amount of AC and LDS 722 dyes occluded cannot be performed following this standard procedure since at those acidic conditions the absorption bands of both dyes overlap in the UV-blue region. To shift the absorption band of the LDS 722 dye towards a less energetic region of the visible spectrum, and thus to avoid the overlapping with the ACH^+ band, after dissolving the powder in 5 M hydrochloric acid, EtOH solvent is added to prepare a 50:50 solution. Under these conditions (50:50 H_2O:EtOH), the absorption band of LDS 722 is placed at 490 nm, red-shifted with respect to its absorption band in pure water, centered at 446 nm, which allows isolating at the same time the ACH^+ band.

Dye content values are given throughout this work as mmol dye per 100 g sample powder, but in the case of AEL samples it is also given as mmol dye per cm^3. The first value is obtained directly from the spectroscopic comparison between the standard solutions of the dyes and the solutions prepared dissolving a known amount of sample powder. The second parameter is calculated then taking into account the molecular weight of a MgAPO-11 unit cell ($Mg_2Al_{18}P_{20}O_{80}\cdot 2EBAH^+$ = 2638.6 g u.c.) and its volume (2128.38 $Å^3$). Thus, 100 g AEL powder would consist on $2.28x10^{22}$ unit cells occupying a volume of 48.58 cm^3.

3.1.5. Structural characterization:

A) X-ray powder diffraction (XRD)

The final phase of each hybrid sample prepared through the above synthesis procedures was determined by means of X-ray powder diffraction. X-ray powder diffraction (XRD) patterns were collected with a Panalytical X'Pro diffractometer using Cu Kα radiation. These measurements were carried out and analyzed at the Catalysis and Petrochemistry Institute, CSIC (Madrid).

B) Scanning Electron Microscopy (SEM)

The size and morphology of the MgAPO materials was characterized by Scanning Electron Microscopy (SEM) in a JEOL JSM-6400 at the University of the Basque Country (SGIKER).

3.2. Preparation of MOF-guest systems

The synthesis and structural characterization of the MOF framework employed in this work were done at the Kyoto University (Japan), and it is described elsewhere.[6] Here, the subsequent incorporation of the aromatic guests is described. Note that after the solvothermal synthesis, MOFs both as powder sample and big crystals, are suspended in N,N-dimethylformamide (DMF) to prevent them from drying. In order to incorporate small aromatic VOC molecules into the framework, the MOF is filtered and then immersed into the neat liquid of the guest of interest in each case, and thus organic molecules enter the MOF pores by diffusion. In the particular case of white-light emitting MOFs, they are immersed in a mixture of solvents in the adequate proportion. In both cases MOF samples are maintained on immersion for several hours in order to reach a homogeneous distribution of the guests into the structure.

3.2.1. Determination of guest content per unit cell

The quantification of the amount of guest molecules occluded per unit cell in the MOF was performed by Thermal Gravimetric Analysis (TGA). This technique gives information about the mass loss as the temperature increases. Those mass-changes can be due to diverse processes such as evaporation processes, adsorptions, desorptions, oxidations and/or thermal decomposition of the different sample components. In the present case, TGA (Mettler Toledo Thermogravimetric Analyzer, model TGA/SDTA851e, in Laboratorio de Química Macromolecular, LABQUIMAC, University of the Basque Country) was carried out on MOF powder in the temperature range of 30-500 ºC under flowing N_2 gas at a heating rate of 10 ºC min^{-1}. The MOF powder was previously dried in vacuum at room temperature for 1 h to remove the guests attached to the outside of the crystals.

3.3. Photophysical characterization of the hybrid materials

In the current section the experimental techniques employed for the photophysical characterization of the different hybrid systems studied in the present work are described. The techniques used range from spectrometry (UV-Vis) and spectrofluorimetry (steady-state and time-correlated) for both solid and liquid samples (measured in cuvettes of 1 cm), and fluorescence microscopies for powder and single particle measurements.

3.3.1. UV-Vis spectroscopy

Absorption spectra of liquid samples (samples and standards for the dye-loading quantification, dyes and photosensitizers in solution) were recorded with a double beam ***UV-Vis spectrophotometer*** (Varian, model Cary 4E). The spectrometer has two emission lamps: a halogen lamp (for the visible region) and a deuterium lamp (for UV region), which are exchanged at 350 nm. The Cary 4E has a double monochromator with 1200 lines/mm with ± 0.1 nm resolution diffraction-net and a Hamamatsu R928 photomultiplier as detector (Figure 3.2.). Absorption spectra were recorded in transmittance from 200 to 800 nm, at 120 nm/min and with a slit width of 1 nm. Signal was corrected placing the solvent which corresponds in the reference beam. In the case of dye-loading quantification in MgAPO samples, MgAPO powder without dye, dissolved in the same conditions as the sample under study, was used as reference.

The absorption spectra of the dye/MgAPO powder samples were recorded by means of an integrating sphere (Internal DRA 900), which detects the reflected light. The respective spectra of MgAPO crystals synthesized in identical conditions but without dye were recorded and subtracted from the sample signal to eliminate the scattering contribution of the particles to the absorption spectra.

Figure 3.2. Double beam UV-Vis spectrophotometer (Cary 4E).

Steady-state luminescence spectra were measured in an Edinburgh Instruments ***Spectrofluorimeter*** (model FLSP920, Figure 3.3.), with 450W continuous xenon arc lamp as excitation source (model Xe900). Fluorescence spectra were corrected from the wavelength dependence of the detector sensitivity.

Fluorescence quantum yields of solutions were obtained using several references such as commercial i) quinine sulfate (ϕ_{fl}^{R} = 0.54 in 1 M H_2SO_4) and coumarin 152

(ϕ_{fl}^{R} = 0.19 in EtOH), ii) fluorescein (ϕ_{fl}^{R} = 0.93 in 0.1 M NaOH) and PM567 (ϕ_{fl}^{R} = 0.84 in EtOH) and iii) nile blue (ϕ_{fl}^{R} = 0.27 in MeOH) and zinc phtalocyanine (0.30 in 1% pyridine in toluene) for UV-blue, green and red emission light, respectively. Absolute fluorescence quantum yields of powder samples were measured in the same spectrofluorimeter by means of an integrating sphere and with a Spectralon white scatterer as reference (see more details in chapter 2, section 2.1.1.1.).

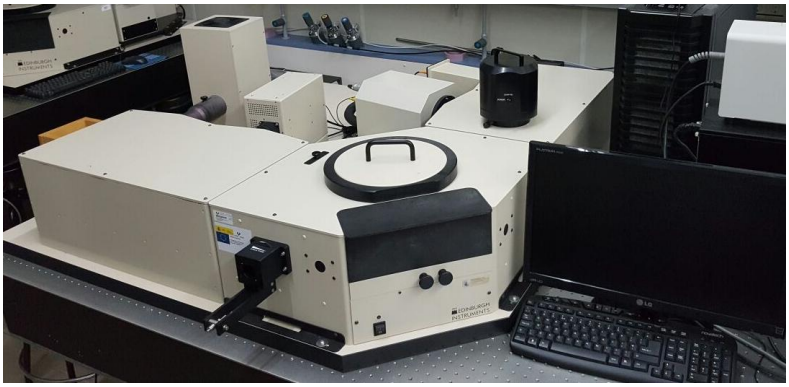

Figure 3.3. Edinburgh Instruments Spectrofluorimeter, model FLSP920.

Phosphorescence spectra of MOF materials (chapter 5) were recorded for the suspension obtained by dispersing the same amount of powder into different solvents under continuous stirring in a ***SPEX spectrofluorimeter*** (model HORIBA Fluorolog-3), exciting the sample at 380 nm with a flash lamp with a 50 μs delay after the flash and a gate time of 61 μs, accumulating 100 flash counts per point.

Fluorescence decay curves were carried out in the above described Edinburgh Instruments Spectroflurimeter, by means of the Time Correlated Single Photon Counting technique.[7,8] Fluorescence decay curves were monitored at the emission maximum (after collecting 10000 counts at the channel with the maximum intensity) after sample excitation by means of a Fianium supercontinuum wavelength-tunable laser with 150 ps FWHM pulses. The erratic scattering signal of the laser was avoided in the detection channel by filtering the excitation light with the corresponding cut off filter (Lambda Research Optics, Inc.) placed between sample and detector. A repetition rate of 10 MHz, in time-windows ranging between 50-100 ns and a power of around 0.5 mW was used.

Fluorescence lifetimes (τ) were obtained from the slope after the deconvolution of the instrumental response signal from the recorded decay curves by means of an

iterative method by the FAST software (Fluorescence Analysis Software Technology). The goodness of the deconvolution process was controlled by the chi-square (χ^2) statistical parameter and the residuals analysis.

Usually, in solid samples a multiexponential behavior is observed, and it is typically ascribed to the high heterogeneity degree of the environment in which molecules are embedded, in comparison with solution.[9,10] Thus, the decay curves are adjusted to a sum of exponential decays by means of:

$$I_{fl}(t) = \sum_i A_i e^{(-t/\tau_i)} \qquad \text{(eq. 3.1.)}$$

where A_i are the pre-exponential factors related to the statistical weights of each exponential, and τ_i are the fluorescence lifetimes of each exponential decay.

Due to the inherent difficulty on the physical interpretation of the decay curves composed of various exponentials, an average lifetime can be estimated according to the following equation:

$$\langle\tau\rangle_{ia} = \frac{\sum A_i \tau_i^2}{\sum A_i \tau_i} \qquad \text{(eq. 3.2.)}$$

where A_i and τ_i are those defined in eq. 3.1. It is a lifetime averaged by its intensity (*ia*, *intensity average lifetime*)[11] and it represents the average lifetime that molecules are in their excited state. In the case of MOF samples in chapter 5, averaged lifetime values are given.

Long luminescence decay curves were measured similarly, in the same spectroflurimeter, exciting the sample with a 60W pulsed xenon flashlamp (model µF920H, Edinburgh Instruments), recording emission at the maximum fluorescence wavelength and accumulating 10000 counts at the maximum channel. Particularly, AY/AEL and AO/AEL samples (chapter 4) were excited at 415 and 440 nm, with a pulse repetition rate of 0.2 Hz and 0.5 Hz and a time window of 4 or 2 s (5-10 times higher than the estimated lifetime), respectively. Long lifetimes for MOF powder samples (chapter 5) were excited at 370 nm with a repetition rate between 10 and 100 Hz and a time window varying from 0.4 to 80 ms depending on the sample (5-10 times higher than the estimated phosphorescence lifetime).

TRES experiments (Time Resolved Emission Spectroscopy) were also carried out in the same set up for AY/AEL and AO/AEL samples (chapter 4). Samples were excited with the pulsed xenon flashlamp at 415 nm or 440 nm (for AY/AEL or

AO/AEL, respectively). Decay curves were recorded as a function of the emission wavelength in the 460-650 nm range (wavelength increment of 5 nm) for a fixed recording time (120 s per wavelength). The emission spectra at different times after excitation were obtained by averaging the integrated fluorescence intensity for different time windows in the microseconds and milliseconds time intervals after the excitation pulse.

Measurements at different temperatures ranging from 77 K to 298 K were done for MOFs (chapter 5) and for the organometallic compounds (chapter 6) by an Optisa DN cryostat and ITC601 temperature controller (Oxford Instruments). In the later case, for phosphorescence emission measurements, a NIR detector integrated in the spectrofluorimeter was required (InGaAs detector, Hamamatsu G8605-23), which is cooled with liquid nitrogen from 2 hours before its use and for the duration of all the measurements.

3.3.2. Singlet oxygen emission detection by direct measurements

The analysis and quantification of singlet oxygen ($^1O_2$) generation are carried out by recording its phosphorescence emission signal[12,13] at 1276 nm on the same Edinburgh Instruments spectrofluorimeter by means of the previously described NIR detector (InGaAs detector, Hamamatsu G8605-23) upon continuous monochromatic excitation (450 W Xenon lamp) of the photosensitizer (PS).

The singlet oxygen signal was recorded in front face configuration, at 40º and 50º to the excitation and emission beams respectively, and leaned 30º to the plane formed by the direction of incidence. The signal was filtered with a low cut-off filter of 850 nm. At least 5 solutions of different concentrations between 10^{-6} M and 10^{-5} M of the photosensitizer under study were analyzed.

The singlet oxygen quantum yield of the PS (Φ_Δ^{PS}) is calculated comparing the obtained singlet oxygen signal with the signal produced by a reference photosensitizer with a known singlet oxygen generation quantum yield (Φ_Δ^{R}), recorded in the same solvent and experimental conditions (equation 3.3.).[14]

$$\Phi_\Delta^{PS} = \Phi_\Delta^{R} \cdot \left(\frac{\alpha_R}{\alpha_{PS}}\right) \cdot \left(\frac{Se_{PS}}{Se_R}\right) \qquad \text{(eq. 3.3.)}$$

where *Se* is the $^1O_2$ signal intensity at 1276 nm for both reference (R) and photosensitizer (PS); and α is an absorption factor given by:

$$\alpha = 1 - 10^{-A} \qquad \text{(eq. 3.4.)}$$

where *A* is the absorbance of the PS at the excitation wavelength. It must be noted that α_{PS} and α_R should not differ significantly.

The compounds used as reference sensitizers are the following: phenalenone (PN) for PSs with absorption bands in the UV-blue region, with Φ_Δ= 1 in most solvents[12,15,16], Rose Bengal (RB) for PSs with absorption bands in the green region, with Φ_Δ= 0.53 in ACN (measured in our set up relative to phenalenone in ACN with Φ_Δ= 1) and New Methylene Blue (NMB) for PSs with absorption bands in the red region of the electromagnetic spectrum, with Φ_Δ= 0.70 in ACN (measured in our set up relative to RB in ACN with Φ_Δ= 0.53).

3.3.3. Laser flash-photolysis

Laser flash photolysis is a technique for studying transient species generated by the short intense pulse from a nanosecond pulsed laser source (pump pulse). This intense light pulse creates short-lived photo-excited intermediates such as excited states, radicals and ions, generated in large enough concentrations to enable direct observation of the associated temporally changing absorption characteristics. The absorption changes are recorded using a spectrally continuous xenon lamp (probe source).

Figure 3.4. LP980 Spectrometer (Edinburgh Instruments).

Nanosecond transient absorption spectra were collected on a LP980 laser flash photolysis spectrometer (Edinburgh Instruments, Figure 3.4.), with a sensitivity of ΔOD = 0.002, *i.e.* the lowest detectable optical density, and a global system response of < 7 ns. Samples were excited at different wavelengths with a computer controlled

Nd:YAG laser/OPO system from LOTIS TII (laser model LS-2134UT-UV3; OPO model LT-2215-PC) working up to 10 Hz. With this OPO coupled laser system, excitation radiation from 420 nm to 2300 nm can be achieved. The probe source is a continuous-wave xenon lamp of 150 W with emission in the 230-900 nm spectral range. The system has a TMS302 monochromator with two output ports, one towards the kinetic PMT detector (Hamamatsu R928) and the other towards the ICCD detector (Andor iStar) for spectral measurements. The transient signals were recorded on a Tektronix TDS 3012C oscilloscope, and lifetime values (by monitoring the decay traces of the transients) were obtained with the LP920 software.

Samples in solution were measured in aerated and deaerated conditions, for which they were purged with N_2 for 10 min before measurement. In the sample holder for liquid samples the intersection between the laser beam and the probe source falls on the center of the cuvette (Figure 3.5.A). On the other hand, there is another holder for solid samples, the diffuse reflectance accessory (Figure 3.5.B), which allows focusing both beams in the same point of the sample and direct then the reflected probe light towards the detector.

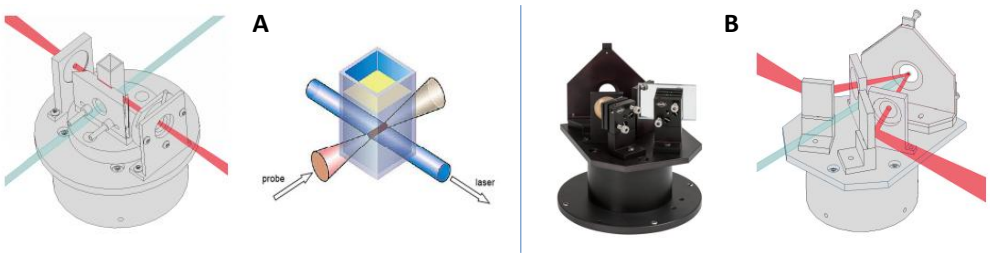

Figure 3.5. A) Sample holder for liquid samples, with an illustration of the intersection between the beams. B) Sample holder for solid samples.

3.3.4. Fluorescence microscopy

Hybrid samples consisting of big crystals such as dye-embedded MgAPO frameworks and MOF systems were studied at single particle level by different fluorescence microscopy techniques.

Fluorescence images were recorded with an optical upright microscope with epi configuration (Olympus BX51), where the emission is collected in the same direction of excitation, equipped with a color CCD camera (DP72). As excitation source a 120 W short arc lamp that provides white light was used (X-Cite® Series 120Q, EXFO).

Excitation radiation and emission range were selected by Chroma band pass and cut-off filters, respectively. For polarized emission experiments, a polarizer (U-AN-360–3) was incorporated before the registration of the image in the CCD camera. Single particle fluorescence spectra and CIE color coordinates were also collected with this microscope by means of an optical fiber coupling to the FLSP920 Edinburgh Instruments Spectrofluorimeter.

Finally, time-resolved fluorescence confocal microscopy was employed to further analyze the particles of the solid samples (model Micro Time 200, PicoQuant, Figure 3.6.).[17] The device has an inverted microscope (Olympus IX 71) with epi illumination.

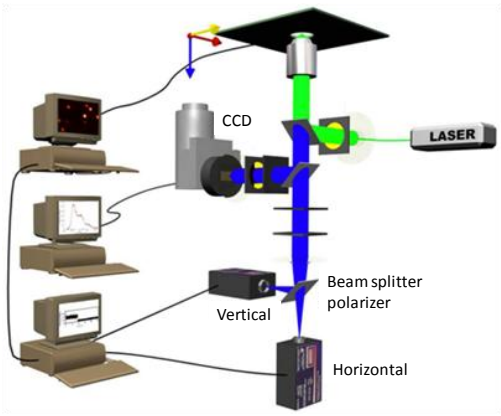

Figure 3.6. Schematic representation of the time-resolved fluorescence confocal microscope PicoQuant Micro Time 200.

Samples were excited by pulsed diode lasers (PicoQuant models LHD 410 and LHD 470) with pulses of 100 ns width and 40 MHz repetition rate, controlled by Multichannel Picosecond Diode Laser Driver "Sepia" (PicoQuant, model PDL 808). Excitation polarization direction was oriented in the axis of the sample holder; however, the linear polarization of the excitation laser was modified to circular polarization by incorporating a λ/4 filter (Thorlabs, WPQ05M-488) at the excitation holder.

Before directing the excitation towards the microscope objective (Olympus UPlanFl model 100x/1.30 Oil), a fraction of the excitation light (around 10%) was deflected by a beam splitter to a photodiode to monitor the excitation intensity. The remaining 90% of the collimated laser beam was reflected by a dichroic mirror (405 nm or 490 nm for 410 and 470 nm excitation, respectively) to the microscope objective where it was focused on the sample. The fluorescence emitted by the sample

was collected again by the objective and transmitted by the dichroic mirror to the detection part after being filtered by a high bandwith long pass filter to avoid any reminiscence of the excitation light (long pass filters of 430 or 500 nm for 410 and 470 nm excitation, respectively). The filtered signal was focused on a 50 μm pinhole which only allow the pass of the radiation emitted by the sample in the focal plane (focal principle), improving the axial resolution of the signal that is going to be detected. By sample scanning 2D images were recorded in the focal plane (XY scanning).

Then, the signal reaches an optical turret where, depending on the experiment that is being carried out, the radiation can be transmitted entirely to a single avalanche detector (Single Photon Avalanche Diode, SPAD, PDM model), or it can be split simultaneously to two detectors. In this study two types of experiments have been done:

i. Polarization experiments, for which a polarizer beam splitter was placed to split the emission light in two perpendicular polarization planes (vertical and horizontal). These signals were then directed to the respective SPAD detector. Comparing the intensities of the signals in each detector, the dichroic ratio "D" was determined, defined as the ratio between the emitted linearly polarized light intensity for perpendicular polarizations ($D = I_{\parallel}/I_{\perp}$). This parameter is used in order to somehow quantify the degree of alignment of the guests inside the MgAPO structures (chapter 4). Thus, large D values will indicate a high degree of chromophore molecules in a preferential order,[18,19] indicating that the dye is mainly occluded into the host. For randomly oriented fluorophore systems D values near unity are achieved. Also twinning in MOF single crystals (chapter 5) was deducted from this type of polarization experiments.

ii. Two color experiments, where a dichroic filter was placed which reflects emission light below certain wavelength, and transmits emission light above that wavelength. In this case a 495DCLP dichroic filter was used to split blue and red emission colors, or blue and green emission colors, for AC-PY/ATS and AC-PY/AEL samples, respectively (sections 4.1.4. and 4.2.4. in chapter 4, respectively). Extra band pass filters were placed before each detector: band pass filters of 470/40 and 620/60, for the detection of the blue and red emissions, respectively, for the AC-PY/ATS system; and 470/40 and 550/50 for the detection of the blue and green emissions, respectively, for AC-PY/AEL.

In this work FLIM technique (Fluorescence Lifetime Imaging Microscopy) was also applied to get further details in the registered 2D images. The detected signals were correlated with time by means of the quantum photon counter technique (TC-SPC, Time Correlated Single Photon Counting), described before in section 3.3.1. The electronic photon-detection system was controlled by the Pico Harp 300 module of PicoQuant that, along with the Symphotime software, allowed carrying out the reconstruction of lifetime images (FLIM). The results presented in this work are averages of at least 10 particles measured.

In addition, a spectrograph (Shamrock, SA3010-A model of 300 mm focal length) and a CCD camera (Andor, Newton EMCCD 1600 x 200 model), incorporated into a side port of the microscope detection part, allowed recording emission spectra at particular points of the sample (XYZ), *i.e.* in certain areas of a single particle, with a spectral resolution of 1 nm.

3.4. Remote excitation experiments: antenna effect

Remote excitation experiments were carried out at the Katholieke Universiteit of Leuven (KUL, Belgium). The measurements were done with a "sandwich" configuration: the sample was placed between top and bottom objectives for excitation and detection of fluorescence, respectively (Figure 3.7.). That is, CW laser light (375/473 nm) was introduced to the top objective (Nikon, PlanFluor, x20, NA 0.85) and it was focused onto the sample. Fluorescence from the sample was collected by the bottom objective (Nikon, PlanApo, x60, NA 0.95) and was guided to a spectrograph (Andor, SR303i) equipped with EM-CCD (Andor, Newton 970). A pinhole (100 μm) was placed at the light path in order to improve the spatial resolution of the detection. A filter (375 excitation: Thorlabs, FEL0400; 473 excitation: Chroma, HQ485LP) rejecting the excitation light was placed in front of the spectrograph.

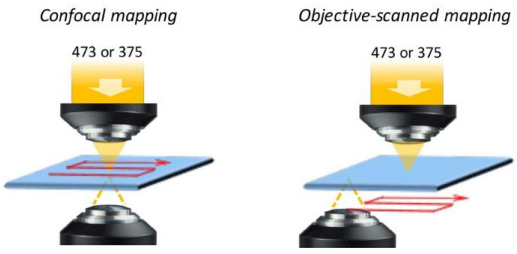

Figure 3.7. Schematic representation of the relative position of the objectives in confocal mapping experiments versus in objective-scanning mapping.

In order to systematically assess an "antenna" effect, two types of mapping methods were conducted: confocal and objective-scanned mappings (Figure 3.7.). First, typical confocal mapping was basically used to know the distribution of J-aggregate region in a crystal, being the top and bottom objectives placed parallel, and scanning the sample. After knowing where the different species (monomer/J-aggregates) were distributed along the crystal, "objective-scanned" was conducted. In this experiment, the top objective, *i.e.* excitation spot, was fixed to a monomer region and the bottom objective was raster scanned (Figure 3.7.)

3.5. NLO measurements

NLO measurements in single crystals of LDS722/AEL sample (section 4.2.3. in chapter 4) were also carried out at the Katholieke Universiteit of Leuven (KUL, Belgium). With this purpose, an ultrafast Ti:sapphire laser (Maitai-SP, SpectraPhysics) was used to generate the 820 nm pulses, 120 fs pulse duration (repetition rate 80 MHz). The laser beam was split into two paths with a ratio of 9:1. The stronger beam was guided to an optical parametric oscillator (OPO) (Inspire HF200, SpectraPhysics) used to generate the 940-1222 nm pulses. The polarization of the 820 nm pulses was controlled by a half-wave plate. Each beam was reflected by dichroic mirror (z750spxrxt, Chroma) after passing through a long-pass filter (HQ800LP, Chroma) in order to reflect stray light generated from the OPO, and then was focused to samples using an objective (PlanApo N.A. 0.95, x60, Nikon).

With this configuration, a wide range of photon flux was available at the sample position. Considering a pulse average power of 0.5 mW at 1180 nm, a minimum number of 1.88×10^{15} photons per pulse per cm^2 is obtained while for a pulse with an average power of 10 mW at 820 nm, a number of 6.41×10^{16} photons per pulse per cm^2 could be achieved. The availability of such a wide range is important for the laser power dependent experiments (see below) where the probability of having one or two photons arriving at the sample at the same time is of key importance in investigating nonlinear processes.

The sample is mounted on 5-axis stage (xyz, rotate, and tilt) which allows to find the most efficient sample orientation, and SHG/fluorescence was collected using a transmission configuration by a different objective (x10, NA 0.3). The generated optical signal is filtered through a short-pass filter (ET750SP-2P, Chroma) to remove

the excitation light, and the emitted light is focused to the entrance slit of a spectrograph (iHR320, Horiba), equipped with a cooled CCD camera (Newton 920, Andor).

For the comparison between the SHG efficiency of the LDS722/AEL single crystals and the reference BBO crystal (EKSMA OPTICS, BBO-652H), a scale factor must be calculated due to thickness differences (1-2 μm and 1 mm for LDS722/AEL and BBO crystals, respectively).

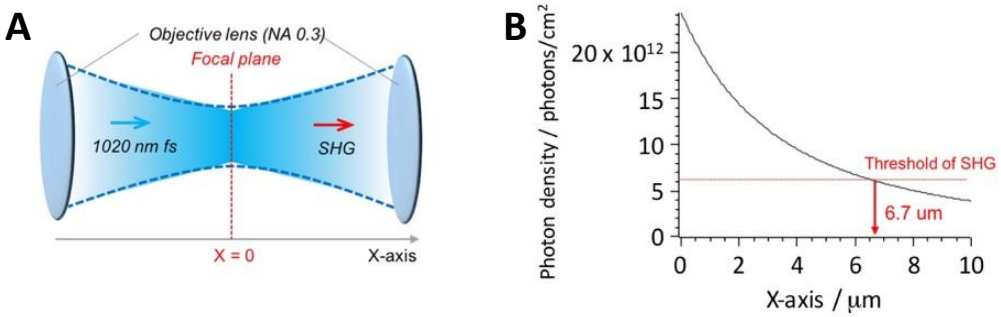

Figure 3.8. A) Schematic illustration of the SHG measuring mode. B) Determined photon density *vs*. z-depth in BBO crystal.

Figure 3.8.A shows a schematic representation of the measuring mode in this experiment. In order to compensate the volume difference between the crystals, first photon density against z-depth (Figure 3.8.B) was calculated in our experimental conditions (averaged laser power of 50 μW, measured after passing the objective lens). Note that x = 0 corresponds to the depth of the focal plane and only the area which has positive x values is plotted in Figure 3.8.B. The red horizontal line represents the threshold photon density of SHG on BBO at 6.09×10^{12} photons/cm^2.[20] From the crossed point between the plot and the line, the effective x-value for SHG is estimated to be 6.7 μm. Considering an average height of AEL crystals of about 1 μm, the scale factor is estimated to be about 27. This value is multiplied to the spectrum obtained on LDS722/AEL crystals and the SHG conversion efficiency is estimated by comparing the obtained value after applying the scale factor with the signal of the BBO.

3.6. Computational details

The direction of the transition dipole moment of the protonated AC (ACH^+) and the energies of the electronic levels of AY and AO dyes were calculated performing quantum mechanics calculations by Gaussian 09.[21] The ground geometry was fully optimized with the B3LYP hybrid functional (DFT) and the vertical absorption transition (Franck-Condon) was simulated by single point calculation of such geometry at the first singlet excited state with the ab initio CIS methods, using in both cases a double-valence basis set.

Calculations regarding MgAPO-11 materials (chapter 4) were carried out by Dr. Luis Gómez-Hortigüela at the Catalysis and Petrochemistry Institute (CSIC). They were based on molecular mechanics simulations as implemented in Forcite module in Materials Studio Software.[22] On the other hand, the DFT calculations in the organometallic **Ir-2** compound (chapter 6) were done by Dr. Hegoi Manzano at the University of the Basque Country (UPV-EHU), using the Gaussian09 code.[21] The simulations were carried out using a B3LYP exchange correlation functional, a LanL2DZ basis set, and a fine integration grid (7000 points per atom) to compute numerically the two-electron integrals and their derivatives. The ground state and triplet state of the molecule were optimized, performing a frequency analysis to ensure that the final states were a local energy minima.

References

(1) Barrer, R. M. Syntheses and Reactions of Mordenite. *J. Chem. Soc.* **1948**, 2158–2163.

(2) Breck, D. W.; Eversole, W. G.; Milton, R. M. New Synthetic Crystalline Zeolites. *J. Am. Chem. Soc.* **1956**, *78*, 2338–2339.

(3) Bieniok, A.; Brendel, U.; Sereni, P.; Musso, M. Raman Spectroscopy and Crystal Structure Investigation of Solvo- and Ionothermally Prepared Microporous Metal-Aluminophosphates with the Laumontite Framework Structure. *Zeitschrift fur Krist. - Cristal. Mater.* **2013**, *288*, 374–381.

(4) Li, D.; Xu, Y.; Ma, H.; Xu, R.; Wang, Y.; Liu, H.; Wang, B.; Tian, Z. Ionothermal Syntheses of Transition-Metal-Substituted Aluminophosphate Molecular Sieves in the Presence of Tetraalkylammonium Hydroxides. *Microporous Mesoporous Mater.* **2015**, *210*, 125–132.

(5) Chen, B.; Huang, Y. Dry Gel Conversion Synthesis of SAPO- and CoAPO-Based Molecular Sieves by Using Structurally Related Preformed AlPO Precursors as the Starting Materials. *Microporous Mesoporous Mater.* **2009**, *123*, 71–77.

(6) Takashima, Y.; Martínez-Martínez, V.; Furukawa, S.; Kondo, M.; Shimomura, S.; Uehara, H.; Nakahama, M.; Sugimoto, K.; Kitagawa, S. Molecular Decoding Using Luminescence from an Entangled Porous Framework. *Nat. Commun.* **2011**, *2*, 168.

(7) Demas, J. N. *Excited State Lifetime Measurements*; Academic Press: New York, **1983**.

(8) O'Connor, D. V.; Phillips, D. *Time-Correlated Single Photon Counting*; Academic Press: New York, **1984**.

(9) Rurack, K.; Hoffmann, K.; Al-soufi, W.; Resch-genger, U. 2,2′-Bipyridyl-3,3′-Diol Incorporated into $AlPO_4$-5 Crystals and Its Spectroscopic Properties as Related to Aqueous Liquid Media. *J. Phys. Chem. B* **2002**, *106*, 9744–9752.

(10) Wiederrecht, G. P.; Sandi, G.; Carrado, K. A.; Seifert, S. Intermolecular Dimerization within Pillared, Layered Clay Templates. *Chem. Mater.* **2001**, *13*, 4233–4238.

(11) Valeur, B. *Molecular Fluorescence: Principles and Applications*; Wiley-VCH Verlag GmbH: Weinheim, **2001**.

(12) Martí, C.; Jürgens, O.; Cuenca, O.; Casals, M.; Nonell, S. Aromatic Ketones as Standards for Singlet Molecular Oxygen Photosensitization. Time-Resolved Photoacoustic and near-IR Emission Studies. *J. Photochem. Photobiol. A Chem.* **1996**, *97*, 11–18.

(13) Braun, A. M.; Oliveros, E. Applications of Singlet Oxygen Reactions: Mechanistic and Kinetic Investigations. *Pure Appl. Chem.* **1990**, *62*, 1467–1476.

(14) Mathai, S.; Smith, T. A.; Ghiggino, K. P. Singlet Oxygen Quantum Yields of Potential Porphyrin-Based Photosensitisers for Photodynamic Therapy. *Photochem. Photobiol. Sci.* **2007**, *6*, 995–1002.

(15) Oliveros, E.; Suardi-Murasecco, P.; Aminian-Saghafi, T.; Braun, A. M.; Hansen, H. J. 1H-Phenalen-1-One: Photophysical Properties and Singlet-Oxygen Production. *Helv. Chicica Acta* **1991**, *74*, 79–90.

(16) Schmidt, R.; Tanielian, C.; Dunsbach, R.; Wolff, C. Phenalenone, a Universal Reference Compound for the Determination of Quantum Yields of Singlet Oxygen $O_2(^1\Delta_g)$ Sensitization. *J. Photochem. Photobiol. A Chem.* **1994**, *79*, 11–17.

(17) Roeffaers, M. B. J.; De Cremer, G.; Uji-i, H.; Muls, B.; Sels, B. F.; Jacobs, P. A.; De Schryver, F. C.; De Vos, D. E.; Hofkens, J. Single-Molecule Fluorescence Spectroscopy in (Bio)catalysis. *Proc. Natl. Acad. Sci. United States Am.* **2007**, *104*, 12603–12609.

(18) Inoué, S.; Shimomura, O.; Goda, M.; Shribak, M.; Tran, P. T. Fluorescence Polarization of Green Fluorescence Protein. *Proc. Natl. Acad. Sci. U. S. A.* **2002**, *99*, 4272–4277.

(19) Martínez-Martínez, V.; Corcóstegui, C.; Bañuelos Prieto, J.; Gartzia, L.; Salleres, S.; López Arbeloa, I. Distribution and Orientation Study of Dyes Intercalated into Single Sepiolite Fibers. A Confocal Fluorescence Microscopy Approach. *J. Mater. Chem.* **2011**, *21*, 269–276.

(20) Zhang, J.; Huang, J. Y.; Wang, H.; Wong, K. S.; Wong, G. K. Second-Harmonic Generation from Regeneratively Amplified Femtosecond Laser Pulses in BBO and LBO Crystals. *J. Opt. Soc. Am. B* **1998**, *15*, 200-209.

(21) Frisch, M. J.; Trucks, G. W.; Schlegel, H. B.; Scuseria, G. E.; Robb, M. A.; Cheeseman, J. R.; Scalmani, G.; Barone, V.; Mennucci, B.; Petersson, G. A.; Nakatsuji, H.; Caricato, M.; Li, X.; Hratchian, H. P.; Izmaylov, A. F.; Bloino, J.; Zheng, G.; Sonnenberg, J. L.; Hada, M.; Ehara, M.; Toyota, K.; Fukuda, R.; Hasegawa, J.; Ishida, M.; Nakajima, T.; Honda, Y.; Kitao, O.; Nakai, H.; Vreven, T.; Montgomery, Jr., J. A.; Peralta, J. E.; Ogliaro, F.; Bearpark, M.; Heyd, J. J.; Brothers, E.; Kudin, K. N.; Staroverov, V. N.; Kobayashi, R.; Normand, J.; Raghavachari, K.; Rendell, A.; Burant, J. C.; Iyengar, S. S.; Tomasi, J.; Cossi, M.; Rega, N.; Millam, J. M.; Klene, M.; Knox, J. E.; Cross, J. B.; Bakken, V.; Adamo, C.; Jaramillo, J.; Gomperts, R.; Stratmann, R. E.; Yazyev, O.; Austin, A. J.; Cammi, R.; Pomelli, C.; Ochterski, J. W.; Martin, R. L.; Morokuma, K.; Zakrzewski, V. G.; Voth, G. A.; Salvador, P.; Dannenberg, J. J.; Dapprich, S.; Daniels, A. D.; Farkas, Ö.; Foresman, J. B.; Ortiz, J. V.;

Cioslowski, J.; Fox, D. J. Gaussian 09. Gaussian, Inc.: Wallingford CT **2009**.

(22) Forcite Module, Material Studio. Accelrys Inc.: San Diego, CA **2013**.

4

DYE-DOPED MgAPOs FOR MULTIPLE OPTICAL APPLICATIONS

4

DYE-DOPED MgAPOs FOR MULTIPLE OPTICAL APPLICATIONS

This chapter aims to obtain new functional hybrid materials useful for diverse optical applications. In this case, hybrid organic-inorganic materials consisting of photoactive molecules, *i.e.* chromophores, embedded into 1D-inorganic hosts have been chosen (synthesized in the research group of Joaquín Pérez Pariente at the Catalysis and Petrochemistry Institute, CSIC). What is sought is not only the protection of the organic molecules by the host, reducing the photo- and thermal degradation of the chromophores, but the synergistic combination of the features of both components to obtain new and/or improved properties. In addition, it is interesting to get systems in which the photoactive molecules or dyes are distributed in a preferential arrangement in order to find applications in the field of nonlinear optics. Therefore, we have chosen zeolitic nanochanneled frameworks, specifically magnesium doped aluminophosphates, as suitable hosts. There are many magnesium aluminophosphates with different pore size, shape and topology, and thus they are very attractive structures to photophysically study different processes such as molecular aggregation, energy transfer between chromophore species, or anisotropic response to the linearly polarized light. An extended description of the aluminophosphate hosts has been included in section 2.2.1. (chapter 2).

4.1.- Dye encapsulation into MgAPO-5 and MgAPO-36: Antenna systems

Something that has always attracted scientists is the study, simulation and mimicry of natural systems and processes. In this regard, an interesting challenge is the design of artificial antenna systems by mimicking the photosynthesis process, in which sunlight is harvested and light-energy is transferred to the specific reaction center where the energy conversion takes place.[1] In fact, sunlight is the most abundant and easily reachable existing energy source, and it will provide a significant fraction of renewable energy as long as researchers find an efficient way of collection, transfer

and storage of solar energy.[2] Although it is difficult to reach the energy conversion rates of natural systems, artificial photonic antenna systems have found numerous applications, such as in solar cells,[3] luminescent solar concentrators (LSC),[4] light emitting devices (LEDs),[5] sensing devices and diagnosis[6].

Generally, in natural antenna systems, the energy of the light is harvested and then transferred sequentially from a donor to an acceptor, usually chromophores.[7] In this sense, to reproduce this process in an artificial antenna system several parameters have to be taking into account, and the control of all of them is not a trivial task. For example, in an artificial antenna system an Excitation Energy Transfer process (EET) takes place, commonly known also as FRET (Fösters Resonance Energy Transfer, see more details in section 2.1.2.2., chapter 2), and the distance between the donor and acceptor chromophores, the relative orientations of their transition dipole vectors and the donor:acceptor ratio affect drastically to the efficiency of this energy transfer.[8]

In this sense, host-guest hybrid materials have shown interesting properties, promoting a FRET process when different organic chromophores are combined within zeolitic matrices, as has been widely studied.[6,9,10] In those systems, dyes absorbing and emitting in different ranges of the electromagnetic spectrum are inserted sequentially into the channels of the zeolite so that the energy can be transferred usually from the center to the edges of the channels (Figure 4.1.) or conversely, from both edges to the center.

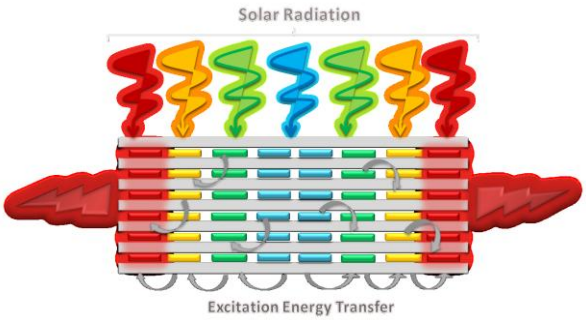

Figure 4.1. Schematic representation of an artificial photonic antenna system.

In any case, these organic-inorganic hybrid systems containing photoactive molecules are developed with the intention of obtaining materials suitable for optical applications, for which optically very dense materials are needed in most cases. However, in these conditions typical fluorescent dyes tend to aggregate, which affects significantly to the photophysical behavior of the monomers.

Hence, to overcome the problem of dye-aggregation in optically dense materials, one approach is the encapsulation of the chromophores into inorganic hosts in an attempt to maintain the molecules isolated from each other. However, this is neither an easy task. Indeed, although *a priori* several 1D matrices look suitable for the occlusion of certain dyes, some kind of aggregation can occur (for more details about molecular aggregation see section 2.1.2.1. in chapter 2). In this sense, magnesium-doped aluminophosphate hosts (MgAPOs) with different pore size and shape are chosen with the aim of controlling the aggregation of the encapsulated dye molecules and achieving a preferential arrangement of those guest molecules. Moreover, the typical post-synthetic approaches to incorporate dye molecules into the zeolitic hosts have been discarded and the "*crystallization inclusion method*" approach has been followed instead for several reasons (see section 2.2.1.2. in chapter 2). Since this one-pot synthesis is not a diffusional approach, it avoids the traffic jam at the entrances of the host pores, decreases considerably the sample preparation time, avoids also the leakage of guest molecules, and very importantly, it allows a very tight fitting between the molecular size of the guests and the pore dimensions of the host. Besides, MgAPO materials, with a net negative charge into the structure, favor the incorporation of commercially available cationic organic fluorophores that show a reasonable solubility in the aqueous synthesis gel.

4.1.1.- MgAPO-5/PY hybrid system[11,12]

MgAPO-5 was the first magnesium aluminophosphate used for the development of new hybrid materials in a previous work performed by our research group. Briefly, it has an AFI structure-type with non-interconnected cylindrical channels of a diameter of 7.3 Å (see section 2.2.1.1., chapter 2). This framework crystallizes relatively easily and its pore size is suitable for the molecular dimensions of many commercial dyes.

Firstly the fluorescent dye Pyronin Y (PY) was chosen as guest due to its molecular dimensions, planarity and cationic nature (Figure 4.2.).

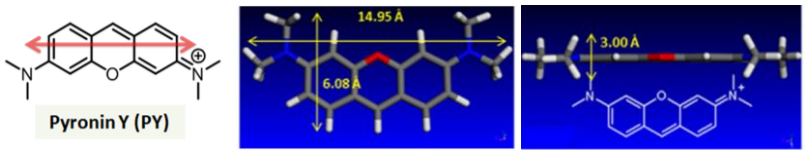

Figure 4.2. Molecular structure of PY (left) together with its molecular dimensions (centre and right). Red arrow in the left image represents the transition dipole moment of the PY molecule.

Pyronin Y has a characteristic pinkish color and bright green fluorescence, which reaches an efficiency of ϕ_{fl} = 0.66 in ethanol at room temperature. In an aqueous medium, similar to the synthesis gel environment, the fluorescent capacity decreases to 0.22, showing its absorption and emission maxima at 548 nm and 566 nm respectively (Figure 4.3.).

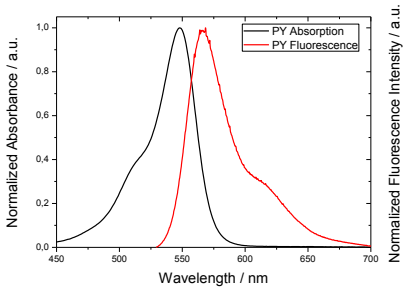

Figure 4.3. Height normalized absorption (black) and emission (red) spectra of PY in diluted aqueous solution.

However PY shows great tendency to aggregate, a typical feature for xanthene-type dyes, both in solution, as the concentration increase, and when it is adsorbed on a surface due to high local concentrations. Certainly, Pyronin Y has been previously used in our research group as photoactive guest to be intercalated into clay minerals, proving its tendency to aggregate.[13–15] As explained in chapter 2 (section 2.1.2.1.), dye aggregation drastically affects the photophysical properties of the dyes. Only as a reminder, there are two main types of aggregates: H-aggregates, undesirable because not only they are non-fluorescent but they also quench the fluorescent emission of the monomers, and J-aggregates, which could be very interesting since they can be potentially fluorescent with characteristic red-shifted emission bands respect to the monomers. In fact, PY is a good candidate for sensing de aggregation state of the molecules into inorganic hosts since its J-aggregates show red fluorescence, in contrast to the intense green emission of its monomers.[16] Therefore, by using PY dye as reference and as representative of the large group of chromophores with similar molecular structures built up by three fused aromatic rings, the aggregation state of the dyes inside the nanocanneled aluminophosphate zeotypes can be easily tracked.

Thus, in principle the molecular dimensions of the dye were in good agreement with the pore-dimensions of the 1-D channeled MgAPO-5 host with AFI structure. Indeed, zeolite L, with a very similar cylindrical pore system to MgAPO-5, has been extensively employed as host for fluorescent dyes incorporated by diffusional

processes (post-synthesis method) resulting in promising antenna materials for light harvesting.[9,17]

Two different dye-loaded microporous magnesium aluminophosphates were prepared by hydrothermal synthesis from gels with the following molar composition: 0.2 MgO: 1 P_2O_5: 0.9 Al_2O_3: 0.75 TEA: *x* PY: 305 H_2O (more details in section 3.1.1. in chapter 3), varying dye amount from $x = 0.008$ to $x = 0.024$ and resulting in the samples named PY/AFI-L and PY/AFI-H, respectively (L = low and H = high dye loading), in order to determine if the luminescent properties of the hybrid material depend on the amount of dye occluded. In both cases, big crystals with hexagonal shape were obtained, showing the typical green fluorescence of the PY dye (Figure 4.4.A, B and C).

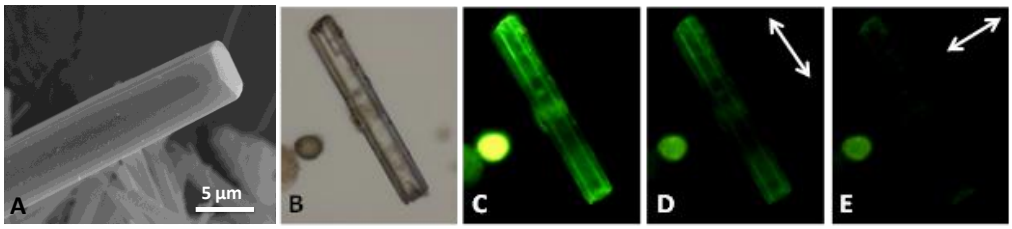

Figure 4.4. (A) SEM image of PY/AFI-L particles. Transmission (B) and fluorescence under blue excitation light (C) images of a PY/AFI-L particle. Polarized fluorescence images parallel to the channels' c-axis, the long axis of the particle (D), and perpendicular to it (E). White arrows indicate the direction of the polarizer.

The dye uptake, estimated spectrometrically (see section 3.1.4. in chapter 3), was only 0.005 mmol PY per 100 g sample powder for PY/AFI-L, while PY/AFI-H sample contains 0.660 mmol/100 g sample (Table 4.1.). The best way to confirm that the dye is actually occluded into the AFI channels is by means of linearly polarized light experiments at single particle level by fluorescence microscopy (see section 3.3.4. in chapter 3). Indeed, microscopy images demonstrated that the chromophore is occluded inside MgAPO-5 (and not adsorbed on the outer surface), preferentially oriented throughout the nanochannels, giving a relatively high anisotropic response (see Figure 4.4.D and E).

By confocal fluorescence microscopy D values (dichroic ratios) of 9-12 and 11-15 were determined for PY/AFI-L and PY/AFI-H samples, respectively (Table 4.1.), corroborating the incorporation of the PY dye molecules into the MgAPO-5 material in a preferential orientation along the channels.

On the other hand, photophysical characterization was performed in bulk powder. First note that the absorption and fluorescence bands of both hybrid samples are broaden and hyspochromically displaced in comparison with PY in aqueous solution (Figure 4.5., Table 4.1.). This is a typical feature for encapsulated dyes in highly constricted environments.

Table 4.1. Dye-loading and photophysical parameters for PY/AFI samples in bulk powder. Same parameters for the dye in aqueous solution are also included for comparison.

System	PY occluded / mmol/100g	λ_{abs} / nm	λ_{fl} / nm	ϕ_{fl}	D
PY/AFI-H	0.660	534	554	<0.01	11-15
PY/AFI-L	0.005	536	555	0.075	9-12
PY (aq)	--	548	566	0.22	--

Despite the broadening of the bands, a change in the shape of the absorption spectra is observed in the samples. It consists of an increase in the vibronic shoulder region, at around 500 nm, with respect to the main band, which could suggest the presence of H-type PY aggregates. In fact, the fluorescence efficiency of the hybrid samples drastically decrease with respect to the dye in aqueous diluted solution (Table 4.1), suggesting again the presence of aggregation, particularly H-aggregation, since the characteristic red emission band of the PY J-aggregates is not observed in the fluorescence spectra.

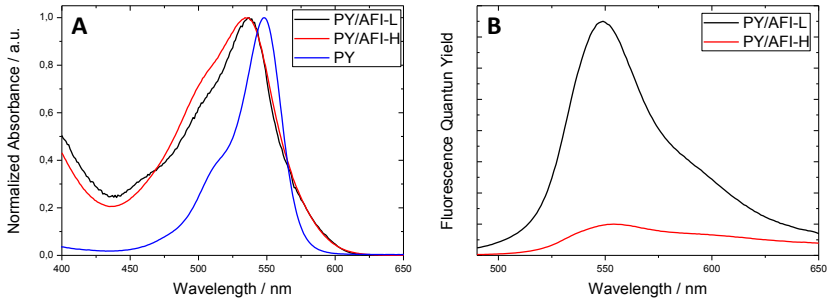

Figure 4.5. A) Height normalized absorption spectra of the bulk samples PY/AFI-L and PY/AFI-H, together with the spectra of the dye PY in dilute aqueous solution for comparison; and B) bulk fluorescence spectra normalized to the quantum yield.

The formation of H-type sandwich aggregates into the MgAPO-5 nanochannels was confirmed by DFT calculations (carried out by Dr. Luis Gómez-Hortigüela at the Catalysis and Petrochemistry Institute, CSIC). The modeling indicated that both

species, monomers and H-aggregates (Figure 4.6.), are thermodynamically feasible since the energy difference between them is relatively small (less than 4 kcal/mol).

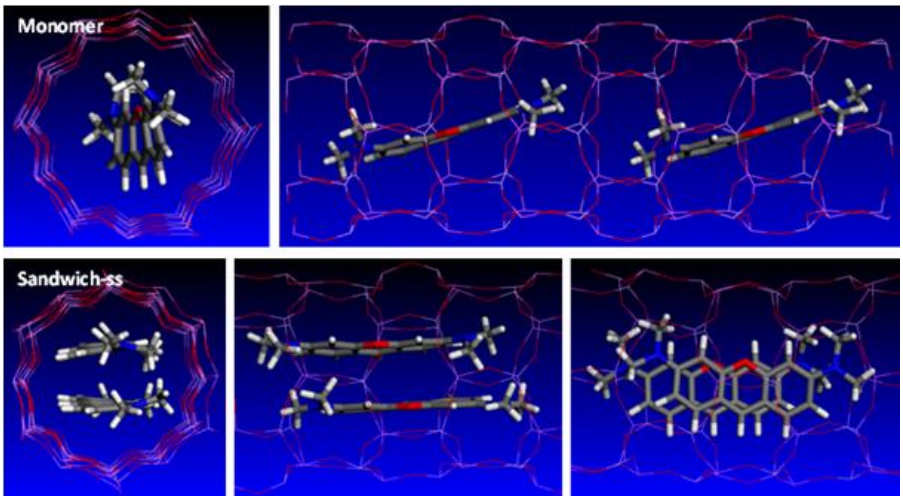

Figure 4.6. Views of the (DTF + D) geometry optimized PY molecules inside the AFI nanochannels. The top images correspond to PY incorporated as monomers, and the bottom images to H-type aggregates with the $N(Me)_2$ groups of the molecules in the same side (ss).

Therefore, contrary to what might be expected, undesirable coplanar H-aggregates are formed into the cylindrical nanochannels of the MgAPO-5 host, quenching the fluorescence of the system and, as a consequence, PY/AFI systems will not be interesting hybrid materials for optical applications.

4.1.2.- MgAPO-36/PY hybrid system[11]

Due to the conclusions deducted from the previous results, another framework with narrower channels was chosen: MgAPO-36. Although it is also a 12-ring one-dimensional channeled inorganic zeolitic host, it has an ATS structure with elliptical pores of 6.7 Å x 7.5 Å (further details in section 2.2.1.1. in chapter 2). In this sense, by slightly reducing one of the dimensions of the pore, the formation of H-aggregates should be prevented.

With this aim, a dye-loaded material was synthesized from a gel with the following composition: 0.2 MgO: 1 P_2O_5: 0.9 Al_2O_3: 0.75 TPA: 0.024 PY: 305 H_2O (details in section 3.1.2. in chapter 3), resulting in pure ATS phase with a dye loading of 0.514

mmol PY per 100 g sample powder. Note here that the total dye amount added to the synthesis gel is equivalent to that in the precursor gel for sample PY/AFI-H.

Table 4.2. Dye-loading and photophysical parameters for PY/ATS sample in bulk powder. Same parameters for the dye in aqueous solution are also included for comparison

System	PY occluded / mmol/100g	λ_{abs} / nm	λ_{fl} / nm	ϕ_{fl}	D
PY/ATS	0.514	513	557 610 660	0.01	5
PY (aq)	--	548	566	0.22	--

Regarding the photophysical properties of the bulk powder, the main absorption band appears centered at 513 nm, hypsochromically blue-shifted respect to the dye in aqueous solution (Figure 4.7., Table 4.2.). Note here that the registered blue-shift is higher than in the case of PY/AFI samples, indicating a more constricted environment for the PY dye into ATS framework. Moreover, a prominent shoulder also appears, but in this case it is registered at higher wavelengths with respect to the main absorption band (Figure 4.7.). Regarding the exciton theory (detailed in chapter 2, section 2.1.2.1.), this red shifted shoulder could be attributed to J-aggregates of the dye.

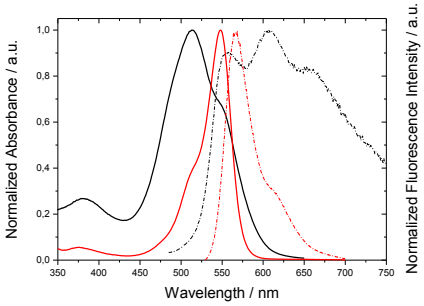

Figure 4.7. Height normalized absorption (solid lines) and emission (dashed lines) spectra of PY/ATS sample in bulk powder (black lines) and PY dye in aqueous diluted solution (red lines).

On the other hand, the emission spectrum of the bulk powder, recorded under blue excitation light (λ_{exc}: 470 nm), shows three peaks centered at around 557 nm, 600 nm and 660 nm (Figure 4.7.), which could be assigned i) to the typical emission band of the PY monomers (once again blue shifted in comparison with the fluorescence of the dye in solution, centered at 566 nm), and ii) to different J-type aggregates formed in

the inorganic matrix (centered at 606 and 660 nm), as will be discussed later. Thus, by using ATS framework, H-type aggregates are prevented in favor of J-aggregates. However, J-aggregation is surely also responsible for the poor fluorescence quantum yield of the sample (ϕ_{fl} = 0.01, Table 4.2).

Indeed, DTF calculations confirm that both J-type dimers (in a zigzag configuration, with an aggregation energy of ca. 2 kcal·mol^{-1}) and monomers fit nicely within the ATS nanochannels (Figure 4.8.).

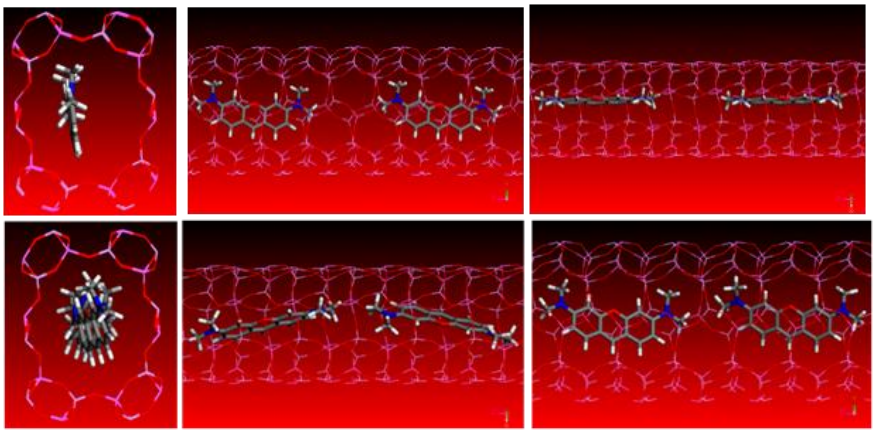

Figure 4.8. (DFT+D) Geometry-optimised structure of (top) PY monomers and (botton) J-aggregates inside ATS.

Through confocal microscopy a D value of 5 was measured for the PY/ATS system, evidencing that the dye is occluded inside the ATS channels (Table 4.2.). By means of fluorescence microscopy it has been observed that the resultant material was composed of needles arranged in bouquets, showing a multicolor emission under blue excitation light, evidencing the co-existence of PY J-aggregates at the bouquet joint (red emission) and PY monomers at the other end of the particles (green emission). Importantly, this arrangement results in an attractive fluorescence color gradation from green to yellow to red along the ATS particles (Figure 4.9.right). Note here that the emission color change along the needles in the fluorescence image corresponds in the transmission image to a gradual increase in the characteristic pink color of PY dye from the joint part of the bouquet towards the other end of the needles (Figure 4.9. left). Thus, this suggests that the dye is incorporated mainly in a J-type association at the initial steps of the crystallization and in monomeric units at the last steps of the crystal growth, as crystallization proceeds from the joint center of the bouquet to the opossite ends.

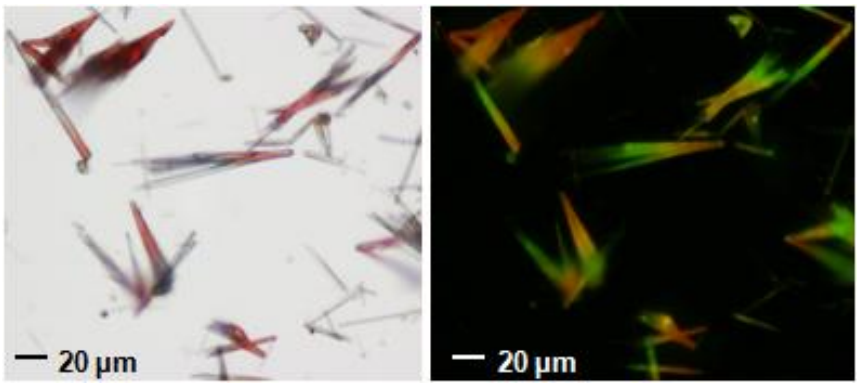

Figure 4.9. Microscopy transmission (left) and emission (right) images of the PY/ATS cystals.

Moreover, the gradual change in the emission colors from green to red correlates with a gradual reduction of average lifetime values. PY monomers show a fluorescence lifetime of around 2-3 ns, whilst that for the J-aggregates is slightly shorter, around 1-2 ns (Figure 4.10.A).[16,18] By means of the emission spectra registered in discrete areas of the particles (≤ 1 µm), it was proven that the lifetimes around 3 ns are ascribed to the monomeric fluorescence band, centered at 557 nm, while the shorter lifetimes recorded in the union of the bouquets correspond to well-defined red-shifted emission bands respect to the monomer, at around 610 and 660 nm (Figure 4.10.B).

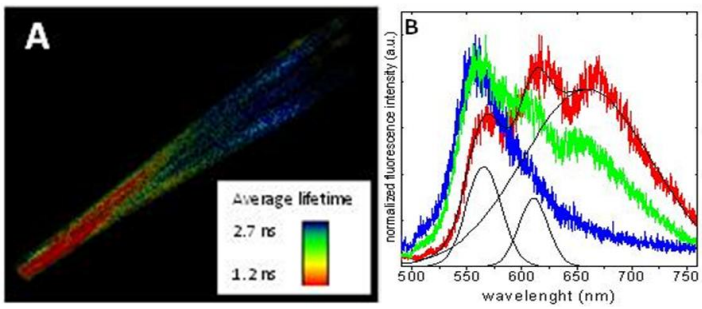

Figure 4.10. A) Fluorescence Lifetime Image (FLIM) of a group of ATS-PY crystals. B) Fluorescence spectra recorded in the discrete areas of the particles. Note that the spectra are represented in the same color as the corresponding area of the particles in A.

Note here that the appearance of different red-shifted emission bands is ascribed to the existence of different J-type Davydov couplings.[19,20] The band centered at around 610 nm should be assigned to J-type dimers, while the band showing the longest red-shift at 660 nm, can be a consequence of a higher incorporation of the dye in the first

steps of crystal growth, leading to a more dense packing, forcing the molecules to stay closer and enhancing the J-coupling and/or increasing the number of monomeric units forming the aggregate, producing high-order J-aggregates.

Thereby, PY/ATS system, can offer an interesting material for light transport. Generally, the design of an artificial photonic antenna systems is based on a one-dimensional energy-transfer process (FRET: Föster Resonance Energy Transfer) between different chromophores sequentially ordered within nanoporous materials, where chromophores are close enough for enabling the coupling of their electronic transition dipole moments.[6,9,17] Interestingly, in the present PY/ATS system the excitation energy can be transported along the particle in one direction, achieving a similar antenna effect but with a unique chromophore due to the particular arrangement of PY species (monomers and J-aggregates) within the nanochannels: the green PY monomers can act as energy transfer donors to the red-shifted PY J-aggregates, which behave as acceptors at the other end of the crystal needles. Thus, an efficient excitation energy transfer process takes place between monomers and identical chromophores that have suffered an exciton splitting of their excited states (*i.e.* aggregates) (see section 2.1.2.1. in chapter 2 for further details). Note that energy migration between the same species is also possible (monomer to monomer and/or aggregate to aggregate). Similar antenna systems have been reported by Calzaferri and de Cola *et al.* in zeolite L crystals,[18,21] though in that systems, the energy was transported from the centre to both ends of the crystals rather than from one end to the other end, as in the PY/ATS system reported here.

In order to confirm the energy transfer between the different PY species (from monomers to J-aggregates) and therefore to obtain experimental evidence of the antenna action in this hybrid system, sophisticated experiments denoted as “remote excitation” (described in section 3.4. in chapter 3) were carried out by Dr. Yasuhiko Fujita at the Katholieke Universiteit of Leuven (KUL, Belgium).

Particularly, a 473 nm cw laser was fixed as excitation source in the green-emitting part of the PY/ATS particles, checked by fluorescence, and the detection was placed at different points along the needle particle (from 1 to 4), as shown in Figure 4.11. Recording the spectrum at position 1, a single band was registered, with its maximum located at around 560 nm, thus it corresponds to PY monomers. On the other hand, moving the recording position several μm far from the excitation, especially at points

3 and 4, three peaks were observed: the most energetic one centered at 560 nm, ascribed to monomers; a second one centered at around 600 nm, and the last centered at 660 nm. The two later bands are attributed to different J-aggregates, as explained before.

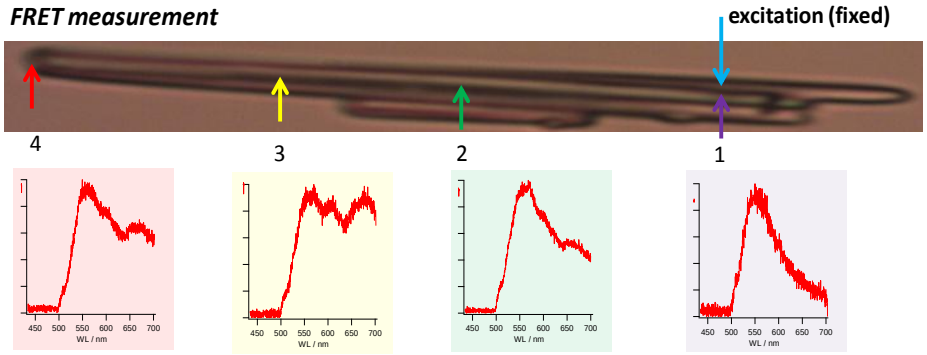

Figure 4.11. Top: transmission image of a group of PY/ATS particles. Bottom: fluorescence spectra detected at points 1 to 4. Note that the 473 nm cw excitation laser was placed at point 1.

These results indicate that effectively a FRET energy transfer process is happening inside the particle channels in one direction, from the PY monomers to the red-shifted J-aggregates, harvesting light spectroscopically and transporting it spatially from end to end of the particles, and energetically from the green to the red region of the visible light spectrum, experimentally proving the antenna effect along the hybrid system.

4.1.3- MgAPO-36/AC hybrid system[22]

Following the same idea described in the previous section, a new hybrid material was synthesized for the achievement of a different artificial antenna system, based on the occlusion of acridine dye (AC) as the photoactive guest into MgAPO-36 host. Acridine dye (AC) has similar molecular structure to PY, consisting of three fused aromatic rings, but being nitrogen in this case the heteroatom in the central ring and without any pendant groups (Figure 4.12.).

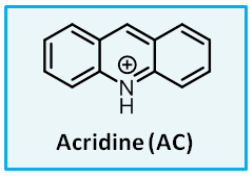

Figure 4.12. Molecular structure of the protonated acridine species. AC is found protonated in the synthesis gel.

In order to discuss the effect of the occlusion of this dye within ATS channels, a spectroscopic study was firstly performed on AC dye in diluted aqueous solution (10^{-5} M) at different pH values, and it was observed that the photophysical properties greatly vary with the pH. The absorption spectra (Figure 4.13A) show a main band centered at 354 nm which become more intense at pH values lower than the pKa value of the AC dye (pKa: 5.4).[23] At the same time, at pH values below pKa a new shoulder appears at higher wavelengths (around 370-450 nm approximately). An isosbestic point at 375 nm confirms the acid-base equilibrium in solution (AC ↔ ACH^+). Regarding the fluorescence spectra (Figure 4.13.B), for pH values above pKa the main band is centered at 430 nm, showing a dark-blue emission color, characteristic of the neutral form of AC. In contrast, for pH values below pKa, the main emission band appears at 477 nm, ascribed to the protonated form of AC (ACH^+), and characterized by an intense cyan emission. In fact, the fluorescence quantum yield of the protonated form, recorded in acidic conditions, is higher than that for the neutral form registered in more basic conditions (ϕ_{fl} = 0.41 and ϕ_{fl} = 0.32 respectively, Table 4.3.).

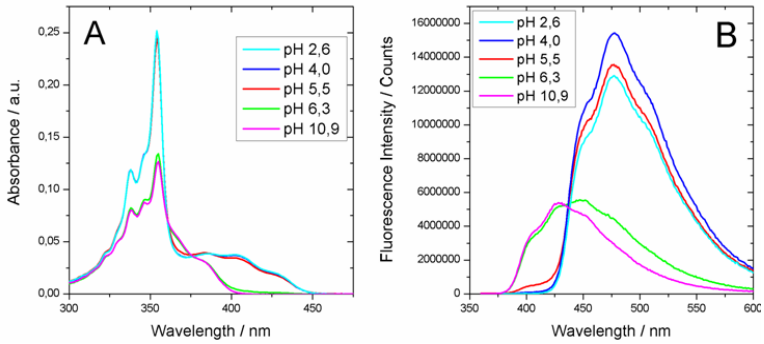

Figure 4.13. A) Absorption and B) emission spectra recorded under 350 nm excitation light of 10^{-5}M AC solutions prepared at different pH values.

Moreover, important differences are also found in the fluorescence lifetime of the AC dye varying the pH. Although it shows biexponential fluorescence decay in all the aqueous diluted solutions, the shortest value of around 8 ns is the major contributor at pH values above pKa; while the longest, of around 30 ns, is the main lifetime under acidic conditions (Table 4.3.). Thus, the short lifetime is ascribed to the neutral form of acridine (AC), and the longest one to its protonated form (ACH^+).

Table 4.3. Photophysical parameters for acridine in aqueous solution at different pH values.

pH	**λ_{abs} / nm**	**λ_{fl} / nm**	**ϕ_{fl}**	**τ_1 / ns %A_1**	**τ_2 / ns %A_2**
> 5.4	354	429	0.32	8.2 (90%)	21.1 (10%)
< 5.4	354	477	0.41	7.5 (10%)	31.2 (90%)

Interestingly, molecular simulations (see experimental section for further details, section 3.6.) indicate that, unlike most common fluorescent dyes, AC dye presents its transition dipole moment in the direction of its short molecular axis (Figure 4.14.) instead of parallel to the long molecular axis of the dye (see Figure 4.2. as an example). Note here that the information about the direction of the transition dipolar moment of dyes is important in order to evaluate their preferential orientation within the matrix since the maximum fluorescence intensity in polarization experiments will be collected when the polarizer is placed parallel to the transition dipole vector.

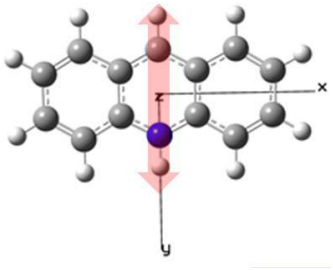

Figure 4.14. ACH^+. Red arrow represents the direction of the transition dipole moment.

The synthesis of the AC/ATS sample was carried out following the same procedure as in the previous system, but with a crystallization time of 24 hours. The initial synthesis gel was prepared with the following molar composition: 0.2 MgO: 1 P_2O_5: 0.90 Al_2O_3: 0.74 TPA: 0.025 AC: 299 H_2O. XRD pattern confirmed that ATS was achieved as the main product, with minor impurities of AFI phase (Figure 4.15.).

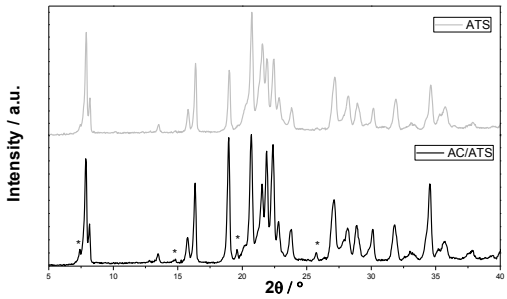

Figure 4.15. XRD patterns of AC containing MgAPO-36 sample, together with a XRD pattern of pure ATS phase for comparison. Note that (*) indicates the diffraction peaks corresponding to AFI-phase impurities.

A dye loading of 4.095 mmol AC per 100g solid product was achieved (Table 4.4.), which represents the 35% of the total dye amount added to the synthesis gel, much higher than the respective yield achieved for PY, of only the 6% of the total amount of

dye added under the same synthesis conditions. This difference in the incorporation rate of the dyes can be attributed to the smaller molecular dimensions of AC with respect to PY and also to the higher solubility of AC in the acidic aqueous medium of the synthesis gel (typical pH values for the gel of around 3-4).

The absorption spectrum of the AC/ATS hybrid material in bulk shows the main band in the UV region, together with a prominent shoulder placed at around 400 nm (Table 4.4., Figure 4.16.), previously ascribed to the protonated ACH^+ species, in acidic aqueous solution. This shoulder can be attributed to a high contribution of the ACH^+ species, but also to the formation of J-type aggregates into the MgAPO-36 nanochannels, which may contribute to the appearance of bands at longer wavelengths with respect to the monomer bands in both absorption and emission spectra, as has been already explained. In this sense, the fluorescence spectrum shows a band centered at 483 nm (Table 4.4., Figure 4.16.), similar to that registered for ACH^+ in aqueous solution (pH < pKa). However, this band appears slightly red-shifted respect to solution, together with a more pronounced shoulder at around 520 nm.

Regarding the fluorescence efficiency of the solid sample, AC/ATS material shows a dramatic decrease in the fluorescence quantum yield (ϕ_{fl} = 0.04, Table 4.4.) in comparison with the dye in aqueous acidic solution (ϕ_{fl} = 0.41). This drastic drop in the fluorescence efficiency may be indicative of the dye aggregation inside the host, since aggregates tend to exhibit lower fluorescence intensities than monomers.

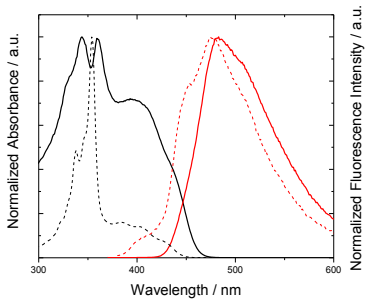

Figure 4.16. Absorption (black curves) and fluorescence (red curves) spectra of acridine ACH^+ species in aqueous acidic solution (dashed lines) and in AC/ATS powder sample (solid lines).

Table 4.4. Dye-loading and photophysical parameters for AC/ATS sample in bulk powder, together with the parameters for the dye in aqueous acidic solution for comparison.

System	ACH^+ occluded / mmol/100g	λ_{abs} / nm	λ_{fl} / nm	ϕ_{fl}	1/D
AC/ATS	4.095	359	483	0.04	3
ACH^+ (aq)	--	354	477	0.41	--

For a deeper characterization of the AC species present in the MgAPO-36 nanochannels, diverse microscopy techniques have been applied at single particle level. First, polarization experiments were carried out to confirm the occlusion of ACH^+ molecules inside the MgAPO-36 host and to estimate their alignment degree. It is worth remembering here that the transition dipole moment of the protonated acridine molecule is placed perpendicular to the long molecular axis. Thus, in this case inverse dichroic ratio or "1/D" values are considered. The lower 1/D value of around 3 obtained for AC/ATS respect to PY/ATS system, indicates a less preferential alignment along the pores, likely as a consequence of the less bulky nature of the ACH^+, which can be disposed with certain tilt angle respect to the channels c-axis.

On the other hand, optical microscopy images show the same shape for AC/ATS crystals as the PY/ATS system, *i.e.* needle-shaped particles arranged in bouquets joint by one end. In the transmission images, particles show a pale yellow color (Figure 4.17.A), but under UV excitation light two emission colors are distinguished in the fluorescence image: the characteristic bright cyan emission probably due to the protonated monomers (ACH^+) at one end of the particles; and a green emission color just in the other end, at the growth-center, where the particles bind (Figure 4.17.B).

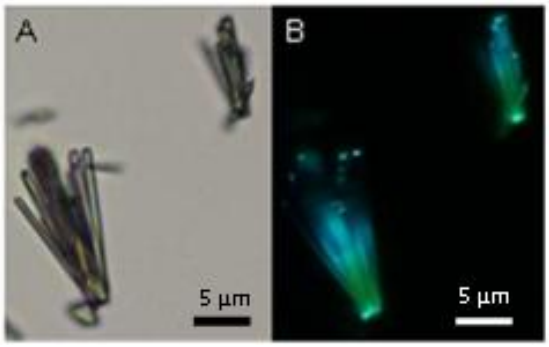

Figure 4.17. A) Transmission and B) fluorescence under UV excitation light images of AC/ATS particles.

This system show a similar trend to that observed in the previous sample PY/ATS (section 4.1.2.); thus, in the present case the green emission would be ascribed to the presence of AC J-aggregates, at lower energies with respect to the characteristic cyan emission of the ACH^+ monomers ($\lambda_{green} > \lambda_{cyan}$). Moreover, FLIM (Fluorescence Lifetime Imaging Microscopy) experiments carried out by confocal microscopy also show a gradation of the average lifetime along the particles: there is a region with long lifetimes, higher than 20 ns, whose value gradually decreases towards the other end of

the particles, where average lifetime values shorter than 9 ns are recorded (Figure 4.18.A and B).

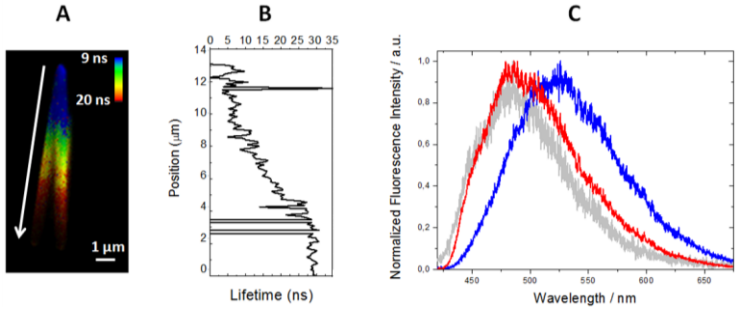

Figure 4.18. A) FLIM image of AC/ATS system. B) Profile of the average fluorescence lifetime values along the needle in A. C) Height normalized fluorescence spectra recorded at the two ends of the particle (blue and red spectra correspond to the blue and red areas in A, respectively). The spectrum registered for AC in acidic aqueous solution has been inserted (gray line), measured by the same technique, as comparative.

Collecting fluorescence spectra in the different areas of the particles distinguished by their lifetime, a fluorescence band centered at around 485 nm, similar to that registered for ACH^+ in aqueous solution, is obtained at the ends where the long lifetimes are found; and an emission band in the green region, centered at around 525 nm, for the short fluorescence lifetime areas (Figure 4.18.C). Thus, it is confirmed that i) AC monomers in the protonated form, responsible for the cyan emission, are located at one edge of the crystals and ii) J-aggregates of the acridine dye, with a characteristic green emission, are distributed mainly at the opposite end.

A deeper fluorescence lifetime characterization in AC/ATS single particles revealed that triexponential fitting is required in the decay curves, giving as a result the following lifetime values: τ_1 = 0.7-1.0 ns (50-55%), τ_2 = 5-6 ns (30%) and τ_3 = 24-25 ns (15-20%). The longest one must be attributed to ACH^+ monomers; the intermediate lifetime between 5 and 6 ns to J-aggregates; and the shorter one should be related to the quenching of the monomer due to the close proximity of the respective dimers in the channels of the MgAPO-36 host framework.[24,25] The fact that the lifetime attributed to ACH^+ monomers is shorter than that assigned to the protonated monomer in aqueous solution is indicative of a FRET energy transfer between ACH^+ monomers (donor) and J-aggregates (acceptor). The FRET process is in fact a non-radiative deactivation process of the protonated monomeric species, producing a decrease in its fluorescence lifetime.[26]

Note here that there is 1 ACH^+ molecule per 180 Å along the channels' c-axis (estimated by the amount of ACH^+ molecules incorporated into the solid, 4.095 mmol per 100 g solid product, Table 4.4., taking into account the unit cell dimensions of MgAPO-36 along the channel direction, c = 5.26 Å, and assuming a homogeneous distribution of the dye molecules along the crystal). Therefore, giving that the typical FRET distances are shorter than 80 Å, this result suggests that FRET does not occur between molecules located in the same channel, but between dye molecules situated in neighboring channels. It is worth remembering that the dye loading rate in this sample is much higher than in the previous one consisting of PY occluded into MgAPO-36 (compare dye loadings for PY/ATS in Table 4.2., with that for AC/ATS in Table 4.4.). In consequence, it can be assumed that the energy transfer in that sample also takes place between neighboring channels.[27,28] Therefore, in the rest of materials under study in this work FRET between neighboring channels will be taken as the general trend.

It can be concluded then that MgAPO-36 inorganic host, due to the size and elliptical shape of its channels, favors the formation of J-type aggregates of dyes with a general molecular structure built up by three fused aromatic rings, as happens with PY and AC, and could be extended for other similar guest dyes. Furthermore, the species distribution, with monomers at one end of the particles and aggregates in the opposite end, empowers once again the usefulness of this type of hybrid materials as artificial antennas.

To really demonstrate that an efficient energy transfer happens from monomers to J-aggregates, and in this sense from one end to the other end of the crystal, "remote excitation" experiments were also performed with this sample.

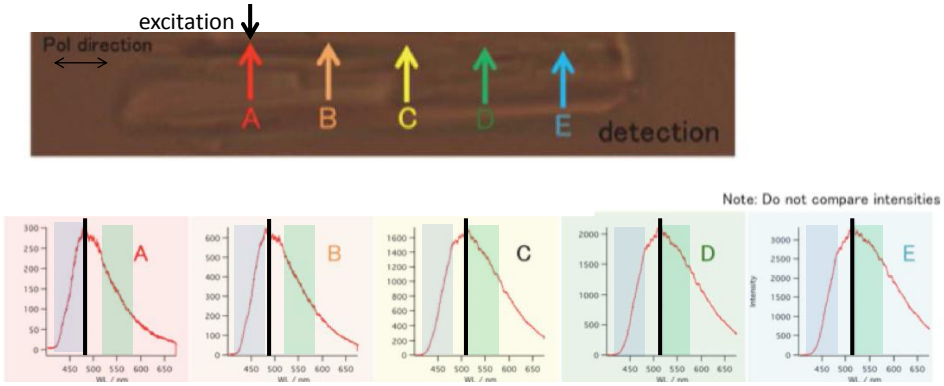

Figure 4.19. Top: transmission image of an AC/ATS needle particle bouquet. Bottom: fluorescence spectra detected at points A to E. Note that the cw 375 nm laser used as excitation light source was fixed at point A.

In the same way, excitation was fixed at the end of the particles were monomers are, and emission spectra were recorded at different spots (points A to E in Figure 4.19.). Since the position of the fluorescence peak shifts to longer wavelengths as the detection point is nearer to the other end of the particle (from 480 nm in A to 520 nm in E), the energy transfer is confirmed in this sample as well, being the monomers the donor species (placed at one end), and J-aggregates the acceptor species (placed at the opposite end). In the present case, UV light can be collected and transferred unidirectionally from side to side of the needle particles, transforming it energetically from the blue to the green.

4.1.4.- MgAPO-36/AC-PY hybrid systems[22]

The results presented above confirm that MgAPO-36 is an excellent inorganic host for the development of artificial photonic antenna systems because ATS structure induces the formation of J-aggregates in dyes with a basic molecular skeleton of three fused aromatic rings. Furthermore, the synthetic pathway offers an anisotropic distribution of the dye species perfect for one-directional energy transfer between dye monomers, disposed in one edge, which collect the light and transport the energy to the red-shifted aggregates, located in the opposite end of the crystals.

Now, with the aim of broadening the range of light harvesting and transport of the system and to extend the antenna action from the UV to the red region of the visible spectrum, both acridine and pyronin Y dyes are encapsulated simultaneously into MgAPO-36 framework. Indeed, these dyes can be an appropriate donor-acceptor pair for several reasons. Firstly, the emission band of ACH^+ overlaps with the absorption band of PY (Figure 4.20.), essential requisite for energy transfer according to the FRET theory (described in chapter 2, section 2.1.2.2). Secondly, ACH^+ can be appropriate as donor due to its relatively high fluorescence quantum yield. Moreover, both dyes have similar molecular structures (see Figures 4.2 and 4.13.), and have demonstrated that their inclusion into MgAPO-36 by the crystallization inclusion method do not disrupt the final phase of the material. Finally, due to the less bulky nature of AC and to its high solubility in the acidic conditions of the synthesis medium (pH ~ 3-4) it will be incorporated in a higher extent than PY, obtaining a high donor-to-acceptor ratio easily, usually required for an efficient FRET process in 1D-systems.[17]

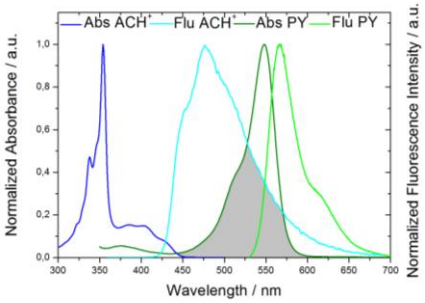

Figure 4.20. Height normalized absorption and fluorescence spectra of ACH^+ and PY in aqueous solution (10^{-5} M). The overlapping area is colored in gray.

The hybrid systems were prepared following the same procedure as in the previous samples, with a crystallization time of 12 hours. Both dyes were simultaneously added to the synthesis gel varying the AC:PY ratio in order to study the best proportion for an efficient FRET, but keeping constant the total dye proportion (0.024) in every synthesis. Thus, the general gel composition is defined as follows: 0.2 MgO: 1 P_2O_5: 0.9Al_2O_3: 0.75 TPA: *x* PY: (0.024-*x*) AC: 300 H_2O. In the next table there are summarized the synthesis parameters for the preparation of each material under study, by means of dye proportion, the obtained crystalline phase, and the dye loading in the final samples:

Table 4.5. Synthesis parameters of the ATS samples containing an AC-PY mix of dyes.

AC-PY/ATS System	AC (0.024-*x*)	PY (*x*)	Product	mmol AC / 100g	mmol PY / 100g
(1:1)	0.012	0.012	ATS	2.092	0.323
(1:3)	0.006	0.018	ATS	1.092	0.511
(1:11)	0.002	0.022	ATS	0.360	0.377

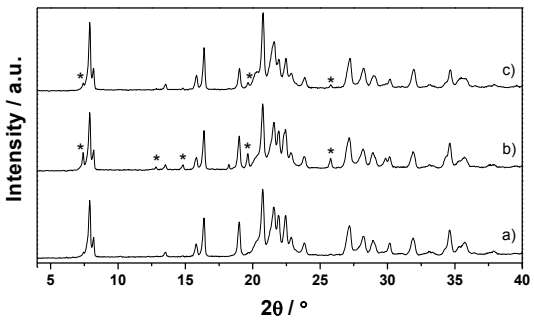

Figure 4.21. XRD patterns of the samples (a) AC-PY/ATS (1:1), (b) AC-PY/ATS (1:3) and (c) AC-PY/ATS (1:11). * indicates diffraction of MgAPO-5 (AFI) impurities.

As can be seen in the XRD patterns (Figure 4.21.), all the synthesis rendered MgAPO-36 as the main phase, although in some cases minor impurities of MgAPO-5 appear. Particularly, pure phase was obtained in the case of equimolar dye ratio (1:1), and the contribution of the impurities present in the other two samples is nearly negligible, especially in the case of AC-PY/ATS (1:11).

Regarding the final dye content in the samples (Table 4.5.), dyes demonstrated a similar incorporation rate to the previous samples, when only one dye was occluded (*i.e.* 35% and 6% for AC and PY, respectively). Indeed, the sample prepared with equimolar proportion of the dyes in the precursor gel actually demonstrated an AC occlusion 6.5 times higher than that for PY (Table 4.5.). Nevertheless, the absorption spectra recorded in bulk powder for the three samples show the characteristic absorption bands of the two fluorophores even in the sample with the lowest PY loading (Figure 4.22.A). As the relative PY content increases in the material, the absorbance corresponding to this dye grows in detriment of that for ACH^+, becoming the main absorption band for the AC-PY/ATS sample with the higher PY content (1:11 ratio).

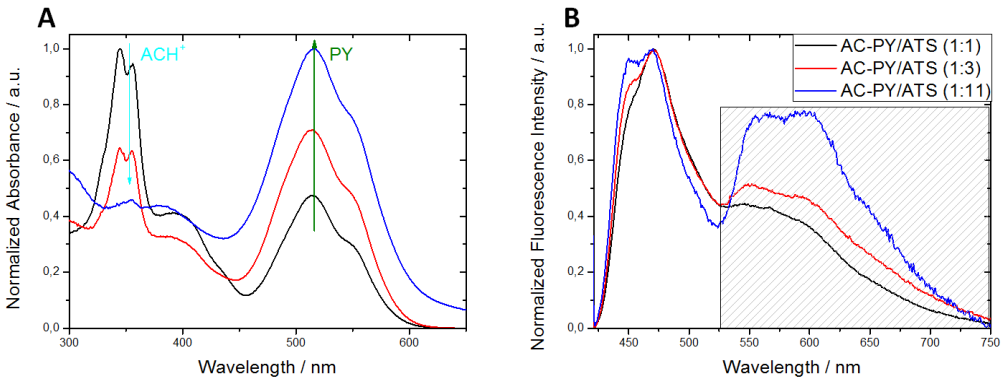

Figure 4.22. Area normalized absorption (A) and height normalized emission (B) spectra (λ_{exc}: 410 nm) of samples AC-PY/ATS (1:1) (black line), AC-PY/ATS (1:3) (red line) and AC-PY/ATS (1:11) (blue line). Striped box in B corresponds to the emission range of PY dye.

Moreover, the emission spectra of the samples AC-PY/ATS also show the fluorescence bands of both dyes (Figure 4.22.B) when AC dye is directly excited under UV light (λ_{exc}: 410 nm, at which the absorption of the PY dye is considered practically negligible; see Figure 4.20.). Particularly, the emission band of ACH^+ appears as the main band, centered at 475 nm, and as shoulders the emission bands of the PY monomers (λ_{em}: ~550-560 nm) and PY J-aggregates (λ_{em}: ~610 nm) are clearly

visible. The fact that exciting only the AC also the emission of PY J-aggregates is detected indicates that an energy transfer process between the dyes takes place, being ACH^+ the donor and PY the acceptor. Note here that the band previously ascribed to AC J-aggregates that appeared at 520 nm (section 4.1.3.) is not perceived in any of the samples consisting of a mixing of dyes. This fact can be attributed to a less favored formation of AC J-aggregates due to the reduction of the total AC loading (compare data in Table 4.5. vs Table 4.4.) or maybe the emission of AC J-aggregates is masked under the stronger emission of the PY.

As the AC:PY ratio decrease (higher PY amount in the precursor gel), the emission bands of the PY species at around 560 nm and 610 nm become more intense. Indeed, if the emission spectrum is recorded exciting directly the PY (λ_{exc}: 470 nm), three resolved bands centered at 550, 605 and 675 nm previously characterized in the PY/ATS system are noticeable (Figure 4.23.). After deconvolution, it was observed that the relative areas under the curve of the three bands are 1:11:19, respectively. The more energetic band was previously ascribed to PY monomeric species, whilst the two red-shifted new bands were attributed to J-aggregates with different geometries, or to the coexistence of dimers and superior aggregate species, respectively, indicating a high contribution of the PY J-aggregates.

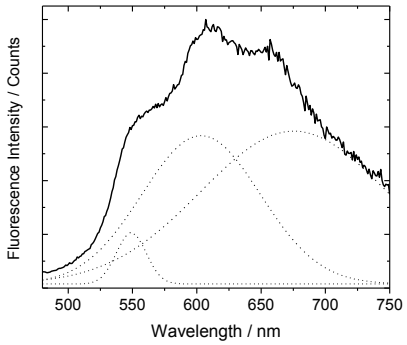

Figure 4.23. Emission spectrum of the sample AC-PY/ATS (1:1) measured in bulk powder exciting PY (λ_{exc}: 470 nm). Doted lines represent the deconvolution of the emission spectrum.

To get more insight, the ATS samples with different AC:PY ratios were studied by microscopy techniques.

In the transmission image of sample AC-PY/ATS (1:1) (Figure 4.24.A), it can be clearly seen the characteristic pink color of PY located at one edge of the particle and the pale yellow color of the acridine in the opposite end. This distribution is correlated

in fluorescence images recorded under UV light (only AC molecules are excited) to the typical cyan emission of ACH^+ in the yellow edge (by transmission), and red emission in the pink zone by transmission (Figure 4.24.B). This red fluorescence is again ascribed to PY J-aggregates. Indeed, under UV excitation light and removing the ACH^+ fluorescence by a 515 nm cut off filter, the crystals show the same species distribution of the previous PY/ATS sample (Figure 4.24.C).

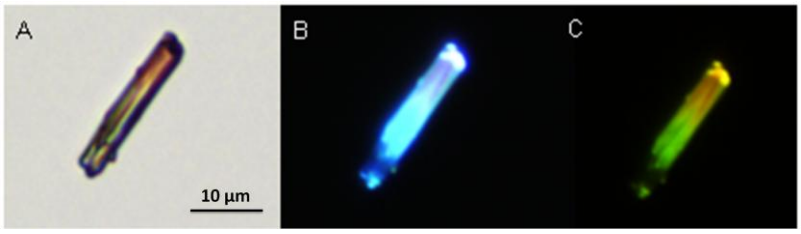

Figure 4.24. Transmission image (A) and fluorescence images under UV excitation light (B and C). In the last image (C) the emission of ACH^+ has been subtracted with a 515 nm cut off filter.

Fluorescence lifetimes were measured in single particles. Three exponentials were required to fit the decay curves of sample AC-PY/ATS (1:1), giving the following lifetime values: τ_1: 1 ns (50%), τ_2: 5 ns (35%) and τ_3: 20-22 ns (15%). The results for the other two samples are summarized in Table 4.6. The longest lifetime is attributed to ACH^+ monomers, which is in this case shorter than in the sample AC/ATS likely due to a major non-radiative deactivation of the protonated acridine monomers due to the FRET process. The intermediate lifetime should be attributed to the presence of PY monomers; and finally, the shortest lifetime could be related to the energy transfer process taking place in the system,[25,26] and/or to the presence of short-lived PY J-aggregates, as stated in section 4.1.2. for PY/ATS system.

Table 4.6. Fluorescence lifetimes registered in single crystals of AC-PY/ATS samples (averaged results from at least 10 particles are shown):

AC-PY/ATS System	τ_1 / ns (%A_1)	τ_2 / ns (%A_2)	τ_3 / ns (%A_3)
(1:1)	1 (50)	5 (35)	20-22 (15)
(1:3)	1 (60)	4 (30)	17-18 (10)
(1:11)	0.5 (60-65)	3 (35)	10-11 (<5)

To completely elucidate and locate all the dye species taking part in the FRET process within the hybrid system, two-color detection experiments were carried out by means of confocal microscopy. Images were simultaneously recorded in two detectors,

which specifically collect emission light in a chosen range, *i.e.* the blue channel (detector 1) collecting the 450-490 nm range (mainly ACH^+ monomers), and the red channel (detector 2) collecting the 590-650 nm range (mainly PY J-aggregates), under direct excitation of AC (λ_{exc}: 410 nm). This way, fluorescence signal recorded in each detector points out the areas where ACH^+ and PY species are distributed along the particles (detector 1 and detector 2, respectively). As it is shown in Figure 4.25., when ACH^+ emission is maximum (detector 1, Figure 4.25.up-left), the emission signal corresponding to PY species is the lowest (detector 2, Figure 4.25.up-right) and *vice versa*. The fluorescence intensity mapping is in agreement with the lifetimes distribution (FLIM images, Figure 4.25.bottom) since the area where detector 1 (dedicated to ACH^+) shows more intense fluorescence signal is also characterized by lifetimes higher 8.5 ns; and detector 2 (dedicated to PY J-aggregates) shows higher emission intensity in the area characterized by average lifetimes lower than 2.5 ns. These results confirm that the main species present in the channel are: protonated monomers of AC dye (with characteristic lifetime higher than 8.5 ns), and PY dye mainly in J-type aggregates (with very short characteristic lifetime values of < 2.5 ns).

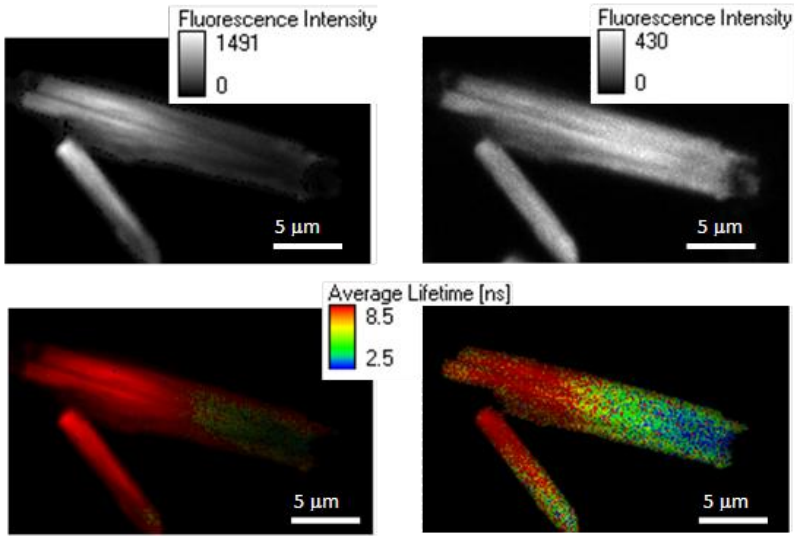

Figure 4.25. Intensity (up) and FLIM (bottom) images of sample AC-PY/ATS (1:1) under 410 nm laser excitation (the colors in the legend indicate average lifetime values: red > 8.5 ns, blue < 2.5 ns) collected in the blue channel (left, detector 1 with 470/40 nm band pass filter) and in the red channel (right, detector 2 with a 620/60 nm band pass filter).

On the other hand, the presence of PY J-aggregates (τ ~1 ns) at that edge and of PY monomers (τ ~5 ns) in the rest of the crystal is seen by direct excitation of PY at 470

nm. In this case, discrete areas with lifetimes > 2.5 ns, typical of the PY monomers, and other ones with lifetimes below 1.5 ns, characteristic of PY J-aggregates, are distinguished (Figure 4.26.A). These assignments have been also confirmed registering emission spectra in the distinct areas of the particles (Figure 4.26.B). The spectra collected in the areas with longer lifetimes show the typical emission band of the PY monomers centered at around 550 nm; and for those regions with short lifetimes (< 1.5 ns), spectra show a broad emission band with shoulders that extend up to 750 nm approximately, indicating the existence of PY J-aggregates, as previously discussed.

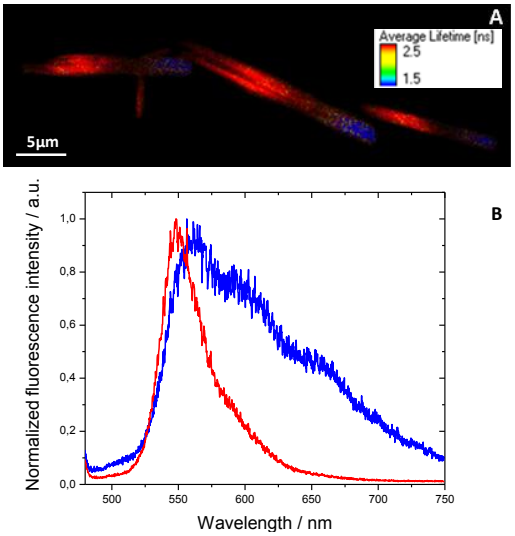

Figure 4.26. A) FLIM image of the sample AC-PY/ATS (1:1) under blue excitation (470 nm, exciting directly the PY dye), where the different lifetimes along the particle needles are seen: $\tau < 1.5$ ns blue caption; $\tau > 2.5$ ns red caption. B) Emission spectra recorded in the different areas of the particles in the FLIM image (the colors of the spectra correspond to the colors of the areas in A where they were collected).

All the results presented in this section are indicative of a cascade of energy from ACH^+ to PY monomers and to its J-aggregates (as depicted in Figure 4.27.) as a consequence of the good spectral overlapping between ACH^+ and PY monomers (Figure 4.20.), among other reasons, and also of a very effective FRET process between PY monomers and its J-aggregates, already demonstrated in sample PY/ATS (section 4.1.2.).

According to the Föster Theory (see section 2.1.2.2.,chapter 2), the relative orientation of the transition dipole vectors of the donor and the acceptor is a very

important factor.[8] For this reason, it is worth remembering that the transition dipole moments of AC and PY dyes are perpendicular to each other (Figure 4.2 and Figure 4.14). This fact would disfavor a FRET process between them when occluded into the rigid MgAPO-36. However, a highly efficient FRET has been demonstrated, and it was attributed i) to the high probability of energy transfer between neighboring channels,[9] and ii) to the tilted arrangement of AC molecules respect to the channels direction (corroborated by the relatively low dichroic ratio values obtained in the AC/ATS system, Table 4.4.).

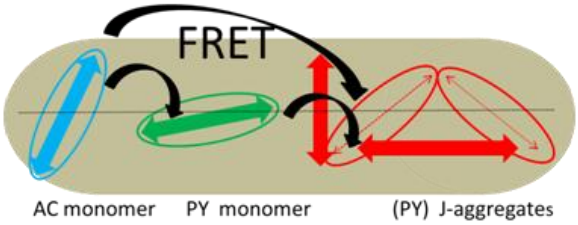

Figure 4.27. Illustrative representation of the orientation of the dipole transition moments (colored thick arrows) of ACH^+ and PY monomers, and PY J-aggregates, and the respective FRET processes between them. Thin arrows in the aggregate indicate dipoles direction.

Moreover, it has to be noted here that also a direct FRET process from the AC monomers to the PY J-aggregates can also take place. Indeed, there are some factors in favor of FRET process between ACH^+ monomers and PY J-aggregates. The most thermodynamically stable PY J-dimer within ATS channels (Figure 4.8.) shows an oblique head-to-tail geometry (case D_2 in Figure 2.6., chapter 2),[11] which is characterized by an absorption spectra with both H- and J-bands and whose dipole transition moments are polarized mutually perpendicular[19,20,29] (depicted with red thick arrows in Figure 4.27.). In this sense, this type of PY J-aggregates would show a larger overlapping between their absorption band and the emission band of ACH^+, owing to its absorption H-band, blue-shifted with respect to the monomer band. Besides, the dipole transition moment of this H-band shows a more favored orientation (more parallel) respect to the transition dipole of ACH^+ (Figure 4.27.) favoring the energy transfer process between both species. As a consequence, the energy transfer will be more efficient in samples with a higher amount of PY J-aggregates within the ATS channels. This fact can be easily explained with data showed in Table 4.6.: the higher the PY content, the higher will be the PY J-aggregates amount, and a higher decrease in the ACH^+ monomer lifetime is registered as a consequence of the radiationless FRET process. That is, in sample AC-PY/ATS

(1:1) the lifetime that corresponds to the ACH^+ monomers shows only a slight reduction with respect to the typical lifetime of the protonated AC monomer in solution (30 ns). Conversely, in the samples with higher PY proportion, this lifetime decreases substantially, reaching 10-11 ns in the case of AC-PY/ATS (1:11) sample, indicating that ACH^+ molecules are involved in a more efficient FRET energy transfer.

As a result, the AC-PY/ATS system can offer a one-directional antenna effect where the light is collected and the energy is transported spatially from side to side of the crystals and spectroscopically from the UV to the red region of the visible spectrum due to the preferred distribution of the dye species (ACH^+ monomers located at one edge and PY J-aggregates mainly located at the other end of the crystals, Figure 4.28.). It is considered an important achievement if they are compared with previously reported materials where the dye guests were loaded by post-synthesis methods which produced a bi-directional antenna effect (*i.e.* from the center to the edges or from the edges to the center).[18,25]

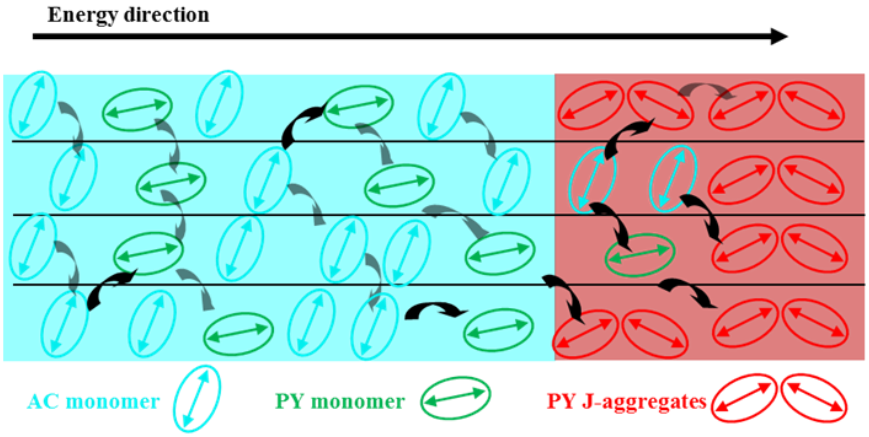

Figure 4.28. Scheme of the distribution of the dye species within the AC-PY/ATS crystals. The excitation energy is transported spatially in one direction (from end to end) along the crystals by energy migration (grey arrows) and energy-transfer (black arrows) processes, along different pore channels.

Finally, the antenna effect was really proven by "remote excitation" experiments. Sample AC-PY/ATS (1:3) was chosen for the testing. In this case, excitation was fixed at point E in Figure 4.29., where has been previously established that the main

species are ACH^+ monomers, and emission spectra were recorded at different spots (points A to E in Figure 4.29.).

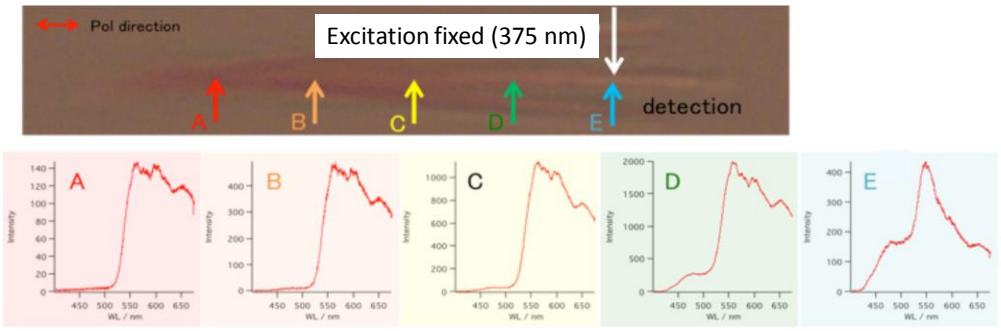

Figure 4.29. Top: transmission image of AC-PY/ATS (1:3) needle bouquet-shaped crystals. Bottom: fluorescence spectra detected at points A to E. Note that the 375 cw laser was used as excitation light source and placed at point E.

The emission spectra collected at the same point as excitation, point E, shows a weak ACH^+ contribution (as a shoulder in the spectrum), and the main band placed at 550 nm is due to PY monomer emission, evidencing the energy transfer between acridine and pyronin Y. As the detection point is shifted far away from the excitation point, the intensity of the ACH^+ emission band is gradually reduced, becoming practically negligible (points A and B), and the emission of both PY monomer and J-aggregates are dominant. Thus, the antenna effect is once again demonstrated in this dye-MgAPO-36 hybrid system, which in this case has its action broaden from the UV to the red, with a FRET process between the different dye species occluded (ACH^+ monomers, PY monomers and PY J-aggregates).

4.1.5.- MgAPO-5/cyanine and MgAPO-36/cyanine hybrid systems

Due to all that have been described so far, it is clear the suitability of dye-MgAPO-36 materials for the achievement of artificial antenna systems. In the search of new combinations, a new class of organic chromophores, cyanines, was then employed.

Cyanine dyes consist generally of two terminal heterocyclic rings with nitrogen centers, one of whose is positively charged. These nitrogen centers are connected to each other through a conjugated chain of an odd number of carbon atoms.[30,31] Owing to their structure, they can be classified as “push-pull” molecules, and they can also show promising properties for nonlinear optical applications.[30]

On the other hand, these dyes are of great interest due to the intriguing properties of their J-aggregates.[32] Indeed, cyanine aggregates have been found in solution in different assemblies such as in ladder, staircase and brickwork-type arrangements, depending on the angle of slippage between molecules.[30] These molecular organizations of cyanine dye molecules have been represented schematically in Figure 4.30.

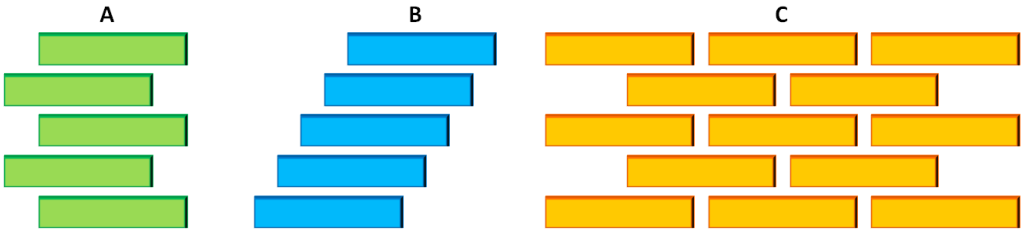

Figure 4.30. Schematic representation of the types of aggregation of cyanine dyes in solution: A) ladder, B) staircase and C) brickwork-type. [30]

Remarkable for cyanine dyes is that both the absorption and fluorescence bands ascribed to J-aggregates are the narrowest found for a dye due to their coherent coupling of excitons.[33] Due to the unique properties of their J-aggregates, they are promising dyes for a wide number of applications, being the light-harvesting systems, non-linear optics components and optical switches among the most appealing.[33]

Particularly, in this work 1,1'-diethyl-2,2'-cyanine has been used, whose molecular structure is shown in Figure 4.31. This cyanine dye is commonly known as PIC or pseudoisocyanine.

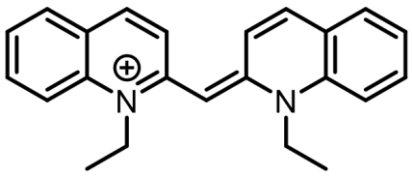

Figure 4.31. Molecular structure of the cyanine dye 1,1'-diethyl-2,2'-cyanine, or PIC.

This dye produces J-aggregates at high dye concentration in aqueous solution. Moreover, the formation of J-aggregates can be also promoted adding salts to the solution or varying the temperature. At room temperature, these J-aggregates show a characteristic narrow absorption band placed at 572 nm, together with a very sharp fluorescence band, almost overlapped with the absorption band, *i.e.* practically without any Stokes shift between them.[34] Spectra are shown in Figure 4.32.

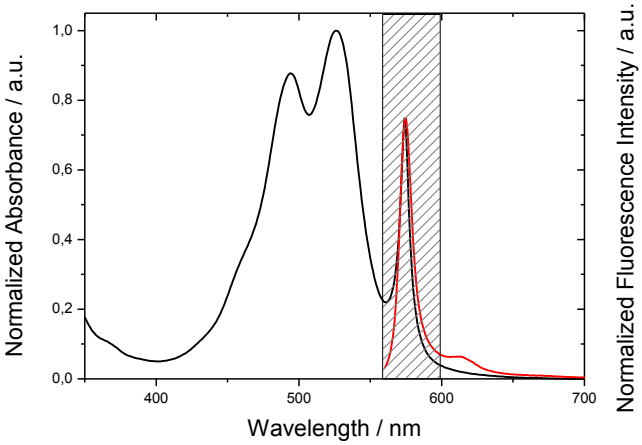

Figure 4.32. Absorption (black) and emission (red) spectra of the PIC dye in aqueous solution normalized to the height of aggregate bands. Patterned area indicates the bands corresponding to J-aggregates. NaCl salt was added to solution to promote the appearance of the J-aggregates.

As has been previously studied in solution and in other media such as solution/solid interfaces, the final spectroscopic properties of these J-aggregates depend on: the aggregation number, packing dimensions and dye molecular orientation.[34–37] In this context, cyanine dyes aroused our interest to be occluded into a one-dimensional host where a head-to-tail arrangement is expected to be induced, promoting linear J-aggregates. Particularly, the two previously described frameworks with different channel dimensions were chosen, MgAPO-5 and MgAPO-36, to study the effect of the matrix on the disposition adopted by the occluded PIC molecules and to evaluate the final photophysical properties of the different J-aggregates formed.

First, PIC cyanine was occluded into the larger cylindrical pores MgAPO-5 (AFI structure) because the molecular dimensions of this PIC dye are larger than the molecular size of the dyes described above, especially due to the ethyl pendant groups of its structure (Figure 4.31.). For PIC/AFI sample, a dye incorporation of 2.94 mmol per 100 g solid product was reached from a precursor gel with the following molar composition: 0.2 MgO: 1 P_2O_5: 0.9 Al_2O_3: 0.75 TEA: 0.024 PIC: 300 H_2O: 50 EtOH. Note here that ethanol was added to the typical gel composition previously defined for AFI structure (section 3.1.1., chapter 3) with the aim of increasing the solubility of the PIC dye. Moreover, the synthesis was carried out under static (standard) and dynamic heating regimes, and pure AFI phase with higher PIC dye loading was achieved only under dynamic conditions (Figure 4.33.). Otherwise, the resulting solid product was composed of a mixture of AFI and ATS phases.

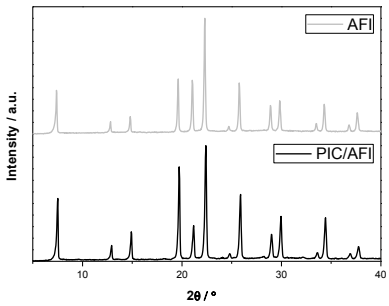

Figure 4.33. XRD pattern of sample PIC/AFI obtained under dynamic regime together with that of a pure AFI phase for comparison.

In the fluorescence image of the PIC/AFI sample, a yellow emission is seen at the center of the rod-shaped particles, while no emission is seen at the other end of the crystals (Figure 4.34.B). This was confirmed by confocal mapping images where the fluorescence was brighter at the central region of the particles with an emission band placed at 560 nm (Figure 4.34.C), which did not show any shift as the detection point was moved to the ends of the particle, where finally no emission was detected.

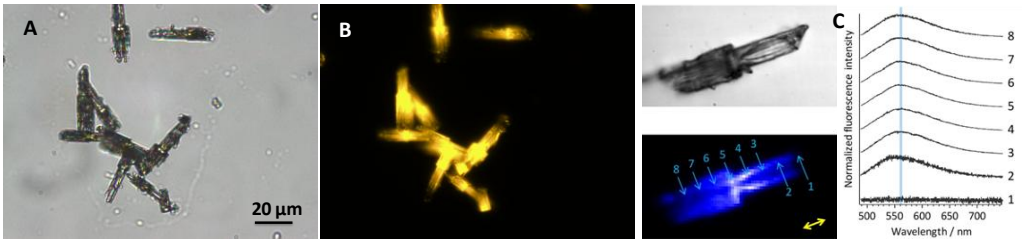

Figure 4.34. Transmission image (A) and fluorescence image under blue excitation light (450-490 nm) (B) of the PIC/AFI particles. C) Fluorescence spectrum recorded at different points (from 1 to 8) of the PIC/AFI crystal (λ_{exc}: 473 nm).

Taking into account the previous results in the former ATS samples (PY/ATS and AC/ATS), with aggregates located at the crystal growth center, this emission is ascribed to the J-aggregates of PIC dye into AFI host (located at AFI crystal growth starting point). For PIC/AFI hybrid material, it can be ascertained that the geometry of the PIC J-aggregates resembles the arrangement they take in solution, since in these conditions the typical band of PIC J-aggregates appears at 575 nm, *i.e.* in the yellow range of the electromagnetic spectrum. Monomers would be likely located at both edges of the rods, and they are not fluorescent. Indeed, the photophysical properties obtained for PIC J-aggregates into MgAPO-5 are similar to those registered for solution, with the J-aggregates emission band in the yellow region of the

electromagnetic spectrum and non-fluorescent monomers.[34] The later fact is a typical characteristic of this type of dyes with flexible molecular structures since the molecular motions induce important non-radiative deactivation pathways. Indeed, this result indicates that the molecular motions of PIC monomer are not impeded once occluded into this framework; or in other words, the rigidity imposed by the AFI matrix is not strong enough to switch on the emission of PIC monomers.

Thus, ATS framework was chosen then to occlude the PIC cyanine. Note here that docking results (theoretical calculations) regarding the occlusion of PIC into ATS host were not very promising. Indeed, the molecular simulations indicate that the interaction energy between the framework and a PIC molecule is lower in the AFI matrix, suggesting a slightly better fitting of the dye within the AFI channels with respect to ATS due to the larger pores of cylindrical shape of the former one. The most stable location for a unique PIC molecule within each framework is reported in Figure 4.35., together with the calculated interaction energies.

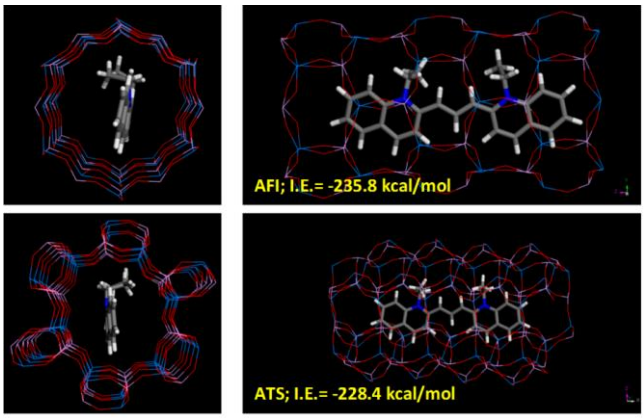

Figure 4.35. Most stable location and interaction energies of cyanine (1 molecule per supercell) in AFI (top) and ATS (bottom) channels.

Nevertheless, different attempts to obtain PIC/ATS material were performed. The best results were achieved with a molar composition of the gel of: 0.2 MgO: 1 P_2O_5: 0.9 Al_2O_3: 0.75 TPA: 0.024 PIC: 300 H_2O: 50 EtOH, and under the usual static heating regime. Under these conditions a predominant ATS phase was obtained with minor AFI impurities (Figure 4.36.). Note that the synthesis under dynamic heating regime was not satisfactory since it led also to phase mixtures of ATS and AFI, but being the later the major phase.

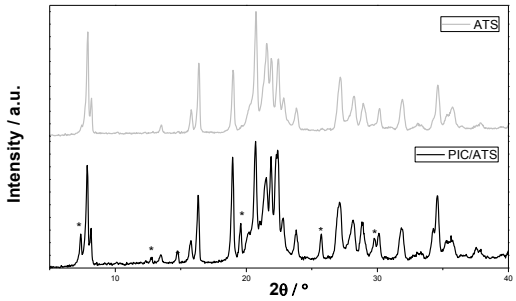

Figure 4.36. XRD pattern of PIC/ATS material together with that of pure ATS phase for comparison. * indicates diffraction of MgAPO-5 (AFI) impurities.

Concerning the dye-loading, it was clear even to the naked eye that the incorporation of PIC dye into ATS is lower than into AFI due to the paler color of PIC/ATS powder, as it was expected due to the narrower nanochannels of the former structure (Figure 2.20 versus Figure 2.19 in chapter 2), and also to the molecular simulations results (Figure 4.35.). In this regard, considering PIC/ATS sample as a pure phase, an amount of 1.52 mmol PIC per 100 g sample powder was achieved, which represents half of the loading obtained previously for the best PIC/AFI sample (2.94 mmol/100g sample powder).

Since completely pure ATS phase was not obtained for the PIC/ATS sample, only results at single particle level are discussed below, in order to avoid the influence of the AFI impurities. Indeed, the most useful information to prove the potential use of PIC/ATS sample as artificial antenna system is collected at single particle level by means of microscopy techniques. Note here that this characterization is possible due to the great difference between the shapes of the particles of each phase. As noticeable in optical microscopy, PIC/ATS crystals grow as independent needles (Figure 4.37.A and B), while PIC/AFI sample is composed of big rod-shaped particles (Figure 4.34.A and B).

It is important to note here that PIC dye shows a similar distribution along the ATS framework as the previous PY/ATS and AC/ATS samples, described above. That is, a darker reddish color is noticed in one of the edge of the needle in the transmission image (Figure 4.37.A) indicative of a higher amount of PIC occluded, and it corresponds to the orange area in the fluorescence image (Figure 4.37.B). This orange color is related to an emission band centered at 610 nm (Figure 4.37.C). At the opposite end of the particles, where less dye amount is occluded, a reminiscent green emission is apparent in the respective fluorescence image (Figure 4.37.B). Thus, once

again a gradual emission color change, in this case from orange to green, is detected in single particles from end to end of the crystals, which is attributed to the strategic distribution of J-aggregates at one end and monomers at the other end of the needles, respectively. In general terms, the emission intensity in PIC/ATS particles is relatively lower than in PIC/AFI sample. However, it is important to note that PIC monomers turn out to be fluorescent in this sample, likely as a consequence of the tight confinement into the ATS matrix, reducing the probability of deactivation through non-radiative pathways (for example, through molecular motions), which represents for us a novel finding. As cited above, this effect was not achieved in the case of MgAPO-5 framework with slightly larger pore dimensions, which would allow molecular motions.

Interestingly, PIC J-aggregates showed different emission color in each framework: a yellow emission characterized by a fluorescence band at 560 nm in AFI host, and a less intense and red-shifted emission, characterized by an orange fluorescence centered at 610nm in ATS structure. These differences are ascribed to J-aggregates adopting a different geometry in each host, and it can be explained by means of the Exciton Theory.[19,20] As has been discussed in section 2.1.2.1. in chapter 2, the angles between the molecules forming the aggregates are decisive for the spectral changes. In this context, the more in-line J-aggregate (small θ angles, see Figure 2.6. in chapter 2), the higher energy splitting of the J-band with respect to the monomer band is expected, and therefore a higher bathochromic shift will be observed in the emission band. Consequently, we can assume that J-aggregates formed in the PIC/ATS sample are more lineal than those in the PIC/AFI case, and thus, the spectral shift of the emission band to the red edge is larger.

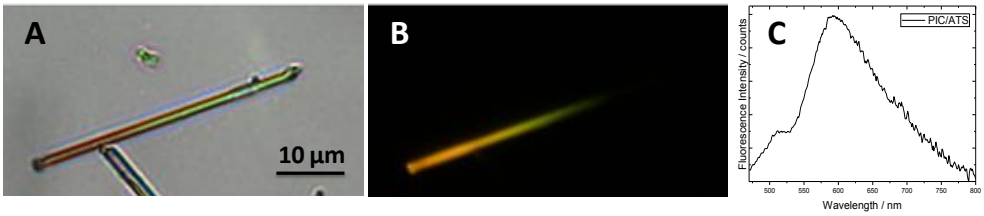

Figure 4.37. Transmission (A) and fluorescence under blue excitation light (450-490 nm) (B) images of a PY/ATS needle-shaped particle. C) Fluorescence spectrum of the PIC/ATS sample (λ_{exc}: 450 nm).

In order to confirm the above statements about the geometry of the J-aggregates inside the nanochannels of the different host structures, molecular simulations were performed once again. To simulate the more stable geometry, two PIC molecules were

loaded into the structures forming J-aggregates in two possible geometries, *i.e.* as perfect in-line head-to-tail J-dimer (case B in Figure 2.6 in chapter 2) or a displaced J-dimer in a sandwich-like disposition (case C in Figure 2.6 in chapter 2, with $\theta < 54.7^{o}$). The relative stabilities and interaction energies calculated clearly show that cyanine dimers are more stable in a displaced J-type disposition in the AFI channels, whilst the in-line J-geometry is the most stable configuration for PIC J-aggregates confined within ATS (Figure 4.38.). Again this is due to the larger cross-section of the AFI channels, whose dimensions are suitable to host the cyanine dyes enabling a π-π interaction between the aromatic rings that stabilizes the system. The smaller cross-section in one dimension of the ATS channels causes a steric hindrance between the aromatic rings of the dye molecules, inducing its disposition as pure in-line head-to-tail J-aggregates.

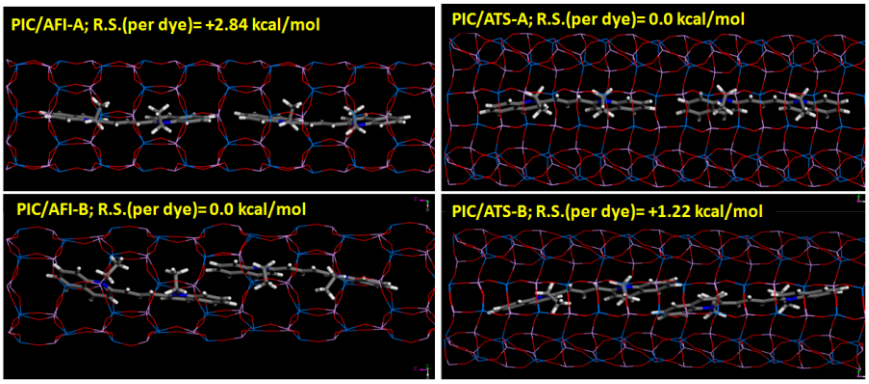

Figure 4.38. Different J-aggregate geometries in AFI (left) and ATS (right) frameworks. The calculated relative stability (R.S.) is also shown for each case.

Summarizing, the larger cross-section of the AFI channels induces a displaced J-aggregate geometry with respect to the totally in-line J-aggregates in the ATS channels (Figure 4.38.). Note here that obviously pure H-aggregates cannot be formed even in the larger AFI channels, because the presence of the ethyl substituents of the molecule prevents this configuration.

Finally, the antenna effect was measured in the PIC/ATS system. Note that only PIC/ATS sample was used since only there the two species (monomers and J-aggregates) were detectable. Fluorescence images in Figure 4.39.b and c correspond to the confocal maps at monomer (550 nm, blue image) and J-aggregate (610 nm, green image) regions, respectively. In order to evaluate the antenna action, the J-aggregate map (Figure 4.39.c) was divided by the monomer map (Figure 4.39.b), as shown in Figure 4.39.d (I_{Jagg}/I_{Mono}). The higher I_{Jagg}/I_{Mono} ratio observed at the J-aggregate region

could indicate that FRET occurs on this sample (Figure 4.39.d). Here, due to the clear spectral separation between the fluorescence bands of the monomers and J-aggregates, the energy transfer is clearly observed by fixing the excitation at the monomer area (red spot in Figure 4.39.a), and collecting fluorescence spectra at different detection points (1 to 5 depicted in Figure 4.39.d). Thus, at point 1 only the band ascribed to the monomers, centered at 550 nm, is detected, while a main emission band at 610 nm, ascribed to the J-aggregates, is recorded at point 5 (Figure 4.40.).

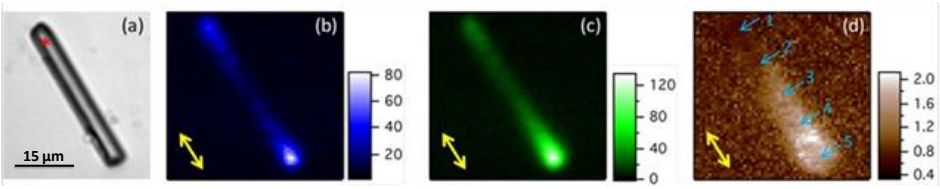

Figure 4.39. (a) Transmission image of a PIC/ATS needle crystal. (b, c) Confocal mapping images at monomer (b) and J-aggregate (c) region. (d) "$I_{J\text{-}agg}/I_{Mono}$" map. 473 nm excitation wavelength with a power of 430 µW was used.

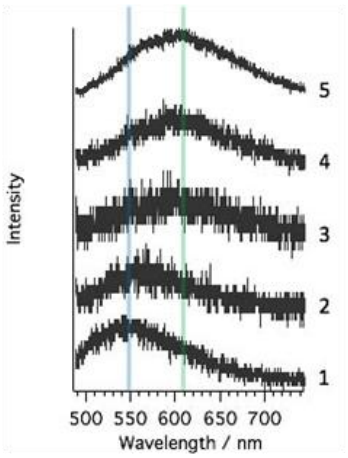

Figure 4.40. Fluorescence spectra recorded at positions 1 to 5 (in Figure 4.39.d).

Therefore, it is demonstrated that in PIC/ATS particles the antenna effect also takes place by a FRET process from monomers to J-aggregates of the PIC cyanine. Particularly interesting in this sample is the fact that the fluorescence band ascribed to the aggregates appears totally isolated from the monomeric band (point 5 in Figure 4.40.), highlighting the efficiency of the FRET process in this case.

4.2.- Dye encapsulation into MgAPO-11: Hybrid materials for diverse optical applications

In the previous section it has been seen the influence of the host channels in the aggregation of the guest molecules. The H-type aggregate formation found for PY dye in AFI structure has been suppressed within the ATS framework, in which red emissive J-type aggregates are formed instead. Although in the later case the formation of J-aggregates has offered a organized multicolour emission system in favor of the development of one-directional artificial antenna systems, interesting for energy transport, the fluorescence capacity of these materials is usually low. Therefore, the next goal is the total suppression of the aggregation to obtain highly fluorescent solid samples. The aim is to reach such a tight confinement of the dyes into a 1-D channeled structure that not only the aggregation is avoided but also an extraordinarily preferential alignment of the occluded chromophores is achieved, leading to important optical applications such as second harmonic generation, delayed fluorescence, emission color switching and white light emission.

In this context, a different 1-D magnesium aluminophosphate was chosen, the MgAPO-11 (AEL structure-type), with a small pore size of 6.5 Å x 4 Å (Figure 4.41.A), close to the molecular dimensions of many fluorescent dyes with a general structure based on three fused aromatic rings (see general molecular structure in Figure 2.22., chapter 2). But not only is the pore size decisive when trying to avoid molecular aggregation; the particular topology of this framework plays the key role for aggregation avoidance. It consists on small pockets disposed along the channel direction that prevent the occluded dye molecules from placing too close to each other, avoiding the coupling between them and thus the dye aggregation even in head-to-tail arrangement (Figure 4.41.B). Further details of this framework structure are given in section 2.2.1.1. in chapter 2.

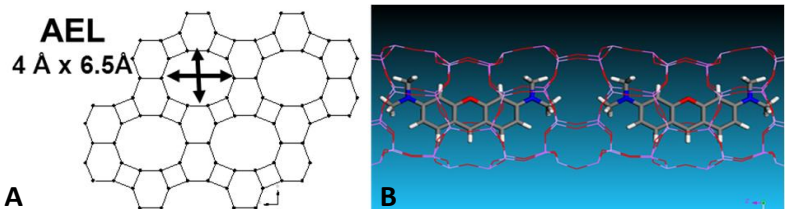

Figure 4.41. A) View along the straight channels of the MgAPO-11 structure, together with B) the representation of two dye molecules into the pockets of the pores.

Here, a series of dyes emitting in the whole spectrum range with molecular dimensions that fit tightly to the pore size of the MgAPO-11 framework have been

encapsulated into the AEL structure by the previously described crystallization inclusion method (section 2.2.1.2. in chapter 2). Note here that this approach is precisely the only way to occlude the following dyes into the AEL channels due to the close match between their molecular size and the pore dimensions, making impossible the incorporation via post synthetic methods (diffusion is totally impeded). For the resultant hybrid materials interesting optical applications are envisaged and later demonstrated.

In the first part of this section, the results are organized depending on the absorption and emission region of the dyes employed as guests, *i.e.*, from the UV-blue to red edge of the visible light spectrum. In the second part, by the proper combination of the most suitable dyes into AEL framework, promising materials for several optical applications will be described.

4.2.1.- Blue emitting dyes into MgAPO-11

Two acridine-type dyes were chosen to be occluded into the MgAPO-11 structure: acridine (AC) and methyl acridine (MeAC) (Figure 4.42.). In both cases, the hybrid materials were hydrothermically prepared following the procedure described in section 3.1.3. in chapter 3. From gels with a molar composition of 0.2 MgO: 1 P_2O_5: 0.9 Al_2O_3: 1 EBA: 0.024 Dye: 300 H_2O, pure AEL phases were obtained in both cases (Figure 4.43.).

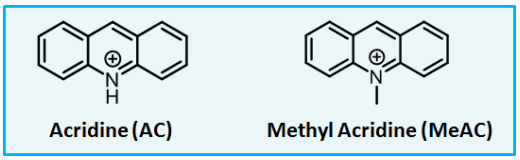

Figure 4.42. Molecular structure of the two blue-emitting dyes used in this section: acridine and methyl acridine.

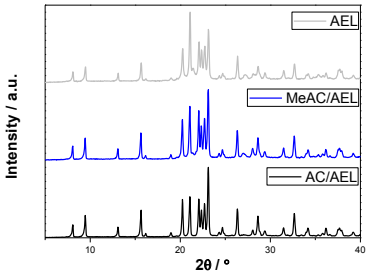

Figure 4.43. XRD diffraction patterns of ACH^+ and $MeAC^+$ containing MgAPO-11 samples, together with a XRD diffraction pattern of pure AEL phase for comparison.

- **AC/AEL**

The first blue emitting dye occluded into the MgAPO-11 was acridine (AC).[38] This dye is considered a good candidate to be occluded into the narrow MgAPO-11 channels due to its small and planar molecular structure (Figure 4.44.)

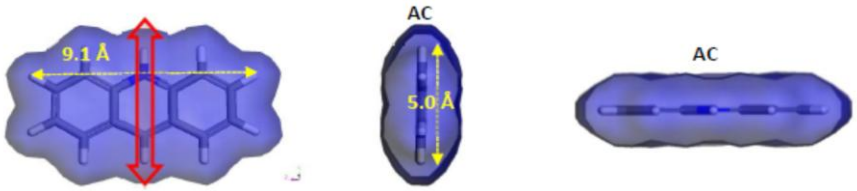

Figure 4.44. Molecular structure and dimensions of acridine dye. Red arrow indicates the direction of the transition dipole moment.

As stated before for the previous ATS framework, due to the acidic medium of the synthesis gel, AC dye should be dissolved in its protonated form, ACH^+. Thus, due to the cationic nature of this species (ACH^+), the dye shows a high solubility in the synthesis medium, and consequently very high dye-loading rates have been achieved, reaching 9.69 mmol of AC dye occluded per 100 g sample powder (0.200 mmol/cm^3).

Measurements in bulk powder determine that the AC/AEL hybrid material shows its main absorption band at λ_{abs} = 414 nm (Figure 4.45.), red-shifted with respect to that of ACH^+ in aqueous solution (λ_{abs}: 354 nm, Table 4.3.). This absorption band of AC/AEL is now placed in the region of the former shoulder that appeared more prominent at acidic pH conditions in aqueous solution, where ACH^+ is the main species (see Figure 4.13.A in section 4.1.3.). This fact suggests that the acidic species of acridine is primarily occluded into AEL. Indeed, the fluorescence band, centered at λ_{fl} = 480 nm (Figure 4.45.) is analogous to that recorded for ACH^+ in aqueous solution at low pH values. Importantly, a highly fluorescent material has been obtained, even at such a high dye-loading, with a fluorescence quantum yield of 0.54, which is higher than that of the dye in aqueous acidic solution (ϕ_{fl} = 0.41, Table 4.3.). Moreover, a monoexponential fluorescence decay curve has been recorded with a single and long-lived fluorescence lifetime of τ_{fl} = 27 ns, ascribed precisely to the protonated ACH^+ monomers, in contrast to that obtained for acridine in solution, which shows biexponential decay due to the equilibrium between the neutral and the protonated form of the dye even at very acidic pH (Table 4.3.). All these data, summarized in Table 4.7., confirm that only monomers of AC dye in its protonated form are occluded

into the channels of MgAPO-11, and any type of aggregate species has been completely suppressed.

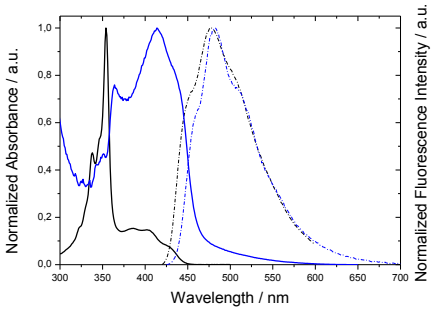

Figure 4.45. Height normalized absorption (solid lines) and emission (dashed lines) spectra of ACH^+ in solution (black lines) and into the MgAPO-11 (blue lines).

Table 4.7. Dye-loading and photophysical parameters for AC/AEL sample in bulk powder. Same parameters for AC in acidic aqueous solution are also shown for comparison.

System	ACH^+ occluded / mmol/100g	λ_{abs} / nm	λ_{fl} / nm	ϕ_{fl}	τ_{fl} / ns	1/D
AC/AEL	9.69	414	480	0.54	27	5
ACH^+ (10^{-5}M)	--	354	477	0.41	31.2 (90%) 7.5 (10%)	--

In order to get further information of this AC/AEL sample, fluorescence microscopy was used at single particle level. Transmission images of AC/AEL (Figure 4.46.A) show crystals of several micrometers with rectangular shape instead of the needles or rods seen before for ATS and AFI samples, respectively, which display a slight pale yellow color. The respective fluorescence images show an intense cyan-blue emission color (Figure 4.46.B), characteristic of ACH^+, under UV illumination.

By means of experiments with linearly polarized light, dichroic ratio values were obtained. In this case, inverse values are also given (1/D), owing to the disposition of the transition dipole moment of S_1-S_0 transition along the short molecular axis of the ACH^+ molecule (Figure 4.44.), and they reached only a value of 5.This value indicates that ACH^+ molecules are not completely aligned along the channels but they are instead disposed with a certain tilt angle. Indeed, this disposition was confirmed by computational results, which indicated that ACH^+ molecules place in the channels with a tilt angle of 9 degree between the major molecular axis of the dye and the channel direction in order to optimize the dye-MgAPO interactions (Figure 4.46.C).

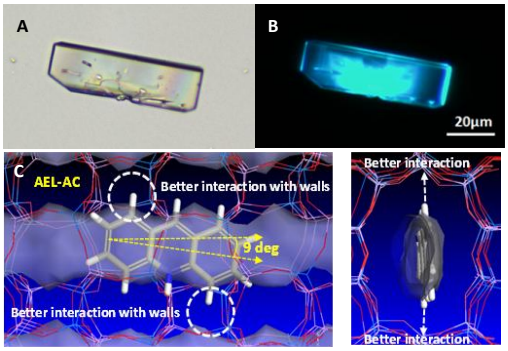

Figure 4.46. Transmission image (A) and fluorescence image (B) of AC/AEL crystals under UV illumination (325-375 nm). C) ACH^+ confined within the AEL channels and its deviation angle; the channel void volume is shown for interpretation help.

Importantly, the total suppression of dye aggregation even for this small dye without pendant groups, rendering hybrid systems with high fluorescence capacity, makes the AEL framework an ideal host for the encapsulation of dyes with a relatively small molecular skeleton of three fused aromatic rings. In this regard, the crystallization inclusion method could be successfully applied for many other typical dyes with a similar molecular structure such as other acridines, xanthenes, oxacines, thionines, etc. This "one-pot" synthetic approach enables the filling of large crystals (long AEL channels) avoiding the "traffic jam" effect at the entrances of the pores and reducing considerably the sample preparation time (less than 24 h) respect to diffusional process, especially for particles larger than several microns (where several days or weeks are required).[6,7] In addition, the leakage of the dye guests out of the channels is impeded by their tight fitting within the matrix and by the presence of the SDA molecules, avoiding the need of closing the channel openings.

- **MeAC/AEL**

In order to obtain a material emitting in the blue edge of the electromagnetic spectrum with a higher order degree, and thus, to achieve also an anisotropic response to the linearly polarized light for its potential use in dichroic applications, methyl acridine dye ($MeAC^+$) was chosen. This $MeAC^+$ dye shows similar photophysical features to AC (as described below), also with its transition dipole moment perpendicular to the long molecular axis. As a difference, $MeAC^+$ has a pendant methyl group, which could force the dye molecules to place more aligned along the channels (Figure 4.42.).

The $MeAC^+$ monomeric absorption band in diluted aqueous solution resembles that for ACH^+ in solution, with the main peak centered at 357.5 nm and a less intense band or shoulder at higher wavelengths (centered at around 415 nm, Figure 4.47.A). Regarding the fluorescent emission of this dye in aqueous solution, it shows an intense fluorescence band centered at 493 nm (Figure 4.47.A), with a fluorescence quantum yield of 0.70. The fluorescence decay of $MeAC^+$ in solution shows monoexponential behavior with a unique and long fluorescence lifetime of 33.5 ns. These results are summarized in Table 4.8.

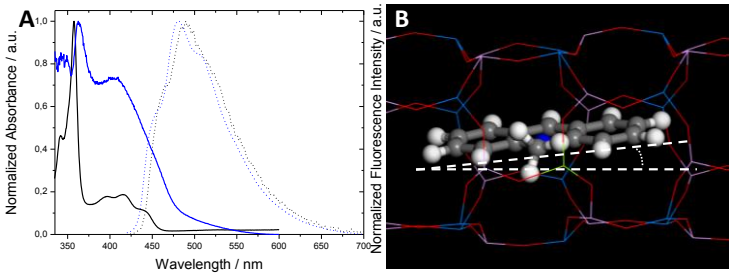

Figure 4.47. A) Height normalized absorption (solid lines) and emission (dashed lines) spectra of $MeAC^+$ in aqueous solution (black lines) and of the MeAC/AEL powder (blue lines). B) Representation of a $MeAC^+$ molecule into AEL, indicating the tilt angle respect to the channels direction.

Table 4.8. Dye-loading and photophysical parameters for MeAC/AEL material and for methyl acridine in aqueous solution.

System	$MeAC^+$ occluded / mmol/100g	λ_{abs} / nm	λ_{fl} / nm	ϕ_{fl}	τ_{fl} / ns	1/D
MeAC/AEL	0.004	362.5	482	0.21	27	7
$MeAC^+$ (10^{-5}M)	--	357.5	493	0.70	33.5	--

The incorporation of MeAC into the inorganic matrix is scarce, only 0.22 mmol dye per 100 sample powder (0.004 mmol/cm^3), possibly due to the bulkier nature of this dye in comparison with AC. Regarding the photophysical properties of MeAC/AEL powder, it shows its main absorption band centered at 362.5 nm (Figure 4.47., Table 4.8.), similar to that for MeAC in solution, previously attributed to the protonated form. The emission spectrum of the MeAC/AEL hybrid material is characterized by the monomeric band of $MeAC^+$ (λ_{fl}: 482 nm), slightly blue-shifted in comparison with the emission band recorded for this dye in aqueous solution (Figure 4.47., Table 4.8.). This is a typical feature for encapsulated dyes in highly constricted environments. In

this sense, it is expected that the more bulky the dye, the greater will be the hypsochromic displacement of the bands. This could be the reason why no hypsochromic shift is noticeable in the case of the less bulky AC dye (Table 4.7.). This effect will be confirmed later for other encapsulated dyes.

However, the resultant hybrid system is not as fluorescent as expected comparing with the dye in aqueous solution ($\phi_{fl,material}$ = 0.21; $\phi_{fl,aq.\ solution}$ = 0.70). This result could be likely due once again to its bigger molecular dimensions with respect to AC caused by the aforementioned pendant group, which may result in distortions of the planarity of the molecule inside the narrow channels of the magnesium aluminophosphate. Finally, inverse dichroic ratios determined were slightly higher than those obtained for AC/AEL crystals ($1/D_{MeAC/AEL}$ = ~7). Indeed, according to molecular simulations, MeAC is disposed with a tilt angle of around 6º with respect to the direction of the AEL channels (Figure 4.47.B).

For all these reasons, *i.e.*, low dye uptake, relatively low fluorescence capacity with respect to AC/AEL system, and only a small improvement in the alignment of the chromophores along the channels, the use of this hybrid system is not as promising as the previous AC/AEL system for optical applications.

4.2.2.- Green emitting dyes into MgAPO-11

This section is dedicated to achieve highly anisotropic green emitting hybrid materials with a high dye loading for optical applications. The green emitting dyes used for this aim are the previously described pyronin Y dye (section 4.1.1.), and two acridine-type dyes: acridine orange (AO) and acridine yellow (AY) (Figure 4.48.). The synthesis of the hybrid materials was carried out exactly as in the previous cases for the blue emitting dyes (see section 3.1.1. in chapter 3), and according to the XRD patterns collected in powder samples (Figure 4.49.), the three syntheses rendered practically pure AEL phases.

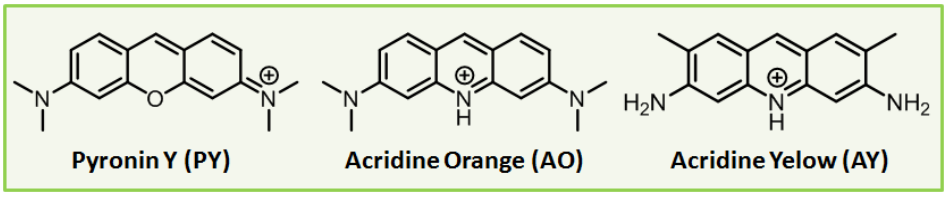

Figure 4.48. Molecular structure of the green-emitting dyes used in this section: pironin Y, acridine orange and acridine yellow. AO and AY are found protonated at neutral pH.

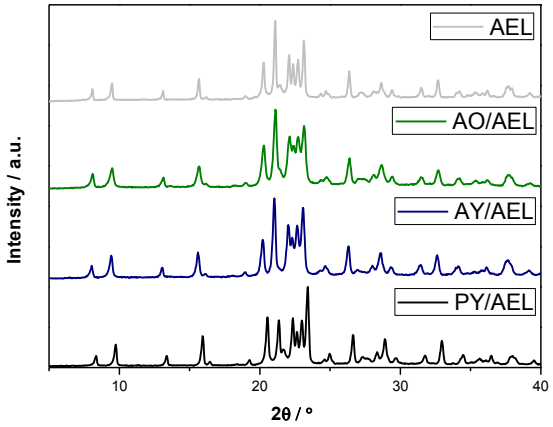

Figure 4.49. XRD diffraction patterns of PY, AY and AO containing MgAPO-11 samples, together with a XRD diffraction pattern of pure AEL phase for comparison.

- **PY/AEL**

The first attempt to obtain a hybrid material with green emission was made with the dye PY. Excitation and emission spectra of the resultant PY/AEL powder are depicted in Figure 4.50. Both bands, centered at 524 and 544 nm respectively, are blue-shifted with respect to those recorded for PY dye in diluted aqueous solution (Table 4.9.), effect ascribed to the confinement imposed by the framework. Indeed, the molecular size of the PY dye (6.2 Å x 3.2 Å x 13.7 Å) is very close to the channels dimensions of the AEL structure (4 Å x 6.5 Å).

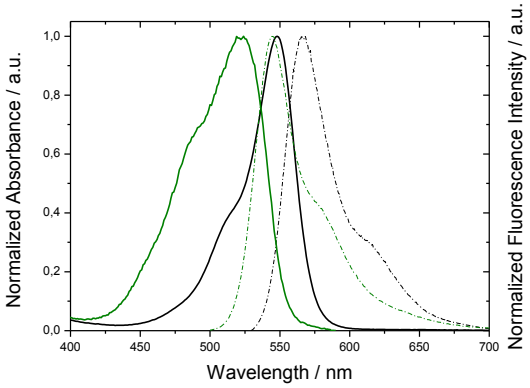

Figure 4.50. Height normalized absorption (black solid line) and emission (black dashed line) spectra of PY in solution and height normalized excitation (solid green) and emission (dashed green) spectra of PY/AEL material.

Table 4.9. Dye-loading and photophysical parameters for PY/AEL powder and the same parameters for PY in aqueous solution.

System	PY occluded / mmol/100g	λ_{abs} / nm	λ_{fl} / nm	ϕ_{fl}	τ_{fl} / ns	D
PY/AEL	0.280	524	544	0.29	4.2	58
PY (10^{-5}M)	--	548	566	0.22	2.0	--

The fluorescence capacity and lifetime of the PY is increased within the MgAPO-11 material with respect to the dye in aqueous solution (ϕ_{fl} = 0.29 *vs* ϕ_{fl} = 0.22, and τ_{fl} = 4.2 ns *vs* τ_{fl} = 2 ns, for PY/AEL and PY in diluted aqueous solution, respectively) as a consequence of the rigidity imposed to the dye by the host matrix, which reduces its molecular motions and consequently the probability of non-radiative deactivation processes. Moreover, due to this tight fitting of the PY dye into the MgAPO-11 host, an extraordinarily-preferential alignment of the molecules along the channels is expected. Certainly, polarized fluorescence measurements carried out in single particles showed that the dye is highly aligned along the MgAPO-11 channels, giving a highly anisotropic response to light (Figure 4.51.B and C), with dichroic ratios as high as D = 58, which is to our knowledge the highest value found so far.[11] The very tight fitting is also responsible for the relatively large hypsochromic shift of about 25 nm found in this sample with respect to solution (Figure 4.50., Table 4.9.).

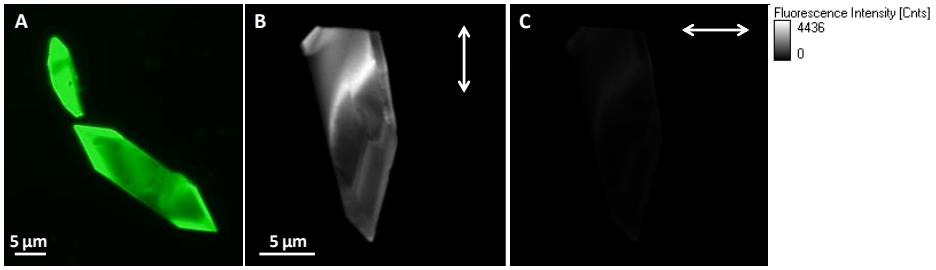

Figure 4.51. A: Real fluorescence image of PY/AEL particles under blue excitation light (450-490 nm). B and C: Fluorescent intensity images recorded by confocal microscopy (λ_{exc}: 470 nm) for mutually perpendicular polarizations. White arrows indicate the direction of the polarization.

All these experimental evidences have been confirmed by geometry-optimized calculations in AEL channels with PY arranged as monomers. The vertically-oriented methyl groups of the PY molecules site in the pockets of the AEL channels. The particular channel topology and dimensions implies that at least one pocket has to

remain empty between two consecutive PY molecules to avoid steric intermolecular repulsions. Therefore, to preserve the sitting of methyl groups in the pockets, PY molecules locate at a certain distance from each other (at least with half unit cell along the channel direction in between them), thus only the incorporation of PY monomers is allowed in this structure. Moreover, the calculation predicts a total alignment in the direction of the pores (Figure 4.52.). On the other hand, the modelling indicates that PY molecules undergo a deviation from planarity of around 4.8º. This is a direct consequence of the tight confinement, which contributes to the hypsochromic shift in the absorption and fluorescence bands respect to PY in aqueous solution (Table 4.9.).

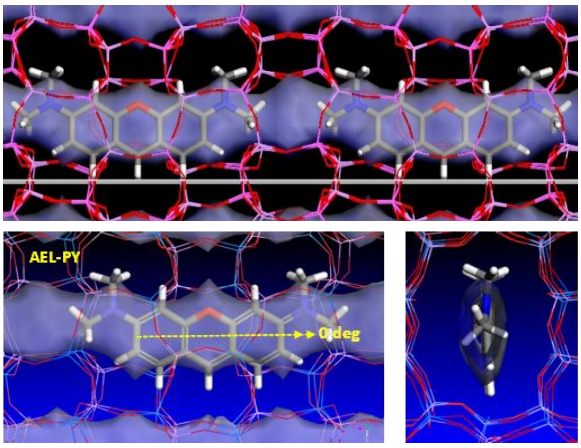

Figure 4.52. Top) Detail of the topology of geometry-optimized AEL channels with PY arranged as monomers, showing the free-volume calculated using a probe radius of 1 Å. Botton) PY confined within the AEL channels and its deviation angle.

However, as happened in the case of MgAPO-36 framework, PY showed a poor incorporation rate into the structure; only 0.28 mmol dye per 100 g sample powder (or 0.006 mmol/cm^3). This fact was previously ascribed to the bulkier nature of the PY with respect to ACH^+, and/or to the low solubility of PY in the synthesis medium (section 4.1.4.). Furthermore, computational results indicate a lower quality of the intermolecular AEL-dye interactions in the case of PY with respect to ACH^+.[38]

- **AO/AEL and AY/AEL**

As alternative to achieve materials emitting in the green region of the electromagnetic spectrum with higher dye loading for optical applications, two different acridine-type dyes with similar molecular structure to PY (Figure 4.48.),

acridine orange (AO) and acridine yellow (AY), were selected to be occluded into AEL.

Both dyes are pH-sensitive. Three different species can be formed: the diprotonated species (AOH_2^{2+} and AYH_2^{2+}) are present at very low pH values (pKa ~ 0.5-1), while the monoprotonated species are common at intermediate pH values (AOH^+ and AOH^+), and their respective neutral species (AO and AY) are detectable at high pH values (pKa = 10.25 and pKa = 8.9 for the AO and AY,[39,40] respectively). Due to the acidic conditions of the synthesis gel (pH ~3-4) and mainly to the intrinsic acidic nature of the MgAPO owing to the substitution of some Al atoms by Mg that generates Brønsted acid sites (see Figure 2.18, chapter 2), only the photophysical properties of the mono and di-protonated forms in solution will be described below.

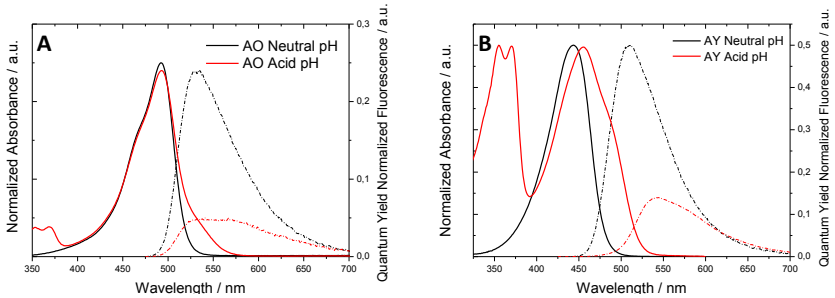

Figure 4.53. Height normalized absorption (solid lines) and emission spectra normalized to the quantum yield value (dashed lines) for AO (A) and AY (B) in aqueous diluted solution at different pH values. Black lines correspond to neutral pH (pH = 7) and red lines to acid pH (pH < 1), respectively.

Depending on the protonation state of these dyes, they show different photophyscial features, as it is shown in Figure 4.53. The absorption and emission bands of the monoprotonated species of AO, recorded at neutral pH, are placed at 492 nm and 535 nm, respectively (Figure 4.53.A). Regarding AY dye, the monoprotonated species shows its absorption and fluorescence bands centered at 443 nm and 512 nm, respectively, which are blue-shifted with respect to the homologous AO dye, (Figure 4.53.B). Moreover, in diluted aqueous solution, AYH^+ shows higher fluorescence efficiency and longer lifetimes (ϕ_{fl} = 0.50 and τ = 5.03 ns) than those registered for AOH^+ (ϕ_{fl} = 0.24 and τ = 1.59 ns). All these data are summarized in Table 4.10. The differences found between both dyes are attributed to the different alkylation of the amino groups, as it has been previously studied for other dyes such as rhodamines.[41,42] Briefly, the decrease in the τ and ϕ_{fl} upon alkylation of the amino groups was explained by the increase of the rate constants of the internal conversion. On the other

hand, the increase of the alkylation usually induces bathocromic shifts due to a higher electron-donating capacity of the alkylated amino groups.

Table 4.10. Photophysical parameters for acridine orange and acridine yellow in aqueous diluted solution at different pH values.

	pH	λ_{abs} / nm	λ_{fl} / nm	ϕ_{fl}	τ / ns (%A)
AO	0.8	493	535/570	0.05	0.48 (100)
	7	492	535	0.24	1.59 (100)
AY	0.4	455	544	0.14	2.76 (86) 0.25 (14)
	7	443	512	0.50	5.03 (100)

In very acidic conditions, the fluorescent emission is drastically reduced and the emission bands of the diprotonated species appear about 30-35 nm red-shifted with respect to the monoprotonated ones (Table 4.10), placed specifically at 570 nm and 544 nm for AOH_2^{2+} and AYH_2^{2+}, respectively. Particularly, in the case of AO dye, due to the low fluorescence emission of its diprotonated form, the contribution of the monoprotonated species is also detected in the emission spectrum at low pH values, which is in this case constituted of the two bands, at 535 and 570nm, assigned to AOH^+ and AOH_2^{2+}, respectively. On the other hand, no significant changes are seen in the absorption spectrum at low pH.

It is important to mention here that these dyes have a high tendency to aggregate, in particular AO dye, as reflect the changes in the absorption spectra produced by the increase of the dye concentration in aqueous solution (Figure 4.54.). As mentioned before, aggregation can be a serious problem because it affects the photophysical properties of the dyes. However, it is expected that by the encapsulation into the MgAPO-11 framework this situation will be prevented even at high dye loadings.

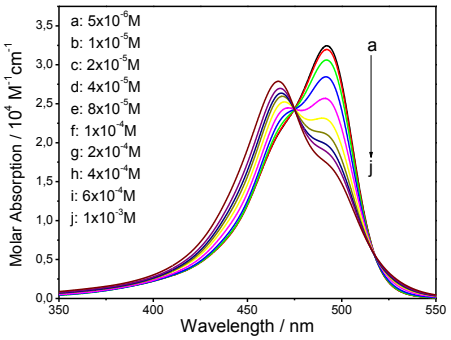

Figure 4.54. Evolution of the absorbance of AO in water increasing the concentration.

Another interesting photophysical feature of both dyes is that in aqueous solution they show experimental evidence of the population of the triplet state. This is confirmed by means of laser flash photolysis through transient absorption experiments (Figure 4.55. and Figure 4.56.). The large negative peak around the maximum of the absorption band (490 nm) in the transient absorption spectra of AO in aqueous solution is attributed to the depletion of the ground state, while the broad positive band in the less energetic range (550-700 nm) is assigned to the triplet-triplet absorption. From the kinetic profile recorded at 630 nm, a triplet lifetime of around 765 ns is obtained for AO dye in neutral aqueous solution while it increases up to around 20 μs after purging the solution with argon to suppress the quenching effect of molecular oxygen (Figure 4.55.). In a similar way, transient absorption spectrum for AY dye in neutral aqueous solution shows the ground state depletion peak at 443 nm, and the triplet-triplet absorption appears from around 500 nm. The kinetic profile was in this case recorded at 600 nm, obtaining as a result triplet lifetimes of around 1 μs in aerated aqueous solution and again of 20 μs in deaerated solution(Figure 4.56.).

More details about the triplet levels are discussed below.

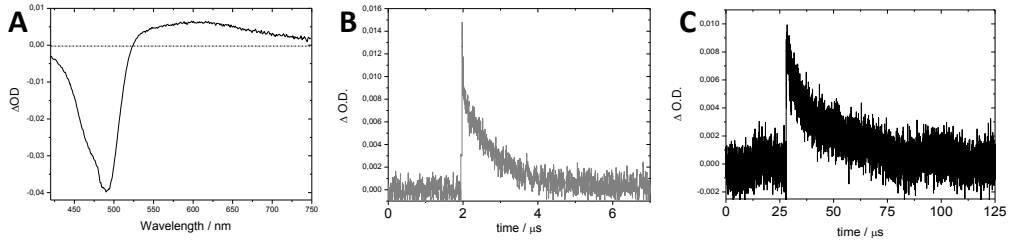

Figure 4.55. Transient absorption spectrum for AO at room temperature in deareated aqueous solution under 465 nm excitation light (A). Transient decay curves recorded at 630 nm in aerated (B) and deaerated (C) aqueous solution.

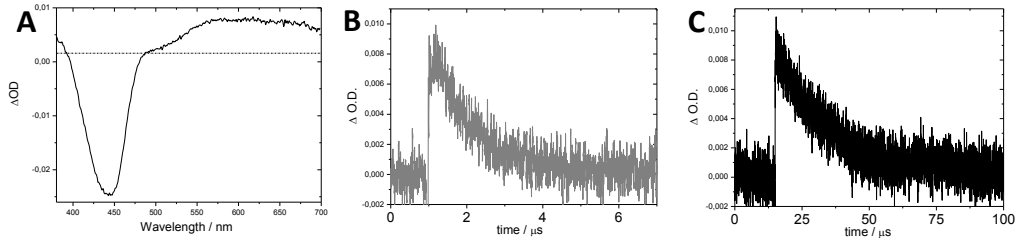

Figure 4.56. Transient absorption spectrum for AY at room temperature in deareated aqueous solution under 443 nm excitation light (A). Transient decay curves recorded at 600 nm in aerated (B) and deaerated (C) aqueous solution.

Once AO is encapsulated into the MgAPO-11, it is remarkable for the hybrid system that the final AO dye loading (1.12 mmol/100g sample powder) was four times higher than that obtained for the analogous PY dye into MgAPO-11 (0.28 mmol dye per 100 g sample). Given that the molecular structures of these two dyes only differ in the central heteroatom of the aromatic ring, being nitrogen in AO and oxygen in PY (see Figure 4.48.), the difference in the amount of dye loaded should be related to the different solubility in the synthesis gel, since there is not a clear relationship between the interaction energy with the inorganic matrix and the nature of the central heteroatom of the organic guest (data not shown).

Regarding the photophysical properties of AO/AEL powder, it shows a very broad and blue shifted absorption band with respect to the AOH^+ in diluted aqueous solution (Figure 4.57., Table 4.11.). As previously mentioned, this effect is usually originated in solid-state dyes, and it is typically ascribed to the confinement effect which can slightly modify the geometry of the chromophore (deviation from the planarity), inducing differences in vibrational and rotational energies of the dyes in such a rigid medium with respect to solution.[11,38] Indeed, molecular simulations indicated a deviation from planarity of 5.1º for AO molecules occluded into AEL (Figure 4.57.B), similar to previous results obtained for PY guest.[12] Conversely, the excitation spectrum of AO/AEL powder shows a much narrower band, similar to that registered for the dye in aqueous solution (Figure 4.57.A). As previously demonstrated for the analogous PY dye, aggregation of this type of dyes is impeded into the MgAPO-11 due to both the tight confinement and the special pore topology, thus, the broadening of the absorption band could be indicative also of non-fluorescent electronic transitions contributing in the blue edge of this band.

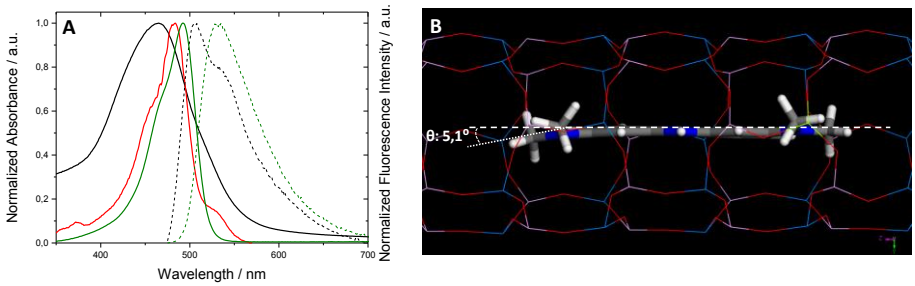

Figure 4.57. A) Height normalized absorption (solid lines) and emission (dashed lines) spectra of AO/AEL powder sample (black lines) together with those spectra for AO in neutral diluted solution (green lines). Excitation spectrum of AO/AEL powder is also shown (red line). B) Representation of an AO molecule into AEL, indicating the angle of deviation from planarity.

Table 4.11. Dye-loading and photophysical parameters for AO/AEL sample in bulk powder together with those photophysical parameters for AO in neutral aqueous solution.

System	AOH^+ occluded / mmol/100g	λ_{abs} / nm	λ_{fl} / nm	ϕ_{fl}	τ_{fl} / ns (%A)	D
AO/AEL	1.12	465	505	0.06	3.40 (64) 1.22 (36)	17-20
AO (10^{-5} M)	--	492	535	0.24	1.59 (100)	--

In this context, energy levels have been simulated in aqueous solution due to the impossibility to perform it in the encapsulated-state. According to the simulation for the mono-protonated acridine orange AOH^+ (assured as the main species occluded into MgAPO-11 regarding its pKa = 10.4 in aqueous solution), it shows two close-lying singlet excited states S_1 and S_2 with ππ* and nπ* character, respectively (Figure 4.58.). Note here that according to the Group Theory and spectroscopic selection rules,[43,44] in a centrosymmetric environment the n-π* transition is forbidden by symmetry and it is characterized by low molar absorptivities ($\varepsilon < 2000$ $M^{-1}cm^{-1}$), whereas π-π* transition is allowed, generally showing high molar extinction coefficients at the absorption maximum ($\varepsilon \geq 10000$ $M^{-1}cm^{-1}$).

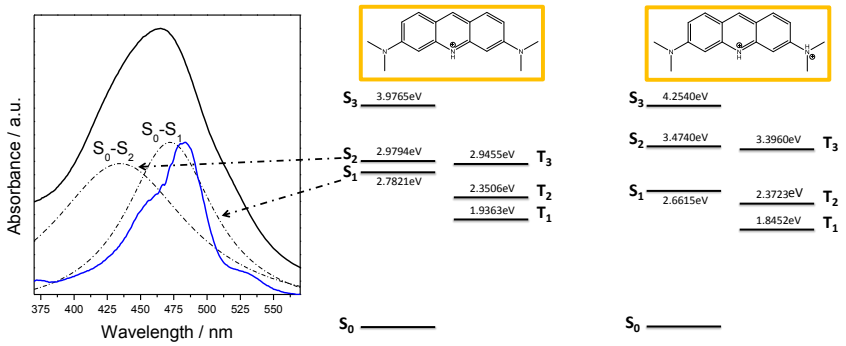

Figure 4.58. Calculated energy levels for AOH^+ (center) and AOH_2^{2+} (right) in water; and the deconvoluted absorption band of AO/AEL system (left, black solid line, the bands resulting from the deconvolution are depicted as dashed lines), together with the excitation spectrum of the same hybrid system (blue line), normalized to the height of the theoretical band ascribed to the S_0-S_1 transition. Deconvolution with a correlation of R^2: 0.9977 was obtained. Arrows indicate the energy levels related to each band.

Although the S_0-S_1 should be the unique allowed transition in aqueous solution, the probabilities of these transitions could be altered due to the tight confinement of AOH^+ into the AEL framework as a consequence of geometrical distortions associated

to different electron configurations. As a result, transitions that would be theoretically forbidden could be weakly allowed. Thus, the wide absorption band of AO/AEL could be also a consequence of the contribution of both electronic transitions (S_0-S_1 and S_0-S_2, with ππ* and nπ* character, respectively), and in this case, the narrow band detected in the excitation spectrum of AO/AEL powder should be assigned to the S_0-S_1 transition with ππ* character, the only responsible for the fluorescence. Indeed, as a general rule, although S_2 can be populated as well upon excitation (very close in energy to S_1, see Figure 4.58. left), it will return to the lowest excited S_1 state non-radiatively (by rapid vibrational relaxation and internal conversion), and consequently the fluorescence only arises from the S_0-S_1 (π-π*) transition. In fact, after the deconvolution of the AO/AEL absorption band, the derived Gaussian curves are placed at 435 and 470 nm, which supposes a displacement that is in agreement with the theoretical energy difference between S_1 and S_2 of AOH^+ species (gap of around 0.21 eV) (Figure 4.58.).

Regarding the fluorescence properties of AO/AEL, it shows the main fluorescence band centered at 505 nm, which is blue-shifted with respect to that recorded for the dye in aqueous solution (530 nm). Note here that this blue shift (~25 nm) is comparable to that registered in previous AEL sample containing the homologous PY dye. This fact indicates a linkage between the magnitude of the hypsochromic shift in the emission band of the hybrid sample and the confinement degree, which induces a slight deviation of the planarity of the dyes inside such a rigid framework.[12] In fact, as it has been mentioned above, molecular simulations indicated a comparable planarity deviation angle for AO and PY into AEL (5.1º and 4.8º, respectively, Figure 4.57.B).

By means of polarization experiments in the florescence confocal microscope, the alignment of the AO molecules along the channels was confirmed, with dichroic ratio values of around 17-20 (Table 4.11.). However, the fluorescence quantum yield registered for the AO/AEL hybrid material is lower than expected (ϕ_{fl}: 0.06, Table 4.11.). It could be explained by different facts. First note that the fluorescence spectrum of AO/AEL powder, together with the main band, shows a prominent shoulder at around 540 nm (Figure 4.57.A), which, as previously detailed, cannot be ascribed to the formation of J-aggregates since they are totally impeded within the AEL channels. Instead, the appearance of this red-shifted shoulder could be assigned to the contribution of the diprotonated species of the dye, previously described in very acidic AO solution, which is characterized by much lower fluorescence efficiency with respect to the monoprotonated form (Figure 4.53., Table 4.10.). Note here that

the absorption bands for both species are very similar, and hence, the coexistence of them would not induce changes in the absorption spectrum. In this sense, the existence of AOH_2^{2+} could be a consequence of the Brønsted acid sites in the MgAPO channel walls due to the incorporation of magnesium in the framework,[45,46] as detailed in section 2.2.1., chapter 2. In this context, the biexponential behavior of the fluorescence decay curve of AO/AEL agrees well with this postulation, attributing the longer lifetime of 3.4 ns (64%) and the shorter lifetime of 1.2 ns (36%) to the contribution of the mono- and diprotonated species (AOH^+ and AOH_2^{2+}), respectively. The larger lifetime values obtained in the powder with respect to those registered for the dye in solution (1.6 ns at neutral pH and 0.5 ns at pH < 1, Table 4.10.), are in agreement with former results found for PY into AEL, as a consequence of the rigidity imposed by the matrix.

Another plausible explanation of the low fluorescence quantum yield in this AO/AEL sample could be an enhancement of the intersystem crossing process with respect to AO dye in solution. The simulated energy levels for AOH^+ (Figure 4.58.) revealed that two triplet states lie below the emitting singlet state S_1, together with a third triplet state, T_3, practically isoenergetic to the second singlet excited state S_2, facilitating ISC from both singlet states. Since, as has been discussed above, the probability of the transition from the ground state to the S_2 electronic level is likely enhanced into AEL, the intersystem crossing process between the close-lying S_2 and T_3 states would be also more favored. Indeed, as other authors have claimed, the spin-coupling is usually more probable between singlet and triplet states of different configurations, *i.e.* from S ($n\pi^*$) to T ($\pi\pi^*$),[47] which is precisely the present case. The importance of these processes will be considered later.

With the aim of achieving a hybrid material with higher fluorescence capacity and relatively high amount of dye occluded, the other acridine-type dye, acridine yellow (AY), characterized by higher fluorescence quantum yield in solution, was encapsulated into the AEL.

In AY/AEL sample, the dye loading was in fact higher than in AO/AEL sample: 2.00 mmol dye per 100 g sample (0.041 mmol/cm^3). This result is consistent with the slightly lower molecular size of the AY, in which the pendant amino groups are not methylated (see Figure 4.48.). Indeed, the fluorescence band of AY/AEL, placed at

511 nm and ascribed to AYH^+ monomers, did not show any hypsochromic shift with respect to the dye in solution (Figure 4.59., Table 4.12.).

Table 4.12. Dye-loading and photophysical parameters for AY/AEL sample in bulk powder together with those photophysical parameters for AY in neutral aqueous solution.

System	AYH^+ occluded / mmol/100g	λ_{abs} / nm	λ_{fl} / nm	ϕ_{fl}	τ_{fl} / ns (%A)	D
AY/AEL	2.00	418	511	0.16	5.72 (58) 1.90 (42)	14-16
AY (10^{-5} M)	--	443	512	0.50	5.03 (100)	--

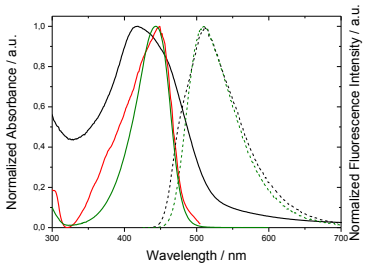

Figure 4.59. Height normalized absorption (solid lines) and emission (dashed lines) spectra of AY/AEL powder sample (black lines) together with those spectra for AY in neutral diluted solution (green lines). Excitation spectra of AY/AEL powder is also shown (red line).

Accordingly, molecular simulations indicated in this case a practically negligible deviation from the planarity of the chromphore of around 1º. However, although the fluorescence quantum yield (ϕ_{fl}: 0.16, Table 4.12.) is higher than in AO/AEL sample, it is relatively low in comparison with AYH^+ in aqueous solution (ϕ_{fl}: 0.50, Table 4.12.). The biexponential kinetics of the fluorescence decay curve of AY/AEL sample with lifetimes of τ_1 = 5.72 ns (58%) and τ_2 = 1.90 ns (42%), could also indicate the presence of monopronotaned and diprotonated forms of acridine yellow inside the MgAPO-11 channels. In the same way than in AO/AEL system, the existence of the latter species could be responsible for the lower fluorescence capacity of the powder.

Furthermore, the absorption spectrum of the AY/AEL bulk powder also shows the same asymmetric broadening in the blue-edge of the band as AO/AEL sample, while a narrower band similar to that for AY in aqueous solution is registered in the excitation spectrum (Figure 4.59.). Since this AY dye shows a similar energy levels distribution than the AO, *i.e.* two close-lying excited singlet states, S_1 and S_2, and two triplet states below the emitting singlet state S_1, together with a third triplet state, T_3, practically

isoenergetic to the S_2, same postulations as detailed before in the AO/AEL system are assumed for the explanations of the band-broadening found in the AY/AEL absorption spectrum.

Once again, the alignment of the AY molecules along the channels was confirmed by fluorescence confocal images with polarized light, giving dichroic ratio values of around 14-16 (Table 4.12).

More importantly, both systems AO/AEL and AY/AEL exhibit the so-called delayed fluorescence phenomenon (see section 2.1.1.3., chapter 2), as it will be described below.

Delayed fluorescence

As previously described (section 2.1.1.3., chapter 2), one mechanism for the appearance of delayed fluorescence involves a reverse intersystem crossing (RISC) from a triplet state to an excited singlet state with a small energy gap between them. However, the reverse intersystem crossing should compete against nonradiative deactivation processes of the triplet state, which are generally triggered by the molecular motions (vibration and rotation of the molecules since molecular collisions are discarded into the MgAPO-11) at room temperature. Thus, by the encapsulation of AOH^+ and AYH^+ dyes into the rigid AEL, on the one hand, dye monomers are isolated, avoiding any molecular aggregation, and on the other hand, the molecular motions of the dyes are restricted, minimizing the probability of the nonradiative deactivation pathways from the triplet state to the ground state, and therefore it could give rise to room temperature delayed fluorescence (Figure 4.60.).

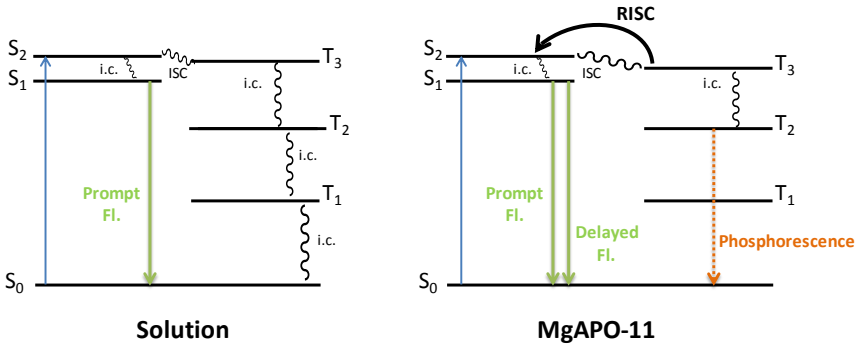

Figure 4.60. Schematic representation of the deactivation pathways taking place for AY and AO dyes in solution at room temperature (left) and within the MgAPO-11 framework.

Effectively, for both AO/AEL and AY/AEL materials, green delayed fluorescence emission, identical to the prompt fluorescence (ns range), but with much longer lifetimes (ms range), is registered, which makes it noticeable to the naked eye after removing the excitation source.

To deeper characterize the long-lived fluorescence lifetime of AO/AEL and AY/AEL samples, decay curves were recorded and Time Resolved Emission Spectroscopy (TRES) experiments were performed for long time ranges using a microsecond pulsed lamp as excitation source. The average lifetimes derived from decay curves were 190 ms and 140 ms for AO/AEL and AY/AEL, respectively (Figure 4.61.A). Even though, the emission band of the monoprotonated species of the dyes remains even seconds after the excitation pulse (Figure 4.61.B).

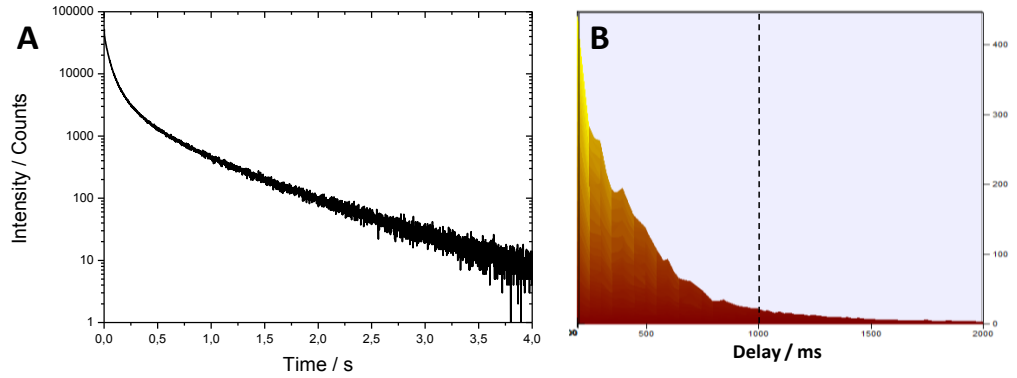

Figure 4.61. A) Fluorescence decay curve of AY/AEL in seconds rage. B) Evolution of the emission intensity recorded for AO/AEL at the fluorescence maximum. Fluorescence signals in B were collected from 200 ms after the excitation pulse (to avoid any prompt fluorescence or phosphorescence residuals) and at different delays until 2s. Highlight that emission is still detected 1 s after the excitation pulse, marked with a dashed line.

In the TRES experiments for AO/AEL, as well as for AY/AEL since similar tendencies were found, practically no signal is detected until a band placed at 620 nm, ascribed to the phosphorescence of AO as other authors have demonstrated,[48] is activated at the specific time of around 28 μs after the pulse (Figure 4.62.A), which is slightly longer than the triplet lifetime previously recorded in solution by laser flash photolysis technique (20 μs). According to the distribution of the energy levels found by theoretical simulations (Figure 4.58.), this phosphorescence should correspond to the emission from the T_2 state. However, this phosphorescence band rapidly disappears, giving rise to the activation of the delayed fluorescence emission at 505

nm. Thus, after the population of T_3 ($\pi\pi^*$) triplet state through S_2 ($n\pi^*$) singlet state, it preferably undergoes a reverse intersystem crossing process (RISC) again to the S_2 state, likely triggered by thermal activation at r.t. Indeed, the calculated energy gap between S_2 and T_3 from the electronic levels of 0.03 eV (Figure 4.58.) is the unique energy barrier that can be overcome by thermal energy at r.t. (0.026 eV). As soon as RISC takes place, S_1 ($\pi\pi^*$) state is populated by fast internal conversion from S_2, which radiativelly deactivates to the ground state giving the characteristic fluorescence emission centered at 505nm.

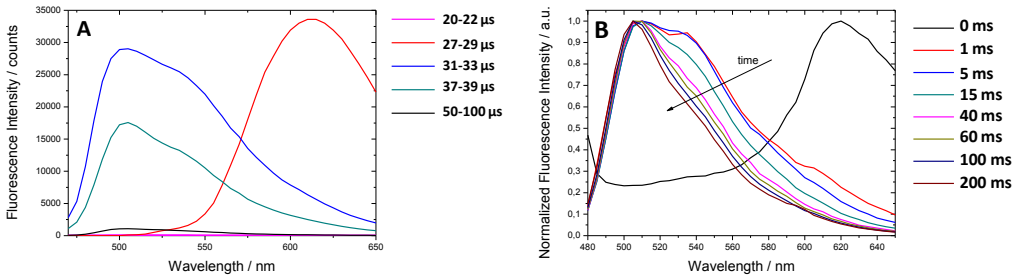

Figure 4.62. A) Emission spectra recorded for AO/AEL powder in TRES experiments at different µs ranges after the excitation pulse. B) Height normalized emission spectra of AO/AEL sample powder recorded in TRES experiments milliseconds after the excitation pulse.

Note here that the emission band shows also a remarkable shoulder 535 nm, previously ascribed to the diprotonated species AOH_2^{2+}, at relatively short times after the activation of the delayed fluorescence. Indeed, this shoulder is detected even in the millisecond range, but it gradually decreases (Figure 4.62.B) at longer times after the excitation pulse. Since the excited electronic levels distribution of the diprotonated AO species does not allow RISC process because of the high triplet-singlet energy gap between S_1 and T_2 ($\Delta E_{S\text{-}T} > 0.100$ eV), and the impossibility of populating the S_2 due to the large energy gap with respect to S_1 ($\Delta E_{S1\text{-}S2} = 0.812$ eV, which means more than 100 nm, Figure 4.58. right), its contribution to these emission spectra could be attributed to a further protonation of the AOH^+ in the excited state. Indeed, it has been previously demonstrated that acridine dyes are stronger bases in the excited state than in the ground state (pKa* > pKa),[39] and since the lifetime of delayed fluorescence is closely associated to the triplet states (characterized by much longer lifetimes), the equilibrium can be likely attained in this time scale. However, the deprotonation would occur while the dye relaxes to the ground state.

Finally, by comparing the emission intensity of the fluorescence band immediately after excitation with the emission signal after several microsecond, where the prompt fluorescence is already turned off, the ratio between prompt and delayed fluorescence in both samples AO/AEL and AY/AEL is estimated, [49,50] $\theta_{delayed}/\theta_{prompt}$ =1.0-1.5 x 10^{-2}.

Summarizing, both AO/AEL and AY/AEL solid systems, can undergo the unusual phenomenon of delayed fluorescence at r.t. due to the tight confinement, probably because i) the absorption probability of the S_2 singlet excited state, practically isoenergetic to the triplet T_3 state, should be enhanced in AEL likely due to a disruption of the dye symmetry, ii) the non-radiative deactivation processes from the triplet state are minimized because molecular motions are restricted into AEL, and iii) molecular aggregation is totally suppressed within the framework.

4.2.3.- Red emitting dyes into MgAPO-11

The above sections were dedicated to blue- and green-emitting dyes occluded into the MgAPO-11 structure, and now our interest is focused on the encapsulation of dyes with red fluorescence into AEL with the aim of attaining ordered hybrid materials emitting in the less energetic range of the electromagnetic spectrum. For this purpose, the following dyes were chosen: oxazine 1 (Ox1), oxazine 4 (Ox4), methylene blue (MB) and LDS 722 (Figure 4.63.). Except for the LDS 722 dye, these hybrid materials were synthesized following the procedure described previously (see section 3.1.1. in chapter 3). The XRD patterns of the obtained samples with Ox1, Ox4 and MB are shown in Figure 4.64.

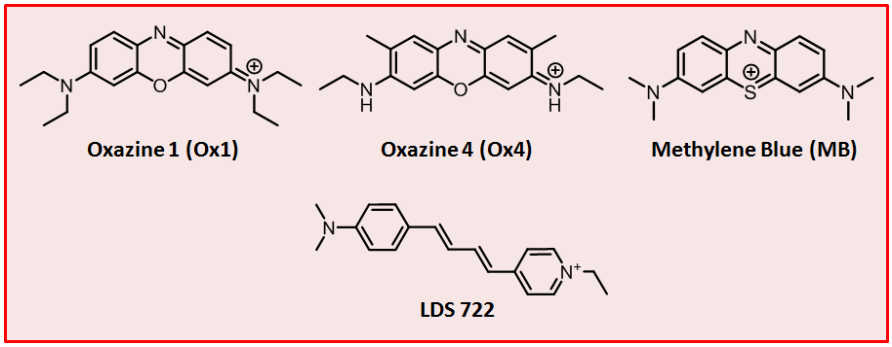

Figure 4.63. Molecular structure of the red-emitting dyes used in this section: oxazine 1, oxazine 4, methylene blue and LDS 722.

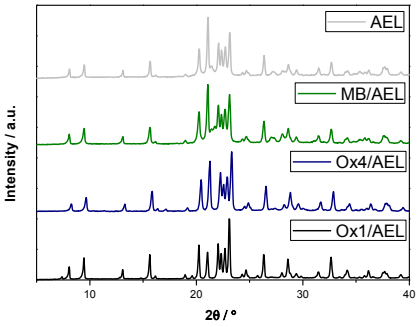

Figure 4.64. XRD patterns of Ox1, Ox4 and MB containing MgAPO-11 samples, together with the XRD pattern of pure AEL phase for comparison. Results regarding LDS722/AEL samples will be discussed later in this section.

- **Ox1/AEL and Ox4/AEL**

The first red emitting dyes chosen to be occluded into the MgAPO-11 material were two oxazine-type dyes (oxazine 1 and oxazine 4). The election of these xanthene derivatives was based on their interesting properties, such as suitability as efficient laser dyes or fluorescence probes,[41,51] which make them promising to be used in optical and photonic devices.[52] Furthermore, they are sensitive to their environment,[53] thus, more information about the internal MgAPO-11 nanochannels was expected to be acquired.

Despite the interesting features of these dyes, they seem not to be appropriate to be occluded into the MgAPO-11 material since in both cases very little colored powder was obtained as a result, with a grayish tone, very different from the colors expected. Dye quantification into the AEL solid product revealed that a practically negligible fraction of the total dye amount added to the synthesis gel got occluded into the inorganic structure, and the resulting hybrid materials were nearly no fluorescent. In these cases, the low occlusion rate could be a consequence of the bulky nature of these dyes, and/or the dyes might not endure synthesis conditions and discompose during the crystallization process.

- **MB/AEL**

Thus, another oxazine-type dye was chosen, methylene blue (MB) dye. This dye also shows interesting properties, and it has been widely used for labeling proteins or

for singlet oxygen generation.[51,54] The molecular structure of the MB is analogous to that of PY and AO dyes but with an extra heteroatom (-S) in the central ring (Figure 4.63. and Figure 4.48., respectively).

MB dye shows its absorption and emission bands centered at 665 and 690 nm, respectively, in diluted aqueous solution. The fluorescence properties are characterized by a quantum yield of 0.04 and a lifetime of 0.4 ns. However, at very acidic conditions (pH < pKa, being the pKa = 0.5)[55] a new and red-shifted absorption band, centered at 745 nm appears (Figure 4.65.). This new band is slightly noticeable even at pH = 1.5, and it is ascribed to the protonated species of the methylene blue, MBH^{+2},[56] which is not fluorescent.

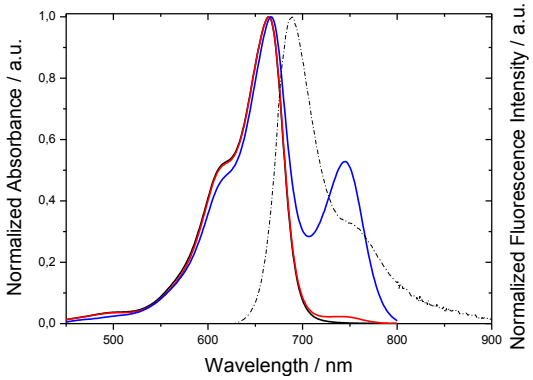

Figure 4.65. Height normalized absorption spectra (solid lines) for the dye MB in aqueous diluted solution at different pH values: at neutral pH (black), at pH = 1.5 (red) and pH = 0.3 (blue); together with the emission spectrum at neutral pH (dashed black line).

Regarding the hybrid material, the MB^{+} enters reasonably well into the host material, giving a dye loading of 0.96 mmol dye per 100 g sample powder, 0.020 mmol/cm^3, a considerably higher amount than that obtained for the homologous PY dye into AEL (~3.5 times), but similar to that obtained in AO/AEL sample (1.12 mmol/100 g). Intense blue powder was achieved as a result (Figure 4.66.). Due to the similarity of the molecular structures of PY, AO and MB, but their distinct incorporation rate into the MgAPO-11 material, calculations were carried out also to study the specific interactions of the MB dye molecules with the matrix and elucidate if these interactions play an important role in the occlusion rate of the chromophores, just like in the previous comparison between AO and PY. Note that efforts were focused in the specific interactions of the different heteroatoms of the central aromatic ring of the mentioned dye molecules (Figure 4.48. and Figure 4.63.). However, it was

concluded once again that there is not a clear relationship between the interaction energy and the dye loading, which suggests that other factors might come to play during the crystallization of the solid materials, possibly the effect of the acidity of the synthesis gel on the dye, solubility, etc.

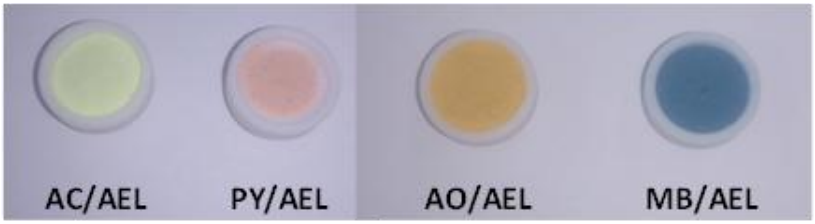

Figure 4.66. AC/AEL, PY/AEL, AO/AEL and MB/AEL powder samples under ambient light.

Focusing now on the photophysical properties of the MB/AEL system, the main absorption band of MB^+ into the inorganic host is placed at 630 nm, once again hypsochromically displaced (35 nm) with respect to the dye in aqueous solution (λ_{abs}= 665 nm, Figure 4.67., Table 4.13.). In this case, as a consequence of the tight confinement, simulations also indicated a deviation from planarity of around 2.5º that should be the responsible for the blue-shift with respect to solution. Note here that it is also recorded a red-shifted band centered at 735 nm (Figure 4.67.), which is ascribed to the protonated species, as stated for the dye in very acidic aqueous solution (Figure 4.65.). Thus, the presence of acid sites within MgAPO-11 is also confirmed by the incorporation of methylene blue. Due to this fact, the resultant MB/AEL system is not suitable for optical applications since it shows a very poor fluorescence capacity (ϕ_{fl} = 0.01, Table 4.13.).

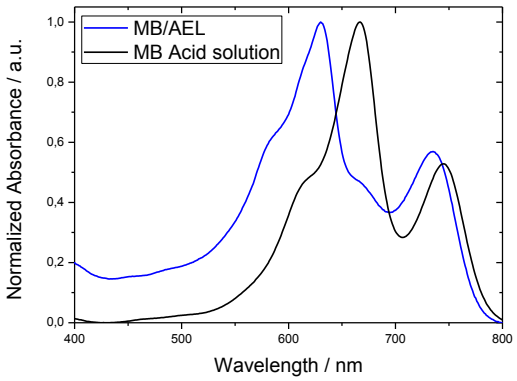

Figure 4.67. Height normalized absorption spectra recorded for MB/AEL hybrid material in bulk powder (blue line) and for the MB dye in aqueous solution at pH = 0.3 (black line).

Table 4.13. Dye-loading and photophysical parameters for MB/AEL sample in bulk powder together with those photophysical parameters for MB in neutral aqueous solution.

System	MB^+ occluded / mmol/100g	λ_{abs} / nm	λ_{fl} / nm	ϕ_{fl}	τ_{fl} / ns
MB/AEL	0.96	630	650	0.01	--
MB^+ (10^{-5}M)	--	665	690	0.04	0.4

- **LDS722/AEL**[57]

Due to the lack of an appropriate dye emitting in the red region of the electromagnetic spectrum to be occluded into the MgAPO-11 with similar molecular structure to AC and PY dyes (built up by three fused aromatic rings), a dye with a completely different molecular structure but similar molecular size, LDS 722 or Styryl 722, was then chosen (Figure 4.63.), since the other red emitting dyes used i) did not endure the synthesis conditions, ii) the intake into the material was too low and/or iii) they showed a very low fluorescence quantum efficiency.

LDS 722 is a hemicyanine-type dye. Generally, the hemicyanine-type chromophores are aromatic compounds which contain a strong electron-donating group in one end of their molecular structure and a strong electron-withdrawing group in the opposite end, connected through methylene groups. In this case, the electron-donating group is aniline, and the electron-withdrawing group is pyridinium. The molecular structure of the hemicyanine LDS 722 is shown in Figure 4.63.

In general, styryls and particularly LDS 722, have high absorption capacity in the blue region of the visible spectrum. On the other hand, their fluorescence band appears very red-shifted with respect to the main absorption band (Figure 4.68.). This large Stokes shift is consequence of their "push-pull" nature (Figure 4.63.), since the fluorescence emission arises from an intramolecular charge transfer state (ICT).[58–60] That is, upon excitation the electronic charge of the aniline moiety is transferred to the pyridinium moiety at the opposite end of the molecule, inducing a large change in the dipole moment of the molecule and high first hyperpolarizability values (β). Note that β is a nonlinear optical property of a molecule, specifically the molecular second-order response coefficient[61] (more details in chapter 2, section 2.1.3.2.). These are advantageous features for i) minimizing the inner filter, particularly interesting for laser applications and ii) NLO applications[62] such as Second Harmonic Generation (SHG) or two photon absorption (TPA).

However, organic π-conjugated molecules tend to crystallize centrosymetrically in an anti-parallel stacking, which is an impediment to achieve NLO properties. In addition, these very flexible molecules usually present poor fluorescence quantum yields in solution due to rotational motions around the different bonds, giving rise to non-radiative deactivation such as *cis-trans* isomerization or the formation of non-fluorescent twisted intramolecular charge transfer states (TICT).[63–66] In this sense, a tight confinement of the dye LDS 722 in a 1D-nanoporous host will be interesting to limit its flexibility and induce an aligned arrangement of the dyes along the channels. Indeed, the dimensions of the elliptical nanochannels of the rigid MgAPO-11 (4 Å x 6.5 Å) are supposed to impose a strong constraint to the LDS 722 chromophore molecules with a molecular size of 2.5 Å x 4.9 Å x 18.6 Å.

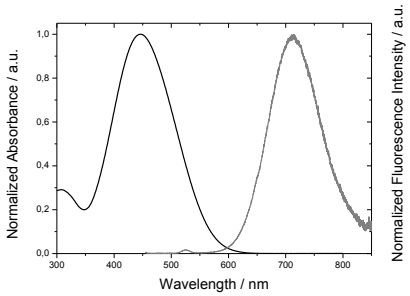

Figure 4.68. Height normalized absorption (black) and emission (grey) spectra recorded for the dye LDS 722 in aqueous neutral solution.

Up to now, the synthesis of the dye-containing hybrid materials has been presented as something straightforward. However, this is not the case of the preparation of LDS 722 containing AEL material. By applying the typical synthesis conditions described for the rest of AEL samples (section 3.1.1. in chapter 3), and adding LDS 722 to the synthesis gel, pure MgAPO-5 phase is obtained. Although the amount of dye in the precursor gel is much lower than that for the ethylbuthylamine (EBA) used as SDA (0.2 MgO: 1 P_2O_5: 0.9 Al_2O_3: 1 EBA: 0.024 Dye: 300 H_2O), the result indicates that LDS 722 itself acted as a strong structure directing agent towards the formation of AFI phase, thermodynamically more favored than AEL. For this reason, an optimization of the synthesis conditions was required in order to obtain pure LDS722/AEL material.

In this sense, a systematic variation of the synthesis conditions was carried out, changing i) synthesis gel composition (Mg, SDA and dye contents), ii) crystallization temperature and time, and iii) heating regime, being static (as usual) or dynamic regime (samples heated under continuous rotation).

Note that the synthesis performed under dynamic regime resulted in pure AFI phases and therefore static regime was applied to achieve AEL phase. On the other hand, the variation of the crystallization time did not affect on the final phase selectivity. Hence, samples were prepared in conventional static heating regime fixing the crystallization time at 24 hours. The most significant experiments, varying the synthesis gel composition (Mg, SDA and dye content) and the temperature are summarized in Table 4.14. XRD patterns of the samples are shown in Figure 4.69.

Table 4.14. Gel compositions: x MgO: 1 P_2O_5: (1-*x*/2) Al_2O_3: *y* EBA: *z* LDS 722: 300 H_2O and synthesis conditions (crystallization temperature, T) used in this work. The amount of dye loaded in the samples is expressed as mmol of dye per 100 grams solid product, and as percentage of the dye loaded with respect to the initial amount in the gel. Main phases of the obtained products are denoted first and minor phases in a second place; down arrows indicate a minor presence, and * traces.

Sample	*x*	*y*	*z*	T / ºC	Phase	mmol / 100g	Dye uptake / %
1	0.2	1	0.024	180	AFI+AEL(↓)	5.16	35
2[a]	0.2	1	0.024	180	AFI	8.70	71
3	0.2	1	0.008	180	AEL+AFI(↓)	1.32	27
4	0.2	1	0.008	195	AEL	0.88	18
5	0.2	0.75	0.008	180	AEL	0.60	15
6	0.2	0.75	0.008	195	AEL+ cristobalite	0.45	11
7	0.2	1.5	0.008	180	AFI+AEL(↓)	8.15	52
8	0.3	1	0.008	180	AEL+AFI	1.11	27
9	0.3	1	0.008	195	AEL+AFI	0.87	18
10	0.1	1	0.008	180	AEL+AFI(↓)	1.16	29
11	0.1	1	0.008	195	AEL*	2.20	44
12	0.1	1	0.016	180	AEL+AFI(↓)	3.60	43
13	0.1	1	0.016	195	AEL+AFI(↓)	3.60	43
14	0.1	1	0.024	180	AEL+AFI(↓)	8.47	59

[a] Sample prepared under dynamic heating regime, *i.e.* the gel was submitted to rotation during the hydrothermal crystallization.

Although high dye-loadings are desired, the first step was the reduction of the LDS 722 amount in the synthesis gel to 0.008 in proportion (from 0.024), since it induces the formation of AFI phase. As a result, it was observed a higher tendency to crystallize as AEL (synthesis **3** *vs* **2**, Table 4.14.), confirming the SDA effect of this hemicyanine towards AFI. Since still not pure AEL phase was obtained, a higher

temperature was set in the crystallization process for the same synthesis gel (from 180 to 195 ºC, sample **4** *vs* **3**, Table 4.14.). This synthesis rendered pure AEL phase, but the dye uptake achieved was considered low for optical purposes (see the pale colored LDS722/AEL powder in Figure 4.70.).

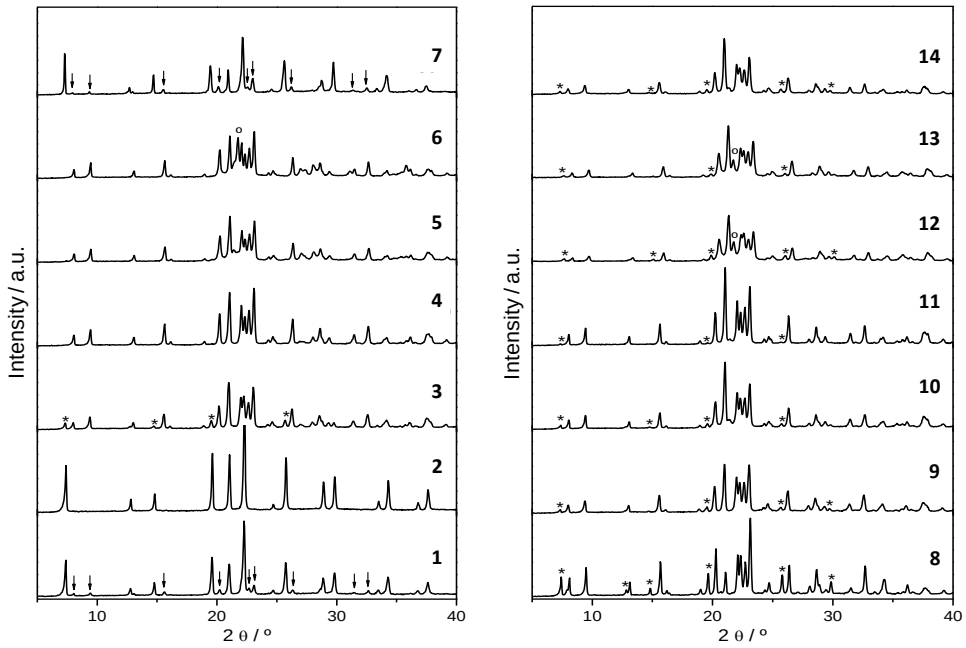

Figure 4.69. XRD patterns of samples prepared under the different synthesis conditions summarized in Table 4.14. Arrows, asterisks and circles indicate AEL, AFI and alfa-cristobalite diffractions, respectively, when they are obtained as impurities of the main phase.

Figure 4.70. Most representative samples (**4**, **11** and **14** in Table 4.14.) under ambient and UV light.

In the next attempt the SDA amount in the synthesis gel was reduced, at two synthesis temperatures (180 and 195ºC, samples **5** and **6** in Table 4.14.). Although it resulted in pure AEL in the case at 180ºC, the dye loading did not improve. Then, the SDA amount was increased to a proportion of 1.5 in the initial gel, but it conversely lead to AFI phase as the major product (sample **7** in Table 4.14. and Figure 4.69.).

At this point, the variation of the magnesium content was accomplished. In the first attempt the proportion in the synthesis gel was increased to 0.3, expecting that more negative charges in the structure (by the isomorphic replacement of Al^{3+} by Mg^{2+} in the host) could induce a higher LDS 722 uptake. However, a mix of AFI and AEL phases was achieved (samples **8** and **9** in Table 4.14. and in Figure 4.69.). Conversely to what might be expected, reducing the Mg to 0.1 in proportion (sample **10** in Table 4.14.), almost pure MgAPO-11 material was obtained (with only a minor presence of AFI crystals, Figure 4.69.) and a slightly higher dye loading was obtained, comparing to the best results achieved up to this point (sample **10** *vs* sample **4** in Table 4.14.). Furthermore, maintaining this composition but increasing the crystallization temperature to 195ºC (sample **11** in Table 4.14.), a practically pure AEL phase was obtained, with only AFI traces (Figure 4.69.), and with a considerably higher dye loading of 2.2 mmol LDS 722 per 100 g sample powder (sample **11** in Table 4.14., Figure 4.70.). This higher dye incorporation upon a decrease of the Mg content, and hence of the negative charge density in the framework, might be related to the smaller charge-density associated to LDS 722 compared to protonated EBA due to its larger size (with the same molecular charge).

Efforts were focused then in reaching higher dye loading rates, keeping the gel composition as in sample **11**, except for the LDS 722 amount added. Firstly, dye proportion was raised to 0.016, and syntheses were performed again at the two temperatures used in this study (180 and 195ºC, samples **12** and **13** in Table 4.14.). Note here that in these cases temperature did not show significant effect upon the total encapsulated dye, rendering in both cases AEL as the main phase, with a dye-uptake of 3.60 mmol LDS 722 per 100 g sample, which is indeed considerably higher than in the former samples. Finally, LDS 722 dye amount was increased to 0.024 in the synthesis gel, yielding a MgAPO-11 material with the highest dye content found so far in LDS722/AEL samples (8.47 mmol/100 g product, sample **14** in Table 4.14., also see the dark colored LDS722/AEL powder in Figure 4.70.). However, this sample also showed a slight presence of the AFI phase, though still in a minor amount.

In summary, in order to reach MgAPO-11 with high dye uptakes, the optimized gel composition would be 0.1 MgO: 1 P_2O_5: 0.95 Al_2O_3: 1 EBA: 0.008-0.024 LDS 722: 300 H_2O, carrying out the crystallization statically for 24 hours at 195 ºC.

With respect to the above results, the photophysical characterization was carried out in the most representative samples. The absorption spectra of bulk powder samples

show the typical band of the LDS 722 dye at 397 nm ascribed to the S_0-S_1 "locally-excited" (LE) transition, hypsochromically shifted respect to the dye in solution, together with a less intense and red-shifted band (Figure 4.71.), attributed to the ICT state in the ground state. The fact that this ICT band is detected only in the hybrid system and not in solution should be a consequence of the stabilization of the ICT state due to the rigid environment imposed by the host matrix.

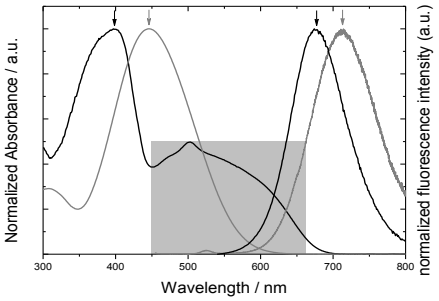

Figure 4.71. Height normalized absorption and emission spectra of LDS722/AEL powder sample (black lines) together with those for LDS 722 in aqueous solution (gray lines) for comparison. Gray square points out the band ascribed to the ICT state in the ground state.

Regarding fluorescence emission, hybrid samples show red fluorescence ascribed to the ICT emission band (Figure 4.71.), but much more intense than that for the dye in aqueous solution. Thus, a dramatic enhancement of the fluorescence capacity of the hemicyanine has been achieved through encapsulation into AEL matrix. Indeed, fluorescence quantum yields recorded for powder samples are two orders of magnitude higher than those in aqueous solution (see data in Table 4.15.), especially when the ICT state is directly populated (λ_{exc} = 530 nm), in comparison with excitation at the LE band (λ_{exc} = 410 nm).

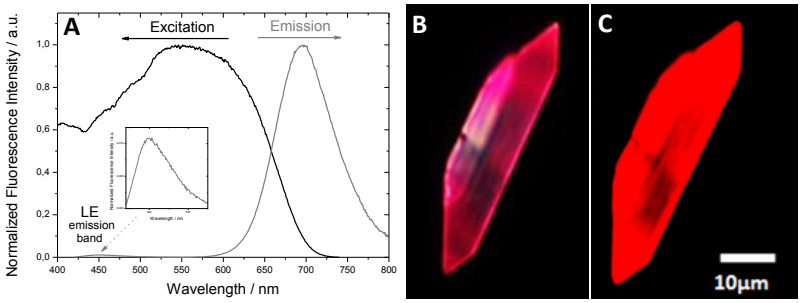

Figure 4.72. A) Intensity-normalized excitation spectrum (λ_{em} = 750nm) and emission spectrum (λ_{exc} = 410 nm) of sample **11** powder. B and C) Emission images of a LDS 722/MgAPO-11 particle upon UV excitation light (B, λ_{exc} = 325-375 nm) and green light (C, λ_{exc} = 515-545 nm).

Actually, exciting the sample upon UV-blue light, a reminiscent emission band at around 450 nm ascribed to the radiative deactivation of LE is recorded together with the more intense ICT emission band (Figure 4.72.). These facts indicate that the population of the ICT in the excited state through relaxation from an excited LE state is not entirely efficient. Excitation spectra (Figure 4.72.), showed the ground ICT band as the main responsible for the emission, in agreement with the aforementioned assumption.

Table 4.15. Chromophore-density (ρ) of different samples and their main photophysical parameters, together with those for the dye in solution: fluorescence quantum yield (ϕ_{fl}), maximum emission wavelength (λ_{fl}) and fluorescence lifetimes (τ).

Sample	ρ / mmol/cm^3	ϕ_{fl}	λ_{fl} / nm	τ / ns (%A)
solution	-	0.01	710	0.08[b]
2 (AFI)	-	0.05	700	0.7 (62) [a] 1.9 (38)
4	0.018	0.55[a] 0.18[b]	677	2.7[a]
5	0.012	0.32[a] 0.13[b]	675	2.5 (79) [a] 0.6 (21)
10	0.024[c]	0.25[a] 0.13[b]	682	2.5 (88) [a] 0.6 (12)
11	0.045[c]	0.41[a] 0.20[b]	696	2.6[a]
12	0.074[c]	0.14[a] 0.09[b]	700	2.4 (62) [a] 0.7 (38)
13	0.074[c]	0.27[a] 0.19[b]	700	2.5 (84) [a] 1.1 (16)
14	0.174[c]	0.15[a] 0.12[b]	705	2.4 (67) [a] 0.8 (33)

[a] Registered under 530 nm excitation; [b] Registered under 410 nm excitation. [c] Assuming all the solid is AEL phase.

The higher luminescent capacity of the dye within the inorganic MgAPO-11 host is in agreement with the fluorescence lifetime values recorded for LDS722/AEL samples of around 2.5 ns, compared to the shorter lifetimes obtained for the dye into MgAPO-5 host or in aqueous solution (Table 4.15.). The longer lifetimes are a direct consequence of the decrease of non-radiative pathways in the rigid medium. It is worth noting that the fluorescence enhancement found in MgAPO-11 is a direct consequence of the space restriction into the constricted host, since into AFI structure with larger channels, although the fluorescent capacity was improved respect to solution, is not as efficient as in LDS722/AEL samples (see sample **2** in Table 4.15.). On the other hand, the variations found in the fluorescence lifetimes of the different samples mainly composed of AEL phase could be ascribed to the presence of AFI impurities, showing biexponential behavior in their respective fluorescence decay

curves versus the monoexponential decay for pure LDS722/AEL samples (samples **5** and **10** *vs* **4** and **11** in Table 4.15.). In the former cases, the longer lifetime of around 2.5 ns is ascribed to LDS 722 dye in AEL structure, and the shorter lifetime of around 0.6 ns, would indicate a less rigid environment, probably LDS 722 in the AFI framework. In fact, in the biexponential decay registered for the pure LDS722/AFI powder (sample **2**, Table 4.15.) the main contribution is actually of a lifetime of around 0.7 ns. Besides, there is a general drop in the fluorescence quantum yield as the dye loading in the MgAPO-11 samples increases: sample **4**, with a dye content of 0.88 mmol/100g, shows a quantum yield of 0.55, compared to sample **14** with a dye loading 10 times higher (8.47 mmol/100 g) but a quantum yield three times lower of 0.15 (Table 4.15., Figure 4.70.). Since molecular aggregation is totally avoided due to the particular topology and narrow size of the AEL nanochannels, the fluorescence decrease must arise from another phenomenon. In the samples with higher dye uptake, along with the lower emission intensity, a red-shift of the fluorescence band of up to 30 nm has been recorded respect to the diluted ones, which suggests that both the shifting and the fluorescence decrease are due to a reabsorption-reemission phenomenon. It should be noted that, although those dyes whose emission takes place from ICT states usually show large Stokes shifts minimizing inner filters, the broad ICT absorption band recorded for LDS722/AEL material overlaps with the emission band (Figure 4.72.), enhancing the possibility of inner-filter effect.

In order to further discuss the favorable effect of the tight confinement imposed by the host matrix to the photophysical features of the flexible hemicyanine LDS 722, molecular modeling was applied. The stability of the different isomers of the flourophore (*trans*, *cis*-1 and *cis*-2 in Figure 4.73.) in the two types of inorganic structures obtained (AEL and AFI) was studied, and it was concluded that preferentially *trans* isomers will be occluded within both structures, being *cis* isomers much less stable. Moreover, *cis* isomers fit even worse within the AEL elliptical and smaller nanochannels than in AFI cylindrical nanochannels.

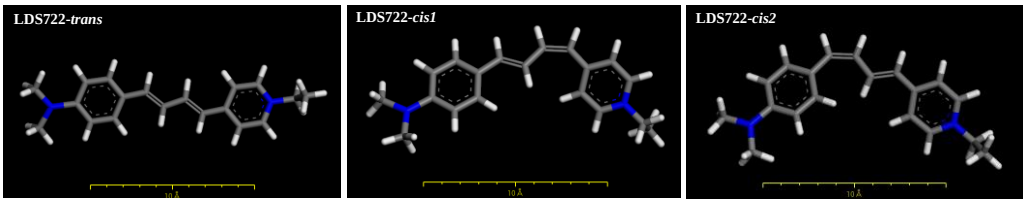

Figure 4.73. Molecular structure of the different LDS 722 isomers studied.

As stated before, constraint is the key factor to enhance the fluorescence of the LDS 722 dye. Therefore, by molecular simulations the flexibility of the molecule inside the different frameworks (AFI and AEL) was analyzed. In this sense, different molecular motions have been taken into account except *cis-trans* photoisomerization, since the presence of *cis* isomers is impeded. The considered motions are: i) deviation from the coplanar configuration between the donor and acceptor rings, since this coplanar configuration, denoted as planar ICT (PICT) state, is the responsible for the fluorescence emission; and ii) rotation of the aniline group around the single C-N bonds, because these twisting motions allow the formation of a twisted ICT (TICT) state, a non-radiative state that efficiently quenches the fluorescence.[65,66] Both aspects (deviation from coplanarity and C-N bond torsion angle) are depicted in Figure 4.74.

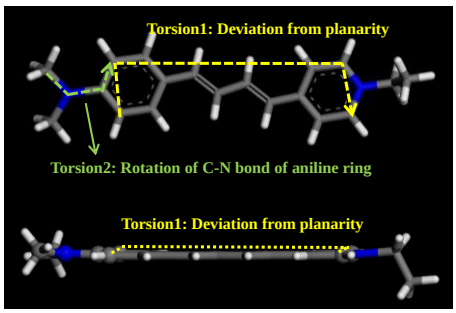

Figure 4.74. Two views of the LDS 722-trans isomer, with the definition of the torsion angles 1 and 2 used for analysis of the deviation from planarity and C-N bond rotation, respectively.

According to the simulations, the deviation from coplanarity and the C-N rotation are strongly impeded within the AEL framework, which imposes a strong constraint on the organic molecules. Conversely, AFI nanochannels seem not to be limiting enough for the prevention of the molecular movements (Figure 4.75.). Thus, these simulations explain the better fluorescence properties of LDS 722 occluded within the AEL framework in terms of a prevention of the deviation from coplanarity and C-N bond rotation because of the tight confinement provided by the AEL host.

Finally, in order to check the viability of this hybrid material for NLO applications, in the first place the alignment degree of the dye molecules along the channels was quantified by fluorescence dichroic ratio values (D). It should be mentioned that the analyses have been focused in sample **11** because it shows high fluorescence efficiency (ϕ_{fl}: 0.41, nearly 40 times higher than that obtained for LDS 722 in aqueous solution, Table 4.15.) with a considerable dye uptake (Table 4.14.), and hence, it has been chosen as the best sample.

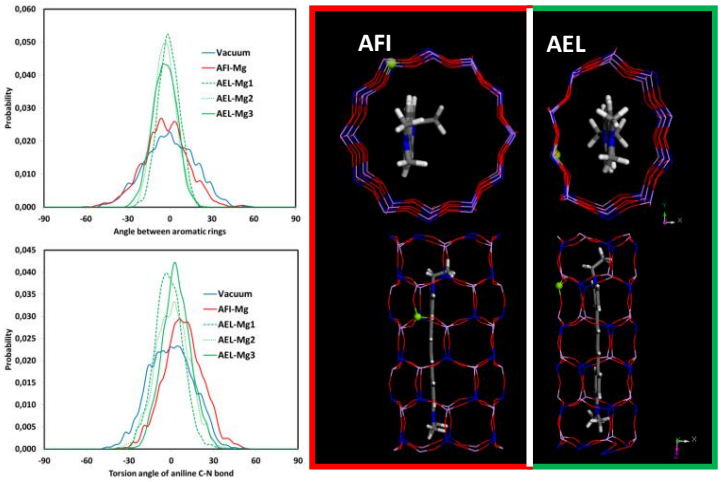

Figure 4.75. Left: Smoothed angle distributions between the aromatic rings (top) and of the C-N torsion angle of the aniline ring (bottom) of LDS 722-trans isomers in a vacuum (blue) or occluded within AFI (red) AEL (green, with different lines as a function of the Mg position into the structure). Right: Two views of the most stable location of the LDS 722-trans isomers within the one-dimensional (cylindrical or elliptical) channels of AFI and AEL frameworks.

Recording fluorescence intensity for mutually perpendicular polarizations, LDS722/AEL particles of sample **11** show dichroic ratios higher than D = 50, which highlights the huge anisotropic response of this material to linearly polarized light (Figure 4.76.). This feature, together with the fact that LDS 722 shows intrinsic NLO properties, makes this hybrid system potential for second-order NLO properties such as second harmonic generation (SHG) and two-photon-induced fluorescence.

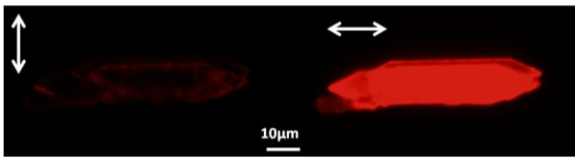

Figure 4.76. Polarized fluorescence images of LDS722/AEL particles under green excitation light (515-545 nm). Arrows indicate the direction of the polarizers.

The study of NLO properties in single LDS722/AEL crystals was carried out exciting the sample with NIR light at 1024 nm and keeping the polarization angle of the incident light parallel to the transition dipole moments of the molecules aligned along the AEL nanochannels. This way, a sharp peak at 512 nm and a broad band centered at around 650 nm were obtained (Figure 4.77.A and B). Since both, the sharp peak and the broad band, show a quadratic power dependence (Figure 4.77.C), they

were assigned to second harmonic signal (SHG) and 2-photon excited fluorescence, respectively.

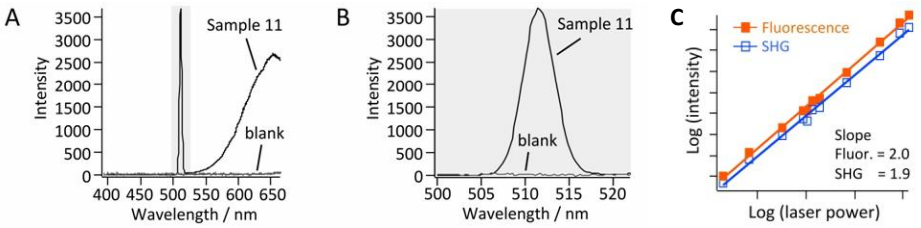

Figure 4.77. A) SHG/2-photon fluorescence spectrum recorded for sample 11, together with the spectrum recorded under the same conditions for a blank AEL crystal (λ_{exc}: 1024 nm, 0.1 mW excitation power). B) Enlarged image of the SHG signal in A centered at 512 nm. C) Laser power dependence of SHG (blue) and fluorescence (orange).

In order to study the wavelength tunability of the hybrid material and identify the most efficient excitation wavelength to generate/excite SHG/fluorescence, the excitation wavelength of the laser light was tuned from 812 to 1222 nm (Figure 4.78.) at the same laser power set at 0.1 mW to minimize photobleaching of the dye (variations of laser power between wavelengths are corrected within 6%). According to the results the most efficient wavelength-range for both SHG and 2-photon fluorescence was between 1000 and 1020 nm (Figure 4.78.). Finally, in order to quantify the SHG conversion efficiency of the LDS722/AEL material, the obtained signal was compared with a reference β-barium borate, BBO, crystal at 1020 nm excitation wavelength. After compensating volume differences (note that AEL crystals are very thin plates of around 1 μm thick *vs* the BBO crystal having 1 mm thickness, see section 3.5. in chapter 3)[57], it was concluded that the SHG conversion efficiency of the present hybrid material is of 17%, relative to that of BBO (Figure 4.78.C).

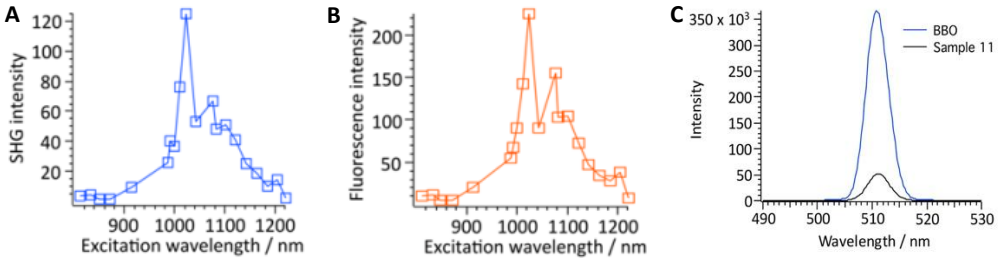

Figure 4.78. SHG intensity (A) and 2-photon fluorescence intensity (B) at different excitation wavelengths from 812-1222 nm with 0.1 mW excitation power. C) Spectra observed on BBO crystal (blue) and on sample **11** (black) crystals after compensating volume differences.

It is important to note here that in order to achieve a hybrid material with NLO properties, the guest dye, LDS 722 in the present case, should have intrinsic Non-Linear Optical properties (π-conjugated molecules with strong electron donor and acceptor groups), because the previous materials reported above, particularly AC/AEL and PY/AEL also provided highly fluorescent hybrid systems with a preferential alignment of the chromophores, but neither of them showed SHG signal.

Summarizing, due to the rigidity imposed by the AEL host matrix, LDS722/AEL system has demonstrated high fluorescence quantum yield, two orders of magnitude higher than that in aqueous solution, in the red part of the visible spectrum. Furthermore, in this material it was proven by polarization experiments that the dye molecules are disposed preferentially aligned along the nanochannels of the MgAPO-11, with dichroic ratios as high as 50, similar to those recorded for PY/AEL hybrid system (D = 58, the highest value found to our knowledge). In fact, this high alignment of the LDS 722 molecules, through the intrinsic non-linear optical properties of the dye, led to a hybrid material with second-order non-linear optical properties such as Second Harmonic Generation and two-photon excited fluorescence.[57]

4.2.4.- New optical properties by combination of dyes into MgAPO-11

It has been proven so far the favorable effect of encapsulating different dyes into the tightly adjusted MgAPO-11 elliptical nanochannels, on the one hand improving their photophysical response and on the other hand triggering new properties that do not appear in solution, such as delayed fluorescence or SHG. Now, with the aim of developing new applications for the hybrid materials, different hybrid systems based on the simultaneous incorporation of several dyes into MgAPO-11 host are considered. In this section, these new samples are fully described together with their applications, such as fluorescence color switching and white light emission.

- **AC-PY/AEL : Optically Switchable Hybrid Material**[38]

Previously in this chapter, hybrid materials consisting of MgAPO framework containing acridine or pyronin Y separately have been described. Now, taking advantage of some features of those systems, a new hybrid material suitable for dichroic applications is aimed to be achieved by the simultaneous encapsulation of AC and PY dyes into MgAPO-11 nanochannels. Particularly, a fluorescence color switching is expected upon UV excitation by applying linearly polarized light, as a consequence of i) an energy transfer from AC dye to PY (suitable par of chromophores for FRET process, as already demonstrated in another magnesium aluminophosphate, MgAPO-36, see section 4.1.4. in this chapter); and ii) the perpendicular orientation of transition dipole moments of the two dyes in a preferential arrangement imposed by the host. Thus, both dyes will respond in a complementarily to the linearly polarized UV light.

The synthesis of the hybrid material was accomplished as stated in section 3.1.3. in chapter 3, and the synthesis process gave as result pure AEL phase (data not shown). Although an equimolar ratio of the dyes was added to the initial synthesis gel, a higher amount of ACH^+ was occluded into the material with respect to PY (1.33 mmol ACH^+ per 100 g sample powder *vs* 0.03 mmol PY per 100 g sample powder). This trend is in agreement with the previous AC/AEL and PY/AEL materials, where a much higher uptake was reached for AC dye in identical synthesis conditions (Table 4.7 *vs* Table 4.9.), attributed to the better AEL-AC dye interactions with respect to PY dye, due to its less bulkier nature,[38] and also to its higher solubility in the synthesis medium.

The resultant material shows a relatively high fluorescence quantum yield (ϕ_{fl} = 0.26) covering a very broad emission range under UV excitation. Indeed, the emission

bands of the two dyes, at 480 and 537 nm for ACH^+ and PY, respectively, with similar intensities, are observed under UV excitation light (Figure 4.79.A, black curve). The fact that the emission of both dyes is clearly seen by exciting only the acridine (under UV light, see Figure 4.45. and Figure 4.50.) indicates that partial FRET process is occurring from the ACH^+ to the PY.

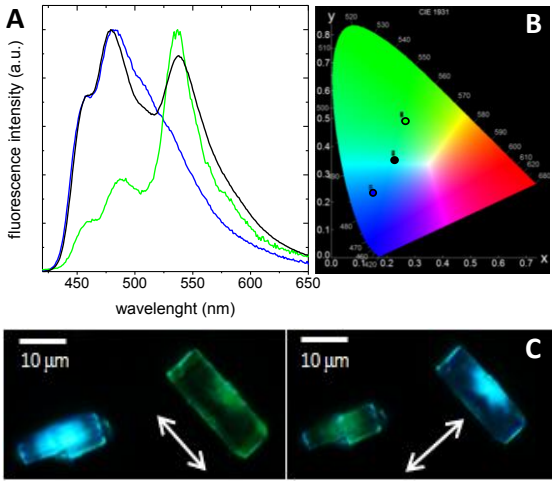

Figure 4.79. A) Emission spectra for AC-PY/AEL powder (black) without polarization and for perpendicular (blue) and parallel (green) polarizations respect to the channel c-axis of a MgAPO-11 single crystal. B) Their corresponding emission colors in CIE with coordinates: x = 0.23 and y = 0.35 (black emission curve); x = 0.15 and y = 0.23 (blue emission curve); and x = 0.26 and y = 0.49 (green emission curve), respectively. C) Fluorescence images of AC-PY/AEL particles with orthogonal polarizations (arrows indicate the direction of the polarizer). In all cases UV excitation light was used (325-375 nm).

Indeed, the relatively high fluorescence efficiency of the donor together with the relatively high overlapping between its emission band and the absorption band of the acceptor (see Figure 4.20.), are favorable factors for FRET.[8] Moreover, as other authors have proposed, relatively large donor:acceptor ratios (*i.e.* 50:1) are preferred for an efficient FRET process,[67] in concordance with the relative contents of the dyes obtained in this hybrid material (48:1), although an equimolar ratio was added to the precursor gel. Conversely, the relative orientation of the transition dipole vectors between both dyes is apparently unfavorable for an energy transfer between the dyes. However, the slightly tilted distribution respect to the channels direction, with a tilt angle of 9 degrees for the ACH^+ monomers into MgAPO-11 according to simulations (see section 4.2.1.), can enable FRET process between them. Indeed, in AC/AEL

system, it was proven that the alignment of the dye along the nanochannes, given by the inverse dichroic ratio value (1/D), was only 5 (section 4.2.1.), indicating only certain ordering degree, but not a perfect alignment. In contrast, PY reaches a dichroic ratio (D) of 58 into the AEL host (section 4.2.2.) and hence the alignment of this chromophore is almost parallel to the channel direction.

In order to confirm the statement of the FRET process, some calculations were carried out. First, assuming a refraction index between η = 1.4-1.55 and a quite unfavored orientation factor for the hetero-FRET along the channels of κ^2~0.1, a Fösters ratio (R_0) of around 23-25 Å was calculated (definition of Fösters ratio given in section 2.1.2.2. in chapter 2). In this regard, considering the dye contents for AC-PY/AEL (1.33 mmol ACH^+/100 g sample and 0.03 mmol PY/100 g sample) and the dimensions of the AEL unit cell along the channel (8.37 Å), and assuming a homogeneous distribution of the dyes along single channels, there would be one ACH^+ molecule every 516 Å and 1 PY molecule every 24502 Å along a particular channel. This result indicates that the probability of finding a PY and an ACH^+ molecule in the same channel in that distance interval is rather small (4 % and 12 % for distances below 20 and 60 Å, respectively, for each PY), unless there is a clustering of dyes within single channels. Another possibility is that FRET process preferentially takes place between chromophore molecules located in different channels, as stated in section 4.1.4. in this chapter. Making an estimation of the probability of finding an ACH^+ monomer around a PY in neighboring channels at a distance of 20 or 60 Å, the result is on the contrary a rather high probability (20 % and 100 %, respectively; Figure 4.80.), despite the low content of dyes, due to the high number of neighboring channels, as other authors have also stated.[9,17]

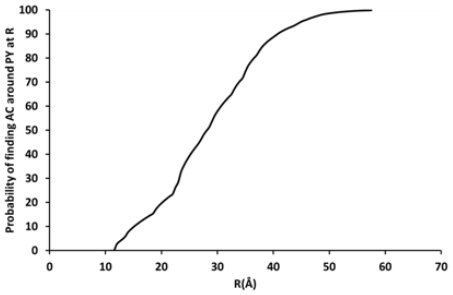

Figure 4.80. Mathematical calculation of the probability of finding an ACH^+ molecule around a given PY molecule in different channels at less than a given (R) distance, performed by Dr. Luis Gómez-Hortigüela at the Catalysis and Petrochemistry Institute (CSIC).

Furthermore, in addition to this hetero-FRET between ACH^+ and PY, an energy migration between ACH^+ monomers (homo-FRET) in neighboring channels must also be taken into account due to the relatively high ACH^+ loading. Besides, orientation factor is more favored ($\kappa^2 = 1$) for parallel transition dipoles. This involves that the excitation energy collected by one ACH^+ molecule can first migrate to other ACH^+ molecules (homo-FRET) until it is transferred to a PY molecule (hetero-FRET).

Indeed, single particle measurements with linearly polarized light demonstrated that the emission of each dye can be separately observed rotating a polarizer placed before detection in the fluorescence microscope (Figure 4.79.C). In this sense, practically pure bands of each dye were recorded at the different polarizations (Figure 4.79.A, blue and green curves): the PY emission is mainly seen in the case of parallel polarization to the channels direction, while the ACH^+ band is mostly detected at perpendicular polarization respect to the channels direction, due to the orientation of their respective transition dipole moments. Registered CIE coordinates of the emission colors (mathematical definition of color spaces by the International Commission on Illumination) indicate also that the emission of the hybrid material in bulk powder corresponds to a combination of the fluorescence of the two chromophores (Figure 4.79.B).

Following with the characterization of the system at single particle level, two color experiments were carried out by means of confocal microscopy, using a dichroic filter to split the emission signal and recording simultaneously the fluorescence of the two dyes in two detectors, with 470/40 (“blue”) and 550/50 (“green”) band pass filters, dedicated to the detection of acridine and pyronin Y, respectively. This way, a fluorescence lifetime of around 24 ns was obtained in the blue detector, while a lifetime of around 8 ns was registered in the green detector. The decrease of the ACH^+ lifetime (with respect to AC/AEL sample, characterized by an average value of 27 ns) should be due to the hetero-FRET process, as a direct consequence of the radiationless energy transfer process from ACH^+ as donor to PY as acceptor. It should be noted that the increase of the lifetime found in the PY detector (respect to PY/AEL sample, τ_{fl} = 4.2 ns) can be a consequence of the difficulty to completely separate the emission signal of PY from that of ACH^+, since the emission band of the later is very broad and could not be perfectly filtered in the green detector. However, the growth (negative contribution) observed in the fluorescence decay curve at the PY detector is again indicative of an excitation via energy transfer process.

Thus, the present hybrid material resulted in a fluorescent system that can display blue or green emission depending on the direction of the polarized light. The fluorescence emission color switching in the AC-PY/AEL hybrid material is an instantaneous and efficient process, completely reversible and reproducible. Moreover, since the switching process does not involve any chemical transformation, the material will present a high fatigue resistance and what is more, although the photoactive units are organic molecules that can suffer degradations with aging, the inorganic nature of the aluminophosphate matrix will protect them from photo-and thermo-degradation. All these properties are fundamental requirements for a practical use in dichroic applications.

- **AC-PY-LDS722/AEL : White Light emission**

In this final section, by the simultaneous encapsulation of several chromophores with fluorescent emission in different regions of the electromagnetic spectrum, an improvement of the light harvesting capacity and also a wider emission range of the material will be attained. In this sense, it would be very interesting to achieve a material with white light emission under UV excitation.

The most common approach to achieve white light emission consists on combining materials with emission in the three fundamental colors (blue, green and red) at the same intensity, and controlling the energy transfer processes between them.[68,69] White light emitters are extremely interesting for lighting systems,[69,70] necessary in any technological device present in everyday life. In this sense, organic compounds are preferred to develop white emitting systems since they allow low-cost fabrication.[68,71] However, the major drawback of purely organic devices is the aging, usually at different rates for each component.[68] In this section, white light hybrid materials are pursued in which organic molecules emitting in the blue, green and red regions of the electromagnetic spectrum are protected from photo and thermo-degradation within the MgAPO-11 inorganic host.

In this context, three dyes previously occluded separately into MgAPO-11 with characteristic blue, green and red emission were chosen: AC, PY and LDS 722, respectively. Acridine dye loaded MgAPO-11 material (AC/AEL) demonstrated a bluish-cyan emission under UV excitation light (λ_{abs}: 414 nm; λ_{fl}: 480nm) with high fluorescence efficiency (ϕ_{fl} = 0.54) and a long fluorescence lifetime of 27 ns. The

green emitting entity, Pyronin Y dye, encapsulated into MgAPO-11 (PY/AEL) revealed an improved green fluorescence with higher quantum yield and longer lifetime (ϕ_{fl} = 0.29, τ_{fl} = 4.2 ns) than PY in diluted aqueous solution (ϕ_{fl} = 0.21, τ_{fl} = 2 ns). Finally, the LDS 722 dye into AEL (LDS 722/AEL) showed a red emitting solid material (λ_{fl} = 670 nm) with a much higher quantum yield (ϕ_{fl} = 0.55) than the dye in solution (ϕ_{fl} ~ 0.01) due to the rigidity imposed by the matrix. Thus, by the optimization of the relative ratio of these dyes, simultaneously encapsulated into AEL channels, a solid state system with efficient white light emission under UV excitation light is expected.

White light emission in this AEL host containing a mixing of dyes must be assisted by a FRET energy transfer process between all the fluorophores. Note here that FRET process between AC and PY into MgAPO-11 has been previously demonstrated in the AC-PY/AEL system, favored by i) the spectral overlap between the emission band of the donor (ACH^+) and the absorption band of the acceptor (PY), ii) the high fluorescence quantum yield of the donor and iii) the high probability to encounter acceptor molecules in neighboring channels. In the present case, PY will be the acceptor in the first step, and then the donor respect to LDS 722. Note here that for this second step the emission band of PY shows also a good overlapping with the ICT absorption band of LDS 722 (final acceptor), being suitable to enable an efficient FRET processes (see Figure 4.20. and Figure 4.71.). Interestingly, LDS 722 dye occluded into AEL shows a very broad absorption region due to the co-existence of two absorption bands, one in the UV region ascribed to the main S_0-S_1 "locally-excited" (LE) transition and the mentioned broad band at higher wavelengths assigned to the intramolecular charge transfer (ICT) state.[57] Thus, in the present system containing the three dyes, the red emitter LDS 722 will be also excited under UV light, although as stated before, it is not the most efficient excitation wavelength for LDS 722 within AEL (see Table 4.15.).[57]

A requirement to obtain the white light emitting material is the optimization of the proportion of dyes occluded into AEL, and consequently the amount and ratio added to the synthesis gel. Note here that the prediction of the incorporation degree of each dye into the inorganic matrix by the crystallization inclusion method it is not an easy task and it is even more difficult when a mixture of dyes is present in the synthesis gel. Apart from the typical parameters such as the solubility, dyes may compete between them and favor/impede the entrance of the others. Therefore, it can be stated that finding the proper proportions of each dye in the synthesis gel is a trial and error

process. As a general approach, materials were prepared as explained in section 3.1.3. in chapter 3, from gels with a general molar composition of: 0.2 MgO: 1 P_2O_5: 0.9 Al_2O_3: 0.75 EBA: *x* dye: 300 H_2O, where *x* = 0.024, which indicates the total amount of the dyes added into the synthesis gel. The proportion of the SDA is lower than in previous samples of AEL to avoid MgAPO-5 phase-impurities triggered by the presence of LDS 722, as explained in section 4.2.3. The *x* is kept constant in the samples, but the relative dye proportions added to the gel are varied. For instance, if a synthesis is denoted with a dye proportion of 3 AC: 1 PY: 1 LDS 722, it means that the molar fraction of ACH^+ in the synthesis gel is three times higher than the molar fraction of PY and LDS 722, being the total molar fraction of dyes into the gel *x* = 0.024.

In this sense, a systematic variation of the relative proportion of the three dyes in the synthesis gel was done. The most representative samples are listed in Table 4.16. The white emission in all samples is confirmed by chromaticity experiments (CIE coordinates in Table 4.16.).

Table 4.16. Relative proportion of the dyes in the synthesis gel with the final amount of dye loaded in the most appropriate samples, expressed as mmol dye per 100 g powder. Fluorescence quantum yield of the powder samples under UV illumination (325-375 nm) and the corresponding CIE coordinates of the overall emission are listed.

Sample	AC:PY:LDS 722	mmol / 100g			ϕ_{fl}	CIE coordinates	
		AC	PY	LDS 722		x	y
AC-PY-LDS722/AEL-1	3:1:1	5.60	0.67	1.07	0.17	0.34	0.34
AC-PY-LDS722/AEL-2	3:2:1	5.18	0.95	1.25	0.03	0.33	0.36
AC-PY-LDS722/AEL-3	3:1:2	6.36	0.60	1.80	0.04	0.35	0.32

The best hybrid material, giving white light emission under UV illumination, was obtained from an initial gel composition of: 0.2 MgO : 0.9 Al_2O3 : 1.0 P_2O_5 : 0.75 EBA : 0.0144 AC : 0.0048 PY : 0.0048 LDS 722 : 300 H_2O; or in other words, with a relative dye ratio in the gel of 3 AC: 1 PY: 1 LDS 722. This sample shows an emission quantum yield of 0.17 (Table 4.16.), and its emission spectrum shows the characteristic bands of each dye, centered in the blue (480 nm), green (540 nm) and red (670 nm) region of the visible spectrum (Figure 4.81.D).

The final amount of dyes loaded in this sample was estimated to be 5.60 mmol ACH^+, 0.67 mmol PY and 1.07 mmol LDS 722 per 100 g sample powder (Table

4.16.), which corresponds to a relative dye proportion of 8.4:1:1.6, respectively. Note here that the incorporation of each dye into the MgAPO-11 structure does not maintain a linear correlation with the initial proportion in the synthesis gel, and the quantification of the uptake of the three dyes was not a trivial task (see more details in chapter 3, section 3.1.4.).

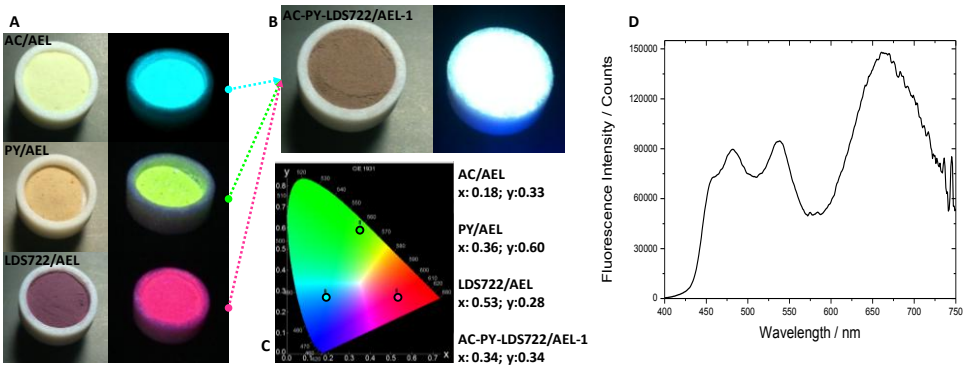

Figure 4.81. Real images of the samples under ambient light and under UV illumination: A) each dye (ACH^+, PY and LDS 722) into MgAPO-11 separately and B) the sample with the optimized mixture of the three dyes (AC-PY-LDS/AEL-1). C) Comission Internationale de l'Eclairage (CIE) coordinates diagram of the fluorescence emission of the four samples under UV light. D) Emission spectra of the sample powder recorded upon UV excitation (325-375 nm).

Note here that white light emission has been measured in bulk powder since, unlike in the previous sample with ACH^+ and PY (AC-PY/AEL), the distribution of the dyes was inhomogeneous. The reason could be the differences in dye-matrix affinity or solubility problems. Through fluorescence microscopy measurements it has been observed that although ACH^+ and PY are located along the whole particle, LDS 722 is mainly distributed at the particle endings (Figure 4.82.).

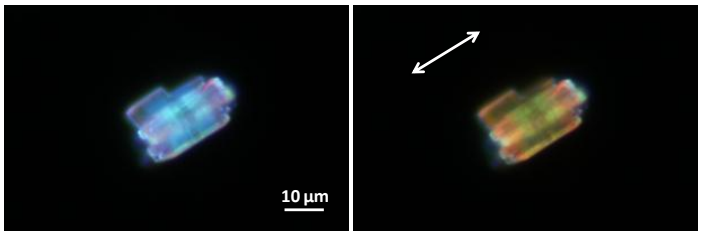

Figure 4.82. Left: Fluorescence image of a AC-PY-LDS722/AEL-1 particle under UV illumination. Right image shows the same particle under UV light but a polarizer was placed before detection in the direction of the white arrow in order to eliminate ACH^+ emission.

It is worth mentioning that, although LDS 722 dye is also directly excited upon UV light by the population of is LE state, the resultant white light emission of the present material is expected to involve FRET among the three dyes. Indeed, the FRET process from ACH^+ to PY into the MgAPO-11 matrix has been already proven.[38] In this context, FRET process is confirmed by the differences found in the fluorescent lifetimes recorded for each dye (λ_{em}: 480 nm, 550 nm and 670 nm for ACH^+, PY and LDS 722, respectively), in the presence of the other two when they are simultaneously occluded, with respect to the lifetimes previously characterized when they are individually encapsulated into the AEL. It is worth noting here that it is not an easy task to discern and assign each lifetime obtained due to the overlap of the emission bands of the dyes, but a general trend was found in the system: i) the fluorescence lifetime of the donor ACH^+ decreases from 27 ns to 20 ns, suggesting the existence of the nonradiative energy transfer process; ii) for PY, which acts here both as acceptor (receiving the energy coming from ACH^+) and as donor (giving energy to the red emitting LDS 722), a lifetime of around 2.7 ns (65 %) is obtained together with a short lifetime of 0.8 ns (35%), denoting an extra quenching of the first excited state that should be a consequence of the energy transfer process to the LDS 722; and iii) although the lifetime derived for LDS 722 in the mixture was the same (τ ~3ns) as in absence of the other dyes, its fluorescence decay curve shows a growth (negative contribution), typical effect for the acceptor entity in a FRET process.

In order to ensure that FRET also takes place from PY to LDS 722, a different sample was prepared keeping constant the initial amount of AC dye added to synthesis gel but changing the amount of PY (sample AC-PY-LDS722/AEL-2 with a proportion of 3 AC: 2 PY: 1 LDS 722 in the synthesis gel, Table 4.16.). The relative increase of the final amount of PY occluded into AEL (with respect to AC-PY-LDS722/AEL-1 sample) could contribute to the increase of the red contribution in the emission spectrum (Figure 4.83.), suggesting a FRET process between PY and LDS 722. As stated before, FRET process is more favored for higher donor-to-acceptor ratios (PY (donor): LDS 722 (acceptor)). Thus, two consecutive FRET processes are expected in this system in which the energy could be transferred from ACH^+ to PY and from PY to LDS 722.

However, this AC-PY-LDS722/AEL-2 sample shows a much lower fluorescence quantum yield with respect to the AC-PY-LDS722/AEL-1 (Table 4.16.). With the aim of studying the effect of the different dye-ratios on the white light emission capacity with respect to the AC-PY-LDS722/AEL-1 sample, a new sample, AC-PY-

LDS722/AEL-3, with higher amount of LDS 722 and keeping constant AC and PY, was synthesized (3 AC: 1 PY: 2 LDS 722 in the synthesis gel). Nevertheless, this later sample shows also a lower fluorescence quantum yield (Table 4.16.). The decrease of the fluorescence quantum yield could be then ascribed to the higher presence of LDS 722 (Table 4.16.). As it has been stated before, LDS 722 can be also excited under UV light, by populating its LE state, but the emission efficiency is much lower in this case than when exciting directly its ICT state (λ_{exc} = 530 nm; see Table 4.15.), and thus, it could contribute to lowering the global fluorescence quantum yield.

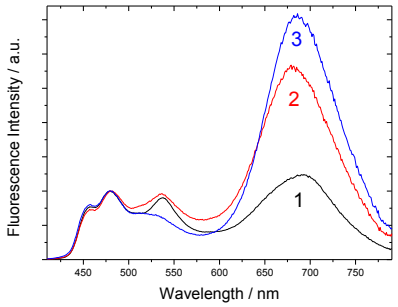

Figure 4.83. Emission spectra normalized at ACH^+ emission intensity of the three samples in bulk powder: AC-PY-LDS722/AEL-1 (black), AC-PY-LDS722/AEL-2 (red) and AC-PY-LDS722/AEL-2 (blue)

The results presented above indicate that it is very difficult to predict the best synthesis conditions in terms of the dye-ratio in the initial gel to achieve a solid state white light emitter material with relatively high fluorescence capacity.

As a brief conclusion, by the combination of suitable dyes with emission properties in the blue, green and red region of the visible spectrum into the one dimensional and narrow pores of AEL framework, a white emitter material is achieved under UV light. The strategic distribution of the dyes in the restricted space of the pores of the aluminophosphate in monomeric units maintains their relatively high fluorescence capacities, and their alignment along the pores enables a FRET energy transfer between them to drive the resulting white fluorescence. Infinite combinations can be tried to achieve the most appropriate mixing in each case, depending on the requirements.

References

(1) Omar, O. H.; la Gatta, S.; Tangorra, R. R.; Milano, F.; Ragni, R.; Operamolla, A.; Argazzi, R.; Chiorboli, C.; Agostiano, A.; Trotta, M.; Farinola, G. M. Synthetic Antenna Functioning As Light Harvester in the Whole Visible Region for Enhanced Hybrid Photosynthetic Reaction Centers. *Bioconjug. Chem.* **2016**, *27*, 1614–1623.

(2) Scholes, G. D.; Fleming, G. R.; Olaya-Castro, A.; Grondelle, R. Van. Lessons from Nature about Solar Light Harvesting. *Nat. Chem.* **2011**, *3*, 763–774.

(3) Hou, Z.; Liu, C.; Feng, G.; Li, Z.; Wang, Y. Near-Infrared Luminescent PMMA Films Containing Yb^{3+}-Complexes: Preparation and Characterization. *Colloid Polym. Sci.* **2016**, *294*, 1495–1501.

(4) Debije, M. G.; Verbunt, P. P. C. Thirty Years of Luminescent Solar Concentrator Research: Solar Energy for the Built Environment. *Adv. Energy Mater.* **2012**, *2*, 12–35.

(5) Cucinotta, F.; Guenet, A.; Bizzarri, C.; Mróz, W.; Botta, C.; Milián-Medina, B.; Gierschner, J.; De Cola, L. Energy Transfer at the Zeolite L Boundaries: Towards Photo- and Electroresponsive Materials. *Chempluschem* **2014**, *79*, 45–57.

(6) Devaux, A.; Calzaferri, G.; Belser, P.; Cao, P.; Brühwiler, D.; Kunzmann, A. Efficient and Robust Host − Guest Antenna Composite for Light Harvesting. *Chem. Mater.* **2014**, *26*, 6878–6885.

(7) Gartzia-Rivero, L.; Bañuelos, J.; López-Arbeloa, I. Excitation Energy Transfer in Artificial Antennas: From Photoactive Materials to Molecular Assemblies. *Int. Rev. Phys. Chem.* **2015**, *34*, 515–556.

(8) Lakowicz, J. R. *Principles of Fluorescence Spectroscopy*, 3rd ed.; Springer: Singapore, **2006**.

(9) Calzaferri, G. Nanochannels: Hosts for the Supramolecular Organization of Molecules and Complexes. *Langmuir* **2012**, *28*, 6216–6231.

(10) Calzaferri, G.; Huber, S.; Maas, H.; Minkowski, C. Host – Guest Antenna Materials Angewandte. *Angew. Chemie - Int. Ed.* **2003**, *42*, 3732–3758.

(11) Martínez-Martínez, V.; García, R.; Gómez-Hortigüela, L.; Pérez-Pariente, J.; López-Arbeloa, I. Modulating Dye Aggregation by Incorporation into 1D-MgAPO Nanochannels. *Chem. - A Eur. J.* **2013**, *19*, 9859–9865.

(12) García, R.; Martínez-Martínez, V.; Gómez-Hortigüela, L.; López Arbeloa, I.; Pérez-Pariente, J. Anisotropic Fluorescence Materials: Effect of the Synthesis Conditions over the Incorporation, Alignment and Aggregation of Pyronine Y within MgAPO-5. *Microporous Mesoporous Mater.* **2013**, *172*, 190–199.

(13) Epelde-Elezcano, N.; Martínez-Martínez, V.; Duque-Redondo, E.; Temiño, I.; Manzano, H.; López-Arbeloa, I. Strategies for Modulating the Luminescence Properties of Pyronin Y Dye-Clay Films: An Experimental and Theoretical Study. *Phys. Chem. Chem. Phys.* **2016**, *18*, 8730–8738.

(14) Meral, K.; Ylmaz, N.; Kaya, M.; Tabak, A.; Onganer, Y. The Molecular Aggregation of Pyronin Y in Natural Bentonite Clay Suspension. *J. Lumin.* **2011**, *131*, 2121–2127.

(15) Grauer, Z.; Grauer, G. L.; Avnir, D.; Yariv, S. Metachromasy in Clay Minerals. *J. Chem. Soc. Faraday Trans* **1987**, *83*, 1685–1701.

(16) Martínez-Martínez, V.; Corcóstegui, C.; Bañuelos Prieto, J.; Gartzia, L.; Salleres, S.; López Arbeloa, I. Distribution and Orientation Study of Dyes Intercalated into Single Sepiolite Fibers. A Confocal Fluorescence Microscopy Approach. *J. Mater. Chem.* **2011**, *21*, 269–276.

(17) Calzaferri, G.; Méallet-Renault, R.; Brühwiler, D.; Pansu, R.; Dolamic, I.; Dienel, T.; Adler, P.; Li, H.; Kunzmann, A. Designing Dye-Nanochannel Antenna Hybrid Materials for Light Harvesting, Transport and Trapping. *ChemPhysChem* **2011**, *12*, 580–594.

(18) Busby, M.; Blum, C.; Tibben, M.; Fibikar, S.; Calzaferri, G.; Subramaniam, V.; De Cola, L. Time, Space, and Spectrally Resolved Studies on J-Aggregate Interactions in Zeolite L Nanochannels. *J. Am. Chem. Soc.* **2008**, *130*, 10970–10976.

(19) McRae, E. G.; Kasha, M. The Molecular Exciton Model. In *Physical Process in Radiation Biology*; Augenstein, L., Mason, R., Rosenberg, B., Eds.; Academy Press: New York, **1964**; pp 23–42.

(20) Kasha, M.; Rawls, H. R.; El-Bayoumi, M. A. The Exciton Model in Molecular Spectroscopy. *Pure Appl. Chem.* **1965**, *11*, 371–392.

(21) Busby, M.; Devaux, A.; Blum, C.; Subramaniam, V.; Calzaferri, G.; De Cola, L. Interactions of Perylene Bisimide in the One-Dimensional Channels of Zeolite L. *J. Phys. Chem. C* **2011**, *115*, 5974–5988.

(22) García, R.; Martínez-Martínez, V.; Sola Llano, R.; López-Arbeloa, I.; Pérez-Pariente, J. One-Dimensional Antenna Systems by Crystallization Inclusion of Dyes (One-Pot Synthesis) within Zeolitic MgAPO-36 Nanochannels. *J. Phys. Chem. C* **2013**, *117*, 24063–24070.

(23) Ryan, E. T.; Xiang, T.; Johnston, K. P.; Fox, M. A. Absorption and Fluorescence Studies of Acridine in Subcritical and Supercritical Water. *J. Phys. Chem. A* **1997**, *101*, 1827–1835.

(24) Pereira, R. V.; Gehlen, M. H. Fluorescence of Acridinic Dyes in Anionic Surfactant Solution. *Spectrochim. Acta - Part A Mol. Biomol. Spectrosc.* **2005**,

61, 2926–2932.

(25) Gartzia-Rivero, L.; Bañuelos-Prieto, J.; Martínez-Martínez, V.; López-Arbeloa, I. Versatile Photoactive Materials Based on Zeolite L Doped with Laser Dyes. *Chempluschem* **2012**, *77*, 61-70.

(26) Rusanov, A. L.; Ivashina, T. V.; Vinokurov, L. M.; Fiks, I. I.; Orlova, A. G.; Turchin, I. V.; Meerovich, I. G.; Zherdeva, V. V.; Savitsky, A. P. Lifetime Imaging of FRET between Red Fluorescent Proteins. *J. Biophotonics* **2010**, *3*, 774–783.

(27) Minkowski, C.; Calzaferri, G. Förster-Type Energy Transfer along a Specified Axis. *Angew. Chemie - Int. Ed.* **2005**, *44*, 5325–5329.

(28) Gfeller, N.; Calzaferri, G. Energy Migration in Dye-Loaded Hexagonal Microporous Crystals. *J. Phys. Chem. B* **1997**, *5647*, 1396–1408.

(29) Martínez Martínez, V.; López Arbeloa, F.; Bañuelos Prieto, J.; López Arbeloa, I. Orientation of Adsorbed Dyes in the Interlayer Space of Clays. 1. Anisotropy of Rhodamine 6G in Laponite Films by Vis-Absorption with Polarized Light. *Chem. Mater.* **2005**, *17*, 4134–4141.

(30) Mishra, A.; Behera, R. K.; Behera, P. K.; Mishra, B. K.; Behera, G. B. Cyanines during the 1990s: A Review. *Chem. Rev.* **2000**, *100*, 1973–2011.

(31) Wang, L.; Xiang, J.; Sun, H.; Yang, Q.; Yu, L.; Li, Q.; Guan, A.; Tang, Y. Controllable cy3-MTC-Dye Aggregates and Its Applications Served as a Chemosensor. *Dye. Pigment.* **2015**, *122*, 382–388.

(32) Sato, N.; Fujimura, T.; Shimada, T.; Tani, T.; Tagaki, S. J-Aggregate Formation Behavior of a Cationic Cyanine Dye on Organic Layered Material. *Tetrahedron Lett.* **2015**, *56*, 2902–2905.

(33) Steiger, R.; Pugin, R.; Heier, J. J-Aggregation of Cyanine Dyes by Self-Assembly. *Colloids Surfaces B Biointerfaces* **2009**, *74*, 484–491.

(34) Yao, H. Mesoscopic Morphology, Optical Anisotropy and Spectroscopic Properties of Cyanine J-Aggregates. In *J-Aggregates*; Kobayashi, T., Ed.; World Scientific: Singapore, **2012**; pp 403–441.

(35) Scherer, P. O. J.; Fischer, S. F. On the Theory of Vibronic Structure of Linear Aggregates. Application to Pseudoisocyanin (PIC). *Chem. Phys.* **1984**, *86*, 269–283.

(36) Daltrozzo, E.; Scheibe, G.; Gschwind, K.; Haimerl, F. Structure of the J-Aggregates of Pseudoisocyanine. *Photogr. Sci. Eng.* **1974**, *18*, 441–450.

(37) Von Berlepsch, H.; Böttcher, C.; Dähne, L. Structure of J-Aggregates of Pseudoisocyanine Dye in Aqueous Solution. *J. Phys. Chem. B* **2000**, *104*, 8792–8799.

(38) Martínez-Martínez, V.; García, R.; Gómez-Hortigüela, L.; Sola Llano, R.; Pérez-Pariente, J.; López-Arbeloa, I. Highly Luminescent and Optically Switchable Hybrid Material by One-Pot Encapsulation of Dyes into MgAPO-11 Unidirectional Nanopores. *ACS Photonics* **2014**, *1*, 205–211.

(39) Schulman, S. G.; Naik, D. V.; Capomacchia, A. C.; Roy, T. Electronic Spectra and Electronic Structures of Some Antimicrobials Derived from Proflavine. *J. Pharm. Sci.* **1975**, *64*, 982–986.

(40) Kellmann, A.; Lion, Y. Acid-Base Equilibria of the Excited Singlet and Triplet States and the Semi-Reduced Form of Acridine Orange. *Photochem. Photobiol.* **1979**, *29*, 217–222.

(41) Drexhage, K. H. Structure and Properties of Laser Dyes. In *Dye Lasers*; Schäfer, F. P., Ed.; Berlin, **1989**; pp 155–185.

(42) Lopez Arbeloa, F.; Lopez Arbeloa, T.; Tapia Estévez, M. J.; Lopez Arbeloa, I. Photophysics of Rhodamines. Molecular Structure and Solvent Effects. *J. Phys. Chem.* **1991**, *95*, 2203–2208.

(43) Harris, D. C.; Bertolucci, M. D. *Symmetry and Spectroscopy: An Introduction to Vibrational and Electronic Spectroscopy*; Oxford University Press, Inc.: New York, **1978**.

(44) Cotton, F. A. *Chemical Applications of Group Theory*, 3rd ed.; Wiley, **1990**.

(45) Hartmann, M.; Elangovan, S. P. Isomerization and Hydrocracking of N-Decane over Magnesium-Containing Molecular Sieves with AEL, AFI, and AFO Topology. *Chem. Eng. Technol.* **2003**, *26*, 1232–1235.

(46) Zhai, J. P.; Li, Z. M.; Li, I. L.; Liu, H. J.; Sheng, P.; Tang, Z. K. Catalyst Effect of Metal Cations on Pyrolysis of Hydrocarbon Molecules and Formation of Carbon Nanotubes in the Channels of $AlPO_4$-5 Crystals. *J. Porous Mater.* **2006**, *13*, 291–295.

(47) El-Sayed, M. A. Spin-Orbit Coupling and the Radiationless Processes in Nitrogen Heterocyclics. *J. Chem. Phys.* **1963**, *38*, 2834–2838.

(48) Steele, R. H.; Szent-Gyorgyi, A. Excitation of Biological Substances. *Proc. Natl. Acad. Sci. United States Am.* **1957**, *43*, 477–491.

(49) Parker, C. A.; Joyce, T. A. Prompt and Delayed Fluorescence of Some DNA Adsorbates. *Photochem. Photobiol.* **1973**, *18*, 467–474.

(50) Berberan-Santos, M. N.; Garcia, J. M. M. Unusually Strong Delayed Fluorescence of C_{70}. *J. Am. Chem. Soc.* **1996**, *118*, 9391–9394.

(51) Sun, C.; Yang, J.; Li, L.; Wu, X.; Liu, Y.; Liu, S. Advances in the Study of Luminescence Probes for Proteins. *J. Chromatogr. B* **2004**, *803*, 173–190.

(52) Gilani, A. G.; Shokri, S. Spectral and Aggregative Properties of Two Oxazine Dyes in Aqueous Solutions Containing Structure-Breaking and Multifunctional Additives. *J. Mol. Liq.* **2014**, *193*, 194–203.

(53) Fleming, S.; Mills, A.; Tuttle, T. Predicting the UV-Vis Spectra of Oxazine Dyes. *Beilstein J. Org. Chem.* **2011**, *7*, 432–441.

(54) Lacombe, S.; Pigot, T. Materials for Selective Photo-Oxygenation *vs*. Photocatalysis: Preparation, Properties and Applications in Environmental and Health Fields. *Catal. Sci. Technol.* **2016**, *6*, 1571–1592.

(55) Lewis, G. N.; Bigeleisen, J. Methylene Blue and Other Indicators in General Acids. The Acidity Function. *J. Am. Chem. Soc.* **1943**, *65*, 1144–1150.

(56) Cenens, J.; Schoonheydt, R. A. Visible Spectroscopy of Methylene Blue on Hectorite, Laponite B, and Barasym in Aqueous Suspension. *Clays Clay Miner.* **1988**, *36*, 214–224.

(57) Sola-Llano, R.; Martínez-Martínez, V.; Fujita, Y.; Gómez-Hortigüela, L.; Alfayate, A.; Uji-i, H.; Fron, E.; Pérez-Pariente, J.; López-Arbeloa, I. Formation of a Nonlinear Optical Host-Guest Hybrid Material by Tight Confinement of LDS 722 into Aluminophosphate 1D Nanochannels. *Chem. - A Eur. J.* **2016**, *22*, 15700–15711.

(58) Reck, G.; Marlow, F.; Kornatowski, J.; Hill, W.; Caro, J. Structure of Dipole Chains in an MFI Type Molecular Sieve. *J. Phys. Chem.* **1996**.

(59) Takenawa, R.; Komori, Y.; Hayashi, S.; Kawamata, J.; Kuroda, K. Intercalation of Nitroanilines into Kaolinite and Second Harmonic Generation. *Chem. Mater.* **2001**, *13*, 3741–3746.

(60) Valeur, B. *Molecular Fluorescence: Principles and Applications*; Wiley-VCH Verlag GmbH: Weinheim, **2001**.

(61) Kanis, D. R.; Ratner, M. A.; Marks, T. J. Design and Construction of Molecular Assemblies with Large Second-Order Optical Nonlinearities. Quantum Chemical Aspects. *Chem. Rev.* **1994**, *94*, 195–242.

(62) Csók, Z.; Szuroczki, P.; Kollár, L.; Ngo, H. M.; Ledoux-Rak, I.; Caturello, N. A. M. S.; Albuquerque, R. Q. Intramolecular Cooperative Effects in Multichromophoric Cavitands Exhibiting Nonlinear Optical Properties. *J. Phys. Chem. C* **2015**, *119*, 12608–12615.

(63) Strehmel, B.; Seifert, H.; Rettig, W. Photophysical Properties of Fluorescence Probes. 2. A Model of Multiple Fluorescence for Stilbazolium Dyes Studied by Global Analysis and Quantum Chemical Calculations. *J. Phys. Chem. B* **1997**, *101*, 2232–2243.

(64) Huang, Y.; Cheng, T.; Li, F.; Huang, C. H.; Wang, S.; Huang, W.; Gong, Q.

Photophysical Studies on the Mono- and Dichromophoric Hemicyanine Dyes III. Ultrafast Fluorescence up-Conversion in Methanol: Twisting Intramolecular Charge Transfer and "Two-State Three-Mode" model. *J. Phys. Chem. B* **2002**, *106*, 10041–10050.

(65) Abraham, E.; Grauby-Heywang, C.; Selector, S.; Jonusauskas, G. Characterization of Hemicyanine Langmuir-Blodgett Films by Picosecond Time-Resolved Fluorescence. *J. Photochem. Photobiol. B.* **2008**, *93*, 44–52.

(66) Mishra, A.; Sahu, S.; Tripathi, S.; Krishnamoorthy, G. Photoinduced Intramolecular Charge Transfer in Trans-2-[4'-(N,N-Dimethylamino)styryl]imidazo- [4,5-b]pyridine: Effect of Introducing a C=C Double Bond. *Photochem. Photobiol. Sci.* **2014**, *137*, 9–14.

(67) Zhu, R.; Kumar, A.; Yang, Y. Polarizing Organic Photovoltaics. *Adv. Mater.* **2011**, *23*, 4193–4198.

(68) Li, Y.; Rizzo, A.; Cingolani, R.; Gigli, G. Bright White-Light-Emitting Device from Ternary Nanocrystal Composites. *Adv. Mater.* **2006**, *18*, 2545–2548.

(69) Vohra, V.; Calzaferri, G.; Destri, S.; Pasini, M.; Porzio, W.; Botta, C. Toward White Light Emission through Efficient Two-Step Energy Transfer in Hybrid Nanofibers. *ACS Nano* **2010**, *4*, 1409–1416.

(70) Guo, X.; Qin, C.; Cheng, Y.; Xie, Z.; Ceng, Y.; Jing, X.; Wang, F.; Wang, L. White Electroluminescence from a Phosphonate-Functionalized Single-Polymer System with Electron-Trapping Effect. *Adv. Mater.* **2009**, *21*, 3682–3688.

(71) Li, G.; Shinar, J. Combinatorial Fabrication and Studies of Bright White Organic Light-Emitting Devices Based on Emission from Rubrene-Doped 4,4′-bis(2,2′-Diphenylvinyl)-1,1′-Biphenyl. *Appl. Phys. Lett.* **2003**, *83*, 5359–5361.

5

LUMINESCENT MOF BY HOST-GUEST INTERACTIONS

5

LUMINESCENT MOF BY HOST-GUEST INTERACTIONS

In this chapter luminescent properties of other type of hybrid materials known as Metal Organic Frameworks (MOF), or Porous Coordination Polymers (PCP) are studied. More details about this type of materials are given in chapter 2 (section 2.2.2.). Particularly, in this work a MOF with an entangled porous structure was employed, so-called $[Zn_2(bdc)_2(dpNDI)]_n$, where bdc and dpNDI correspond to 1,4-benzenedicarboxylate and N,N'-di(4-pyridyl)-1,4,5,8-naphtalenediimide, respectively. Note here that the synthesis of the MOF hybrid material was carried out at the Institute for Integrated Cell-Material Sciences, Kyoto University, Japan, at the research group of Dr. Furukawa and Prof. Kitagawa. Here, luminescence properties arise from the host-guest interaction consequence of the incorporation of small aromatic molecules into the organic-inorganic MOF framework that acts as host. Following the last topic in the previous chapter, a white light emitting hybrid system under UV light is described by embedding different aromatic guests into the pores of this MOF, in an appropriate proportion. Moreover, efficient room temperature phosphorescence was activated by the confinement of small halogenated guest molecules into this particular $[Zn_2(bdc)_2(dpNDI)]_n$ MOF.

5.1.- Overview of preceding works with $[Zn_2(bdc)_2(dpNDI)]_n$[1,2]

Firstly, previous works carried out in our group in collaboration with the Institute for Integrated Cell-Material Sciences of Japan are presented with the aim of establishing the preceding grounds to the research presented in this chapter.

The synthesis of this $[Zn_2(bdc)_2(dpNDI)]_n$ MOF led to the intergrowth of two frameworks, one framework into the other, obtaining as a result an entangled structure formed by two chemically non-interconnected frameworks (Figure 5.1.A). Particularly, the metal-organic framework shows a twofold interpenetration with a dimetal junction that is linked by four layers of benzenedicarboxylate units (bdc) and

two pillar anime linkers (dpNDI), forming a 3D-framework with a primitive cubic topology followed by catenation of the two frameworks. Taking advantage of the structure of the framework, its applicability as chemosensor was proven.[1]

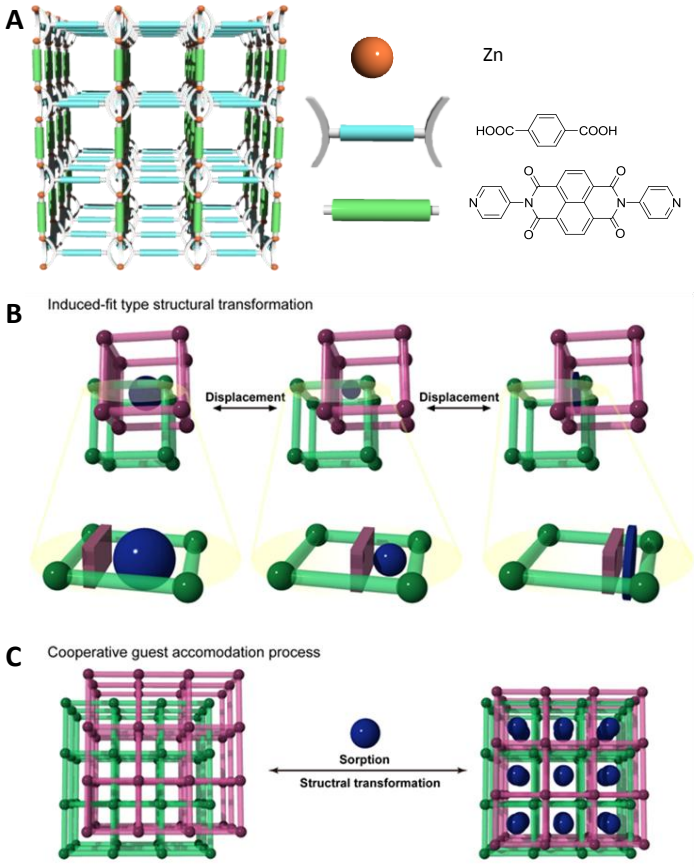

Figure 5.1. A) Illustrative representation of one of the two identical frameworks that compose the $[Zn_2(bdc)_2(dpNDI)]_n$ MOF; B) structural dynamics of a MOF on the accommodation of guest molecules; and C) the crystallinity of an entangled framework demonstrates a cooperative structural transition in response to guest accommodation in its crystal domain.

The entanglement of frameworks provides flexibility on changing the pore size and shape in response to the structure of a target guest molecule. This feature allows structural transformations as a consequence of the inclusion of specific guests, with the aim of maximizing host-guest interactions (Figure 5.1.B). In this specific case, the entangled MOF based on NDI as organic pillar has demonstrated dynamic structural transformation when small aromatic compounds with different substituents are accommodated in its pores. Particularly, those guest molecules were benzonitrile,

benzene, toluene, xylene, anisole and iodobenzene (Figure 5.2.), considered volatile organic compounds (VOC), which are pollutants.

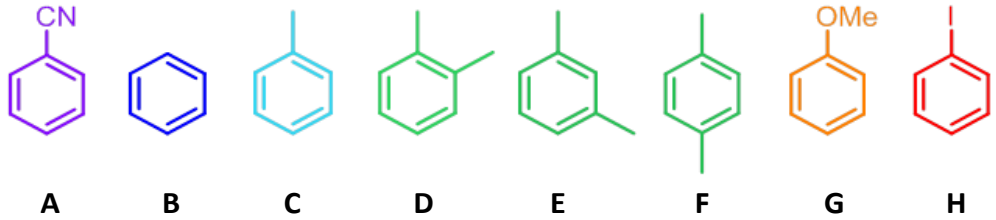

Figure 5.2. $[Zn_2(bdc)_2(dpNDI)]_n$ recognizable VOC molecules: benzonitrile, benzene, toluene, xylene, anisole and iodobenzene, represented in an approximate color to that of the emission resultant from the MOF-VOC interaction.

From the interaction between the guest molecules and the framework interesting photoluminescence properties in the visible region were observed. Indeed, the incorporation of each compound into the MOF is clearly recognizable even by the naked eye since intense emission is observed under UV illumination, and the resulting color is dependent on the chemical substituent of the aromatic guest. Thus, the final system renders different luminescence colors from blue to cyan, green, yellow or red as a consequence of the specific interaction with each guest (Table 5.1., Figure 5.3.). This represents an amazing finding since this host not only detects a single target molecule from among several molecules, but it can interact with diverse embedded aromatic VOCs and decode them with a different readout.

Table 5.1. Ionization potential of the VOCs[1] and luminescence wavelength, quantum yield and average lifetime of the different MOF⊃VOC.

	A	**B**	**C**	**D**	**E**	**F**	**G**	**H**
IP / eV	10.09	9.56	9.18	9.04	9.05	8.99	8.83	8.73
λ_{fl} / nm	421	439	476	496	503	518	592	640
ϕ_{fl}	<0.01	0.05	0.22	0.05	0.09	0.19	0.01	0.03
τ_{fl}	0.3 ns	5.0 ns	14.8 ns	12.1 ns	18.2 ns	22.9 ns	5.6 ns	139 µs

The key factor for the decoding is the incorporation of NDI as the scaffold of the porous MOF. NDI is a photoactive molecule[3] that specifically interacts with aromatic VOCs forming different charge transfer (CT) complexes. Indeed, NDI is characterized by a high electron acceptor capability,[4–6] and it has shown red-shifted emission bands in aromatic hydrocarbon solvents ascribed to the formation of CT complexes.[7] However, the fluorescence efficiency of these bands in solution was really poor ($\phi_{fl} \leq 0.02$).

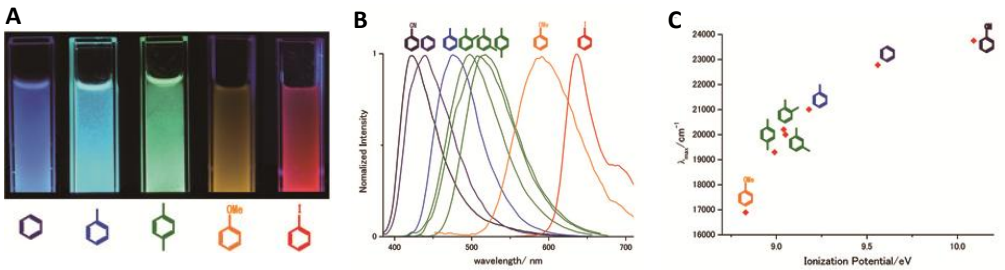

Figure 5.3. A) Luminescence of MOF powder suspended in each VOC liquid after excitation at 365 nm using a commercial UV lamp. B) Height-normalized luminescent spectra of each system after excitation at 370 nm. C) Relationship of the emission energy of MOF⊃VOCs to the ionization potential of each guest.

As mentioned before, in the present case host-guest interactions are optimized by structural dynamics in response to guest accommodation. As a result, VOC guest molecules are tightly confined into the MOF interacting face-to-face with the NDI of the scaffold. Thus, CT interaction between the donor species (organic guests) and the acceptor species (NDI ligand as MOF scaffold, decoding unit) are maximized. In this sense, the higher the ionization potential of the aromatic guest species, the larger the bathochromic shift of the obtained emission band (Figure 5.3.), with quantum yields up to ten times higher than that of the mixture of the NDI derivatives and the aromatic compounds in solution.[7] Note here that besides the fluorescent decoding based on CT complexation, the benzene derivative substituted by a heavy atom (iodine) led to a different type of emission mechanism. This MOF with iodo-benzene as guest (sample H) showed a characteristic red phosphorescence emission at 640 nm (Table 5.1.) with a lifetime higher than 100 μs after excitation at 370 nm (Table 5.1., more details will be given in section 5.3.).

5.2.- White Light emission in $[Zn_2(bdc)_2(dpNDI)]_n$ MOF

In the previous chapter concerning fluorescent dyes into the MgAPO-11 inorganic matrix, white light emission was achieved by the simultaneous encapsulation of three dyes emitting in the blue, green and red region of the electromagnetic spectrum respectively, in an appropriate dye proportion. As described previously, the $[Zn_2(bdc)_2(dpNDI)]_n$ MOF shows VOC guest-dependent emission bands in the whole visible region.[1,2] Therefore, following the same strategy, white light emission is pursued by embedding different small organic molecules into the pores of the MOF

framework. Thus, with an adequate mixing of three different small aromatic molecules, white light emission is envisaged not only in $[Zn_2(bdc)_2(dpNDI)]_n$ powder but also in big single crystals.

To trigger different fluorescence colors in the $[Zn_2(bdc)_2(dpNDI)]_n$ framework, the following species have been employed as potential guests: ethyl benzoate, acetophenone, toluene, ortho-xylene, meta-xylene, para-xylene, anisole and iodobenzene. First, the CIE coordinates were deducted for each MOF-guest complex (Figure 5.4.). Different candidates were chosen then in order to prepare proper mixtures to obtain white light emission, such as toluene/anisole/iodobenzene, which triggers cyan/yellow/red, respectively; and ethyl benzoate/*para*-xylene/iodobenzene or acetophenone/*para*-xylene/iodobenzene for activating blue/green/red emission. Note here that iodobenzene was elected for the three cases since it is the only compound that can bring the pure red component.

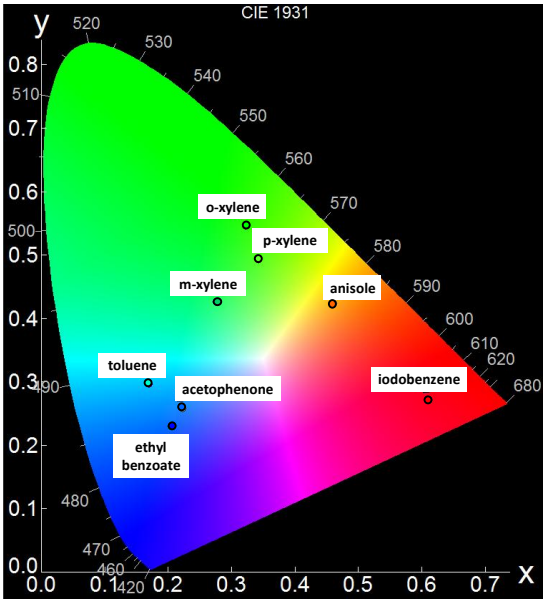

Figure 5.4. CIE coordinates for the MOF⊃VOC prepared containing only one molecule-type embedded.

Interestingly, white light emission was achieved in both MOF powder and single crystals with the three different VOC combinations. For example, with the first combination (toluene/anisole/iodobenzene), the optimum VOC proportion to obtain white light emission was 3.5:2:1 for both powder and single crystals, with CIE coordinates of 0.35,0.34 (x,y) (Figure 5.5.).

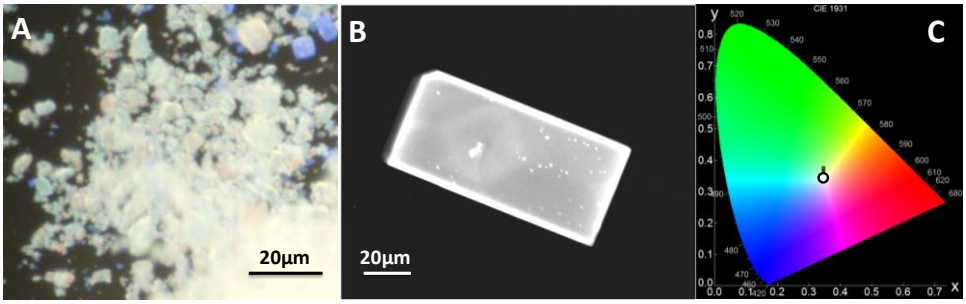

Figure 5.5. Fluorescence images of A) powder and B) single crystal of MOF⊃toluene/anisole/iodobenzene in 3.5:2:1 proportion under UV excitation light (325-375 nm band pass filter). C) CIE diagram for the single crystal shown in B.

In the case of ethyl benzoate/*para*-xylene/iodobenzene mixture, the proportion of the different guests for white light emission in powder or in single crystal slightly differs. In the first case, white emission was achieved with a solvent proportion of 5:1:2.6, obtaining CIE coordinates of 0.34,0.33 (x,y); while in the case of single crystals a proportion of 5:2.5:2.5 was needed for CIE coordinates of 0.33,0.35 (x,y). This fact could be attributed to a more impeded diffusion along the pores of the larger *p*-xylene (with two substituent groups, Figure 5.2.F) with respect to the other guests in big crystals.

However, in the acetophenone/*para*-xylene/iodobenzene combination, the proportions minimally vary for powder or single crystal samples, being the most appropriate 4.5:1:2.6 for powder and 4.5:1:3 for single crystal, giving CIE coordinates of 0.32,0.33 (x,y) in both cases.

Thus, it has been proven that independently of the MOF morphology, white light emission can be achieved by embedding three VOC species into the $[Zn_2(bdc)_2(dpNDI)]_n$. The emission spectra recorded in all cases under UV illumination show that the luminescence of the samples covers the whole visible spectrum (data not shown), with similar intensities in the whole range. All the cases mentioned above showed a fluorescence quantum yield of around ϕ_{fl}: 0.06-0.08. Hence, different guest mixtures can be appropriate to this aim, and many others can also lead to white light emission. However, here only the mixtures that led to the highest emission efficiency have been presented.

Focusing only on the study of single crystals, it should be mentioned that very big crystals are composed of smaller domains. As a consequence, the guest-incorporation in the first step after immersion in the solvent is not progressive from the outside surface of the whole crystal towards the centre, since the diffusion of the aromatic guests is more favored through the boundaries of the domains. Indeed, by means of fluorescence microscopy, much differentiated emission domains across the crystal surface are visualized at short times after the solvent diffusion towards the MOF void spaces starts (Figure 5.6.).

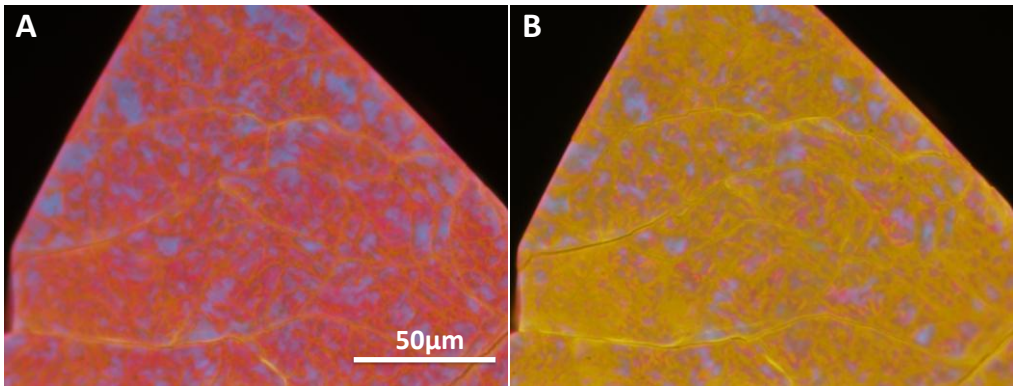

Figure 5.6. Fluorescence image of a MOF immersed in toluene and iodobenzene, A) just after the addition of anisole, and B) 10 minutes later.

As an example, a big particle is shown in Figure 5.6., previously immersed in toluene, and to which iodobenzene was added afterwards. The emission image was collected after adding anisole dropwise. Figure 5.6.A shows the MOF just after the addition of anisole, and Figure 5.6.B the same particle 10 minutes later. In the left image (A) the borders of the domains can be seen colored in yellow. Then, as the anisole diffuses all over the particle, the yellow fluorescence spreads (Figure 5.6.B).

Therefore, in order to obtain white light emission in big crystals, as shown in Figure 5.5., the best strategy is to immerse the MOF crystals into the desired VOC mixture for several hours. This way a homogeneous guest distribution is obtained. Note that if the dropwise adding approach is followed, as for collecting the microscope images in Figure 5.6., another problem that arises is the different volatilization rate of the guests, and thus, it is more difficult to achieve an homogeneously distributed white emission.

Moreover, those domains show complementary response to the linearly polarized light from one another. This fact was analyzed by means of confocal microscopy,

through polarization experiments. Single particles were measured with toluene as guest, since the resultant system demonstrated the highest fluorescence quantum yield (Table 5.1.), and therefore it will show the highest signal-to-noise ratio. Exciting MOF particles with a 410 nm laser, it was proven that specific domains respond in an opposing way to the linearly polarized light, as can be clearly seen in Figure 5.7. Discrete areas (> 1 µm) switch on or off by changing the direction of light-polarization, clearly indicating the existence of microscopic twinned crystals as the crystallographic analysis has also demonstrated.[1] Indeed, by polarized fluorescence microscopy it is easy to recognize the distribution, size and shape of the different twin domains. The detection of those twins by means of fluorescence microscopy with linearly polarized light will help the structural determination since microscopic twinning cannot be detected without prior suspicion.

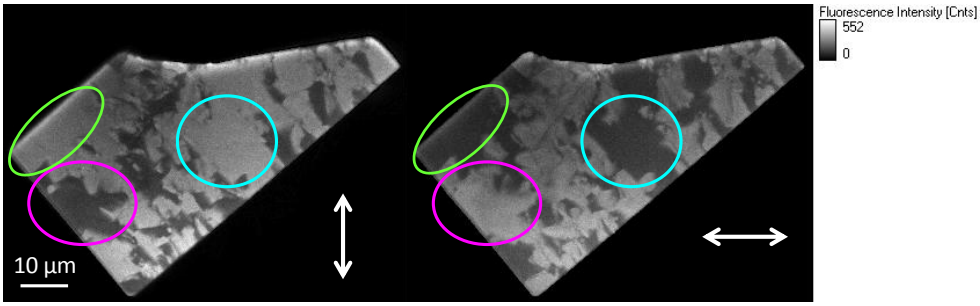

Figure 5.7. Polarization images of a MOF⊃toluene single crystal under 410 nm excitation. White arrows indicate the direction of the polarizers.

To briefly summarize, $[Zn_2(bdc)_2(dpNDI)]_n$ hybrid structure represents an easy and straightforward method to obtain different emission colors in the whole visible spectrum under UV excitation light. Therefore, by embedding diverse small aromatic guest molecules, the whole visible spectral range can be covered. Furthermore, through the proper combination of different guests and simply by immersing the MOF powder or crystals into the mixture of compounds, white light emission can be attained.

5.3.- Phosphorescence MOF at room temperature in $[Zn_2(bdc)_2(dpNDI)]_n$[8]

It have been demonstrated that taking advantage of the interaction between dpNDI ligands as part of the MOF framework and small aromatic guest molecules occluded into its pores interesting photophysical features can be triggered, such as fluorescence emission or its color tunning. In this sense, phosphorescence can be also activated. Phosphorescence is characterized by much longer lifetimes than the fluorescence since it occurs from the long-live triplet state, and it usually requires low temperatures (*i.e.* 77 K) in order to avoid diffusional bimolecular deactivation and minimize molecular motions (more details regarding phosphorescence are given in section 2.1.1.2. in chapter 2). In this context, several approaches have been widely exploited in order to induce phosphorescence in different organic chromophores, such as either incorporating heavy atoms to the molecular structure or placing them very close to the phosphor, to promote the population of the triplet state (ISC) through spin-forbidden transition enhancers.[9–11] Note here that in the previous works presented in section 5.1., when iodobenzene was occluded into the pores of $[Zn_2(bdc)_2(dpNDI)]_n$ MOF, lifetimes in the microsecond range were recorded (Table 5.1.).[1] Thus, the phosphorescence emission in this hybrid system is a consequence of the heavy atom effect of the iodine of the guest molecule, placed very close to the dpNDI moiety of the MOF scaffold.

In this work, different small halide derivatives are embedded in the pores of this MOF in order to achieve room temperature phosphorescence emission, and to deeply study the phosphorescence process. Certainly, NDI itself is an appropriate photoactive scaffold because it undergoes a very fast ISC from the excited π-π^* singlet state to the close lying n-π^* triplet state, responsible for the short fluorescence lifetime of the NDI in solution.[12] On the other hand, this is not the first time that phosphorescence was recorded for NDI-halogenated complexes in solution, but unlike in the present MOF system,[1] cryogenic temperatures were needed.[13]

Firstly, following with the family of compounds employed in previous works,[1,2] different phenyl halides were embedded into the MOF, particularly chlorobenzene, bromobenzene, and the previously cited iodobenzene (Figure 5.8. left).

These aromatic halides are expected to bring about charge-transfer complexation with the NDI ligand, due to their intrinsic electron-donating properties (see the IP values in Table 5.2.), promoting, as described in section 5.1., strong host-guest interaction. Indeed, the MOF undergoes the same structural transformation described

in toluene after the inclusion into the hybrid framework, confirmed by powder XRD (Figure 5.8.right). Thus, due to the formation of CT complexes between the halogenated guests (donor) and the dpNDI of the MOF (acceptor), disposed in a very close arrangement, the population of the triplet state of the dpNDI will be enhanced.[1,2]

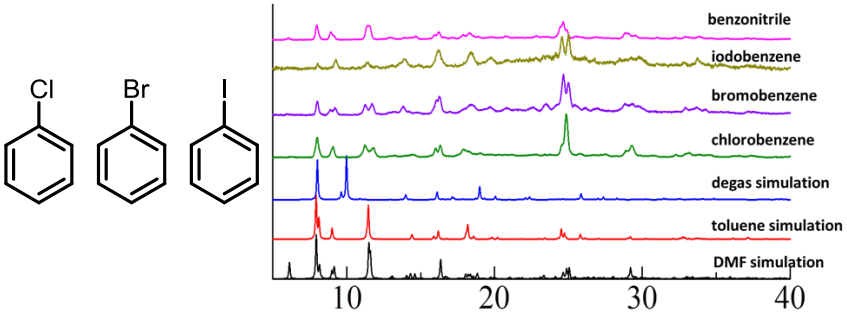

Figure 5.8. Left: Aromatic halides embedded into the $[Zn_2(bdc)_2(dpNDI)]_n$. From the left to the right: chlorobenzene, bromobenzene, and iodobenzene. Right: Powder XRD patterns for different MOF⊃guest systems.

Table 5.2. Ionization potential (IP) of aromatic guests, and fluorescence emission maxima (λ_{fl}), main fluorescence lifetime (τ_{fl}), phosphorescence emission maxima (λ_{ph}) and emission quantum yield (ϕ) recorded in the whole visible range (400-750 nm) of the MOF with the different guests.

Guest	IP / eV	λ_{fl} / nm	τ_{fl} / ns	λ_{ph} / nm	ϕ
Toluene	9.18	476	14.8	-	0.22
Cl-benzene	8.35	452	2.5	-	~0.01
Br-benzene	8.98	455	2.4	628	~0.01
I-benzene	8.73	-	-	637	0.03

In comparison with the inclusion of non-halogenated aromatic guests (*i.e.* toluene), the occlusion of aryl halide guests leads to a marked quenching of the fluorescence emission (*i.e.* with Cl-benzene, ϕ_{fl} = 0.01), together with a sharp decrease in fluorescence lifetimes (Table 5.2.). However, the system shows an interesting switch from fluorescence to phosphorescence emission at room temperature as the size of the halogen atom increases (Cl < Br < I ; Figure 5.9.A). Thus, the fluorescence band, placed at 455 nm and, as previously described, attributed to a NDI–guest CT complex, decreases as a new red-shifted phosphorescence band at around 630 nm appears. Note here that the assignation of the red-shifted band to phosphorescence emission is supported by the respective lifetime values that will be described later in detail.

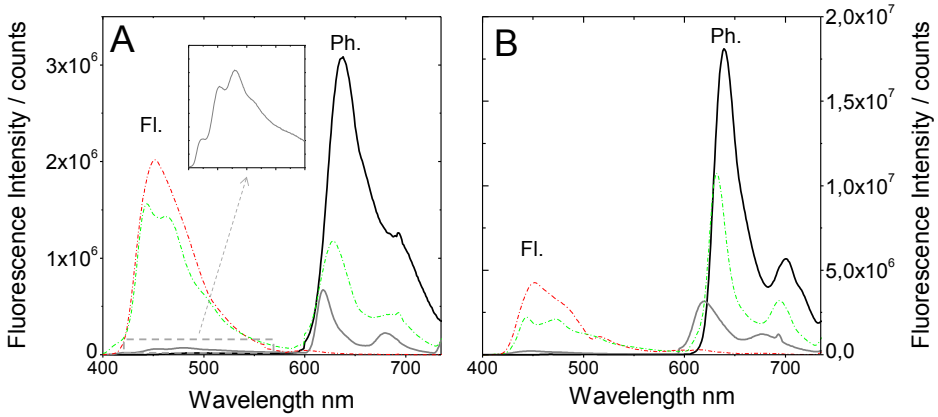

Figure 5.9. Steady-state emission spectra of the MOF with different halogenated guests, collected under λ_{exc} = 380 nm excitation: iodobenzene (solid-black), iodoethane (gray), bromobenzene (dash-green) and chlorobenzene (dash-dot red) at 298 K (A) and 77K (B).

In order to study the effect of CT complexation between halogenated aromatic guests (donor: D) and NDI (acceptor: A) on the phosphorescence process, the nonaromatic guest iodoethane was also incorporated into the pores as reference.

Thermogravimetric analysis (TGA) shows that two molecules are incorporated in each $[Zn_2(bdc)_2(dpNDI)]_n$ unit cell for both iodobenzene and iodoethane guests (Figure 5.10.).

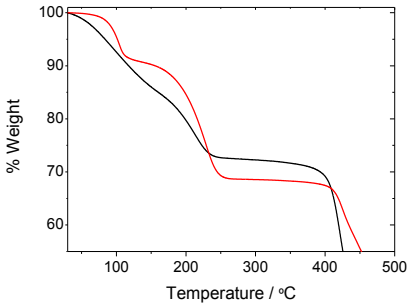

Figure 5.10. TG analysis showing the weight loss in the MOF with iodobenzene (red) and with iodoethane (black) guests. The observed weight losses in the red curve (31 wt %) and in the black TG curve (27 wt %) correspond to the weight of 2 molecules of iodobenzene and 2 molecules of iodoethane per unit cell, respectively.

The luminescence spectra, measured from suspensions with the same powder amount, indicates that although phosphorescence was also detected at room temperature for PCP incorporating iodoethane, its intensity was around six times

weaker than that registered with the homologous aromatic guest, iodobenzene (Figure 5.9.). Indeed, even the system containing Br-benzene, with a lighter halogen, gives twice the phosphorescence signal comparing to iodoethane (Figure 5.9.). In view of these results, it is concluded that the population of the triplet state of the dpNDI ligand is more favored in the case of the aromatic halide guests attributed to a more effective interaction with dpNDI and thus, the spin-orbit coupling is more efficient in the later case in comparison with nonaromatic halide guests such as iodoethane. Note here that the weak emission band detected at the blue region of the electromagnetic spectrum in the MOF⊃I-ethane system cannot be attributed to the emission of a CT complex, as previously deducted for other aromatic guest molecules (section 5.1.), since CT transitions are characterized by broad, structureless bands. Thus, as shown in Figure 5.9.A, the band recorded for the MOF⊃I-ethane, with a clear vibronic structure, should be ascribed to the fluorescence of the dpNDI ligand itself, similar to the bands obtained for analogous naphtalemediimide derivatives studied by other authors.[7]

To confirm the efficient interaction of the dpNDI with the halides inside the MOF framework, steady-state measurements were also done for the free dpNDI ligand dissolved in iodoethane and iodobenzene. In these cases no phosphorescence emission was recorded at room temperature, and only a reminiscent, very weak phosphorescence band centered at 615 nm was recorded in both cases at 77 K (data not shown), due to the reduction of the nonradiative deactivation pathways such as internal conversion processes or collisions with oxygen or solvent molecules at freezing temperatures. For the same reason, the phosphorescence emission detected for the MOF systems with the halogenated guests at low temperatures (77 K) is approximately an order of magnitude higher than that obtained at room temperature. Besides, the MOF-guest systems at 77 K follow the same trend as at room temperature, *i.e.* the sample with the aromatic halide (iodobenzene) gives six times more intense phosphorescence than with iodoethane (Figure 5.9.). It should be also mentioned that in the case of chlorobenzene guest phosphorescence emission is only noticeable at 77 K (Figure 5.9.B), attributed to a less effective heavy-atom effect of the lighter halogen of the aromatic guest.

In accordance with the phosphorescence intensity changes at different temperatures, the corresponding lifetimes gradually increase as the temperature decreases (Figure 5.11, Table 5.3.), attributed again to the reduction of nonradiative deactivation routes (k_{nr}).

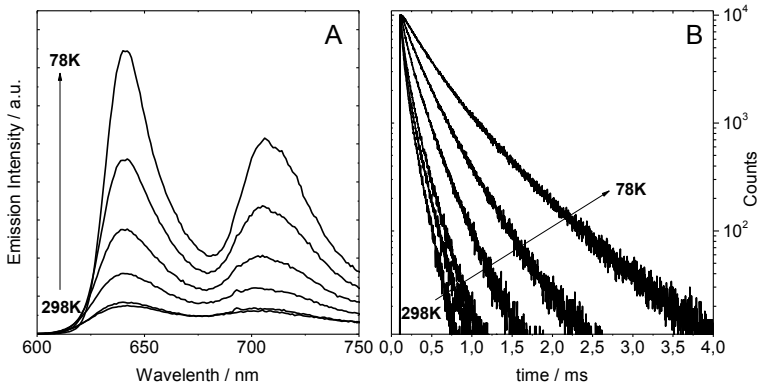

Figure 5.11. A) Steady-state emission spectra and B) phosphorescence decay curves for MOF⊃I-benzene at different temperatures (298, 278, 228, 178, 128 and 78 K).

Table 5.3. Phosphorescence lifetimes (τ_i) of the MOF⊃guest systems (guests: I-ethane, I-benzene and Br-benzene) at different temperatures with their statistical weight (A_i). The average lifetime is also shown (< τ >) (see more details about the determination of the average lifetime in section 3.3.1. in chapter 3).

T / K	I-ethane $\tau_1(A_1)$ $\tau_2(A_2)$ / μs <τ> / μs	I-benzene $\tau_1(A_1)$ $\tau_2(A_2)$ / μs <τ> / μs	Br-benzene $\tau_1(A_1)$ $\tau_2(A_2)$ / μs <τ> / μs
78	550 (41) 230 (59) 192	620 (33) 275 (67) 195	7900 (52) 4300 (48) 3424
128	360 (33) 140 (66) 107	347 (44) 151 (56) 128	6100 (43) 2300 (57) 2186
178	270 (39) 110 (61) 90	220 (41) 89 (59) 76	4400 (43) 1300 (57) 1568
228	220 (59) 90 (41) 109	153 (35) 50 (65) 46	4100 (41) 1200 (59) 1393
278	66 (40) 35 (60) 24	121 (32) 26 (68) 32	3100 (47) 1000 (53) 1210
298	38 (34) 18 (66) 12	104 (32) 20 (68) 28	2300 (56) 800 (44) 1087

Note that the mean phosphorescence lifetimes of the PCPs incorporating iodobenzene and iodoethane are similar to each other (in the microseconds range) while the PCP including brominated or chlorinated guests show much longer mean lifetimes (several milliseconds). Although all these lifetimes are in the typical time range for phosphorescence emission of organic phosphors (≥ several μs),[14] the differences could be ascribed to the weaker spin-orbit coupling induced by the lighter atoms Br and Cl with respect to I atom. That is, according to the following equation

for the phosphorescence lifetime, $\tau_{ph} = 1/(k_{ph} + k_{nr})$, and assuming similar non-radiative processes (k_{nr}) in all the MOF-guest systems with the different occluded halogenated guests, the longer lifetime values can be ascribed to lower phosphorescence radiative constant for Br or Cl atoms, which induce lower spin-orbit coupling than the heavier I atom.

On the other hand, the decay curves recorded for all the samples at any temperature show clearly bi-exponential kinetics (Table 5.3.). The reason of the bi-exponential behavior could be ascribed to several causes; for instance, i) to the coexistence of two different phosphorescent species (the dpNDI and the charge transfer complex), or ii) to different mechanisms for the population of the triplet excited state; that is, not only the triplet state of the dpNDI can be populated by a direct intersystem crossing from its singlet state, but also through the CT complex, as depicted in Figure 5.12. Indeed, similar mechanisms have been described in other systems.[15,16]

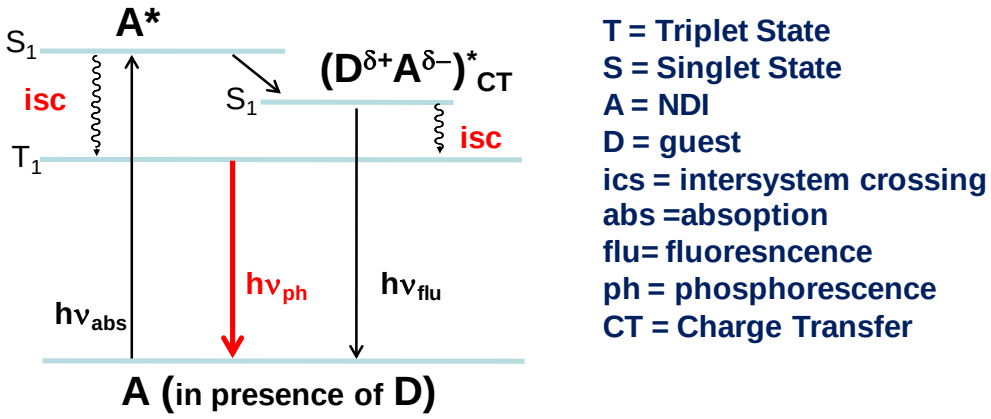

Figure 5.12. Schematic depiction of the energy level diagram of the emissive species and processes in the MOF.

However, given that a bi-exponential fit is also needed in the case of the decay curve registered for the non-aromatic guest (Table 5.3.), other reasons should be found. In this context, two geometrically different adsorption sites have already been reported for this MOF (Figure 5.13.).[1,2] Thus, the two guest molecules occluded into each unit cell (as explained in Figure 5.10.) will occupy different positions in the pores, illustrated as site A and site B in Figure 5.13. Therefore this would mean different positions of the halides respect to the dpNDI ligand, and hence, different distances will induce differences in the spin-orbit coupling.

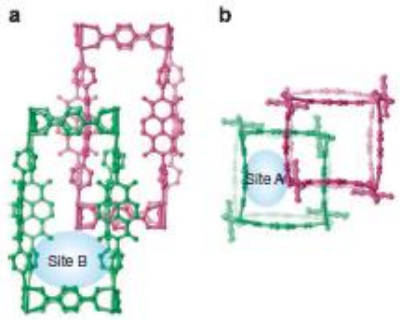

Figure 5.13. Representation of the different adsorption sites for the accommodation of guest molecules into the entangled $[Zn_2(bdc)_2(dpNDI)]_n$ MOF from different views (a and b).[1,2]

From the observations presented above, several conclusions about the phosphorescence emission characteristics of this MOF can be drawn. On the one hand, the similarity between the phosphorescence bands registered in this PCP to those obtained for the free dpNDI ligand in the presence of the halogenated species at low temperature (77 K) indicates that the triplet state responsible for the phosphorescence lies on the dpNDI ligand, and the emission is not interfered by metal-ligand interactions. Besides, the possibility of detecting phosphorescence emission at r.t. in most of the MOF-halide systems (except for Cl-benzene), is related to i) the crystalline nature of the PCP that contributes to the reduction of triplet nonradiative deactivation pathways by avoiding the self-quenching of the dpNDI phosphor observed in liquid phase and ii) the physical confinement of the halide guests into the pores favors an enhanced spin-orbit interaction respect to solution.[15] Finally, the higher phosphorescence efficiency obtained for aromatic halide guests respect to the non-aromatic analogue indicates a more effective population of the triplet state due to CT complexation, activating structural transformations, which enhances dp-NDI-halide interaction and consequently contributes to a more effective spin-orbit coupling. Moreover, the CT complexation between the dpNDI scaffold ligand and the aromatic guests could also enhance the population of the triplet excited state of the dpNDI through intersystem crossing from the CT complex (Figure 5.12.)

The long-lived photo-induced triplet states demonstrated in this material at room temperature may open the door for further applications such as efficient mesoscopic singlet oxygen generators. Moreover, the emission wavelength obtained into the red-

visible/near-IR window could make these MOFs interesting for bio-imaging applications.

Finally, the simplicity of the sample preparation for both white light emission and room temperature phosphorescence demonstrated in the present work, which implies solely the immersion of the MOF powder or crystals into the solvent of interest in each case, adds benefits to the present MOF⊃guest systems.

References

(1) Takashima, Y.; Martínez-Martínez, V.; Furukawa, S.; Kondo, M.; Shimomura, S.; Uehara, H.; Nakahama, M.; Sugimoto, K.; Kitagawa, S. Molecular Decoding Using Luminescence from an Entangled Porous Framework. *Nat. Commun.* **2011**, *2*, 168.

(2) Martínez-Martínez, V.; Furukawa, S.; Takashima, Y.; López Arbeloa, I.; Kitagawa, S. Charge Transfer and Exciplex Emissions from a Naphthalenediimide-Entangled Coordination Framework Accommodating Various Aromatic Guests. *J. Phys. Chem. C* **2012**, *116*, 26084–26090.

(3) Bhosale, S.; Sisson, A. L.; Talukdar, P.; Fürstenberg, A.; Banerji, N.; Vauthey, E.; Bollot, G.; Mareda, J.; Röger, C.; Würthner, F.; Sakai, N.; Matile, S. Photoproduction of Proton Gradients with π-Stacked Fluorophore Scaffolds in Lipid Bilayers. *Science* **2006**, *313*, 84–86.

(4) Andric, G.; Boas, J. F.; Bond, A. M.; Fallon, G. D.; Ghiggino, K. P.; Hogan, C. F.; Hutchison, J. A.; Lee, M. A. P.; Langford, S. J.; Pilbrow, J. R.; Troup, G. J.; Woodward, C. P. Spectroscopy of Naphthalene Diimides and Their Anion Radicals. *Aust. J. Chem.* **2004**, *57*, 1011–1019.

(5) Viehbeck, A.; Goldberg, M. J.; Kovac, C. A. Electrochemical Properties of Polyimides and Related Imide Compounds. *J. Electrochem. Soc.* **1990**, *137*, 1460–1466.

(6) Ilmet, I.; Berger, S. A. Molecular Complexes of Two Naphtalic Anhydrides with Aromatic Hydrocarbons. *J. Phys. Chem.* **1967**, *71*, 1534–1536.

(7) Barros, T. C.; Brochsztain, S.; Toscano, V. G.; Filho, P. B.; Politi, M. J. Photophysical Characterization of a 1,4,5,8-Naphthalenediimide Derivative. *J. Photochem. Photobiol. A Chem.* **1997**, *111*, 97–104.

(8) Martínez-Martínez, V.; Sola Llano, R.; Furukawa, S.; Takashima, Y.; López Arbeloa, I.; Kitagawa, S. Enhanced Phosphorescence Emission by Incorporating Aromatic Halides into an Entangled Coordination Framework Based on Naphthalenediimide. *ChemPhysChem* **2014**, *15*, 2517–2521.

(9) McClure, D. S. Triplet-Singlet Transitions in Organic Molecules. Lifetime Measurements of the Triplet State. *J. Chem. Phys.* **1949**, *17*, 905-913.

(10) Segura-Carretero, A.; Cruces-Blanco, C.; Cañabate-Díaz, B.; Fernández-Sánchez, J. F.; Fernández-Gutiérrez, A. Heavy-Atom Induced Room-Temperature Phosphorescence: A Straightforward Methodology for the Determination of Organic Compounds in Solution. *Anal. Chim. Acta* **2000**, *417*, 19–30.

(11) McGlynn, S. P.; Sunseri, R.; Christodouleas, N. External Heavy-Atom Spin-Orbital Coupling Effect. I. The Nature of the Interaction. *J. Chem. Phys.* **1962**,

37, 1818–1824.

(12) Ganesan, P.; Baggerman, J.; Zhang, H.; Sudhölter, E. J. R.; Zuilhof, H. Femtosecond Time-Resolved Photophysics of 1,4,5,8-Naphthalene Diimides. *J. Phys. Chem. A* **2007**, *111*, 6151–6156.

(13) Green, S.; Fox, M. A. Intramolecular Photoinduced Electron Transfer from Nitroxyl Radicals. *J. Phys. Chem.* **1995**, *99*, 14752–14757.

(14) Yuan, W. Z.; Shen, X. Y.; Zhao, H.; Lam, J. W. Y.; Tang, L.; Lu, P.; Wang, C.; Liu, Y.; Wang, Z.; Zheng, Q.; Sun, J. Z.; Ma, Y.; Tang, B. Z. Crystallization-Induced Phosphorescence of Pure Organic Luminogens at Room Temperature. *J. Phys. Chem. C* **2010**, *114*, 6090–6099.

(15) Wiederrecht, G. P.; Svec, W. A.; Wasielewski, M. R.; Galili, T.; Levanon, H. Triplet States with Unusual Spin Polarization Resulting from Radical Ion Pair Recombination at Short Distances. *J. Am. Chem. Soc.* **1999**, *121*, 7726–7727.

(16) Wiederrecht, G. P.; Svec, W. A.; Wasielewski, M. R.; Galili, T. Novel Mechanism for Triplet State Formation in Short Distance Covalently Linked Radical Ion Pairs. *J. Am. Chem. Soc.* **2000**, *122*, 9715–9722.

6

ORGANOMETALLIC COMPLEXES AS SINGLET OXYGEN PHOTOSENSITIZERS

6

ORGANOMETALLIC COMPLEXES AS SINGLET OXYGEN PHOTOSENSITIZERS

In the previous chapters, phosphorescence and delayed fluorescence emission phenomena have been analyzed in different organic-inorganic systems, phenomena which imply triplet states after their population through an intersystem crossing process (ISC) from a singlet excited state. However, one of the most interesting processes involving ISC is the singlet oxygen generation. Summarizing, the process of photosensitized singlet oxygen generation consists on the excitation of a photosensitizer (PS) after which an ISC occurs to a triplet state, and subsequently an energy transfer to the molecular oxygen happens, yielding the cytotoxic species singlet oxygen, $^1O_2$ (further details about singlet oxygen generation are given in section 2.1.2.3. in chapter 2). Particularly, this chapter is dedicated to the study of the singlet oxygen generation capacity of a family of organic-inorganic hybrid compounds consisting of cyclometalated Ir(III) complexes with anchored BODIPY chromophores.

6.1. BODIPY-Biscyclometalated Iridium (III) complexes

As detailed in chapter 2 (section 2.1.2.3.), photosensitizers are a kind of chromophores useful for photodynamic therapy (PDT) as a promising approach for cancer treatment,[1,2] that would have less side effects than the typical cancer treatment protocols since only the tumor area would be destroyed by light irradiation.

The development of efficient PSs for PDT is focused mainly on the achievement of PSs with i) high molar extinction coefficients within clinic window (650-800 nm) for maximum light penetration, ii) high singlet oxygen generation quantum yield and iii) minimal dark toxicity to minimize side effects. Moreover, the compounds should be relatively inexpensive to make them commercially affordable for extensive utilization.

Several organic PSs dedicated to the production of singlet oxygen are mentioned in chapter 2, such as xhantene dyes, anthracene, porphyrins, anthraquinone and benzophenone derivatives. Indeed, most studies in singlet oxygen photosensitization involve organic molecules. However, some inorganic complexes have also turned out to be efficient photosensitizers. As previously described (section 2.1.2.3. in chapter 2), photosensitizers should undergo intersystem crossing (ISC) in order to be efficient singlet oxygen producers, and one of the best ways to enhance the ISC performance is the heavy atom effect. For this reason, usually efficient ISCs are observed for complexes containing transition metal ions.[3,4] In this sense, medicinal chemistry usually focuses on structurally rigid compounds with close electron shells, such as Ru(II), Os(II) or Ir(III) with stereochemically stable ligands.[5–8] However, there is only a limited number of reported studies on the anticancer activity of organometallic iridium complexes, in spite of the great interest that causes this metal because it is generally considered to be very inert and stable.[7]

Comparing cyclometalated Ir(III) complexes with traditional organic photosensitizers, the major advantage they could offer is the possibility of independently regulating both the emission energy and singlet oxygen production quantum yield by modifying the cyclometalating ligand or the ancillary ligand.[9] However, the most common Ir (III) complexes present 2,2'-bipyridines as ligands, and although these compounds have demonstrated efficient photoinduced singlet oxygen generation, they mostly show absorption bands in the UV region with low molar extinction coefficients, limiting their use in medical applications.[3,9] In order to overcome this drawback, several designing strategies are followed based on the attachment of light-harvesting chromophores to the transition-metal complex,[3,10–12] which can be also promising to achieve materials with combined fluorescence and photosensitization features for simultaneous imaging and treatment of tumor cells. Despite the efforts focused on the development of these dye-containing metallic complexes, few of them have proven to be successful-enough as efficient fluorescent-PDT agents.

In this sense, the boron dipyrromethene chromophores, also known as BODIPY (4,4-difluoro-4-bora-3a,4a-diaza-s-indacene, Figure 6.1.) are suitable to be chelated to the metal center. These dyes have attracted considerable attention due to their favorable chemical-physical features, especially those related to their photophysical characteristics, including high extinction coefficients in the visible region and

resistance to photobleaching.[13] Moreover, their synthesis versatility allows a exhaustive and selective structural modification/funcionalization around the core structure of the chromophore (Figure 6.1.) in order to modulate their properties depending on the needs of each case.[14,15] Generally, BODIPY dyes are known for being highly fluorescent since they usually exhibit negligible triplet formation efficiency.[16] Nevertheless, extensive research is performed to enhance intersystem crossing to the triplet state, for instance by the incorporation of heavy atoms (such as Br or I) directly to the BDP core, thereby favoring spin-orbit coupling and hence ISC to the triplet state.[3,5,13,17]

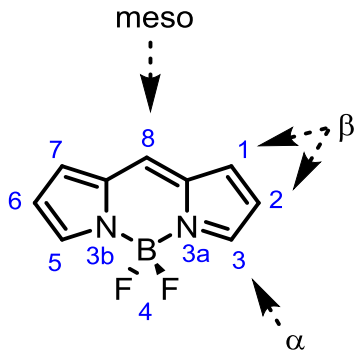

Figure 6.1. General BODIPY structure. Different positions in the BODOPY core are indicated and numbered according to the IUPAC system (blue numbers).

However, in this chapter the aim is to enhance the molar absorption of the organometallic complex in the visible region by attaching BODIPY chromophores to the metallic center, and ideally, reach the clinic window (650-800 nm), where tissue transparency is optimal. In this regard, different cyclometalated complexes with BODIPY chromophores chelated to the coordination center have been already described by other authors.[5,10,11,18] Indeed, the linker between the light-harvesting chromophore and the metallic center is of great importance in the efficiency of the energy funneling towards the excited triplet state manifold.[10,12,19,20] In this sense, on the one hand, lots of works have focused on connecting the metallic center to the chromophore by π-conjugated linkers, generally through 2,2'-bipyridine (bpy) groups (Figure 6.2.A).[10,18,20,21] On the other hand, organometallic complexes have been synthesized also directly attaching the visible-light-absorbing organic ligand to the coordination center, mainly through an acetylide linkage (see Figure 6.2.B).[12,19,20,22] However, the efficiency of the majority of these compounds as fluorescent-PDT agents remains low.

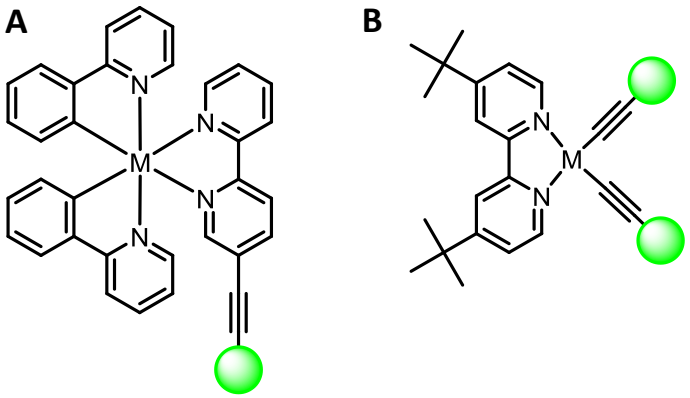

Figure 6.2. Examples of different junctions between the metallic center and the chromophoric units (represented as green circles). The metallic specie (M) in such structures is generally M = Ir or Ru in case A, and M = Pt in B.

Analyzing the molecular structure of BODIPY dyes containing cyclometalated complexes, it is noteworthy that most of them involve the pyridine groups as ancillary ligands.[10,18,21] Notwithstanding, other groups such as acetylacetonate (acac) acting as cyclometallating ligands have also led to organometallic derivatives with outstanding behavior as photosensitizers.[9,23] Attending these precedents, we envisaged a new molecular designing strategy to develop advanced fluorescent-PDT materials based on BODIPY-linked cyclometalated Ir(III) complexes through the *meso* position of the chromophore via an acetylacetonate group (Figure 6.3.). It is interesting that through the junction in the *meso* position of the BODIPY, the possibility of further functionalization in the other positions of the BDP core is open to modulate the final spectroscopic properties of the organometallic compounds. Indeed, by extending the conjugated system, bathochromic shifts in both absorption and emission bands of the BODIPY chromophores can be achieved,[24,25] which is highly desirable to develop therapeutic agents in the clinic window for biomedical applications. In particular, the acetylacetoneBODIPY-biscyclometalated Iridium (III) complexes under study in this chapter are depicted in Figure 6.3., named **Ir-1** and **Ir-2**. **Ir-2** presents two thienyl-groups tethered on 2 and 6 positions of the BDP with the aim of shifting the spectral bands towards the spectral region of biological interest. In order to clarify the relevance of the acac linker in these compounds, the results obtained for **Ir-1** and **Ir-2** will be compared with an analogous compound where the BODIPY chromophore is linked to the metal center by a polypyridyl ancillary group (**Ir-3** in Figure 6.3.). It

should be mentioned that the synthesis of these compounds have been carried out at the research group of Prof. Mª José Ortiz at Universidad Complutense de Madrid, UCM (synthetic protocol not described here).

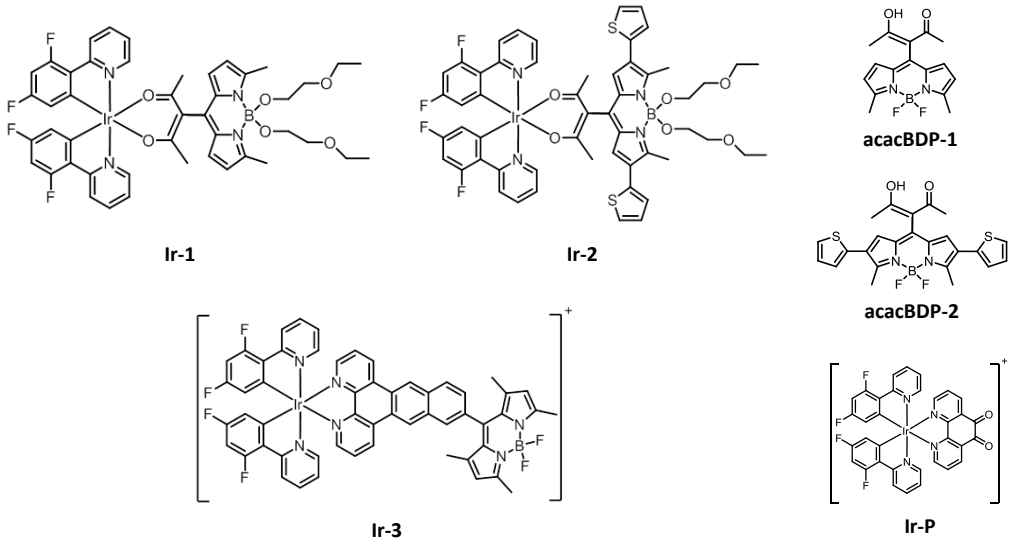

Figure 6.3. Structures of the **Ir-1**, **Ir-2** and **Ir-3** compounds, those for the free BODIPY moieties, **acacBDP-1** and **acacBDP-2**, and the precursor **Ir-P**. Note that compounds **Ir-1** and **Ir-2** have an acac linker between the cyclometallated center and the BODIPY moiety, while in **Ir-3** the junction is through a polypyridyl linker.

Note that in both **Ir-1** and **Ir-2** compounds the fluorine has been displaced on the boron center of the BODIPY moieties by alkoxy groups. The resulting BODIPY chromophores are known as *O*-BODIPY derivatives. As has been already studied, *O*-BODIPYs possess enhanced photostability for laser applications, as well as improved water solubility,[26,27] which is a crucial feature for biological applications. In the particular compounds studied here, the polyethylene glycol (PEG) groups incorporated into the *O*-BODIPY structure are well known as solubilizing groups, and they can also prevent molecular aggregation of the *O*-BODIPYs in water.[27,28]

The photophysical characterization of all the organometallic compounds and the respective free acac-BODIPY dyes (**acacBDP-1** and **acacBDP-2** for **Ir-1** and **Ir-2**, respectively, Figure 6.3.) was carried out in aerated acetonitrile at room temperature. The absorption spectra of **Ir-1** together with those of the free **acacBDP-1** ligand and the **Ir-P**, as reference, are shown in Figure 6.4.A. First note the poor absorption of the **Ir-P** precursor in the visible region (above 400 nm). Conversely, **Ir-1** shows an

intense absorption band centered at 517 nm, in good agreement with the absorption spectra of the respective **acacBDP-1** chromophore (Table 6.1., Figure 6.4.A), indicating that there is not any noticeable electron coupling between moieties in the ground state, as will be corroborated later by molecular modeling. Although there is not a significant spectral shift on the absorption band of the BODIPY moiety upon complexation with Ir(III), the molar coefficients (ε) at the maximum absorption considerably increase with respect to the electronically-isolated BODIPY chromophore (Table 6.1.). This enhancement could be attributed to the replacement of fluorine atoms in the boron center by alcoxy groups, as other authors have observed.[26]

Table 6.1. Photophysical properties of the free ligands and the organoiridium (III) complexes in aerated acetonitrile solution at room temperature with a molar concentration of 10^{-5} M: maximum absorption and emission wavelengths (λ_{abs} and λ_{fl}), molar absorption (ε) at the absorption maximum, fluorescence quantum yield (ϕ_{fl}) and singlet oxygen production quantum yield (Φ_{Δ}) measured exciting the sample at 530, 605 and 370 nm for **Ir-1**, **Ir-2** and **Ir-3**, respectively.

Compound	λ_{abs} / nm	ε / 10^{-4} $M^{-1}cm^{-1}$	λ_{fl} / nm	ϕ_{fl}	Φ_{Δ}
acacBDP-1	515	0.99	526	0.90	0
acacBDP-2	600	0.41	677	0.09	0
Ir-1	517	4.46	528	0.08	0.86
Ir-2	597	3.38	652	0.22	0.60
Ir-3	502	2.60	546	0.01	0.51

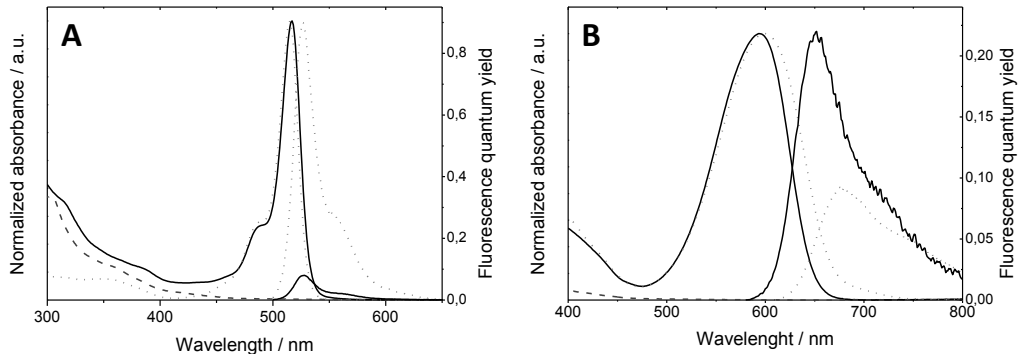

Figure 6.4. A) Height-normalized absorption spectra and emission spectra normalized to the quantum yield value of **Ir-1** (solid lines), **acacBPD-1** (dotted line) and **Ir-P** ligand (dashed line). B) Height-normalized absorption spectra and emission spectra normalized to the quantum yield value of **Ir-2** (solid line) and the **acacBPD-2** (dotted line).

Regarding fluorescence properties, in spite of the intense fluorescent emission of the free **acacBDP-1** (ϕ_{fl} = 0.90), weak fluorescence at room temperature was recorded for the corresponding **Ir-1** complex (ϕ_{fl} = 0.08, Table 6.1.). This remarkable fluorescence quenching should be related to an enhancement of the intersystem crossing (ISC) to the triplet excited state. Certainly, **Ir-1** showed effective singlet oxygen generation (Φ_{Δ} = 0.86, Table 6.1.) upon visible excitation light (λ_{exc} = 530 nm), whereas **acacBDP-1** chromophore does not enable $^1O_2$ sensitization. This last result is in agreement with the above mentioned low triplet population probability in this type of chromophores.

An even more interesting behavior was found for **Ir-2**. With regard to the chromophoric ligand herein selected, thienyl groups tethered on positions 2 and 6 on the BDP core in the **acacBDP-2** caused a red-shift in both the absorption and fluorescence bands, placing them within the spectral region of biological interest. The large Stokes shift (77 nm) is attributed to geometry relaxation of the molecular structure upon photoexcitation, as other authors have stated, particularly for BODIPYs with thienyl substituents at positions 2 and 6.[29] This process significantly affects the energy levels of molecular orbitals since the geometry of the first singlet excited state, *i.e.*, the S_1 state, remarkably differs from the ground-state geometry (S_0 state).On the other hand, one may think that the low fluorescence efficiency of the **acacBDP-2** with respect to **acacBDP-1** could be attributed to a non-emissive intramolecular charge transfer process (ICT) from the thiopenyl sustituents to the BDP core. However, the fluorescence quantum yield of **acacBDP-2** ligand does not increase in less polar solvent (*i.e.* dicloromethane). Therefore, the low fluorescence efficiency of **acacBDP-2** ligand is also related to the geometry relaxation process which is well-established as the main non-radiative deactivation process in these derivatives.[29]

As regards **Ir-2**, it exhibits an intense absorption band centered at 597 nm, which corresponds to the absorption of the **acacBDP-2** unit, suggesting again that there is not a perceptible electron coupling between the two moieties, and also with a higher molar extinction coefficient (ε) at the maximum absorption, in this case around ten times higher than that for the free BODIPY (Table 6.1.). On the other hand, the fluorescence band of the organometallic complex **Ir-2** is blue-shifted with respect to the free **acacBDP-2** ligand by about 25 nm, and the emission efficiency significantly increases (ϕ_{fl} = 0.22) with respect to the **acacBDP-2** ligand (ϕ_{fl} = 0.09, Table 6.1.), indicating that the metallic complexation considerably reduces the geometry relaxation of the

acacBDP-2 molecular structure after photoexcitation. As a result, **Ir-2** does not show such a high $^1O_2$ photosensitizing capability (Φ_Δ = 0.60, λ_{exc} = 605 nm; Table 6.1.) with respect to **Ir-1**, which is in agreement with its relatively high fluorescence efficiency, being *ca.* 3-fold than that for the **Ir-1**. In this sense, **Ir-2** shows an interesting balance between the singlet oxygen generation and the fluorescence quantum yield, triggered by red excitation light, which makes it a promising material for PDT and also for theragnosis (imaging + treatment).

As regards the **Ir-3** compound, a π-extended metalated Ir(III) complex bearing the same cyclometalating ligands as **Ir-1** and **Ir-2** but with a polypyridyl unit acting as ancillary ligand to the BODIPY moiety instead of an acac linker, it shows strong absorption in the visible region (Figure 6.5., Table 6.1.) but its fluorescence is practically quenched and, more importantly, it is non-effective in generating singlet oxygen species upon excitation in the visible range. Indeed, for **Ir-3**, a moderate $^1O_2$ quantum yield of 51% is achieved only exciting directly the metallic center under UV irradiation (λ_{exc} = 370 nm; Table 6.1.). Hence, the unique responsible for the singlet oxygen generation in this **Ir-3** complex is the cyclometalated unit, with no impact due to the attachment of the BODIPY fluorophore via a polypyridyl ancillary ligand.

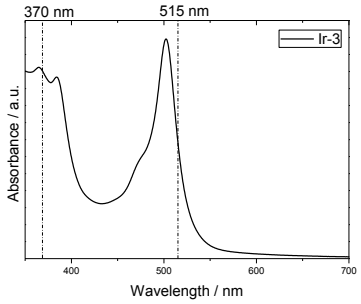

Figure 6.5. Absorption spectrum of **Ir-3** compound in aerated acetonitrile. The two wavelengths used for excitation in singlet oxygen measurements are indicated: 370 and 515 nm, exciting directly the metallic center or the BODIPY moiety, respectively.

To shed light on the mechanism involved in the singlet oxygen generation of **Ir-1** and **Ir-2** compounds, nanosecond time-resolved transient absorption experiments were performed. Upon pulsed laser excitation, broad positive transient absorption (TA) bands in the range of 400-450 and 550-700 nm were observed for **Ir-1** (Figure 6.6.A). The band corresponding to the depletion of the ground state for **Ir-1** is located at 517

nm, which is in good agreement with the steady-state absorption measurements (Figure 6.4.A), indicating that there is not photoproduct generation in these conditions.[30] Regardless of the excitation wavelength, similar decay curves from both TA bands were recorded, leading to a lifetime of 8.4 μs in deaerated conditions, which becomes drastically reduced up to 385 ns in aerated solutions, typical feature of triplet states (Figure 6.6.B and C). The TA spectrum of **Ir-2** is similar to that of **Ir-1**, with the bleaching band centered at 595 nm and positive transient absorption values in the range of 330-480 nm and 655−850 nm (Figure 6.7.A). In this case the lifetime values were 9.6 μs in deaerated solutions and 480 ns in aerated ones.

The spectral signatures of both **Ir-1** and **Ir-2** compounds suggest that the excited state, characterized by a long lifetime (around 10 μs), could be ascribed to the lowest-lying BODIPY-centered triplet state (^{3}LC, "Ligand Centered Triplet State"), in good agreement with the conclusions reached for other dye-containing metallic complexes.[10,11,18] Note here that although it is not possible to measure the triplet excited-state lifetime of the **Ir-P** compound for comparison in our experimental set up (**Ir-P** does not have any absorption band in the visible region and our laser does not provide excitation wavelengths below 420 nm), these type of Ir(III) complexes usually show relatively short triplet excited-state lifetimes.[10,18,31,32] Indeed, other authors have reported lifetime values in the range of 300-350 ns for similar Ir (III) cyclometalated complexes.[18,33]

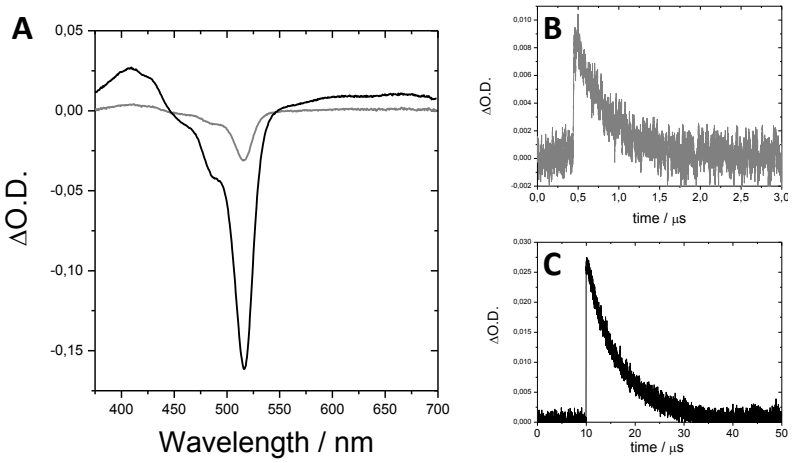

Figure 6.6. A) Transient absorption spectrum for **Ir-1** at room temperature in deareated (black line) or aerated (gray line) acetonitrile under 515 nm excitation light. B) and C) Transient decay curves recorded at 615 nm in aerated (B) and deaerated (C) acetonitrile solution.

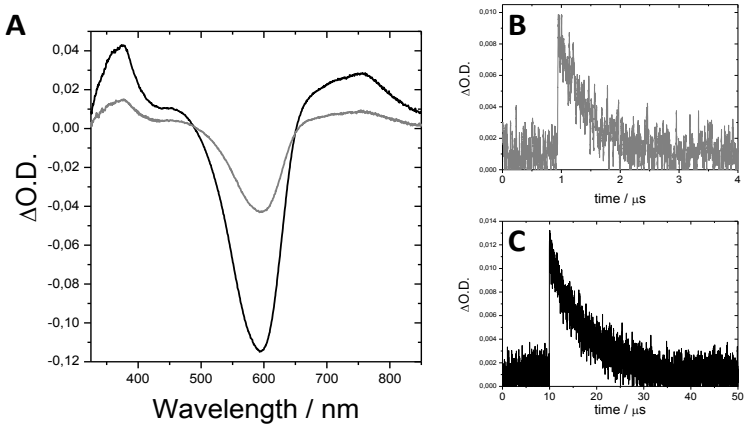

Figure 6.7. A) Transient absorption spectrum for **Ir-2** at room temperature in deareated (black line) or aerated (gray line) acetonitrile under 595 nm excitation light. B) and C) Transient decay curves recorded at 755 nm in aerated (B) and deaerated (C) acetonitrile solution.

In order to ensure the statement above, the luminescence properties of the compounds were analyzed at 77 K in glassy ethanol solutions. In the case of **Ir-1**, a very intense emission band centered at 528 nm (data not shown), previously assigned to fluorescence emission, and a very weak band centered at 749 nm (Figure 6.8.A), ascribed to phosphorescence, were recorded. The lifetime recorded at the red-shifted band is characterized by a long lifetime of 2.4 ms (inset in Figure 6.8.A), which indicates that the phosphorescent emission is originated from a purely organic species.[11] Indeed, if the phosphorescent emission would fall on the ^{3}MLCT state of the metallic center, the emission would be expected at wavelengths lower than 700 nm and with much lower associated phosphorescence lifetimes.[11,34] Similar spectral features were recorded for the **acacBDP-1** ligand, although its phosphorescence emission intensity (data not shown) is much lower than that registered for the corresponding **Ir-1** complex. On the basis of these results, the long-lived emission can be properly assigned to the phosphorescence from the BODIPY unit, whose emission intensity is significantly enhanced by attaching this moiety to the cyclometalated Ir(III) complex. The emission of **Ir-2** at 77 K is similar to that described for **Ir-1**, but with its long-wavelength band centered at 948 nm (Figure 6.8.B). As a consequence, a NIR detector was required for the measurement of this band, and thus, it is not possible a proper comparison between the phosphorescence emission intensities of the

two organoiridium compounds **Ir-1** and **Ir-2**. Note here that no phosphorescence emission was registered for the respective free **acacBDP-2** ligand.

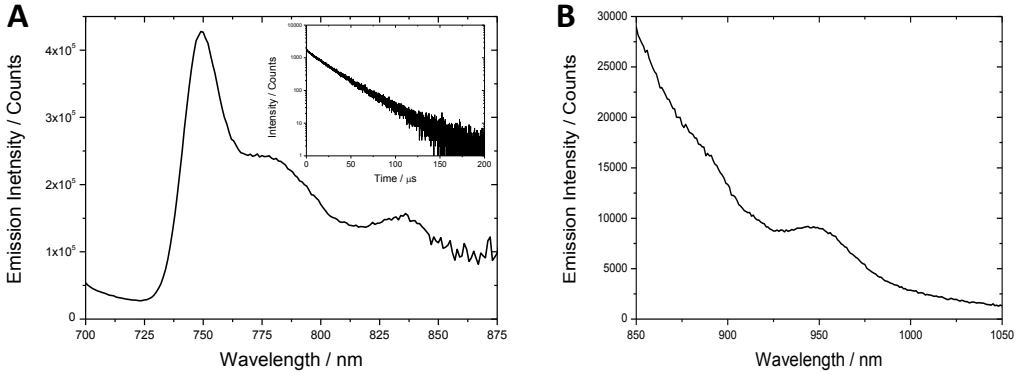

Figure 6.8. A) Phosphorescence band of **Ir-1** measured in glassy ethanol at 77 K and its corresponding lifetime decay as an input. B) Phosphorescence band of **Ir-2** measured in glassy ethanol at 77 K.

Thus, according to the above presented results, a suitable mechanism to promote $^{3}\pi$-π^* BODIPY level could be through an effective ISC process after the excitation of its fluorescent $^{1}\pi$-π^* state. The ISC should be favored by an enhanced spin-orbit coupling due to the close presence of the Ir(III) heavy atom. In particular, probably the interaction between the BODIPY $^{3}\pi$-π^* state and the close-lying metal-based ^{3}MLCT level enhances the spin-orbit coupling in the BODIPY fragment, as other author have demonstrated in similar compounds.[10,11,18]

With the aim of supporting the conclusions derived from the experimental results described above, the photophysical properties of the **Ir-2** compound were theoretically analyzed by density functional theory (DFT) in the University of the Basque Country (UPV-EHU) by Dr. Hegoi Manzano.

The optimized ground state geometry of **Ir-2** complex shows that the BODIPY takes a perpendicular orientation with respect to the acac linker and hence it is not expected any π-conjugation between the BODIPY and the iridium center. On the other hand, the thienyl groups are perfectly aligned with the BODIPY core, therefore allowing the extension of the π-conjugation. This result is in agreement with the experimentally observed red-shift of both the absorption and emission bands of this

complex in comparison with the **Ir-1** without π-substituents at positions 2 and 6 of the BDP.

The absorption wavelength, calculated assuming a Franck-Condon vertical transition, is centered at 564 nm (2.20 eV), more energetic but close to the experimental result, centered at 597 nm (Table 6.1.). HOMO and LUMO orbitals are involved in this $S_0 \rightarrow S_1$ transition, both localized in the BODIPY moiety (Figure 6.9.). The emission wavelength was calculated after an optimization of the dye excited state conformation. The calculated $S_1 \rightarrow S_0$ emission wavelength was 633 nm (1.96 eV), again slightly blue-shifted with respect to the experimentally recorded band centered at 652 nm (Table 6.1.). Stokes shift predicted by the simulation (69 nm) is therefore in reasonably good agreement with the experimental one (55 nm).

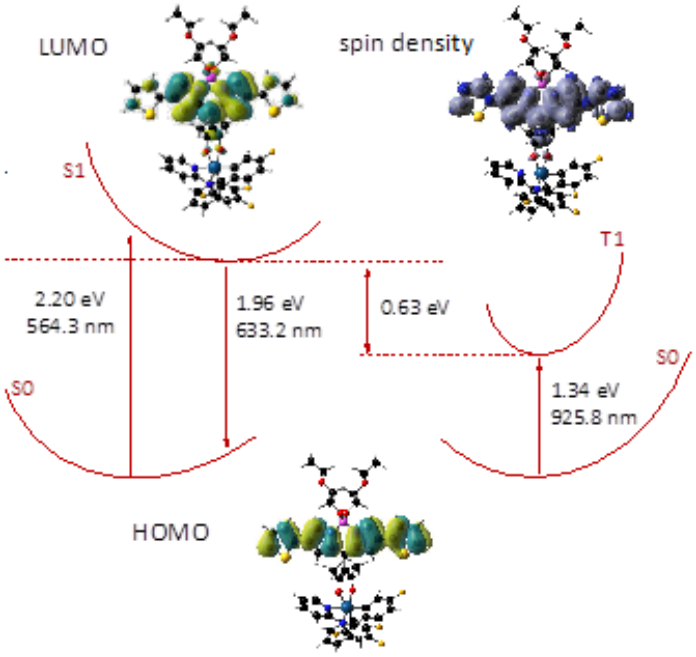

Figure 6.9. Schematic representation of the photophysical process in the **Ir-2** compound. Arrows indicate the direction of each transition, with the corresponding energy and wavelength. S_0, S_1, and T_1 states represent the ground state and the first singlet and triplet excited states respectively. The spatial location of the HOMO and LUMO atomic orbitals and spin density results are also included.

The adiabatic energy gap between the optimized S_0 and T_1 states, 1.34 eV (926 nm), is in good agreement with the experimental phosphorescence band, centered at

948 nm. The calculations also indicate that the involved orbitals are again the HOMO and LUMO, and hence the T_1 state can be attributed to a ^{3}LC state (Ligand Centered triplet state), *i.e.* to the $^3\pi$-π* state of the BODIPY fragment.

To complete the theoretical study, the localization of the spin density in **Ir-2** was analyzed. The isosurface map (Figure 6.9.) shows that the spin density is localized exclusively in the BODIPY, in agreement with the previous assignment of ^{3}LC state for the triplet. Thus, calculations results coincide with the conclusions reached by experimental observations.

Summarizing, due to the synergism between organic-inorganic moieties linked in a proper way, the present materials show outstanding properties as singlet oxygen photosensitizers which are also fluorescent emitters, especially in the case of **Ir-2**. Thus, the compounds presented in this work could be well-suited for theragnostic activity. Furthermore, the light-harvesting region of the cyclometalated Iridium (III) photosensitizer has been extended from the UV to the visible range, and in the particular case of **Ir-2**, reaching the region of medical interest.

Due to the interesting properties shown above by **Ir-1** and **Ir-2** complexes, *in vitro* cytotoxicity studies with and without light exposure were carried out at the group of Prof. Angeles Villanueva at the Universidad Autónoma de Madrid (UAM), in order to analyze their capacity as potential biomedical tools.

The PDT activity of both compounds was analysed on HeLa cells, which were incubated with the photosensitizer at different concentrations (from 5×10^{-9} M to 10^{-7} M for **Ir-1** and **Ir-2**, respectively) for 24 h.

First note that none of the compounds exhibit dark toxicity at those concentrations (Figure 6.10. and Figure 6.11.), *i.e.* they are no-toxic for the cells when there is no irradiation. This property is highly important if a material is to be used in photodynamic therapy (PDT). Then, phototoxicity experiments were carried out under green light for **Ir-1** and under red illumination for **Ir-2**, at different irradiation powers. The results for **Ir-1** and **Ir-2** are shown below in Figure 6.10. and Figure 6.11., respectively.

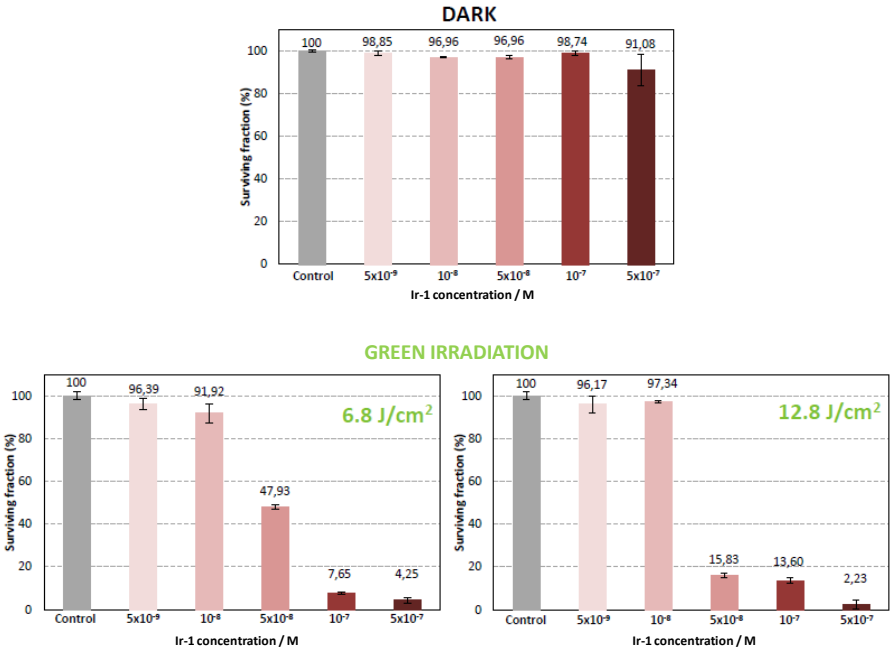

Figure 6.10. The surviving fraction of HeLa cells 24 h after incubation with **Ir-1** at different concentrations without irradiation and with green irradiation at different light power.

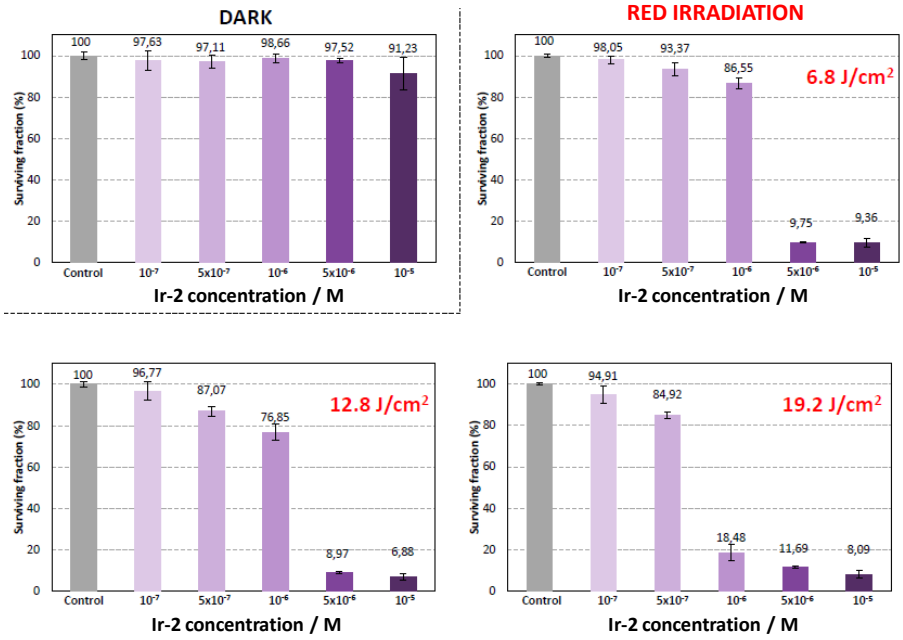

Figure 6.11. The surviving fraction of HeLa cells 24 h after incubation with **Ir-2** at different concentrations without irradiation and with red irradiation at different light power.

Both compounds trigger phototoxicity on HeLa cells. Indeed, apoptotic morphologies of the cells were seen (Figure 6.12.) after the photodynamic treatment (incubation and irradiation).

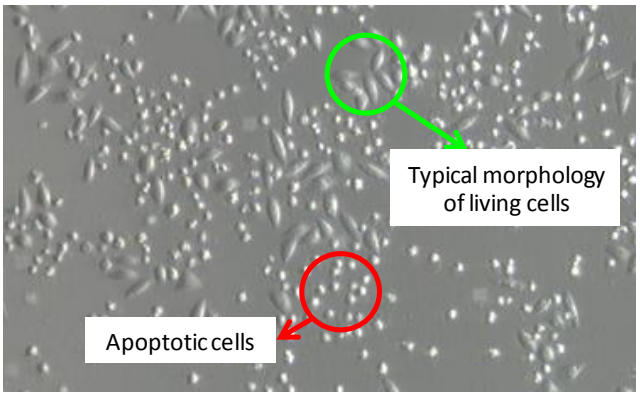

Figure 6.12. Images of the HeLa cells obtained by differential interference contrast (DIC) microscopy after the photodynamic treatment with **Ir-2** (after red irradiation).

Apparently, **Ir-1** shows much efficient phototoxic properties than **Ir-2**. **Ir-1** is capable to induce high cell death rates at very low concentrations. Indeed, at 5 x 10^{-8} M, it provokes 50-85% of cell death depending on the light doses (Figure 6.10.). Although **Ir-2** shows less efficient singlet oxygen production than **Ir-1** (Table 6.1.), the reason for the lower phototoxicity can be that the red irradiation source used (λ_{exc} = 632 nm) does not excite the compound in its absorption maxima (λ_{abs} = 597 nm, Figure 6.4.B). Although apparently higher concentrations of **Ir-2** are needed (5 x 10^{-6} M), at this level the dark toxicity is negligible and the cell-death rate is also efficient, so the results can be considered as successful. At a more appropriate excitation wavelength (closer to the absorption maximum of **Ir-2**), lower PS concentration would result in higher cell death rates.

For all the results presented above, it can be concluded that the two compounds under study, the **Ir-1** and the **Ir-2**, are efficient photosensitizers with singlet oxygen generation quantum yields of Φ_Δ = 0.86 and Φ_Δ = 0.60, respectively. Indeed, with the acac attachment to the cyclometalated core, the ISC to the BODIPY triplet state has been promoted resulting in singlet oxygen photosensitization. Besides, the organometallic photosensitizers have extended their light-harvesting region to the visible range, reaching the red edge of the electromagnetic spectrum (near the clinic

window) in the case of **Ir-2**. Furthermore, due to the good balance between fluorescence and $^1O_2$ generation, they can be also suitable materials for imaging and PDT applications, specially the **Ir-2** compound. The photodynamic therapy (PDT) activity of the new organometalic systems was demonstrated by *in vitro* experiments, exhibiting low dark- and high photo-toxicity, even at low PS concentration (5×10^{-8} M for **Ir-1**), which endorses the reported compounds as valuable platforms to develop, through costless and straightforward synthetic routes, advanced materials for theragnosis.

References

(1) Chen, J.; Keltner, L.; Christophersen, J.; Zheng, F.; Krouse, M.; Singhal, A.; Wang, S.-S. New Technology for Deep Light Distribution in Tissue for Phototherapy. *Cancer J.* **2002**, *8*, 154–163.

(2) Silva Jr, Z. S.; Bussadori, S. K.; Santos Fernandes, K. P.; Huang, Y.-Y.; Hamblin, M. R. Animal Models for Photodynamic Therapy (PDT). *Biosci. Rep.* **2015**, *35*, 1–14.

(3) Zhao, J.; Wu, W.; Sun, J.; Guo, S. Triplet Photosensitizers : From Molecular Design to Applications. *Chem. Soc. Rev.* **2013**, *42*, 5323–5351.

(4) You, Y.; Nam, W. Photofunctional Triplet Excited States of Cyclometalated Ir(III) Complexes: Beyond Electroluminescence. *Chem Soc Rev* **2012**, *41*, 7061–7084.

(5) Zhao, J.; Xu, K.; Yang, W.; Wang, Z.; Zhong, F. The Triplet Excited State of Bodipy: Formation, Modulation and Application. *Chem Soc Rev* **2015**, *44*, 8904–8939.

(6) Stacey, O. J.; Pope, S. J. New Avenues in the Design and Potential Application of Metal Complexes for Photodynamic Therapy. *RSC Adv.* **2013**, *3*, 25550–25564.

(7) Liu, Z.; Sadler, P. J. Organoiridium Complexes: Anticancer Agents and Catalysts. *Acc. Chem. Res.* **2014**, *47*, 1174–1185.

(8) Geldmacher, Y.; Oleszak, M.; Sheldrick, W. S. Rhodium(III) and iridium(III) Complexes as Anticancer Agents. *Inorganica Chim. Acta* **2012**, *393*, 84–102.

(9) Djurovich, P. I.; Murphy, D.; Thompson, M. E.; Hernandez, B.; Gao, R.; Hunt, P. L.; Selke, M. Cyclometalated Iridium and Platinum Complexes as Singlet Oxygen Photosensitizers: Quantum Yields, Quenching Rates and Correlation with Electronic Structures. *Dalt. Trans.* **2007**, *34*, 3763–3770.

(10) Rachford, A. A.; Ziessel, R.; Bura, T.; Retailleau, P.; Castellano, F. N. Boron Dipyrromethene (Bodipy) Phosphorescence Revealed in $[Ir(ppy)_2(bpy\text{-}C{\equiv}C\text{-}Bodipy)]^+$. *Inorg. Chem.* **2010**, *49*, 3730–3736.

(11) Galletta, M.; Campagna, S.; Quesada, M.; Ulrich, G.; Ziessel, R. The Elusive Phosphorescence of Pyrromethene-BF_2 Dyes Revealed in New Multicomponent Species Containing Ru(II)-Terpyridine Subunits. *Chem. Commun.* **2005**, 4222–4224.

(12) Sun, H.; Guo, H.; Wu, W.; Liu, X.; Zhao, J. Coumarin Phosphorescence Observed with N^N Pt(II) Bisacetylide Complex and Its Applications for Luminescent Oxygen Sensing and Triplet–triplet-Annihilation Based Upconversion. *Dalt. Trans.* **2011**, *40*, 7834-7841.

(13) Yogo, T.; Urano, Y.; Ishitsuka, Y.; Maniwa, F.; Nagano, T. Highly Efficient and Photostable Photosensitizer Based on BODIPY Chromophore. *J. Am. Chem. Soc.* **2005**, *127*, 12162–12163.

(14) Ulrich, G.; Ziessel, R.; Harriman, A. The Chemistry of Fluorescent Bodipy Dyes: Versatility Unsurpassed. *Angew. Chemie - Int. Ed.* **2008**, *47*, 1184–1201.

(15) Loudet, A.; Burgess, K. BODIPY Dyes and Their Derivatives: Syntheses and Spectroscopic Properties. *Chem. Rev.* **2007**, *107*, 4891–4932.

(16) Pavlopoulos, T. G. Scaling of Dye Lasers with Improved Laser Dyes. *Prog. Quantum Electron.* **2002**, *26*, 193–224.

(17) Kamkaew, A.; Lim, S. H.; Lee, H. B.; Kiew, L. V.; Chung, L. Y.; Burgess, K. BODIPY Dyes in Photodynamic Therapy. *Chem. Soc. Rev.* **2013**, *42*, 77–88.

(18) Sun, J.; Zhong, F.; Yi, X.; Zhao, J. Efficient Enhancement of the Visible-Light Absorption of Cyclometalated Ir(III) Complexes Triplet Photosensitizers with Bodipy and Applications in Photooxidation and Triplet-Triplet Annihilation Upconversion. *Inorg. Chem.* **2013**, *52*, 6299–6310.

(19) Rachford, A. A.; Goeb, S.; Castellano, F. N. Accessing the Triplet Excited State in Perylenediimides. *J. Am. Chem. Soc.* **2008**, *130*, 2766–2767.

(20) Zhao, J.; Ji, S.; Wu, W.; Wu, W.; Guo, H.; Sun, J.; Sun, H.; Liu, Y.; Li, Q.; Huang, L. Transition Metal Complexes with Strong Absorption of Visible Light and Long-Lived Triplet Excited States: From Molecular Design to Applications. *RSC Adv.* **2012**, *2*, 1712–1728.

(21) Wu, W.; Sun, J.; Cui, X.; Zhao, J. Observation of the Room Temperature Phosphorescence of Bodipy in Visible Light-Harvesting Ru(II) Polyimine Complexes and Application as Triplet Photosensitizers for Triplet–triplet-Annihilation Upconversion and Photocatalytic Oxidation. *J. Mater. Chem. C* **2013**, *1*, 4577-4589.

(22) Wu, W.; Zhao, J.; Guo, H.; Sun, J.; Ji, S.; Wang, Z. Long-Lived Room-Temperature near-IR Phosphorescence of BODIPY in a Visible-Light-Harvesting N^C^N Pt^{II}-Acetylide Complex with a Directly Metalated BODIPY Chromophore. *Chem. - A Eur. J.* **2012**, *18*, 1961–1968.

(23) Gao, R.; Ho, D. G.; Hernandez, B.; Selke, M.; Murphy, D.; Djurovich, P. I.; Thompson, M. E. Bis-Cyclometalated Ir (III) Complexes as Efficient Singlet Oxygen Sensitizers. *J. Am. Chem. Soc.* **2002**, *124*, 14828–14829.

(24) Gómez-Durán, C. F. A.; Esnal, I.; Valois-Escamilla, I.; Urías-Benavides, A.; Bañuelos, J.; López Arbeloa, I.; García-Moreno, I.; Peña-Cabrera, E. Near-IR BODIPY Dyes À La Carte-Programmed Orthogonal Functionalization of Rationally Designed Building Blocks. *Chem. - A Eur. J.* **2016**, *22*, 1048–1061.

(25) Lu, H.; Mack, J.; Yang, Y.; Shen, Z. Structural Modification Strategies for the Rational Design of red/NIR Region BODIPYs. *Chem. Soc. Rev.* **2014**, *43*, 4778–4823.

(26) Durán-Sampedro, G.; Agarrabeitia, A. R.; Cerdán, L.; Pérez-Ojeda, M. E.; Costela, A.; García-Moreno, I.; Esnal, I.; Bañuelos, J.; Arbeloa, I. L.; Ortiz, M. J. Carboxylates versus Fluorines: Boosting the Emission Properties of Commercial BODIPYs in Liquid and Solid Media. *Adv. Funct. Mater.* **2013**, *23*, 4195–4205.

(27) Brizet, B.; Bernhard, C.; Volkova, Y.; Rousselin, Y.; Harvey, P. D.; Goze, C.; Denat, F. Boron Functionalization of BODIPY by Various Alcohols and Phenols. *Org. Biomol. Chem.* **2013**, *11*, 7729–7737.

(28) Tokoro, Y.; Nagai, A.; Chujo, Y. Nanoparticles via H-Aggregation of Amphiphilic BODIPY Dyes. *Tetrahedron Lett.* **2010**, *51*, 3451–3454.

(29) Chen, Y.; Zhao, J.; Guo, H.; Xie, L. Geometry Relaxation-Induced Large Stokes Shift in Red-Emitting Borondipyrromethenes (BODIPY) and Applications in Fluorescent Thiol Probes. *J. Org. Chem.* **2012**, *77*, 2192–2206.

(30) Montejano, H. A.; Amat-Guerri, F.; Costela, A.; García-Moreno, I.; Liras, M.; Sastre, R. Triplet-State Spectroscopy of dipyrromethene·BF_2 Laser Dyes. *J. Photochem. Photobiol. A Chem.* **2006**, *181*, 142–146.

(31) Ragni, R.; Orselli, E.; Kottas, G. S.; Omar, O. H.; Babudri, F.; Pedone, A.; Naso, F.; Farinola, G. M.; De Cola, L. Iridium(III) Complexes with Sulfonyl and Fluorine Substituents: Synthesis, Stereochemistry and Effect of Functionalisation on Their Photophysical Properties. *Chem. - A Eur. J.* **2009**, *15*, 136–148.

(32) Baranoff, E.; Fantacci, S.; De Angelis, F.; Zhang, X.; Scopelliti, R.; Grätzel, M.; Nazeeruddin, M. K. Cyclometalated Iridium(III) Complexes Based on Phenyl-Imidazole Ligand. *Inorg. Chem.* **2011**, *50*, 451–462.

(33) Yi, X.; Zhang, C.; Guo, S.; Ma, J.; Zhao, J. Strongly Emissive Long-Lived ^{3}IL Excited State of Coumarins in Cyclometalated Ir(III) Complexes Used as Triplet Photosensitizers and Application in Triplet-Triplet Annihilation Upconversion. *Dalt. Trans.* **2014**, *43*, 1672–1683.

(34) Juris, A.; Balzani, V.; Barigelletti, F.; Campagna, S.; Belser, P.; Von Zelewsky, A. Ru(II) Polypyridine Complexes: Photophysics, Photochemistry, Eletrochemistry, and Chemiluminescence. *Coord. Chem. Rev.* **1988**, *84*, 85–277.

CONCLUSIONS

CONCLUSIONS

All the results presented throughout this work regarding the different hybrid systems described lead to the following main conclusions:

- Dye incorporation into different 1D-magnesium aluminophosphates, synthesized by the crystallization inclusion method, allows the control of the aggregation state of the chromophores with a general molecular skeleton built up by three fused aromatic rings. Indeed, an advantageous distribution of dye monomers and J-aggregates was achieved within the MgAPO-36 framework, giving as a result one-directional artificial antenna systems via energy transfer (FRET) process. Moreover, the total suppression of aggregation was attained by tight confinement of dyes into MgAPO-11 framework, with smaller pore dimensions. Thereby, highly fluorescent hybrid materials were achieved with significant anisotropic response to linearly polarized light, and with interesting optical properties such as room temperature delayed fluorescence, second harmonic generation, emission color switching and white light emission.
- White light emission was also achieved through the straightforward incorporation of different small aromatic molecules in a suitable proportion into the entangled Metal Organic Framework $[Zn_2(bdc)_2(dpNDI)]_n$, in which the photoactive dpNDI (a naphtalenediimide derivative) pillar interacts with those guests forming charge transfer complexes. Furthermore, by embedding halogenated aromatic guests into the same hybrid structure, phosphorescence at room temperature was switched on.
- Finally, through the rational attachment of BODIPY chromophores to a cyclometalated iridium centre, organometalic complexes with strong absorption capability in the visible range of the electromagnetic spectrum, high singlet oxygen production and efficient PDT action were developed. In addition to the photosensitizing features, the hybrid compounds showed dual action, emitting also fluorescence, and thus with applicability in bioimaging.

FUTURE OUTLOOK

FUTURE OUTLOOK

The reported work demonstrates that different types of organic-inorganic hybrid materials are very promising for their future implementation in diverse fields. Moreover, the systems presented here still have plenty of possibilities for further broadening the range of application, besides the improvement of the described ones. Thus, in order to continue with this topic, different experiments are now considered. Some of the approaches listed below are undergoing at this moment and others will be performed in a near future.

- One of the most interesting systems obtained is the LDS722/AEL. Generally, materials exhibiting non-linear optical features are very attractive for optoelectronic devices, storage systems and so on. In this sense, other dyes with intrinsic NLO properties are being encapsulated into this inorganic host in order to obtain SHG at different wavelength ranges and/or to increase the efficiency of the SHG. Particularly, the chosen dyes are trans-2-[4-[(Dimethylamino)styryl] benzothiazole (DMASBT) and trans-4-[4-(Dimethylamino)styryl]-1-methylpyridinium (4-DASPI) (Figure 8.1.), homologous to the former LDS 722. It has been previously demonstrated (section 4.2.3. in chapter 4) that the most efficient excitation wavelength to get intense SHG signal in the LDS722/AEL system was around 1000 nm. With these dyes, a higher efficiency together with a tuning of the excitation wavelength for SHG is pursued.

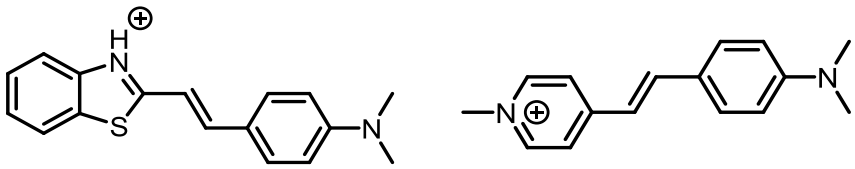

DMASBT **4-DASPI**

Figure 8.1. Molecular structures of the NLO dyes DMASBT and 4-DASPI.

In this regard, some syntheses have been already performed with these new NLO dyes, using the gel composition and synthesis conditions optimized for LDS 722 owing to the similarity between dyes (0.1 MgO: 1 P_2O5: 0.95 Al_2O_3: 1 EBA: 0.024 dye: 300 H_2O, heated statically for 24 hours at 195 ºC).

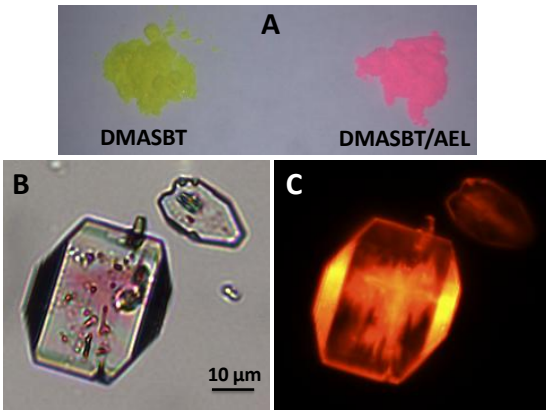

Figure 8.2. A) Solid DMASBT dye (yellow) and DMASBT/AEL powder (pink). Transmission (B) and emission under green excitation light (515-545 nm) (C) images of DMASBT/AEL crystals.

The synthesis with DMASBT dye rendered pure AEL phase. It is interesting that, while this dye in solid state is yellow, the DMASBT/AEL powder is bright pink (Figure 8.2.A), suggesting some kind of modification in the dye. It has been proven that the ICT ground state of the dye, characterized by a red-shifted absorption band with respect to the "localy-excited" (LE) band, is stabilized, as happened in the case of LDS722/AEL material. Importantly, the fluorescence efficiency, in the orange region of the visible spectrum (λ_{fl} = 595 nm, Figure 8.2.C) is the highest found so far among the previously described dye/MgAPO-11 systems, with a quantum yield of ϕ_{fl} = 0.84 under green excitation light (λ_{exc} = 525 nm). This suggests that the inherent flexibility of the molecule is highly impeded. The tight confinement of the dye in a preferential arrangement is also confirmed by confocal microscopy, recording dichroic ratio values up to 30. Also by means of microscopy techniques it has been seen that this sample is composed of large and regular-shaped crystals, but they are not homogeneously filled, and are only colored in the central area (Figure 8.2.B). Indeed, only 0.12 mmol DMASBT per 100 g solid sample are occluded into the MgAPO-11. Therefore, efforts will be focused on increasing the dye-loading rate by different approaches, for

instance adding ethanol to the precursor gel in order to enhance dye-solubility in this medium.

With respect to 4-DASPI dye, the synthesis also resulted in AEL phase but with AFI impurities. In this case, an optimization process is required to reduce or, in the best case, eliminate the AFI contribution and obtain pure 4-DASPI/AEL powder. Interestingly, a high amount of dye is occluded in this case, 6.93 mmol 4-DASPI per 100 g solid sample, giving as a result powder with a very intense red color and a homogeneous dye-incorporation into the crystals (Figure 8.3.). The resultant 4-DASPI/AEL sample shows its fluorescence band at around 610 nm, with a relatively low fluorescence quantum yield of ϕ_{fl} = 0.14 under green excitation light. This fact could be attributed to the high dye-loading, triggering reabsorption-reemission processes. Consequently, further synthesis will be performed with a lower dye-amount in the synthesis gel.

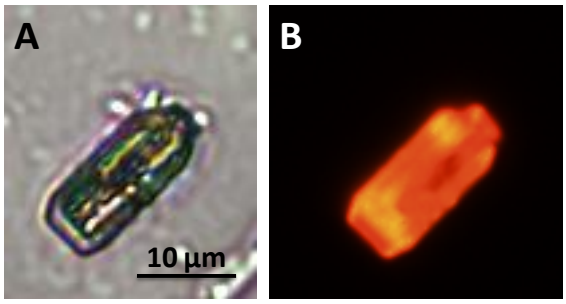

Figure 8.3. Transmission (A) and emission under green excitation light (515-545 nm) (B) images of a 4-DASPI/AEL particle.

Then, similar SHG characterization as that done for LDS722/AEL crystals will be performed with the new crystals at the KUL (Belgium).

➢ Regarding the previously described LDS722/AEL system and the homologous materials cited above with DMASBT and 4-DASPI dyes into AEL, it is worth noting that they can show interesting features for micro-laser or laser gain in a single microcrystal. This phenomenon is based on the fact that the laser emission necessarily occurs in a suitable resonant cavity for the feedback, and in this case the external surface of the crystal would act as a resonant cavity similar to a Fabry-Perot-type cavity.[1,2] Thus, the synthesis of sufficiently large magnesium aluminophosphate crystals with well defined geometrical shape would provide a simple approach to

achieve microlasers without the need for cutting, polishing and coating. Hence, efforts will be focused on attaining bigger particles of LDS722/AEL or homologous systems, DMASBT/AEL or 4-DASPI/AEL, mentioned in the previous point, since these dyes would show also laser action. One approach could be the growth of crystals by seed assisted approach,[3] a common strategy to control the particle size of the final product in zeolite-synthesis;[4] or a modification of the synthesis in terms of composition of the synthesis gel, reactants and heating time, as in the work reported by Chen *et al*.[5] The microlaser action will be studied in collaboration with Prof. Melanie Lebental of the group of Joseph Zyss at the Laboratory of Molecular and Quantum Photonics (ENS Cachan, France).

➢ Another goal for further studies is to achieve dye/AEL crystals with a more homogeneous size distribution, and also to reduce sample preparation time. With this purpose, synthesis conditions will be optimized by applying the microwave heating technique. In comparison with the synthesis performed in conventional oven, microwave heating will reduce the synthesis time from hours or even days to several minutes since it is a rapid and homogeneous heating procedure that accelerates nucleation, yielding also particles with uniform size distribution.[3,6,7]

➢ Besides the magnesium aluminophosphates used in chapter 4 (MgAPO-5, MgAPO-36 and MgAPO-11 with AFI, ATS and AEL structures, respectively), there are lots of different and interesting zeolite-type inorganic frameworks for the encapsulation of organic dyes. In a near future, new zeolitic structures will be studied, for example EUO-type structures with diagonally aligned pockets (Figure 8.4.A), could be attractive systems to accommodate the aromatic rings of dyes with similar molecular structure to the previously mentioned LDS 722, DMASBT or 4-DASPI, and also cyanines (see Figure 8.4.B), at both sides of the channels, while the conjugated chain (of different lengths) between these rings would be in the channels that connects the pockets. Also the encapsulation of neutral and large dyes such as perylene derivatives or BODIPY laser dyes within zeolitic structures without charge in their structure and with larger pore size could give as a result interesting hybrid materials. New synthesis will be developed since those neutral dyes are not highly soluble in aqueous medium.

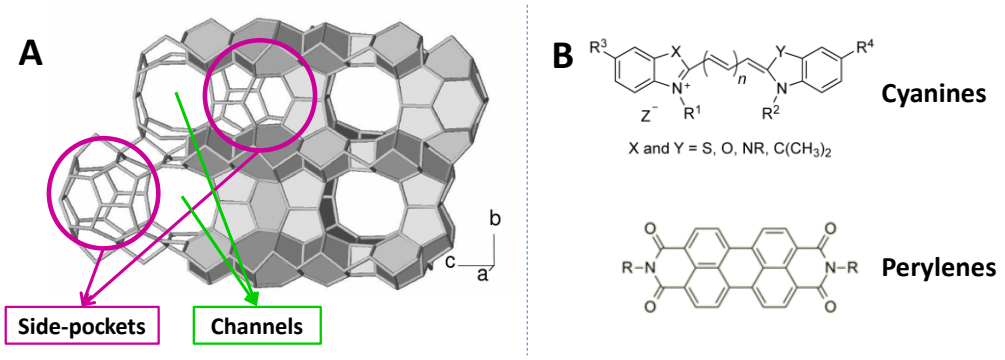

Figure 8.4. A) Framework structure of EOU-type zeolites. The channels and the side channels of the structure are pointed out.[8] B) General molecular structures of cyanine dyes and some perylene derivatives.

➢ In this regard, the neutral pores of different known MOFs such as MIL-101, MIL-53, MOF-74 or IRMOF-3 could be also suitable for the encapsulation of such neutral dyes. Moreover, MOFs can also serve as scaffold to hold photosensitizers. Indeed, it could be a promising approach since some MOF structures are flexible and depending on de medium they can show what is called "breathing", *i.e.* expansion or contraction of the structure. Thus, they could be used as a release system to delivery photosensitizers in a region of interest. On the other hand, the organic pillars of the MOF scaffolds can present -NH_2 groups for further functionalization with photoactive moieties. In this sense, photosensitizers containing carboxylic groups, such as the commercially available Rose Bengal (Figure 8.5.), could be easily grafted.

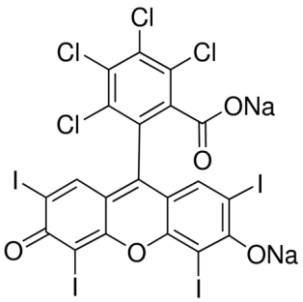

Figure 8.5. Molecular structure of Rose Bengal.

➢ Finally, related to the above mentioned proposal and also to the research carried out in chapter 6, new efficient photosensitizers based on BODIPY dyes are

being obtained. As has been discussed, it is possible to promote the population of the triplet state of the BODIPYs by enhancing the ISC process as a result of the close proximity of a heavy atom. In this sense, new photosensitizers based on BODIPY chromophores are being developed by using halogen atoms instead of the heavy Ir metal. Particularl, iodine atoms as substituents of the BODIPYs,should promote a more efficient ISC than the respective chlorine or bromine atoms. In this sense, different iodinated BODIPYs (see the general structure in Figure 8.6.A) have been already synthesized in order to study their suitability as PSs. Diverse substituent groups, being R_1 = electron donor or acceptor group, and R_2 = π-conjugated groups, have been attached to the BDP core at *meso* and 3 and 5 positions, respectively.

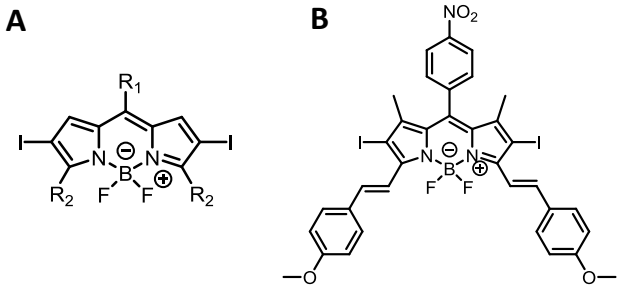

Figure 8.6. General molecular structure of the new BODIPYs under study (A) and an example of already synthesized one (B).

The effect of the different donor/acceptor substitution pattern at the *meso* position (R_1) of the BODIPY on the ICT process will be studied, since it is strongly related to their singlet oxygen production, as has been already studied in our research group with other BODIPY structures.[9] Moreover, by extending the π-conjugation of these compounds with R_2 substitution at the positions 3 and 5 of the BODIPY, PSs with absorption in the region of biological interest are pursued. Indeed, previous investigations demonstrated that π-conjugated substituents in those positions produce very large bathochromic shifts in the spectral bands.[10] In this sense, one of the most promising compounds under study is shown in Figure 8.6.B, which not only shows a relatively high singlet oxygen generation capacity ($\Phi_\Delta = 0.50$) but it also shows bright red fluorescence ($\phi_{fl} = 0.22$, $\lambda_{fl} = 762$ nm) upon red excitation light ($\lambda_{abs} = 705$ nm), allowing its use in theragnosis.

References

(1) Lafargue, C.; Bittner, S.; Lozenko, S.; Lautru, J.; Zyss, J.; Ulysse, C.; Cluzel, C.; Lebental, M. Three-Dimensional Emission from Organic Fabry-Perot Microlasers. *Appl. Phys. Lett.* **2013**, *102*, 251120.

(2) Gozhyk, I.; Boudreau, M.; Haghighi, H. R.; Djellali, N.; Forget, S.; Chénais, S.; Ulysse, C.; Brosseau, A.; Pansu, R.; Audibert, J. F.; Gauvin, S.; Zyss, J.; Lebental, M. Gain Properties of Dye-Doped Polymer Thin Films. *Phys. Rev. B - Condens. Matter Mater. Phys.* **2015**, *92*, 1–14.

(3) Mintova, S.; Gilson, J.-P.; Valtchev, V. Advances in Nanosized Zeolites. *Nanoscale* **2013**, *5*, 6693–6703.

(4) Majano, G.; Darwiche, A.; Mintova, S.; Valtchev, V. Seed-Induced Crystallization of Nanosized Na-ZSM-5 Crystals. *Ind. Eng. Chem. Res.* **2009**, *48*, 7084–7091.

(5) Chen, Y.; Zhai, J.; Xu, X.; Li, I.; Ruan, S.; Tang, Z. Synthesis of Large MgAPO-11 Single Crystals in a F^- Free System. *CrystEngComm* **2014**, *16*, 2984-2989.

(6) Tompsett, G. A.; Conner, W. C.; Yngvesson, K. S. Microwave Synthesis of Nanoporous Materials. *ChemPhysChem* **2006**, *7*, 296–319.

(7) Gharibeh, M.; Tompsett, G. A.; Conner, W. C. Microwave Reaction Enhancement: The Rapid Synthesis of SAPO-11 Molecular Sieves. *Top. Catal.* **2008**, *49*, 157–166.

(8) Baur, W. H.; Fischer, R. X. *Zeolite-Type Crystal Structures and Their Chemistry. Framework Type Codes DAC to LOV*; Baur, W. H., Fischer, R. X., Eds.; Springer: Berlin, **2002**.

(9) Epelde-Elezcano, N.; Palao, E.; Manzano, H.; Prieto-Castañeda, A.; R. Agarrabeitia, A.; Tabero, A.; Villanueva, Á.; de la Moya, S.; López-Arbeloa, I.; Martínez-Martínez, V.; Ortiz, M. J. Advanced Photosensitizers Based on Orthogonal BODIPY Dimers: Rational Design to Finely Modulate Singlet Oxygen Generation. *Submitted*.

(10) Lu, H.; Mack, J.; Yang, Y.; Shen, Z. Structural Modification Strategies for the Rational Design of red/NIR Region BODIPYs. *Chem. Soc. Rev.* **2014**, *43*, 4778–4823.

List of publications:

Published

- García, R.; Martínez-Martínez, V.; Sola Llano, R.; López-Arbeloa, I.; Pérez-Pariente, J. One-Dimensional Antenna Systems by Crystallization Inclusion of Dyes (One-Pot Synthesis) within Zeolitic MgAPO-36 Nanochannels. *J. Phys. Chem. C* **2013**, *117*, 24063–24070.
- Martínez-Martínez, V.; García, R.; Gómez-Hortigüela, L.; Sola Llano, R.; Pérez-Pariente, J.; López-Arbeloa, I. Highly Luminescent and Optically Switchable Hybrid Material by One-Pot Encapsulation of Dyes into MgAPO-11 Unidirectional Nanopores. *ACS Photonics* **2014**, *1* (3), 205–211.
- Martínez-Martínez, V.; Sola Llano, R.; Furukawa, S.; Takashima, Y.; López Arbeloa, I.; Kitagawa, S. Enhanced Phosphorescence Emission by Incorporating Aromatic Halides into an Entangled Coordination Framework Based on Naphthalenediimide. *ChemPhysChem* **2014**, *15* (12), 2517–2521.
- Sola-Llano, R.; Martínez-Martínez, V.; Fujita, Y.; Gómez-Hortigüela, L.; Alfayate, A.; Uji-i, H.; Fron, E.; Pérez-Pariente, J.; López-Arbeloa, I. Formation of a Nonlinear Optical Host-Guest Hybrid Material by Tight Confinement of LDS 722 into Aluminophosphate 1D Nanochannels. *Chem. - A Eur. J.* **2016**, *22*, 15700–15711.

Submitted

- Palao, E.; Sola-Llano, R.; Manzano, H.; Agarrabeitia, A. R.; Tabero, A.; Villanueva, A.; López-Arbeloa, I.; Martínez-Martínez, V.; Ortiz, M. J. AcetylacetonateBODIPY−Biscyclometalated Iridium (III) Complexes: Effective strategy towards smarter fluorescent-photosensitizer agent.

In preparation

- Unlimited Optical Applications by Encapsulation of Commercial Dyes into 1D Alumonophosphate of Small Pore Size.
- Antenna effect: Energy transfer from monomers to J-Aggregates in 1D systems